# Precision Diagnostics of Pulsation and Evolution in Helium-Rich Low-Mass Stars

**Pamela Martin, B.A. (Mod).**
**Armagh Observatory and Planetarium** & **Trinity College Dublin**
**2019**

SCHOOL OF PHYSICS
UNIVERSITY OF DUBLIN
TRINITY COLLEGE

# Declaration

I declare that this thesis has not been submitted as an exercise for a degree at this or any other university and it is entirely my own work.

I agree to deposit this thesis in the University's open access institutional repository or allow the Library to do so on my behalf, subject to Irish Copyright Legislation and Trinity College Library conditions of use and acknowledgement.

**Name:** Pamela Martin

**Signature:** ........................................ **Date:** ...........................

# Abstract

In this thesis we discuss many types of low mass stars linked by their un-usually low hydrogen atmospheric abundance, usually completely replaced with helium. We begin with the hot subdwarfs; subdwarf O and B (sdB, sdO) stars are low-mass core helium burning stars with extremely low-mass hydrogen envelopes. Their atmospheres are generally helium deficient; how-ever a minority have extremely helium-rich surfaces. An additional fraction have an intermediate surface-helium abundance, occasionally accompanied by peculiar abundances of other elements. LS IV$-14°$116 is a non-radially pulsating slowly-rotating chemically-peculiar helium-rich sdB with a 4 dex surface excess of zirconium, yttrium, and strontium. The pulsations are un-expected and unexplained, as the star is 6 000K hotter than the blue edge of the hot subdwarf g-mode instability strip. The presence of pulsations offers a rare opportunity to study the structure of the photosphere. Using a time series of ultraviolet and visual spectra from the Very Large Tele-scope (VLT) we have measured high precision radial velocities in individual spectral lines thoughout the entire spectrum. We confirm that the presence of the photometric variability results in the physical motion of the photo-sphere, resolving the different layers proves difficult due to the horizontal nature of the propagation of a gravity wave.

In the case of BX Cir, a short-period pulsating extreme helium supergiant, the absence of hydrogen opacity allows us to see deeper into the atmosphere than in any other star. High resolution spectra from the Southern African Large Telescope (SALT) has allowed us to apply the methodology developed for LS IV$-14°$116 to resolve the motion in the atmosphere of BX Cir. Our aim was to resolve the motion of different layers within the photosphere, and the passage of the outward travelling waves.

We have investigated the kinematics of three groups of hot subdwarf stars to determine whether they belong to similar or different Galactic popula-

tions. We confirm that the majority of helium-deficient subdwarfs show a kinematic distribution similar to that of thick disk stars. Helium-rich sdBs show a more diverse kinematic distribution. Although the majority are probably disk stars, a minority show a much higher velocity dispersion consistent with membership of a Galactic halo population.

Since the discovery of R Coronae Borealis in 1795, several classes of hydrogen-deficient stars have been identified (Jeffery, 2008) but, despite their great intrinsic brightness, their members are so rare that virtually all lie at distances too great to measure directly from the ground. Reliable measurements have only become possible for a significant number following the second release of data from the astrometric space mission *Gaia*.

Following this data release the new parallax measurements and more precise proper motions have allowed us to calculate the Galactic space velocities and orbits for over 200 hydrogen-deficient low-mass stars. Distances, and hence luminosities, are critical for explaining the origin and life histories of stars which possess so little surface hydrogen that, in several cases, its abundance cannot be measured. We discuss the formation and evolution of some of the rarest stars in the Galaxy.

*For my Mum.*

# Acknowledgements

# List of Publications

1. **Martin P.**, Jeffery, C. S., Naslim, N., and Woolf, V. M. (2017). Kinematics of Subluminous O and B Stars by Surface Helium Abundance. MNRAS, 467:68-82.

2. Jeffery, C. S., Baran, A. S., Behara, N. T., Kvammen, A., **Martin, P.**, Naslim, N., Ostensen, R. H., Preece, H. P., Reed, M. D., Telting, J. H., and Woolf, V. M. (2017). Discovery of a variable lead-rich hot subdwarf: UVO 0825+15. MNRAS, 465:3101-3124.

3. **Martin, P.** and Jeffery, C. S. (2017). LS IV$-14°116$ : A Time-Resolved Spectroscopic Study. Open Astronomy, 26:240-245

4. **Martin, P.** and Jeffery, C. S. in prep. First *Gaia* results for hydrogen-deficient supergiants and related stars.

# Contents

# List of Figures

# List of Tables

# Introduction

<div style="text-align: right">**1**</div>

In essence all information about astronomical objects outside the solar system comes through the study of electromagnetic radiation as it reaches us. The most detailed astrophysical information is obtained from high resolution studies which involve detecting the light arriving at the Earth as a function of its component wavelengths. This allows detailed spectroscopic features to be identified separately from broadband features such as colour. For lines observed in an astronomical spectrum one can use laboratory data to extract information on composition, temperature, abundance, motions, pressure and magnetic fields.

The relative strengths and shapes of the absorption lines in a stars spectrum are used to classify a star by effective temperature and photospheric pressure, a process referred to as assigning a spectral type. In principle, spectral classification separates the observed stars into about 60 temperature steps. These are arranged from the hottest to the coolest thought the sequence O B A F G K M with 10 subdivisions per letter group. The mass and age of a star, and to a lesser extent its chemical composition and rotation, determine the luminosity, radius, and temperature of the star.

## 1.1   The Hertzsprung-Russell diagram

The Hertzsprung-Russell diagram (HR diagram) is one of the most important tools in the study of stellar evolution. Developed independently in the early 1900s by Ejnar Hertzsprung and Henry Norris Russell. The theoretical HR diagram plots the temperature of stars against their luminosity (Fig. 1.1) and the observational HR diagram (or colour-magnitude diagram) plots the stars temperature against their absolute magnitude.
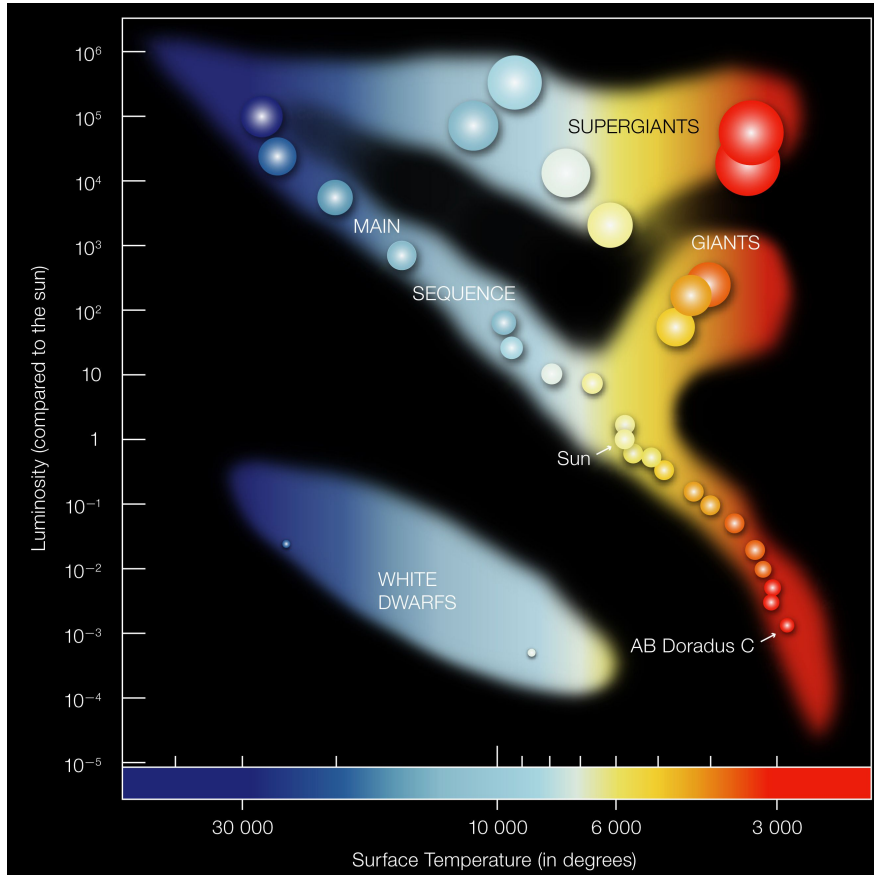
**Figure 1.1:** A Hertzsprung-Russell diagram

Luminosity is the total amount of energy emitted per unit of time, values for luminosity are often given in the terms of the luminosity of the Sun, $L_\odot$. Assuming a blackbody:

$$L = 4\pi R^2 \sigma T_{\text{eff}}^4 \tag{1.1}$$

where R is the stars radius, $T_{\text{eff}}$ is the effective temperature and $\sigma$ is the Stefan–Boltzmann constant.

Depending on its initial mass, every star goes through specific evolutionary stages dictated by its internal structure and to some extent chemical composition. Each of these stages corresponds to a change in the temperature and luminosity of the star, which can be seen to move to different regions on the HR diagram as it evolves.

There are 3 main evolutionary stages of the HR diagram:

• The main sequence dominates the HR diagram comprising of hot, luminous stars

and cool, faint stars. It is here that stars spend about 90% of their lives burning hydrogen into helium in their cores. The Sun is a main sequence star with a luminosity of $1\,L_\odot$ and a temperature of around 5,777 Kelvin.

- Red giant and supergiant stars lie above the main sequence. They have low surface temperatures and high luminosities which, and hence have large radii (eq. 1.1.) Stars enter this evolutionary stage once they have exhausted the hydrogen fuel in their cores and have started to burn helium and other heavier elements.

- White dwarfs are the final evolutionary stage of low to intermediate mass ($<8\,M_\odot$) stars, and are found below the MS. These stars are compact and have a low luminosity.

In short, the HR diagram can be used to summarise the evolution of stars, or to investigate the properties of a collection of stars.

## 1.2 A Short Introduction to Stellar Evolution

The evolution of a star after its main sequence phase depends on the stellar mass. Stars are classified as low-mass stars if their mass is $<2M_\odot$, intermediate-mass stars if their mass is between 2 and $8M_\odot$, and massive stars[1] if their mass is $>8M_\odot$.

Low-mass stars with masses between 0.8 and 2 $M_\odot$ develop a degenerate helium core after their main sequence phase, leading to a relatively long-lived red giant branch phase and to the ignition of helium in such helium flash. Intermediate-mass stars ignite helium stably in a non-degenerate core and after the central helium burning they develop a degenerate carbon-oxygen core. Both low- and intermediate-mass stars shed their envelopes by strong stellar winds at the end of their evolution and their remnants are CO white dwarfs.

Taking the example of a $1\,M_\odot$, the star leaves the main sequence when the hydrogen in its core is consumed. The core can no longer maintain equilibrium. It begins to contract and heat up, the outer layers of the star expand. Hydrogen fusion continues

---

[1]Massive stars ignite carbon and heavier elements in the core until an iron core is formed which collapses. These will not be discussed in this thesis.

in a shell around the core that now consists of 98% helium, and 2% heavier elements. The hydrogen-burning shell adds helium to the core beneath it, which consequently contracts and heats. At the same time, the shell becomes hotter, thinner and more luminous. The hydrogen-rich outer layers expand, and the star evolves upwards along the so-called red giant branch (RGB). As the core continues to contract and heat up, fusion reactions in the surrounding shell increase, due to the higher temperature in the shell. The star's total luminosity increases as it continues to expand and it becomes a red giant.

Once the helium core reaches a critical mass, nuclear burning of helium begins, producing carbon and oxygen in a relatively long-lived phase of evolution. The energy derived from helium-burning heats the helium core and forces it to expand. Thus the hydrogen-burning shell may actually get weaker at this point, the overall luminosity drops and the star contracts. When the core temperature reaches about 100 million K, helium begins to fuse into carbon, through the triple-alpha process. At this high temperature, helium nuclei can violently collide and fuse. Three helium nuclei fuse to form carbon. Other helium nuclei collide with the carbon nuclei and produce oxygen.

Igniting the helium core under degenerate conditions results in a run-away process, called the helium flash. Afterwards the star settles again on a sequence called the Horizontal branch. Now the star has a helium burning core, surrounded by a hydrogen burning shell, causing a raise in the luminosity and a shift to the red end of the HR Diagram as the C/O core grows. This is called the asymptotic giant branch (AGB) phase.

As helium is exhausted in the core, it contracts again, the outer layers expand more and the star becomes redder and even more luminous. Now hydrogen fuses in an outer shell, and helium fuses within an inner shell, building an extremely hot, but inert core composed of carbon and oxygen. At this point, the nuclear burning ends and the core contracts to an incredibly dense sphere of degenerate matter, called a white dwarf. The outer layers are ejected in the interstellar medium, stripping about 30% of the star's mass. For several thousand years, this expanding shell, called a planetary nebula, is illuminated by the intense ultraviolet radiation of the now exposed stellar core. Gradually the nebula expands and fades away, returning its substance to the

interstellar medium.

White dwarfs slowly cool down from their initial temperatures of about 100 000K, trapping up to 1.4 M$_\odot$ of plasma into an Earth-sized (R$\sim$6000km) balls. The white dwarf scenario is the fate of (almost) all low-mass stars, including our own Sun.

## 1.3 Basic Galactic Structure

A galaxy is a stellar system, a gravitationally bound assembly of stars or other point masses. The behaviour of these systems is determined by Newton's laws of motion and Newton's law of gravity, and the study of this behaviour is the branch of theoretical physics called stellar dynamics. The kinematics of a galaxy on the other hand is the observational description of the positions and motions of the stars in the system.

Our own galaxy, the Milky Way, is a spiral galaxy, Figure 1.2 highlights its main features. In the centre of the Milky Way, surrounding the black hole, is a central group of stars call the Galactic bulge. It contains a mixture of old and young populations and in the inner regions active star formation occurs. The disk can be separated into two populations, the thin disk that contains a young population of stars as well as gas and dust where there is active star formation. The stars of the thick disk are older and have lower metallicities than those of the thin disk. About 1% of the stellar mass in the Galaxy is contained in the stellar halo, which contains old stars of low metallicity, globular clusters and tidal streams. Stars belonging to different populations show widely differing kinematic behaviour. Studying the motions of a sample of stars give important insights into the general structure of the Galaxy.

### 1.3.1 Radial Velocities

A stars radial velocity is the measurement of a stars motion in the direction of the observer, it is an essential observation in the calculation of a stars galactic velocities and orbit. Light from an object with a substantial relative radial velocity will be subject to the Doppler effect, so the frequency of the light decreases for receding objects (redshift) and increases for objects that are approaching (blueshift). If we know the rest wavelength ($\lambda$) of the line and by how much it is shifted ($\Delta\lambda$) it is easy to calculate
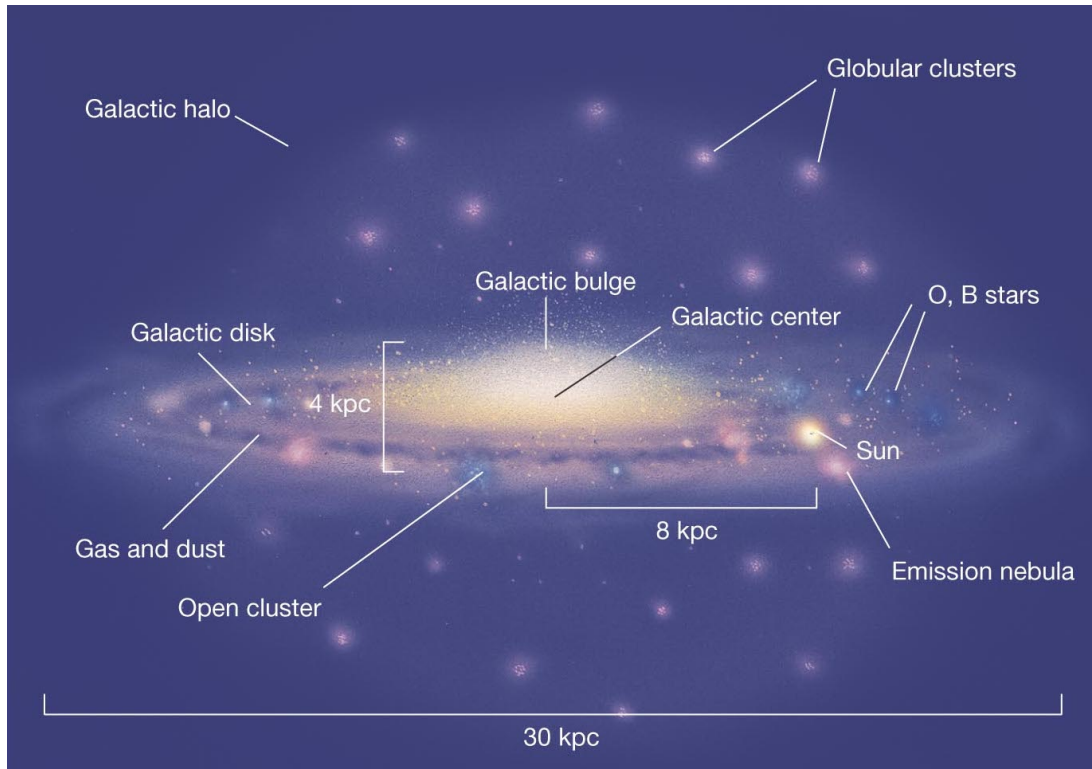
**Figure 1.2:** Schematic of the structure of the Milky Way ©Pearson, 2008.

the velocity, $v$ using the doppler equation 1.2.

$$v = \frac{\Delta\lambda c}{\lambda} \qquad (1.2)$$

where $c$ is the speed of light.

Corrections need to be applied to account for the heliocentric motion, this can be done using programs such as STARLINK's RV which produces a report listing the components, in a given direction, of the observer's velocity on a given date.

The measurement of radial velocity by the doppler measurement also includes the gravitational redshift. The expected amount of gravitational redshift for light from the surface of the star reaching the observer is proportional to the object's mass and surface gravity.

$$z_g = \frac{1}{c^2}\sqrt{GMg} \qquad (1.3)$$

where $c$ is the speed of light, $G$ is the gravitational constant and $M$ is the mass of the star.

For hot subdwarfs star of mass $\sim 0.5\,\mathrm{M_\odot}$ the effect of the gravitational redshift is of the order of $2\,\mathrm{km\ s^{-1}}$. But for the more compact WD stars the effect is much greater and must be corrected for.

### 1.3.2 Galpy

`galpy` is a python package for Galactic-dynamic calculations (Bovy, 2015). It contains a model, MWPotential2014, for the Milky Way's gravitational potential that is designed to provide a simple, easy-to-use model in cases where a realistic model for the Milky Way is required. It consists of a bulge modelled as a power-law density profile that is exponentially cut off with a power-law exponent of –1.8 and a cut-off radius of 1.9 kpc, a Miyamoto-Nagai Potential disk (Miyamoto and Nagai, 1975), and a dark-matter halo described by a Navarro-Frenk-White potential (Navarro et al., 1996). The values for these constraints that the parameters of the model are fit to are summarised in the middle section of table 1.3 and are discussed in detail in (Bovy, 2015). MWPotential2014 does not contain the supermassive black hole at the centre of the Milky Way.

Figure 1.4 displays the rotation curve and its decomposition into bulge, disk, and dark-halo contributions. The masses of the three components are given in Table 1.3 as well as other key properties.

## 1.4 Helium-Rich Low-Mass Stars

The focus of this thesis is on stars which have departed from the canonical evolution channels and have evolved to have a helium enriched atmospheres. I will introduce these stars in the following sections.

### 1.4.1 Hot Subdwarf Stars

Hot subluminous stars or subdwarfs are traditionally classified into three types by their spectra (Drilling et al., 2003). Subdwarf B (sdB) stars have a surface effective temperature $T_{\mathrm{eff}}$ in the range 20,000–40,000 K and hydrogen-Balmer absorption lines

Parameters and Properties of `MWPotential2014`

| Parameter | MWPotential2014 | Constraint |
|---|---|---|
| $R_0$ (kpc) | 8 | Fixed |
| $v_c(R_0)$ (km s$^{-1}$) | 220 | Fixed |
| $f_b$ | 0.05 | $\cdots$ |
| $f_d$ | 0.60 | $\cdots$ |
| $f_h$ | 0.35 | $\cdots$ |
| Bulge power$-$law exponent | $-1.8$ | Fixed |
| Bulge cut$-$off radius (kpc) | 1.9 | Fixed |
| $a$ (kpc) | 3.0 | $\cdots$ |
| $b$ (pc) | 280 | $\cdots$ |
| Halo $r_s$ (kpc) | 16 | $\cdots$ |
| $\sigma_b$ (km s$^{-1}$) | 109 | $117 \pm 15$ |
| $F_Z(R_0, 1.1\,\text{kpc})\,(2\pi G\,M_\odot\,\text{pc}^{-2})$ | 72 | $67 \pm 6$ |
| $\Sigma_{\text{vis}}(R_0)\,(M_\odot\,\text{pc}^{-2})$ | 53 | $55 \pm 5$ |
| $F_Z$ scale length (kpc) | 3.2 | $2.7 \pm 0.1$ |
| $\rho(R_0, z=0)\,(M_\odot\,\text{pc}^{-3})$ | 0.10 | $0.10 \pm 0.01$ |
| $(d\ln v_c/d\ln R)|_{R_0}$ | $-0.10$ | $-0.2$ to $0$ |
| $M(r < 60\,\text{kpc})\,(10^{11}\,M_\odot)$ | 4.1 | $4.0 \pm 0.7$ |
| $M_b\,(10^{10}\,M_\odot)$ | 0.5 | $\cdots$ |
| $M_d\,(10^{10}\,M_\odot)$ | 6.8 | $\cdots$ |
| $R_d$ (kpc) | 2.6 | $\cdots$ |
| $\rho_{\text{DM}}(R_0)\,(M_\odot\,\text{pc}^{-3})$ | 0.008 | $\cdots$ |
| $M_{\text{vir}}\,(10^{12}\,M_\odot)$ | 0.8 | $\cdots$ |
| $r_{\text{vir}}$ (kpc) | 245 | $\cdots$ |
| Concentration | 15.3 | $\cdots$ |
| $v_{\text{esc}}(R_0)$ (km s$^{-1}$) | 513 | $\cdots$ |

**Figure 1.3:** Parameters and Properties of MWPotential2014 (Bovy, 2015).

wider than in normal B stars; subdwarf O (sdO) stars, with $T_{\text{eff}}$ ranging from 40,000–80,000 K have strong He$^+$ absorption lines; subdwarf OB (sdOB) stars represent a transition between O and B types (Heber, 2009; Moehler et al., 1990). These objects are located below the upper main sequence on a HR diagram (Fig. 1.5). Identified as low-mass core-helium burning stars with low-mass envelopes, they are also known as extreme horizontal branch (EHB) stars. The atmospheres of sdB stars are generally helium deficient, as radiative levitation and gravitational settling cause helium to sink below the hydrogen-rich surface (Heber, 1986), deplete other light elements and enhance many heavy elements in the photosphere (O'Toole and Heber, 2006). However almost 10% of the total subdwarf population comprises stars with helium-rich atmospheres
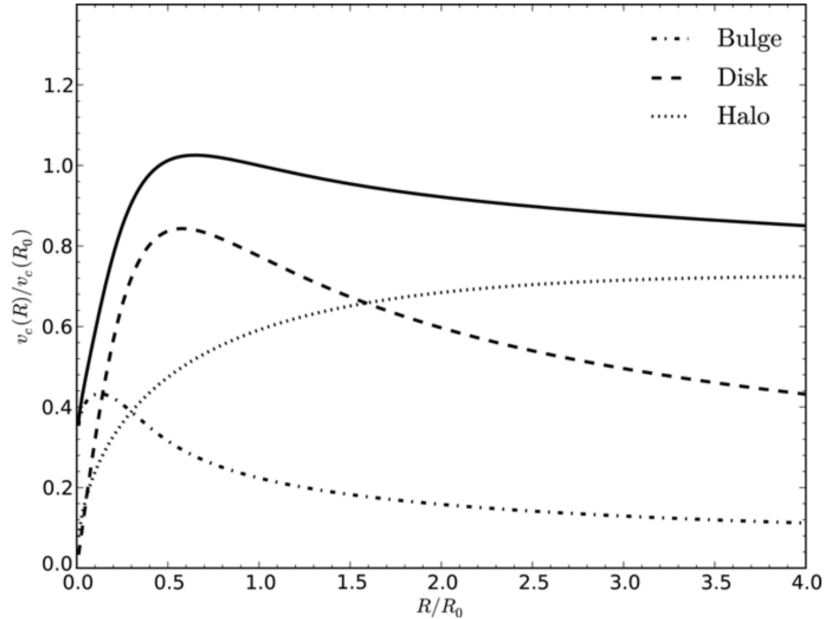
**Figure 1.4:** Rotation curve of MWPotential2014 out to 32 kpc and its decomposition into bulge, disk, and halo contributions (Bovy, 2015).

(Geier et al., 2017). The helium-rich subdwarfs may be further divided into extremely helium-rich stars and a small number of intermediate helium-rich stars, a number of show extreme chemical peculiarities (Naslim et al., 2011, 2013).

### 1.4.2 Extreme Helium Supergiants

Extreme helium stars (EHes) are low-mass supergiants of spectral types Ap and Bp, the peculiarity being that the Balmer lines are either exceptionally weak or totally absent, their place being taken by neutral helium. The absence of hydrogen means that the metallic-line spectrum is much stronger than in a normal star. Nevertheless, carbon, nitrogen and, in some stars, oxygen are abnormally strong. These peculiarities point to a highly-processed stellar surface and hence to a very late stage of stellar evolution. There are approximately 25 of these stars known.

### 1.4.3 R Coronae Borealis and Hydrogen Deficient Carbon stars

Pigott and Englefield (1797) reported the discovery of a star, R Coronae Borealis, which showed a sudden decline in brightness in 1795. Since then over 100 R CrB
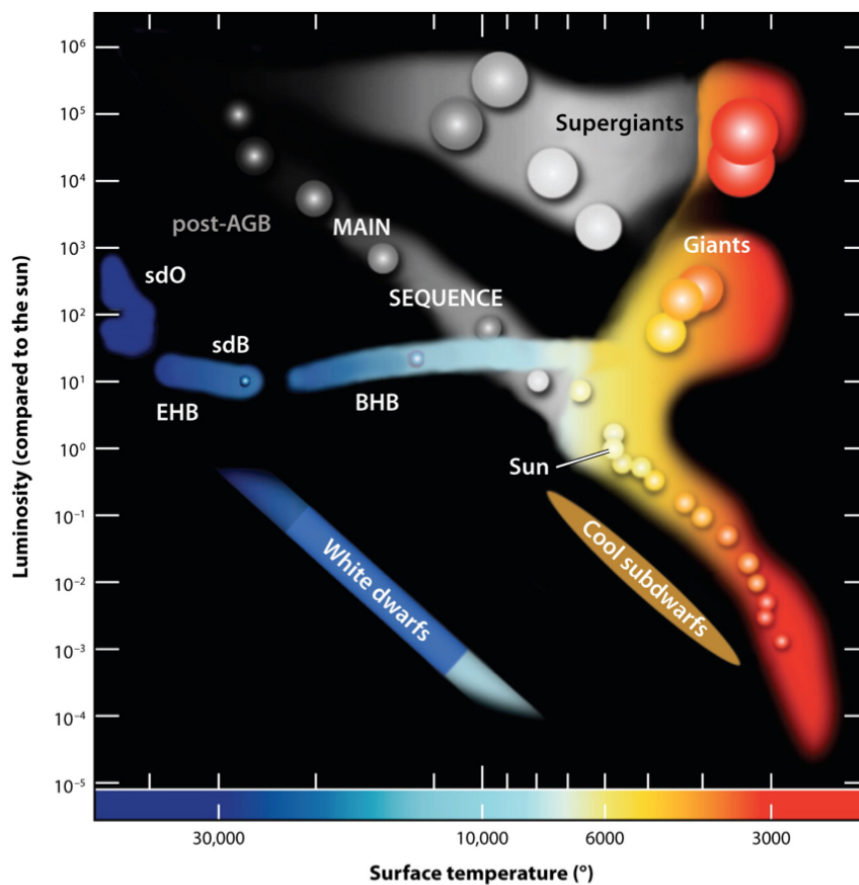
Heber U. 2009.
Annu. Rev. Astron. Astrophys. 47:211–51

**Figure 1.5:** Hertzsprung-Russell diagram (Heber, 2016).

stars have been discovered in our Galaxy (Tisserand et al., 2018). Most R CrB stars resemble F-or G-type supergiants and all undergo massive declines of up to 8 mag due to the formation of carbon dust at irregular intervals. Apparently related to the RCrB stars are the hydrogen-deficient carbon (HdC) stars. The five known HdC stars are similar to the RCrB stars spectroscopically but do not show declines or IR excesses (Warner, 1967). There are a few scenarios which predict how these stars create their dust shells. One scenario suggest that dust forms near the star and moves quickly away due to radiation pressure, expanding to cover the photosphere and parts of the emission regions (Figure 1.6).
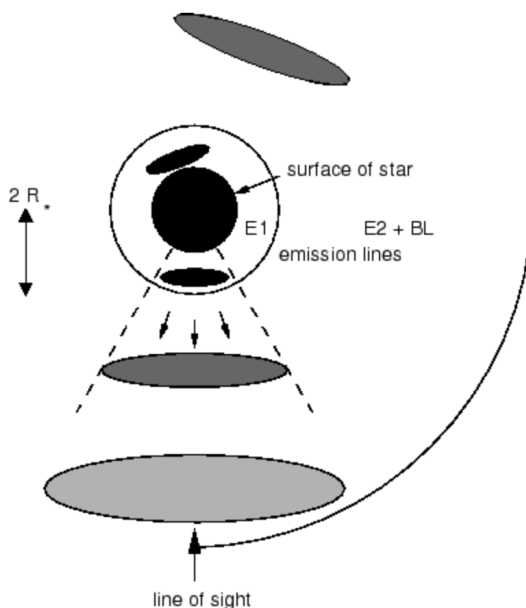
**Figure 1.6:** Scenario for Near-Star dust formation. In this scenario, dust forms near the star and moves quickly away due to radiation pressure, expanding to cover the photosphere and parts of the emission regions. Small dust clouds may form during each pulsation cycle of the star. Declines only occur when a cloud forms along the line of sight (Clayton, 1996).

### 1.4.4 [WC] stars

The [WC] stars are central stars of planetary nebulae (CSPNe) which present a similar spectroscopic appearance to the massive carbon-rich Wolf-Rayet stars. They are in the late stages of evolution of low or intermediate mass stars with only a few dozen examples known in the Milky Way plus a handful in the Magellanic Clouds. They present with an unusual surface chemical composition with approximate 50% helium by mass, 10% oxygen and the rest carbon (Crowther, 2008a). The defining characteristic amongst Milky Way stars is the presence of a bright nebula for [WC] stars.

### 1.4.5 PG1159 stars

The PG 1159 stars were revealed in the Palomer-Green survey as a new spectral class of H-deficient post-AGB stars. They are dominated by absorption lines of highly ionised He, C and O (Wesemael et al., 1985) and are in transition between being the central star of a planetary nebula (PN) and being a hot white dwarf.

Currently, 51 stars are members of the PG 1159 family, which span a wide domain

in the log$g$ - T$_{\text{eff}}$ diagram: $5.5 < \log g < 8$ and $75\,000K < T_{\text{eff}} < 200\,000K$.

### 1.4.6  O(He) stars

O(He) stars have higher effective temperatures and surface gravities than the EHe stars and are classified spectroscopically by an almost pure HeII optical absorption spectrum. There are 9 such objects known to date, they are found with and without nebulae. Figure 1.7 shows the effective temperature and log$g$ for all known O(He) stars (red), the EHe stars (green) and the hot white dwarfs (black).

I frequently discuss the last three groups of stars together, referring to them as CSPNe, as they are all have members known be surrounded by planetary nebulae.
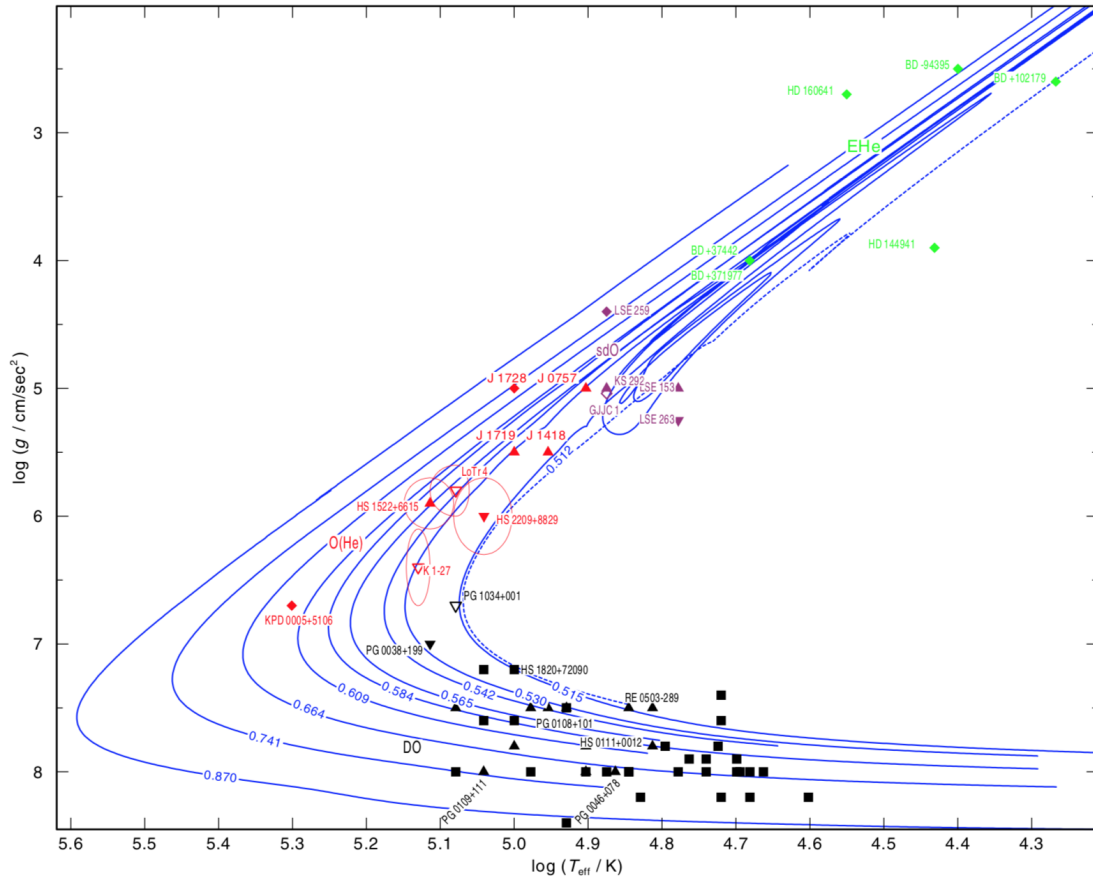


**Figure 1.7:** Effective temperature and log$g$ for O(He) stars and related objects (Reindl et al., 2014). Open points indicate the detection of a planetary nebula.

## 1.5 Evolution channels

### 1.5.1 Hot-Flasher Scenario

In general low mass stars undergo the helium core flash (HeCF) at the tip of the red giant branch (RGB). If there is sufficient mass loss on the RGB the star can depart from the RGB and experience the HeCF while descending the hot white dwarf cooling track (Castellani and Castellani, 1993). One channel that achieves this is common envelope ejection. This is where, in a close binary system, a giant star fills its Roche lobe near the tip of the giant branch and experiences dynamical mass transfer onto its companion. The secondary is now unable to accrete all of the transferred matter and starts to fill and ultimately overfill its own Roche lobe. This leads to the formation of a common envelope surrounding both stars, forming an immersed binary system. Because of friction with the envelope, these two components spiral towards each other until enough orbital energy has been released to eject the envelope (Paczynski, 1976). This leaves a close binary with an orbital period typically between 0.1 and 10d, consisting of the core of the giant (the hot subdwarfs) and the secondary.

One can also achieve this mass-loss with stable Roche lobe overflow (RLOF) or with high stellar winds. The stage at which they experience the HeCF effects the evolution channel and the abundances.

1. Early hot flashers: HeCF during the stage of constant luminosity after leaving the RGB-tip. These become hot subdwarfs with standard H/He envelopes (Fig. 1.8b)

2. Late hot flashers with shallow mixing. Become He-enriched hot subdwarfs due to convection dilution of the envelope into deeper regions of the star (Fig. 1.8c).

3. Late hot flashers with deep mixing in which the H-rich envelope is engulfed and burned in the convective zone generated by the primary HeCF (Fig. 1.8d).
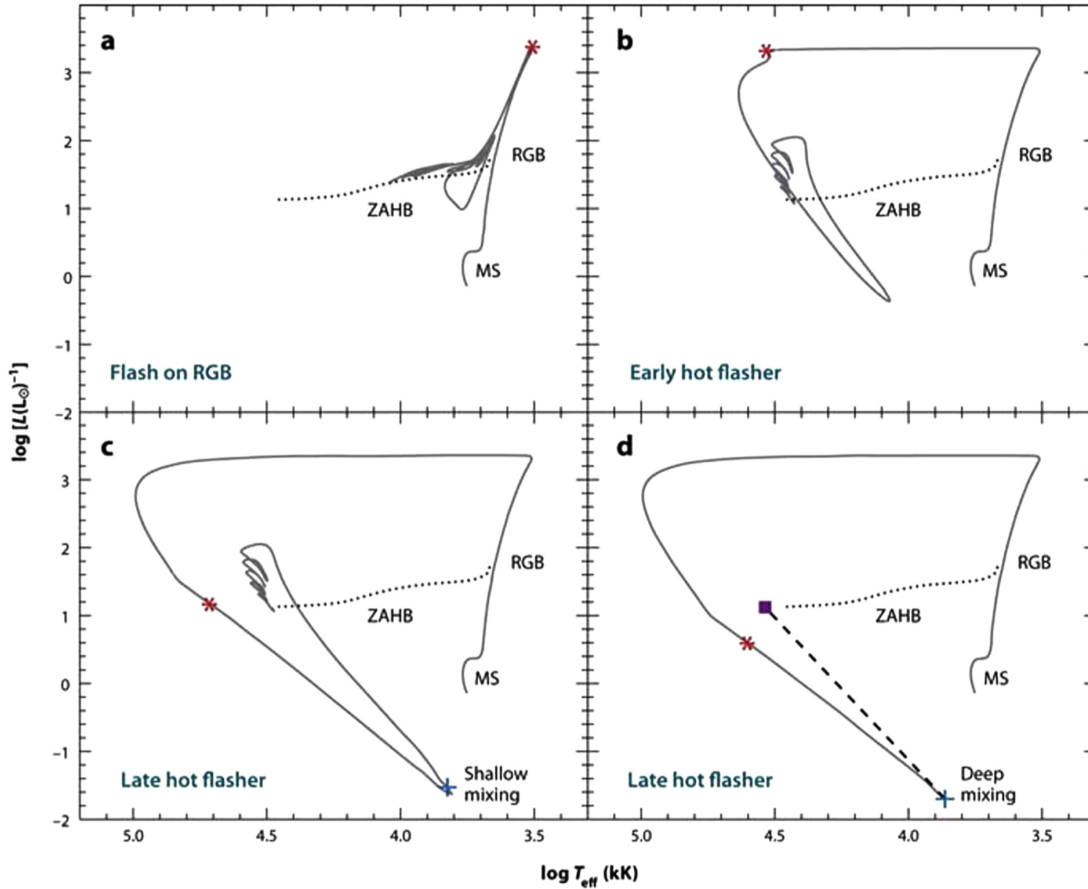
**Figure 1.8:** Evolution of a solar metallicity star from the main sequence through the helium flash to the zero-age horizontal-branch (Heber, 2016).

### 1.5.2 Merging of White Dwarfs

The merging of two white dwarfs (WD) is one way to produce a single star with a helium-rich atmosphere. This is important as the EHes, R CrB and HdC stars have never been detected to have a companion[1] .

There are quite a few models computing the evolution of double white dwarf mergers but here I will describe the He+He WD mergers from Zhang and Jeffery (2012) as an example. Figure 1.9 shows the evolution of a $0.3\,M_\odot WD + 0.3\,M_\odot WD$ in luminosity (right) and radius (left). The less massive WD is disrupted and part of the debris forms a hot corona, the remainder forms a disk which subsequently accretes onto the surviving WD. Fast accretion occurs on the timescale of minutes which occurs in a

---

[1]With the exception of DY Cen who's status as a binary system is under revision.

hot corona with more than half the mass of the donor star. During the slow accretion the remaining material is accreted from a keplerian disk onto the hot corona. During the slow accretion the helium burning shell heats the corona and forces it to expand. Subsequently when accretion has ended the star undergoes roughly a dozen helium flashes each decreasing in intensity and luminosity until the flame reaches the centre of the star. At this point the standard core-helium burning phase is established. For the lower mass mergers (i.e 0.3 + 0.3 HeWD) we are left with a carbon and oxygen (C/O) core and the star will contract onto the WD cooling track. For the mergers of higher mass (i.e. 0.4+0.4 HeWD ) a helium shell will ignite and burn above the C/O core causing the star to increase in luminosity and pass through a giant phase before cooling onto the WD cooling track.
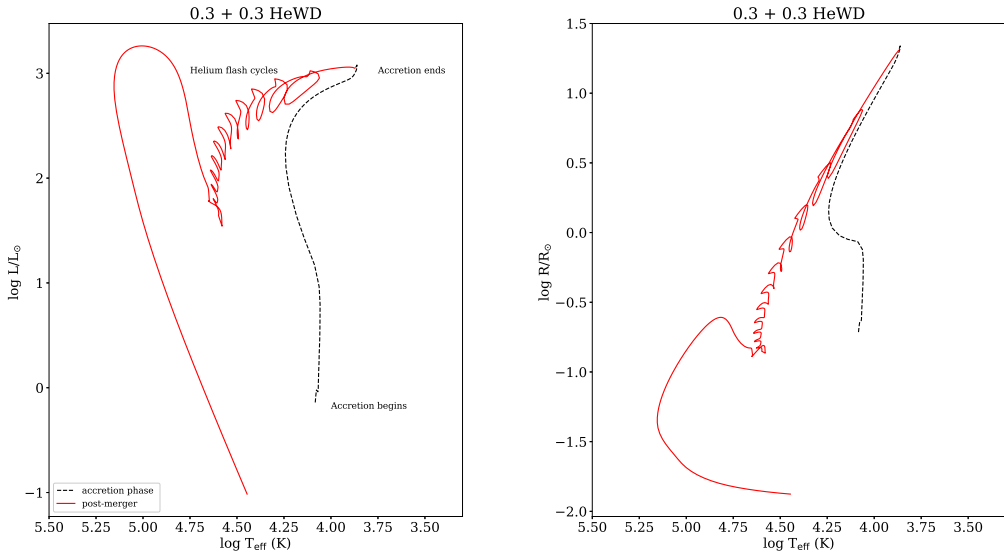


**Figure 1.9:** A $0.3\,\mathrm{M_\odot}$ WD + $0.3\,\mathrm{M_\odot}$ WD merger track from Zhang and Jeffery (2012), showing the evolution in luminosity (left) and radius (right). The dashed black lines shown the evolution during accretion.

We can also have a merger between a CO-WD and a He-WD. In this case we have the helium WD accreting onto the CO core and following the helium shell igniting and moving inward, the star expands to become a yellow giant. The star will stay a giant until accretion is ceased. When the mass above the helium-burning shell becomes sufficiently small, the surface temperature begins to increase and the star evolves blueward

nearly horizontally on the HR diagram. As before it then cools as a white dwarf.

### 1.5.3 Thermal Pulses

This evolution channel is similar to the late hot flashers, the key difference lies in the composition of the core. If the core is composed of C/O when the helium is re-ignited then it is dubbed a thermal pulse, in the hot-flasher scenario the core is composed of helium.

This channel is dubbed a "born-again" episode (Iben, 1984). The carbon-oxygen core is now surrounded by helium with an outer shell of hydrogen. If the helium is re-ignited and a thermal pulse occurs on the WD cooling track the star quickly returns to the AGB, becoming a helium-burning, hydrogen-deficient stellar object and is termed a very late thermal pulse (VLTP). If the star still has a hydrogen-burning shell when this thermal pulse occurs, it is called a late thermal pulse (LTP).

## 1.6 Pulsation in sdBs

A significant fraction of the sdB stars shows non-radial oscillations, thus opening up the way for detailed asteroseismic investigations. The existence of pulsating sdB stars was predicted by Charpinet et al. (1996) simultaneously with their observational discovery (Kilkenny et al., 1997). The pulsation of a star is characterised by expansion followed by contraction. If the pulsating star preserves its spherical symmetry then the mode of pulsation is known as radial. Otherwise the pulsation is called non–radial. While the radial oscillation has only the spectrum of the pressure mode ($p$–mode) or acoustic mode, the non–radial oscillation shows the spectrum of the gravity wave mode as well. For the $p$–modes, pressure is the restoring force for a star perturbed from equilibrium. These $p$–modes are acoustic waves and have gas motion that are primarily vertical. For the $g$–modes, or gravity modes, buoyancy is the restoring force and the gas motions are primarily horizontal. Three important properties of $p$– and $g$–modes are

1. As the number of radial nodes increases the frequencies of the $p$– modes increase, but the frequencies of the $g$–modes decrease.

2. The $p$–modes are most sensitive to conditions in the outer part of the star, whereas $g$–modes are sensitive to conditions in the deep interior of the star.

3. For radial order $(n) >>$ degree $(l)$ there is an asymptotic relation for $p$–mode saying that they are approximately equally spaced in frequency, and there is another asymptotic relation for $g$–mode pointing out that they are approximately equally spaced in period.

Pulsating sdBs come in two groups featuring either short period variations due to low-order, low-degree p-modes (V361 Hya stars discovered by Kilkenny et al. (1997)) or long period modulations due to mid/high order, low degree g-modes; (V1093 Her stars discovered by Green et al. (2003)). Some sdB stars, called hybrid pulsators, belong to both classes as they show modulations due to both $p-$ and $g-$modes (Schuh et al., 2005).

In order for an oscillation to be overstable, its propagation zone or trapping region should coincide with the region where some excitation mechanism is very effective. According to thermodynamics, such an excitation mechanism has to provide an entropy increase or a heat input during the high temperature phase in an oscillation cycle. The positive temperature dependance of the opacity and the high temperature sensitivity of the nuclear energy generation are known to provide the excitation mechanism called the $\kappa$–mechanism and the $\epsilon$–mechanism, respectively. Since the $\kappa$–mechanism is connected with opacity, for this mechanism to be effective there must be plenty of opacity so major drivers are Hydrogen and Helium. Simplistically, in the ionisation layers for H and He opacity blocks radiation, the gas heats and the pressure increases causing the star to swell past its equilibrium point. But the ionisation of the gas reduces the opacity, radiation flows through, the gas cools and cannot support the weight of the overlying layers, so the star contracts. On the contraction the H or He recombines and flux is once again absorbed. An opacity bump associated with iron ionisation turns out to be an efficient driving mechanism. The atomic diffusion process that are at work in sdB stars, particularly radiative levitation, imply that iron becomes overabundant in the driving zone. Whenever this overabundance leads to a local Z–value of above 0.04 in the partial ionisation zone of iron, low order $p$–mode oscillations are excited,

the same instability mechanism is found in the $g$–mode pulsators (Fontaine et al., 2003; Jeffery and Schönberner, 2006).

Another major driving mechanism that operates in the Sun and solar–like oscillators is stochastic driving. In this case the heat–engine mechanism is not able to drive the oscillations and the modes are intrinsically stable. However, there is sufficient acoustic energy in the outer convection zone in the star that the star resonates in some of its natural oscillation frequencies where some of the stochastic noise is transferred to energy of global oscillation. The third major theoretical driving mechanism is the $\epsilon$– mechanism where in this case the $\epsilon$ refers to the energy generation rate of the core of the star, however there has been no confirmed case to date.

### 1.6.1   LS IV$-14°116$

LS IV$-14°116$ was classified as an sdO star by Kilkenny and Pauls (1990) and as an He-rich sdO star by Viton et al. (1991). Subsequent analyses confirmed the excess helium abundance and high effective temperature ($T_{\mathrm{eff}}$), making it one of relatively few such stars (Ahmad and Jeffery, 2003; Ahmad and Jeffery, 2004), and the only one to show photometric variability (Ahmad and Jeffery, 2005).

Naslim et al. (2011) discovered the superabundances (4 dex) of zirconium, yttrium, strontium, and, to a lesser extent, germanium. It has been argued that these could be associated with a dynamical self-stratification of the photosphere as a young subdwarf contracts towards the extreme horizontal branch (Naslim et al., 2013), suggesting that LS IV$-14°116$ is a proto-sdB star which will eventually develop a helium-poor atmosphere.

Follow-up photometry confirmed the star to be a multi-periodic variable, almost certainly a non-radial $g-$mode oscillator (Green et al., 2011; Jeffery, 2011) with a dominant pulsation signal at 1953 s (=0.022d) and weaker signals at 2620, 2872, 3582, 4260 and 5084 s. Current models of sdBs fail to explain how a star such as LS IV$-14°116$ can excite long-period $g-$modes and not short-period $p-$modes, given its location on the effective temperature - surface gravity diagram. Figure 1.10 illustrates this problem.

Jeffery et al. (2015a) conducted a search for radial velocity variability LS IV$-14°116$
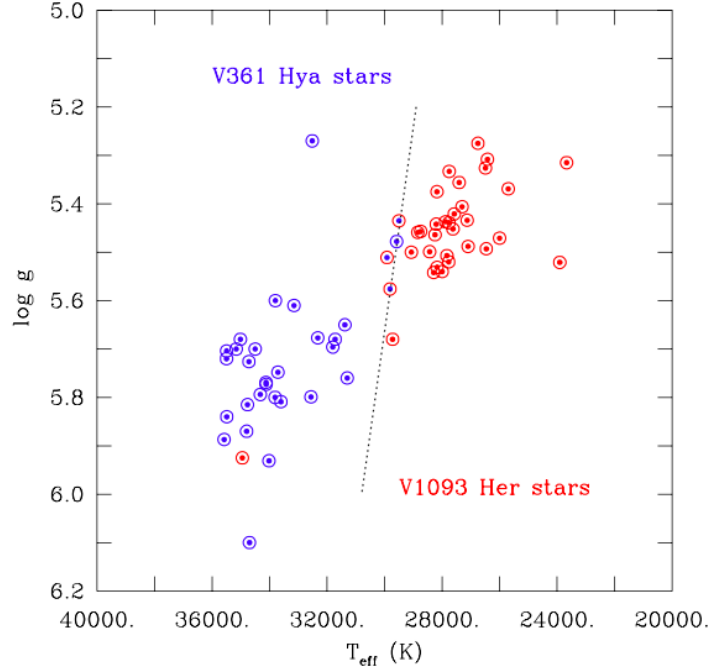
**Figure 1.10:** Distribution of the pulsating sdB stars in the effective temperature-surface gravity plane. The short-period $p-$mode pulsators are in blue and the long-period $g-$mode variables are shown in red. Three hybrid pulsators, showing simultaneously both $p-$modes and $g-$modes, are shown in red and blue. LS IV$-14°116$ (the red symbol in the $p-$mode domain) totally out of place and, therefore, represents quite a puzzle (Green et al., 2011).

and demonstrated that at least one periodic variation identified photometrically is also observable as a radial velocity variation with a semi-amplitude in excess of $5\,\mathrm{km\ s^{-1}}$ (Fig. 1.11). This provides strong evidence that both are due to an oscillatory motion of the surface and are hence most likely due to pulsation. Additional evidence from the light/velocity amplitude ratio argues that the pulsation cannot be a radial mode, whilst supporting arguments from pulsation theory (Green et al., 2011) confirm that the observed pulsations are due to a non-radial gravity mode.

## 1.7 Pulsation in EHes

Pulsations have been established in extreme helium stars for a long time (Landolt, 1975). Three classes have been identified: FQ Aqr, V2076 Oph and V652 Her. The latter are hydrogen-deficient B stars showing low-amplitude variations in light (0.1 mag in V) and radial velocity with a unique and regular period of a few hours. Theoreti-

# 1. INTRODUCTION
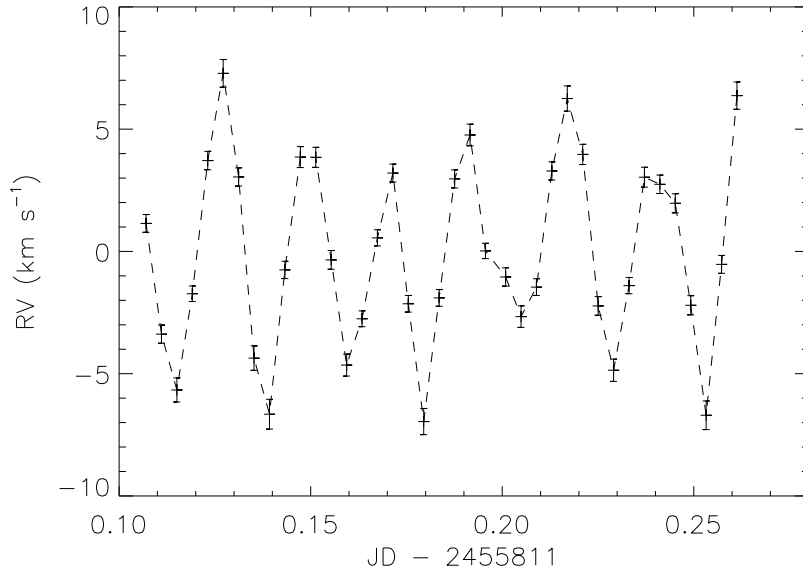


**Figure 1.11:** VLT/UVES radial velocities of LS IV−14°116 measured from a single ZrIV absorption line (Jeffery et al., 2015a).

cally, these are interpreted as low-luminosity radial pulsators driven by the $\kappa$ mechanism through Z-bump instability (Saio, 1993). The class comprises V652 Her and BX Cir. V652 Her and BX Cir make superb subjects for experiment, with single periods of $\sim 0.1$d. High signal-to-noise high-resolution studies from the ground and space have allowed the projected radial velocity, the effective temperature and the effective surface gravity to be measured throughout the pulsation cycle. From these, mean absolute radii and masses can be measured directly. For V652 Her, Jeffery et al. (2001b) obtained $2.32 \pm 0.02$ R$_\odot$ and $0.59 \pm 0.18$ M$_\odot$. For BX Cir , Woolf and Jeffery (2000) and Woolf and Jeffery (2002) obtained $2.31 \pm 0.10$ R$_\odot$ and $0.47 \pm 0.03$ M$_\odot$ . Although they have virtually identical periods and radii, the light curves of V652 Her and BX Cir are significantly different. Non-linear modelling shows that this is probably a consequence of their masses being different by $\sim 20\%$ (Montañés Rodríguez and Jeffery, 2002). Figures 1.12 and 1.13 show the radial velocity curves for V652 Her and BX Cir respectively.

Any acoustic wave propagating upwards through a stellar atmosphere is likely to form a train of shocks, unless dissipation can damp the waves first. It has never previously been possible to study such shock-induced line profile variation in any stars in detail, but in the case of the short-period pulsating extreme helium stars, where the

20
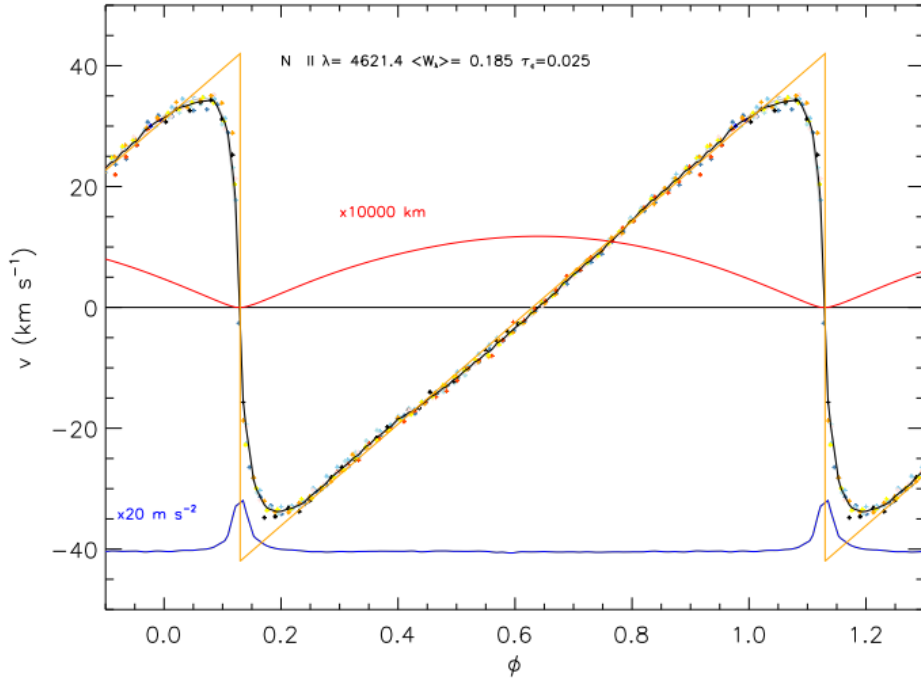
**Figure 1.12:** V652 Her absorption line velocities and related quantities as a function of pulsation phase for a single absorption line: in this case N II 4621 Å. Each + represents an individual radial velocity measurement, each colour refers to a single pulsation cycle. The solid black curve represents the phase-averaged velocity curve, v, obtained from the line velocities ($\mathrm{km\ s^{-1}}$). The solid red line represents the integral of the phase-averaged expansion velocity curve with a constant chosen such that the total displacement over one pulsation cycle is zero and, in this case, that minimum radius corresponds to a displacement of zero (Jeffery et al., 2015b).
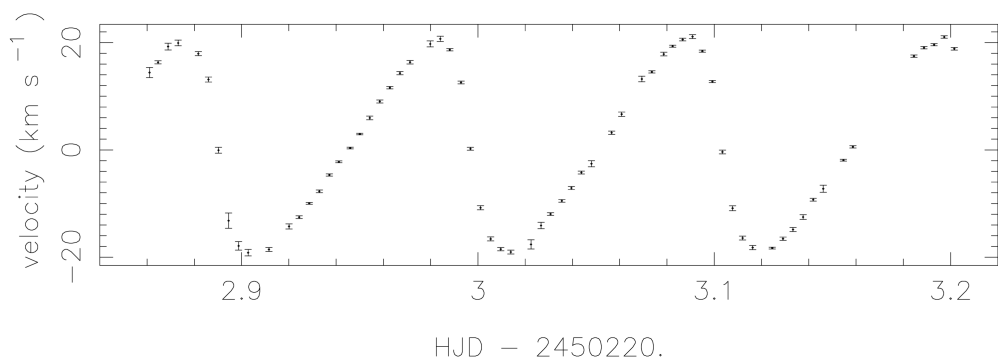


**Figure 1.13:** Radial velocity curve for BX Cir, with error bars shown for velocity (Woolf and Jeffery, 2000).

absence of hydrogen opacity allows us to see deeper into the atmosphere than in any other star, we have a golden opportunity. This has bee recently demonstrated for V652

## 1. INTRODUCTION

Her using HDS on Subaru (Jeffery et al., 2015b), Figure 1.12 shows the absorption line velocities and related quantities as a function of pulsation phase for N II.

## 1.8    Science Goals

This thesis is divided in to three research topics unified by the abundances and evolutionary scenarios of the stars being in question. The first is a detailed study of two pulsating helium enriched stars, dealing with the precise measurements of radial velocities to explore their dynamical photospheres. The following topic addresses multiple populations of stars in the Galaxy and what clues we may glean from their orbits as to their evolutionary history. Lastly, after the calculation of the fundamental stellar properties, luminosity, mass and radius, we explore the stars unorthodox evolutionary scenarios.

**Chapter 3** is dedicated to the analysis of the pulsation behaviour of LS IV$-14°116$ through the physical motion of the photosphere. LS IV$-14°116$'s pulsations, as discussed previously, are unexpected due to the stars surface parameters. We aim to create a depth-dependent profile of pulsation amplitude in the photosphere and to gain insight into the reason for these pulsations. The second pulsating helium enriched star, BX Cir, is in a rare, and not fully understood, stage of stellar evolution. High precision observations offer us a unique opportunities to explore the effect of pulsation on the photosphere itself. In **Chapter 4** we use a time-series of spectra to search for evidence of a weak shock signature at minimum radius of the pulsation.

LS IV$-14°116$'s halo status has raised the question of whether the helium-rich hot subdwarfs all belong to this halo minority and the "normal" sdO/Bs are a disk population. We search for differences in the Galactic velocities and orbits of these three groups of hot subdwarf stars in **Chapter 5**.

The second Gaia data release has allowed us to expand our initial kinematic sample of subdwarfs, we aim to follow up on our initial analysis and (**Chapter 6**). Applying the same methods we aim to distinguish Galactic populations of other hydrogen-deficient stars to search for possible evolutionary links. In **Chapter 7** we aim to create a hydrogen-deficient HR diagram. With this tool we intend to compare new calculation of the luminosities of all hydrogen-deficient stars classes discussed thus far to their proposed evolutionary models.

# 1. INTRODUCTION

# Instrumentation and Data Reduction 2

## 2.1 *Gaia*

*Gaia* measures the positions, distances, space motions and many physical characteristics of some one billion stars in our Galaxy and beyond. It provides us with a detailed 3D distributions and space motions of all these stars, complete to 20th magnitude. The measurement precision, reaching a few millionths of a second of arc, is unprecedented. This allows our Galaxy to be mapped, for the first time, in three dimensions. The spacecraft carries two identical telescopes, pointing in two directions separated by a 106.5 degree basic angle and merged into a common path at the exit pupil.
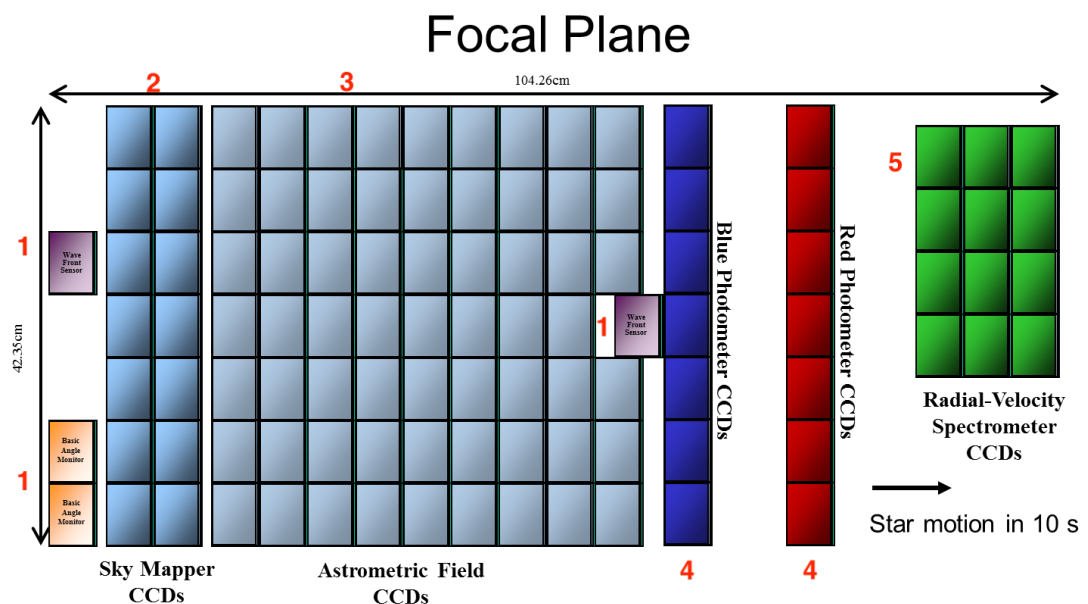


**Figure 2.1:** A schematic of the focal plane assembly of *Gaia*. credit:ESA

The *Gaia* focal-plane contains 106 CCDs with a total of almost 1,000 million pixels.

## 2. INSTRUMENTATION AND DATA REDUCTION

The assembly is common to both telescopes and serves five main functions labelled in Figure 2.1.

1. Wave-front sensor and basic-angle monitor. For the purpose of re-aligning the telescopes in orbit to cancel errors due to mirror micro-settings and gravity release.

2. Sky mapper. This is 7 CCDs (per telescope), which detect objects entering the fields of view and communicates details of the star transits to the subsequent CCDs.

3. Astrometric field. 62 CCDs are devoted to angular-position measurements, providing the five astrometric parameters.

4. Photometric instrument. Two low-resolution prisms dispersing all the light entering the field of view. One disperser Blue Photometer (BP) operates in the wavelength range 330-680 nm and the other Red Photometer (RP) covers the wavelength range 640-1050 nm. The photometers contain seven CCDs each.

5. Radial Velocity Spectrometer. This is a medium-resolution ($\lambda/\Delta\lambda \sim 11500$), integral-field spectrograph operating in the near-infrared (845-872 nm). It has 12 CCDs allowing for the derivation of radial velocities and stellar atmospheric parameters of objects brighter than 17th magnitude.
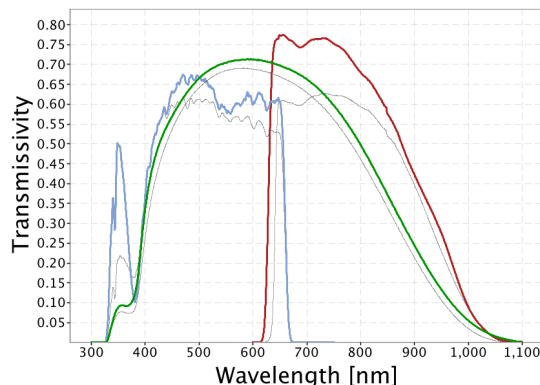


**Figure 2.2:** The coloured lines in the figure show the passbands defining the Gaia DR2 photometric system, (green: G; blue: BP; red: RP).

26

### 2.1.1 Data Release 2

*Gaia* released its second catalog (DR2) in April 2018, based on data collected over 22 months. Its contents include the five-parameter astrometric solution - positions on the sky (right ascension and declination), parallaxes, and proper motions for more than 1.3 billion sources.

Median radial velocities are provided for stars with a mean G magnitude between about 4 and 13 and an effective temperature in the range of about 3550 to 6900 K. Mean magnitudes are given in three passbands. Figure 2.2 shows the passbands as green, blue, and red solid lines for the G, $G_{BP}$, and $G_{RP}$ bands. Epoch astrometry for 14,099 known solar system objects are also included in the data release.
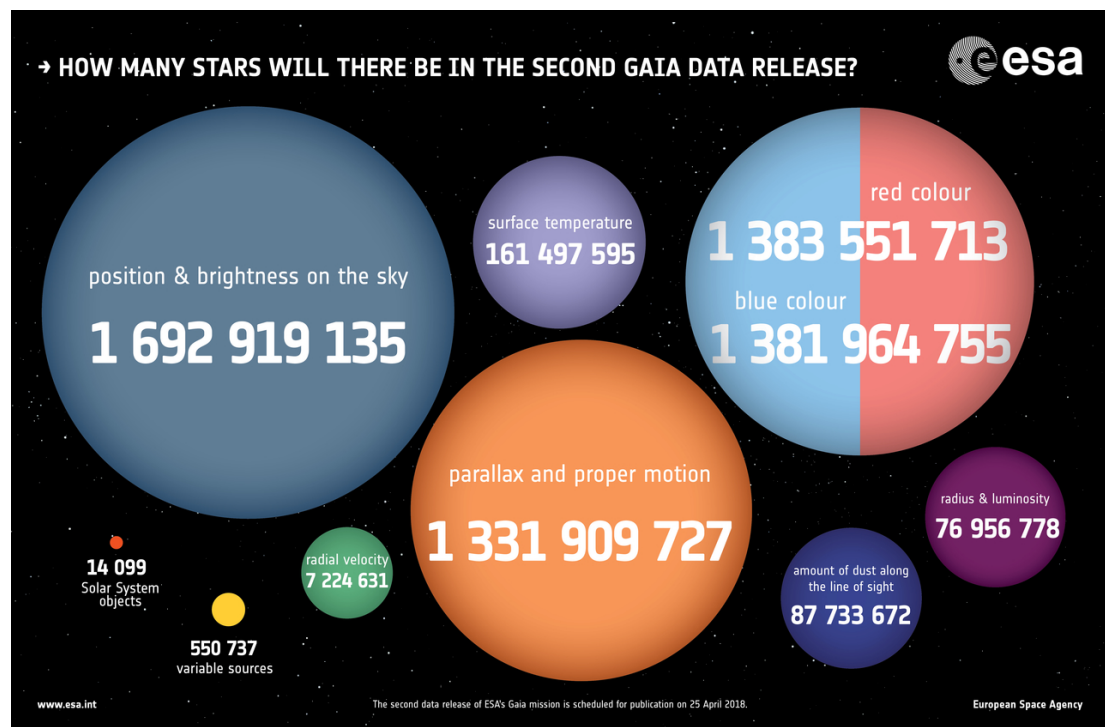


**Figure 2.3:** Numbers of measurements provided in *Gaia* DR2. Credit: ESA, CC BY-SA 3.0 IGO.

Figure 2.3 shows the exact numbers of stars which have measurements of the parameters mentioned above. Future data releases are planned and will increase the baseline of observations and hence the precision. The next data release is planned in early 2021.

## 2.2   Echelle Spectrographs

All astronomical spectrographs contain the essential elements: a slit, a collimator, a disperser, a camera and a detector. The slit sits on the focal plane and usually has an adjustable width. The image of the object being observed is focused onto the slit, the light beam continues to the collimator which take the divergent beam and converts it to parallel light and redirects it towards the disperser. In most astronomical spectrographs the disperser is a grating. The light then enters the camera which takes the dispersed light and focuses it onto the charge-coupled device (CCD).

It is possible to deflect most of the light into one preselected order. This is achieved by inclining the reflecting surfaces of the individual grooves in the grating relative to the grating plane The angle between the normal to the reflecting groove surfaces and the normal to the grating plane is called the blaze angle. Light reaching the grating at the blaze angle is reflected back in the same direction. For this light a reflection grating reaches its maximal efficiency.

The relation between the incident and diffraction angles, and the wavelength is given by the grating equation :

$$d(sini + sin\theta) = m\lambda \tag{2.1}$$

- $i$ is the angle of incidence

- $\theta$ is the angle of diffraction

- $m$ donates the order number

- $d$ is the groove spacing of the grating and

- $\lambda$ is the wavelength of the light

The spectral resolution of an instrument is determined by the separation ($\Delta\lambda$) between two spectral peaks that can just barely be detected as separate with the instrument. The grating can be described by its resolving power R:

$$R = \frac{\lambda}{\Delta\lambda} = mN$$

where $m$ is the diffraction order and $N$ is the total number of grooves on the entire grating surface. R depends only on the number of interfering beams and the order of interference.
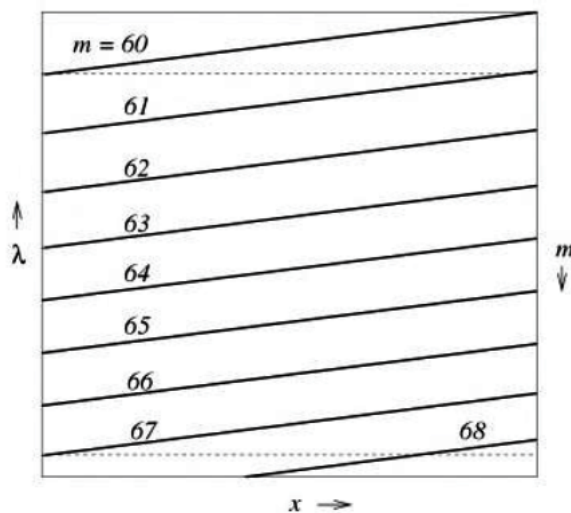


**Figure 2.4:** Schematic geometry of the orders of an echelle spectrogram. the horizontal broken lines indicate constant wavelengths (Appenzeller, 2013).

Conventional spectrographs image a single order at a given time so on a large two-dimensional array most of the area is wasted with the spectrum of the sky unless one is observing multiple objects. Echelle spectrographs use a second dispersing element to cross disperse the orders spreading them across the detector. Figure 2.4 shows a schematic example of the geometry of orders across the CCD. Echelle spectrographs are designed to work at high orders and both the angle of incidence and the angle of diffraction are large. Echelle gratings typically have blaze angles $\geq 63.5$ degrees and grating spacings of the order of 3–40$\mu$m and most echelle spectrometers operate at diffraction orders of m $>$ 40. High–resolution spectrometers are Nasmyth–focus instruments. The Nasmyth focus position moves with the azimuthal motion of the telescope, but a spectrograph at this focus always feels the same direction of Earth's gravitational acceleration. Thus, if the spectrograph is properly mounted, mechanical bending effects due to the telescope's movement tend to be small.

To retain a high efficiency at all operating wavelengths modern high-resolution spectrometers are often split into two or more arms which are optimised for different

wavelength bands. Where the different configurations can be used alternatively or if a dichroic beam splitter is used, simultaneously. Figure 2.5 shows the optical layout of the echelle spectrograph on the Southern African Large Telescope, section 2.4 describes the telescope and instrument in more detail.
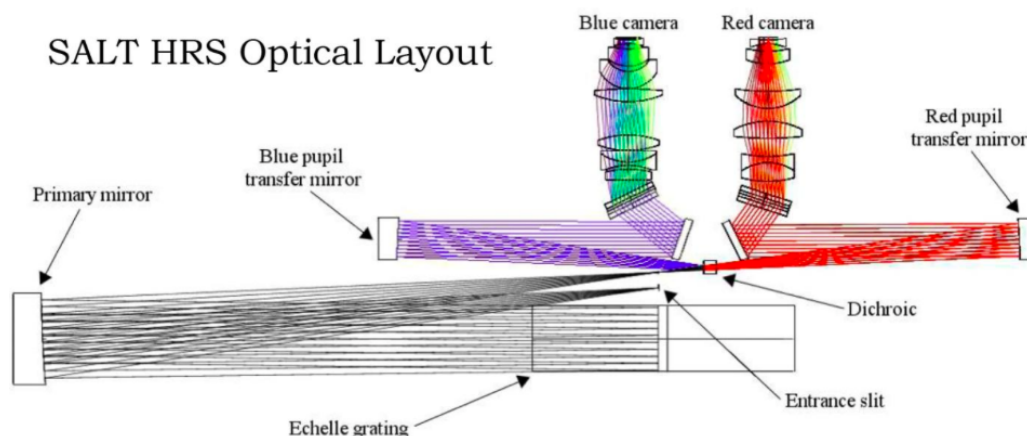


**Figure 2.5:** Optical layout for the High Resolution Spectrograph on the Southern African Large Telescope (Barnes et al., 2008)

## 2.3 Very Large Telescope (VLT)

The Very Large Telescope (VLT) consists of an array of four 8-metre telescopes which can work independently or in combined mode. The unit telescope has alt-azimuth mount. In such a mount the telescope tube moves around a horizontal axis called elevation axis. The two bearings which support the tube are mounted on a fork rotating around a vertical axis, called azimuth axis, thus allowing for pointing over the entire sky.

### 2.3.1 Ultraviolet and Visual Echelle Spectrograph (UVES)

The Ultraviolet and Visual Echelle Spectrograph (UVES) is a dual beam echelle spectrograph installed at the Nasmyth focus of the UT2 telescope of the ESO VLT. It can reach a resolution of 80 000 and 115 000 in the blue and red arms respectively and covers a wavelength range of 3 000–11 000Å. The light from the telescope is fed to two separate entrance slits by dichroic and after being dispersed by two large echelle gratings (one

per arm) and a grating cross disperser (two per arm) is focussed by dioptric cameras on two large, high efficiency CCD detectors.

The instrument consists of two main parts

1. The calibration system, a removable iodine cell, a slide with image slicers and an optical de–rotator (which is permanently installed in the beam) are all mounted on the rotator which remains stationary while the telescope adaptor rotates to follow the field rotation.

2. The second part is the two armed cross–dispersed echelle spectrograph. This is mounted on a steel table fixed to the floor of the Nasmyth platform and is covered by a light–tight enclosure which also provides thermal insulation and protection from dust. The light beam from the telescope is focussed on the red arm entrance slit or is directed to the blue arm slit by a mirror.

Two dichroics are available to work in parallel with the two arms. The blue and red arm have an identical layout. The design of both arms is of the white–pupil type. With a beam of 200mm, the off–axis parabolic collimators illuminate the echelle gratings of 214 x 840 x 125mm with a large blaze angle of 76 degrees. They are operated in quasi–Littrow mode, that is with the angle of incidence and diffraction equal buy in a different plane to maximise efficiency. The grating cross-dispersers provide an order separation larger than 10 arcsecs at any wavelength in the spectral range 300–1100nm. The cameras are dioptric (no central obstruction) and provide a large field, good image quality and high optical transmission. The two arms of UVES are equipped with CCD detectors, one single chip in the blue and a mosaic of two chips in the red arm. A continuous flow of liquid nitrogen coolant for the CCDs is supplied by an external vessel with an antonomy of at least two weeks. These measures lead to high stability and repeatability of calibrations both over short and extended periods of time. Table 2.1 summarises the capabilities and performance of UVES.

### 2.3.2   Observations

Observations were obtained from proposal ID 087.D-0950(A) observed in visitor mode by the Principle Investigator (C. S Jeffery) and myself. LS IV$-14°116$ was observed

**Table 2.1:** The measured observational capabilities and performance of UVES. Modified from Dekker et al. (2000)

| Parameter | Blue Arm | Red Arm |
|---|---|---|
| Wavelength Range | $300 - 500$nm | $420 - 1100$nm |
| Max. resolution | 80000 (0.4" slit) | 110000 (0.3" slit) |
| Echelle | 41.59g/mm | 31.6g/mm |
| Min. Order Separation | 10 arcsec | 12 arcsec |
| Overall detective quantum efficiency | 12% at 400 nm | 14% at 600 nm |

with UVES between the 23rd and 27th of August 2015 for a total of 22.6hrs. Each exposure was 200s in duration. For all four nights the weather was clear, Table 2.2 shows the general weather conditions.

**Table 2.2:** General weather conditions at Paranal between the 23rd and 27th of August 2015

| August | Seeing (arcsec) | Humidity (%) | Wind (ms$^{-1}$) | Temperature (°C) |
|---|---|---|---|---|
| 23/24 | $0.6 - 3.1$ | $13 - 24$ | $1 - 8$ | $11 - 13$ |
| 24/25 | $0.4 - 2.0$ | $4 - 20$ | $3 - 12$ | $9 - 14$ |
| 25/26 | $0.6 - 2.5$ | $9 - 19$ | $0 - 6$ | $9 - 12$ |
| 26/27 | $0.9 - 2.7$ | $7 - 13$ | $0 - 9$ | $13 - 14$ |

### 2.3.3 Data Reduction

ESO provide software for the reduction of raw data. EsoRex is a command line tool used to run the pipeline recipes with commands that can be easily scripted and users are permitted to change default parameters of each recipe in order to have more control over the data reduction process. EsoRex also provides estimates of the errors in the data reduction process. A disadvantage of EsoRex is that the user must be responsible for defining the input set-of-frames (SOF) and the appropriate configuration parameters for each recipe run. The SOF is an ASCII file containing for each input frame the full path file name and its category. The pipeline will access the listed files when required. A more detailed description of the software provided by ESO can be found in Ballester et al. (2000).

The reduction of raw spectra was achieved by using the recipes provided by EsoRex

which are described below in the order they should be run.

1. `uves_cal_mbias`: This recipe generates a master bias frame from a set of raw bias frames. Each bias frame is corrected by the sigma-clipped mean of all the pixels and then they are combined by median combining.

2. `uves_cal_predict`: This recipe is used to generate guess order tables and line tables, which subsequently allow automatisation of the order and wavelength calibration steps. The guess line table is also used to monitor the spectral format against predictions from the physical model.

3. `uves_cal_orderpos` This recipe measures the echelle order positions. A median boxcar filter is applied to the input flat-field frame. The inter-order background is subtracted. The orders are then traced and the traces are fitted with a global polynomial of automatic degree. The polynomial degrees are increased in steps of one or two, as long as the fit RMS decreases by more than 10%. The product is an order table.

4. `uves_cal_mflat` This recipe generates a master flat frame from a set of flats.

5. `uves_cal_wavecal` This recipe performs the wavelength calibration using previously determined solutions for the guess line table and the order table. A master bias is subtracted from the arc lamp frame. The bias corrected arc lamp frame is divided by the master flat-field. The spectrum is extracted and emission lines are detected in the extracted spectrum. It obtains a first solution by estimating the x-shift of the detected lines with respect to the locations of the lines in the guess line table, and then apply this shift to the guess dispersion relation. Iterative line identification is performed and updates of the dispersion relation, until no new line identifications can be made. The extracted spectrum is then wavelength calibrated and the orders are merged. The spectral resolution is computed by determining the line width for each of the identified lines in the merged spectrum

6. `uves_obs_scired` This recipe reduces a science frame. The master bias is subtracted. The inter-order background is estimated and then subtracted. The

corrected science frame is divided by the master flat field. Then the object is extracted, cosmic rays are detected and rejected, and the sky is fitted and subtracted during the extraction. Then the master flat field is extracted using the object weights, and the object spectrum is divided by the extracted master flat field spectrum. The spectrum is resampled to equidistant wavelength steps. Finally the orders are then merged and flux calibrated to physical units (if the instrument response curve is provided).

## 2.4  Southern African Large Telescope (SALT)

The Southern African Large Telescope (SALT) is the largest single optical telescope in the southern hemisphere. It has a hexagonal primary mirror array 11 metres across, comprising 91 individual 1m hexagonal mirrors. The telescope is free to rotate in azimuth, but the elevation axis of the structure is fixed at $37^o$ from the zenith. A tracker assembly at prime focus then moves about all six translational and rotational axes in order to track an object as it travels across the annulus of accessible sky (Fig. 2.6). SALT is thus able to follow celestial targets for between one and six hours, depending on their declination. A target with intermediate declination may be tracked for the full 2 hour viewing zone but at the declination extremes the track time is shortened. However the source may continue to be tracked by moving the tele- scope in azimuth and re-acquiring. Therefore quasi-continuous viewing for 6 hours is achievable in the south and up to 4 hours in the north.

SALT HRS is a single object high-resolution spectrograph operating from 3 700–8 900Å. The spectrograph is a dual beam white pupil design, with a single echelle grating, a dichroic beam splitter and volume phase holographic grating cross dispersers. The echelle grating has 41.6 grooves/mm and is illuminated with a 200mm diameter beam. Two fully dioptic cameras are used to acquire the complete wavelength range at a maximum resolving power of R = 70 000 and a fixed spectral format. The instrument has four modes each with object and sky fibres: low (R~15 000), medium (R~40 000), high resolution (R~65 000) and high stability (R~65 000) . The low resolution mode has improved background sampling and is useful in spectroscopy of diffuse interstellar
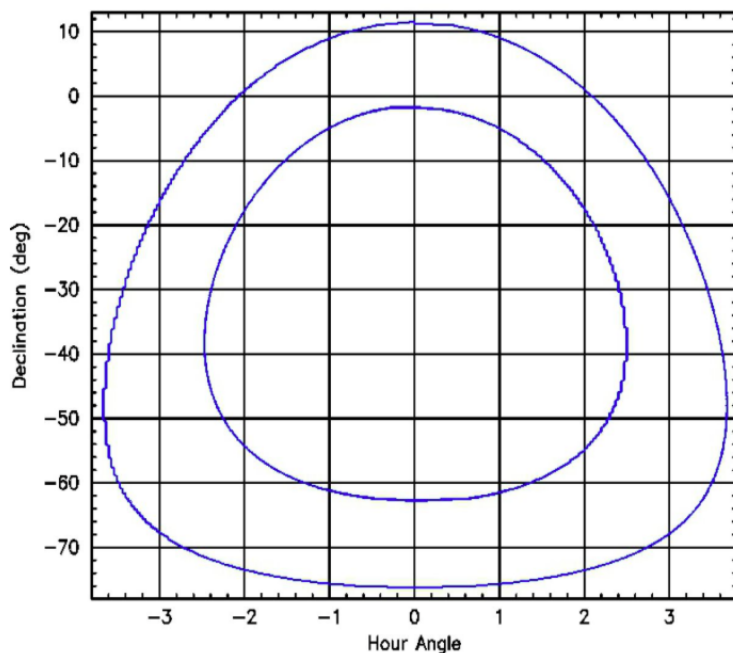
**Figure 2.6:** The SALT sky viewing annulus as function of declination and hour leads to variance in tracking time depending on the declination of the target. Only objects inside the annular region are observable by SALT at any given time.

bands against lines of sight to distant stars or quasars, and molecular band analysis of stars in Local Group galaxies. Medium resolution mode has a larger fibre diameter and thus has potentially better seeing-related throughput than high resolution. Stars in which the Balmer line strength measurements are the principle aims are recommended to use this mode. High resolution is for projects involving line profile variations in stellar atmospheres or exploring absorbing structures in the ISM or IGM. High stability mode is optimised for precision radial velocity measurements. The light path includes a permanent double-scrambler to improve the radial scrambling of the fibres and reduce the spectral shifts due to the star moving on the input face of the fibre. The efficiency of this mode is about half of that of the normal high resolution mode and thus it would normally only be used where the level of wavelength stability is essential. Table 2.3 gives a summery of the properties of the different modes of HRS.

**Table 2.3:** Summary of the four SALT HRS modes and the associated options. Modified from Crause et al. (2014)

| Parameter | Low Resolution | Medium Resolution | High Resolution | High Stability |
|---|---|---|---|---|
| Fibre Diameter (arcsec) | 2.23 | 2.23 | 1.56 | 1.56 |
| Slit Width (arcsec) | 0.710 | 0.710 | 0.355 | 0.355 |
| Blue Arm Resolving Power | 15 000 | 43 000 | 65 000 | 65 000 |
| Red Arm Resolving Power | 14 000 | 40 000 | 74 000 | 65 000 |
| Fibre Mode Scrambling | No | No | No | Permanent |
| Iodine Cell | No | No | No | Optional |
| Simultaneous ThAr | No | No | No | Optional |

### 2.4.1 Observations

Approximately 20 hours of observations of BX Cir were obtained in 2015 (proposal ID 2015-1-SCI-009) taken in service mode. I am co-investigator of the proposal and completed the phase II proposal in which the observations were scheduled into time blocks and phased to the pulsation cycle in order to obtain full coverage. Most exposures are 200s in duration. An overview of the observations are presented in Chapter 4.

### 2.4.2 Data Reduction

The package `PyHRS` provides steps for reducing and extracting data from the High Resolution Spectrograph. This Python package includes sub-packages to assist with the processing and reduction of the data (Crawford, 2015). It follows the same data reduction steps as described in the EsoRex recipes.

1. Create an observing log. To read and store the relevant header information such as observation type (i.e. arc, bias ...)

2. `create_masterbias` takes the raw bias frames (usually 6) over-scanned, corrected, trimmed and co-added to create a master bias.

3. `create_masterflat` the raw frames are over-scanned, corrected, trimmed, master bias subtracted then medium combined to create the master flat.

4. `create_orderframe` creates an initial detection kernel for the orders which is used to step through each order to create the order frame. The frame is normalised so to eliminate scattered light and make identification of the individual orders easier.

5. `wavelength_calibrate_arc` is used to find the wavelength solution.

6. The science frame is divided by the master flat, the orders are extracted and a wavelength solution is applied.

7. The orders can then be merged and blaze corrected.

The HRS spectra were reduced to 1-dimension (total counts versus wavelength) object and sky orders using this pipeline. The orders were rectified, mapped onto a common wavelength grid, equally spaced in log wavelength, and merged using an order-management tool written for echelle spectra (Jeffery priv. comm).

# A Very Peculiar Intermediate-Helium sdB: LS IV−$14°116$
<div style="text-align:right">3</div>

LS IV−$14°116$ is a very unusual subdwarf B star. It pulsates non-radially with high-order g-modes, these pulsations are unexpected and unexplained, as the effective temperature is 6 000K hotter than the blue edge of the hot subdwarf g-mode instability strip. Its spectrum is enriched in helium which is not seen in either the V361 Hya (p-mode pulsators) or the V1093 Her stars (g-mode pulsators). Even more unusual is the 4 dex overabundance of zirconium, yttrium, and strontium. It is proposed that these over-abundances are a result of extreme chemical stratification driven by radiative levitation. We have over 20hrs of VLT/UVES spectroscopy from which we have obtained radial velocity curves for individual absorption lines. We explore ways in which to resolve the photospheric motion as a function of optical depth.

The majority of this work is published in Open Astronomy (Martin and Jeffery, 2017).

## 3.1    LS IV−$14°116$ : A History

The hot subdwarf LS IV−$14°116$ was discovered in a follow-up study of stars with ultraviolet excesses (Viton et al., 1991). It was initially classified as a subdwarf O star (Kilkenny and Pauls, 1990) owing to the weakness of its hydrogen and the strength of its ionized helium lines. The remarkable surface abundances discovered by Naslim et al. (2011) made it the prototype of a growing group of "heavy metal" helium-rich hot subdwarfs.

Randall et al. (2015) found that LS IV−$14°116$ is on a retrograde orbit around the Galactic centre, implying that it belongs to the halo population. Martin et al. (2017, see Figs 5 & 6) have computed the Galactic orbit of LS IV−$14°116$ in which we see the retrograde orbit as well as the high eccentricity confirming LS IV−$14°116$'s halo status.

## 3. A VERY PECULIAR INTERMEDIATE-HELIUM SDB: LS IV$-14°116$

**Table 3.1:** Photometric frequencies detected in LS IV$-14°116$

| Ahmad and Jeffery (2005) mHz | Green et al. (2011) mHz | Jeffery et al. (2015a) mHz |
|---|---|---|
| $0.5119 \pm 0.0001$ | $0.51184 \pm 0.00001$ | $\sim 0.5$ |
| - | $0.38164 \pm 0.00003$ | - |
| $0.3484 \pm 0.0001$ | $0.34815 \pm 0.00002$ | - |
| - | $0.27919 \pm 0.00002$ | - |
| - | $0.23475 \pm 0.00003$ | - |
| - | $0.19671 \pm 0.00002$ | - |

LS IV$-14°116$ shows photometric variability first seen by Ahmad and Jeffery (2005) who found two periods. They concluded that the variability was likely due to non-radial g-mode pulsations. This made LS IV$-14°116$ the proto-type He-sdB variable (He-sdbV) (Kilkenny et al., 2010) and unique until UVO 0825+15 was discovered recently (Jeffery et al., 2017). UVO 0825+15 shows two long period non-radial oscillations as well as an unusual surface chemistry rich in elements heavier than argon — although not as enriched in zirconium, yttrium and strontium as LS IV$-14°116$. A follow up photometric study of LS IV$-14°116$ by Green et al. (2011) confirmed the two previous known periods and detected four others (Table 3.1). The authors came to the same conclusion that these are most likely non-radial g-mode pulsations and highlighted a problem with this conclusion. With a temperature of $\sim 35$kK and $\log g \sim 6$ LS IV$-14°116$ lies in a region of the $T_{\mathrm{eff}}$–$\log g$ diagram occupied by p-mode pulsators. Current models fail to explain how a star such as LS IV$-14°116$ can excite long-period g-modes. The excitation mechanism for the pulsations seen in LS IV$-14°116$ is still not known.

Consequently, the question must be asked - are these truly pulsations? Jeffery et al. (2015a) conducted a search for radial velocity variability, as surface motion should be detectable in the radial velocity data at periods equal to the light variations. In 2011, four hours of observations were obtained with the Ultraviolet and Visual Echelle Spectrograph (UVES) at the European Southern Observatory's Very Large Telescope (VLT). Fourier analyses of radial velocity measurements from 39 spectra reveal a small-amplitude peak at a frequency consistent with the most dominant photometric period of $\sim 1953$ s. This behaviour is seen in numerous ranges of the spectrum with no evidence for long-period or large amplitude variability that might suggest motion within a binary system. These measurements support the thesis that the photometric variations are

caused by surface pulsations.

The aim of the current study is to extend the earlier VLT/UVES observations in order to improve the frequency resolution and refine the sensitivity, especially for individual absorption lines. With improved frequency resolution we aim to detect the additional frequencies seen in the light curve. Since absorption lines from different elements may be formed at different depths in the photosphere, we also want to analyse the motion in the different lines in order to resolve the differential motion through the photosphere.

## 3.2 Observations & Methods

Observations were obtained with UVES during four half nights from 2015 August 23 – 27. All spectra were obtained with an exposure time of $200\,\text{s}$ (compared with the principal pulsation period of $\sim$1950 s) In total 355 pairs of spectra were obtained covering the wavelength regions 328nm - 456nm (blue arm) and 472nm-684nm (red arm. The mean signal-to-noise ratio (SNR) for the blue spectra is 16.6 and for red spectra is 18.6. The spectral resolution $R$ lies between 58 640 and 66 320. The data were reduced using the UVES pipeline tool EsoRex (Ballester et al., 2000; ESO CPL Development Team, 2015) which performs bias and flat-field correction, optimal extraction, and wavelength calibration.
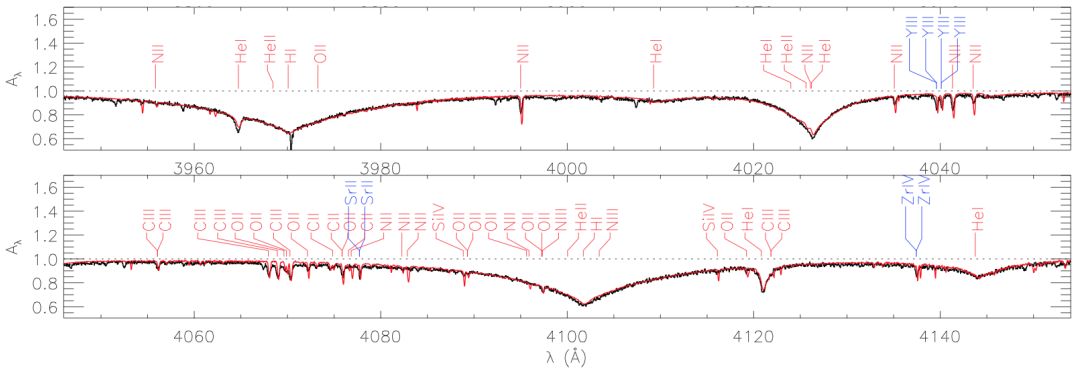


**Figure 3.1:** Fit of mean observed spectrum to the synthetic spectrum used to locate lines suitable for radial velocity analysis, 'heavy metals' are labeled in blue.
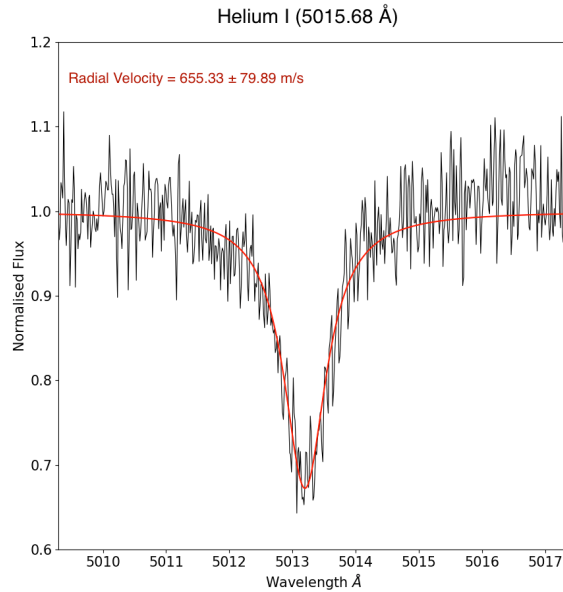
**Figure 3.2:** Final fit (after step 2) to a He I line for a single spectrum. Radial velocity shown has been corrected for heliocentric motion.

### 3.2.1 Radial Velocity Curves

In order to identify the absorption lines that may be suitable for radial velocity measurements a synthetic spectrum was computed (Figure 3.1). The spectrum was fit using the LTE code SPECTRUM (Jeffery et al., 2001b) with effective temperature $T_{eff} = 34\,000\,\mathrm{K}$, surface gravity $\log g/(\mathrm{cm\,s^{-2}}) = 5.6$ and abundances as in (Naslim et al., 2011). A recalculation of the atmospheric parameters or abundances was not performed. Each spectrum was normalised to unity by using a simple parabolic fit to the regions with no absorption lines. A two-step process was introduced to measure individual line positions. In step 1, the spectra were first smoothed using a Savitzky-Golay filter (Savitzky and Golay, 1964). The individual absorption lines were fit with a Lorentzian profile using least squares curve fitting using initial guesses from the model fits for the width and wavelength of the absorption line. The range of allowed solutions was relatively large. This step was necessary in order to fit spectral lines en masse, including weak lines and cases when the spectra become noisy due to poor observing conditions. In step 2, the same fits were performed on the un-filtered spectra using the fit parameters
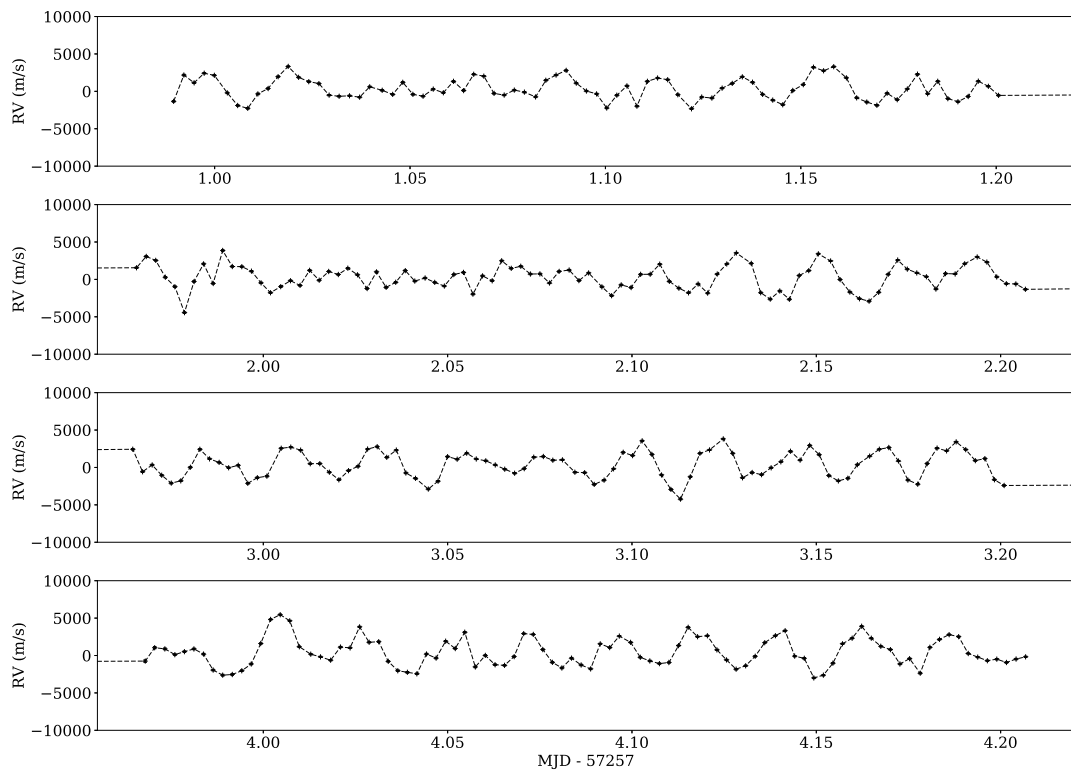
**Figure 3.3:** Radial velocity curve for He I 5015Å. The four windows correspond to the different nights of observation and time is represented in Modified Julian date.

from step 1 as starting values, and with stricter ranges for the allowed solutions. Figure 3.2 shows a typical fit to a spectral line.

## 3.3 Results

### 3.3.1 Radial Velocity Curves

We have obtained 57 radial velocity curves for 11 elements (Table 3.2). Figure 5.1 shows a typical radial velocity curve; errors are of the order of $100 \mathrm{m\,s}^{-1}$. The measurements suggest a change in the pulsation amplitude during a night of observation, which could imply frequency beating. This is not surprising considering that there are at least six detected photometric frequencies, and suggests that there is more than one frequency present in the radial velocity curve. Each radial velocity curve follows broadly the same

**Table 3.2:** Amplitudes ($a_{rv}$) and frequencies ($\nu$) for elements used in radial velocity analysis.

| | $\lambda$ (Å) | $a_{rv}$ (m/s) | $\pm$ | $\nu$ (mHz) | $\pm$ | | $\lambda$ (Å) | $a_{rv}$ (m/s) | $\pm$ | $\nu$ (mHz) | $\pm$ |
|---|---|---|---|---|---|---|---|---|---|---|---|
| C II | 3918.98 | 1954.20 | 505.60 | 0.51258 | 0.00031 | He III | 3613.64 | 2226.10 | 546.83 | 0.51204 | 0.00049 |
| | 3920.69 | 1395.00 | 199.90 | 0.51186 | 0.00032 | Ne II | 3965.02 | 1683.60 | 378.10 | 0.52337 | 0.00039 |
| | 4267.27* | 1433.50 | 136.60 | 0.51204 | 0.00029 | N II | 3995.00 | 1693.00 | 105.70 | 0.51168 | 0.00014 |
| | 5145.16 | 2196.90 | 314.00 | 0.51222 | 0.00031 | | 4041.31 | 1351.60 | 262.80 | 0.51204 | 0.00022 |
| | 6578.05 | could not detect frequencies | | | | | 4043.53 | 1836.20 | 286.00 | 0.51186 | 0.00032 |
| C III | 4056.05 | 2149.60 | 516.90 | 0.51204 | 0.00032 | | 4236.93 | 1445.60 | 447.60 | 0.51186 | 0.00028 |
| | 4067.94 | 1379.10 | 218.70 | 0.51204 | 0.00034 | | 4241.78 | 1265.90 | 375.10 | 0.51186 | 0.00028 |
| | 4068.91 | 1796.00 | 248.50 | 0.51222 | 0.00026 | | 4803.29 | 1629.70 | 347.40 | 0.48955 | 0.00043 |
| | 4070.26 | 1442.20 | 341.30 | 0.51168 | 0.00027 | | 5005.15 | 1275.90 | 116.10 | 0.51204 | 0.00019 |
| | 4186.90 | 1808.90 | 209.40 | 0.51186 | 0.00026 | | 5007.33 | 1320.90 | 244.90 | 0.51150 | 0.00052 |
| | 5695.92 | 1296.70 | 175.50 | 0.50052 | 0.00028 | | 5045.09 | 1923.60 | 327.50 | 0.51240 | 0.00040 |
| H I | 3703.85* | 2541.33 | 528.49 | 0.52265 | 0.00044 | | 5676.02 | 1120.20 | 266.00 | 0.50142 | 0.00073 |
| | 3889.05 | could not detect frequencies | | | | | 5666.63 | 1584.98 | 222.74 | 0.52391 | 0.00028 |
| | 3970.07 | could not detect frequencies | | | | | 5679.56 | 1448.00 | 175.40 | 0.51186 | 0.00023 |
| | 4340.46 | could not detect frequencies | | | | | 5686.21 | 2012.50 | 549.84 | 0.51276 | 0.00054 |
| | 4861.32 | 1397.09 | 299.04 | 0.51186 | 0.00042 | | 5941.65 | could not detect frequencies | | | |
| | 6562.80* | 1522.81 | 122.79 | 0.50034 | 0.00037 | 'Heavy Metals' | | | | | |
| He I | 3819.60* | 2232.57 | 425.86 | 0.52337 | 0.00040 | Ge III | 4178.96 | 1866.60 | 226.00 | 0.51204 | 0.00016 |
| | 3867.47 | could not detect frequencies | | | | | 4291.71 | 1857.27 | 451.47 | 0.52247 | 0.00048 |
| | 3888.65 | 1640.60 | 163.50 | 0.51240 | 0.00019 | Sr II | 4077.71 | 1452.90 | 127.30 | 0.51204 | 0.00023 |
| | 4026.19 | 1371.50 | 446.10 | 0.51204 | 0.00034 | | 4215.52 | 1699.97 | 303.40 | 0.51096 | 0.00036 |
| | 4120.81 | 1706.90 | 172.00 | 0.51204 | 0.00016 | Y III | 4039.60 | 1181.80 | 155.80 | 0.51186 | 0.00028 |
| | 4143.76 | could not detect frequencies | | | | Zr IV | 3686.91 | 1727.90 | 355.90 | 0.51168 | 0.00019 |
| | 4387.93* | 1337.29 | 365.77 | 0.51222 | 0.00052 | | 3764.32 | 1784.10 | 260.20 | 0.49999 | 0.00035 |
| | 4437.55 | 2374.66 | 513.22 | 0.51186 | 0.00043 | | 4137.44 | 1592.38 | 193.32 | 0.51186 | 0.00024 |
| | 4471.47 | 1282.08 | 319.00 | 0.51276 | 0.00049 | | 4198.27 | 1553.70 | 96.80 | 0.51204 | 0.00013 |
| | 4921.93 | 1712.20 | 137.10 | 0.51186 | 0.00018 | | 4317.08 | 1383.00 | 118.60 | 0.51186 | 0.00019 |
| | 5015.68 | 1684.50 | 81.50 | 0.51204 | 0.00010 | Telluric | 6299.23 | could not detect frequencies | | | |
| | 5047.74 | 1799.30 | 141.30 | 0.51204 | 0.00015 | | | | | | |
| | 5875.61 | 1886.20 | 92.40 | 0.51204 | 0.00010 | | | | | | |
| | 6678.15 | 1762.80 | 114.90 | 0.51204 | 0.00013 | | | | | | |

* Signal-to-noise < 3.0

**(a)** Carbon II 3920Å



**(b)** Nitrogen II 3995Å



**(c)** Carbon III 4070Å



**(d)** Germanium III 4178Å



**(e)** Zirconium IV 4198Å



**(f)** Strontium II 4077Å
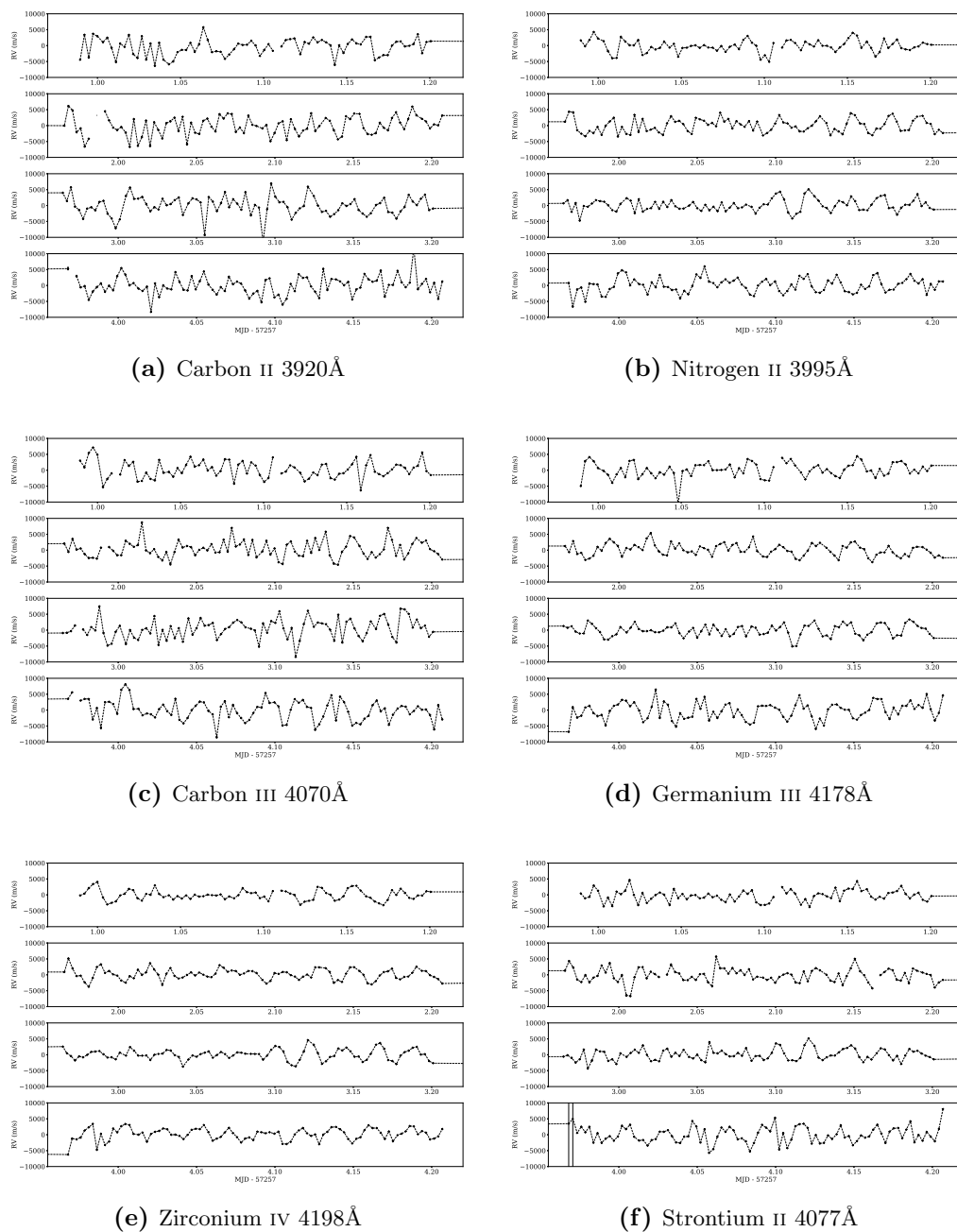
**Figure 3.4:** Radial velocity curves of six other lines.

trend, Figure 3.4 shows the velocity curves for six elements.

Telluric absorption lines were also measured, the radial velocity measurements for which give an essentially flat curve with a standard deviation of $370 \mathrm{m\,s^{-1}}$ . This should be compared with the stellar absorption lines which vary with an amplitude of

$> 5\,000\mathrm{m\,s^{-1}}$. The Fourier transform of the telluric radial velocities showed no peaks above $2\sigma$ (Fig. 3.5).

### 3.3.2 Fourier Transforms

Using the software package PERIOD04 (Lenz and Breger, 2005), the classical Fourier power spectrum was computed. We measured the frequency and semi-amplitude of the highest peak (Fig 3.6). This corresponds, in every case, to the dominant period of 0.5 mHz. Each of the 50 lines for which we obtained a good solution yielded the same frequency with a peak amplitude $>5\,\sigma$. The data were pre-whitened to ascertain if any further peaks could be detected. For HeI (4921Å), three other frequencies can be seen that agree with the photometric frequencies, but with a signal to noise after pre-whitening of between 2 and 3. We identify these as significant peaks because we already expect these frequencies to be present. 88% of all lines measured show equivalent peaks at $2-3\sigma$. All 6 photometric periodicities were detected this way, with different frequencies appearing in different lines.

### 3.3.3 Line Profile Variations

We investigated if the line profile changes during different stages of the pulsation. Non radial pulsations are often associated with line-profile variations but usually in rapidly-rotating stars where temperature variations across the surface produce more or less flux at different velocities. LS IV$-14°116$ is known to be a slowly rotating star. Figure 3.7 shows the line profile of a Zirconium IV line averaged at different stages of the pulsation. The spectra were co-added at the phase minimum of the pulsation (–2,000 m/s), the maximum of pulsation (+2,000 m/s) and around the mean (±500 m/s), the straight mean of the line profile is also shown here. No asymmetries can be seen at any phase. To be certain we measured the 3rd moment to ascertain if there is any significant skewness in the line profile at any of the four stages highlighted here, and was repeated for all lines with measured radial velocities. The values we obtained are equivalent to a lorentzian profile with the same signal to noise ratio as the spectral line. This indicates that the line profiles are as symmetric as we can discern from these data.
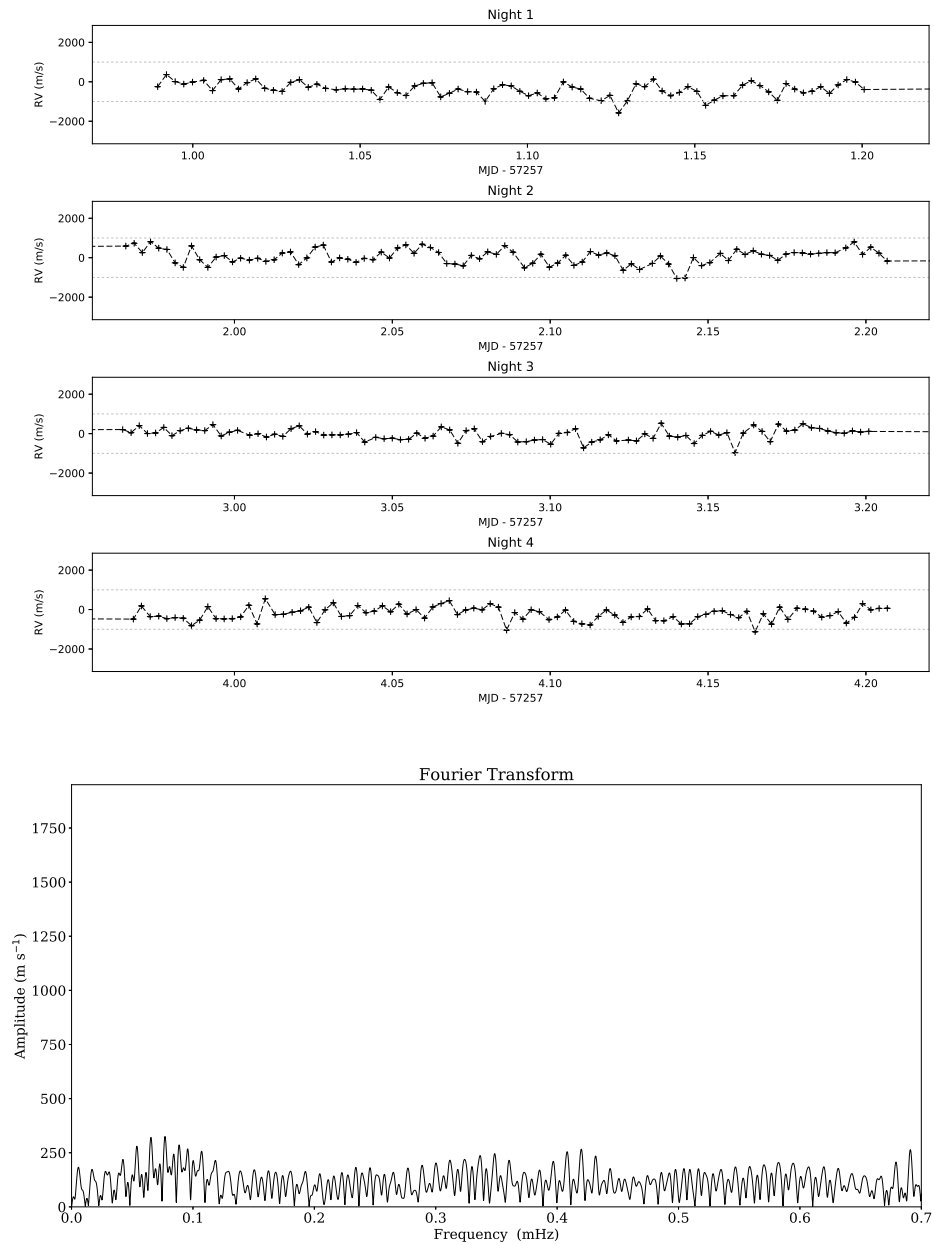
**Figure 3.5:** Top: Radial velocities for a telluric line, the dashed lines represent $\pm$ 1000 m s$^{-1}$. Bottom: Fourier transform of telluric velocities.
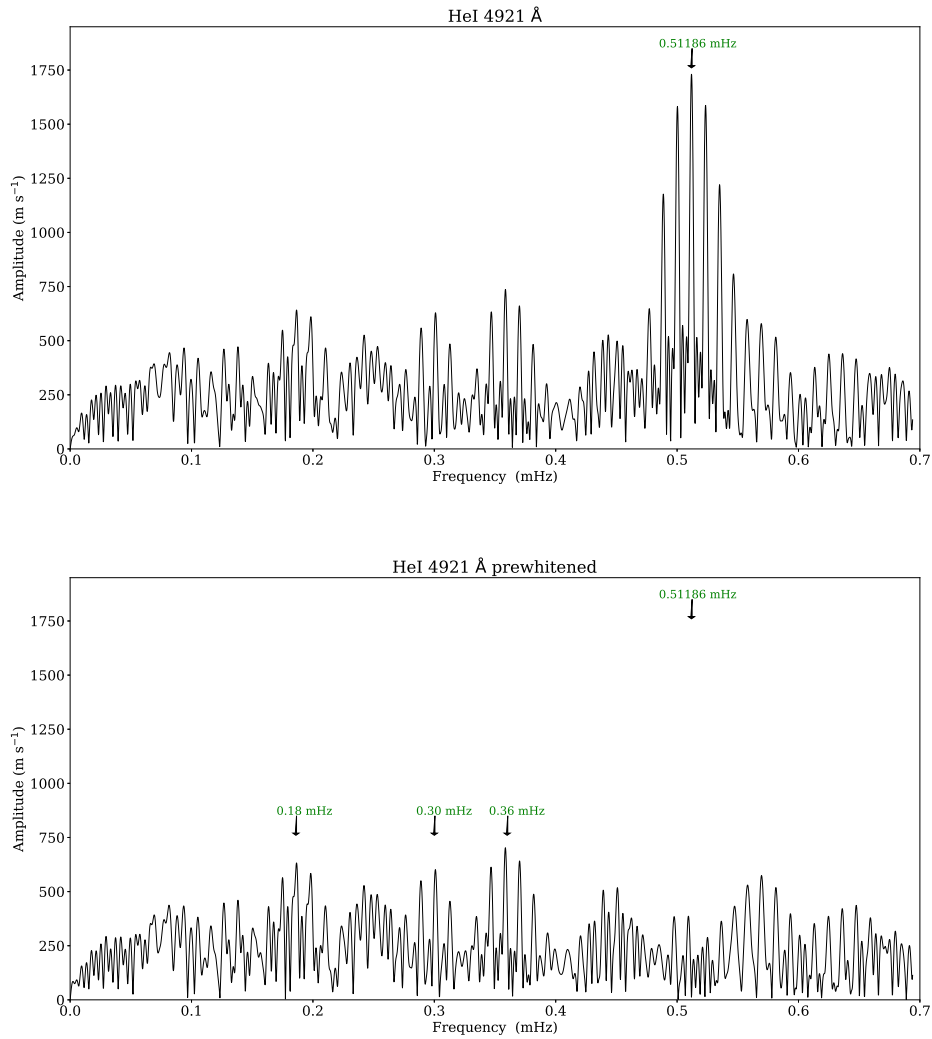
**HeI 4921 Å**

**Figure 3.6:** Top: Fourier transform of radial velocity data for HeI 4921Å. Bottom: Fourier transform of the same data pre-whitened by a fit to the period at 0.51186 mHz. The marked frequencies correspond approximately to previously detected photometric frequencies.
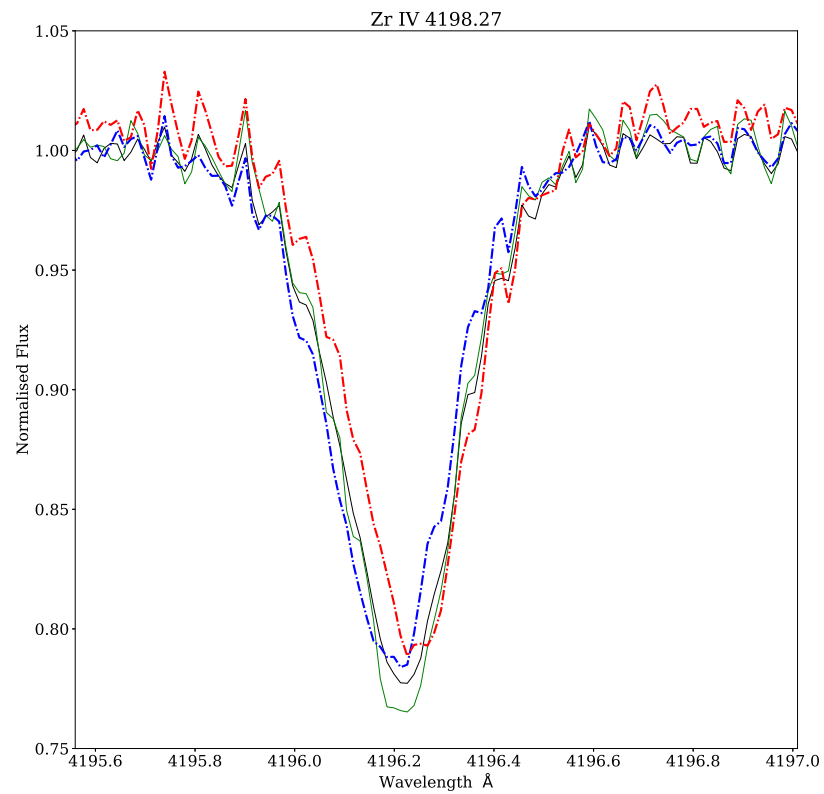
**Figure 3.7:** Line profile of Zr IV. The blue profile is a mean of spectra with radial velocities less than –2 000 m/s, the red profile has been average with spectra with velocities greater than +2 000 m/s, the mean spectra with |rv| < 500 m/s are shown in black and the straight mean profile is in green.
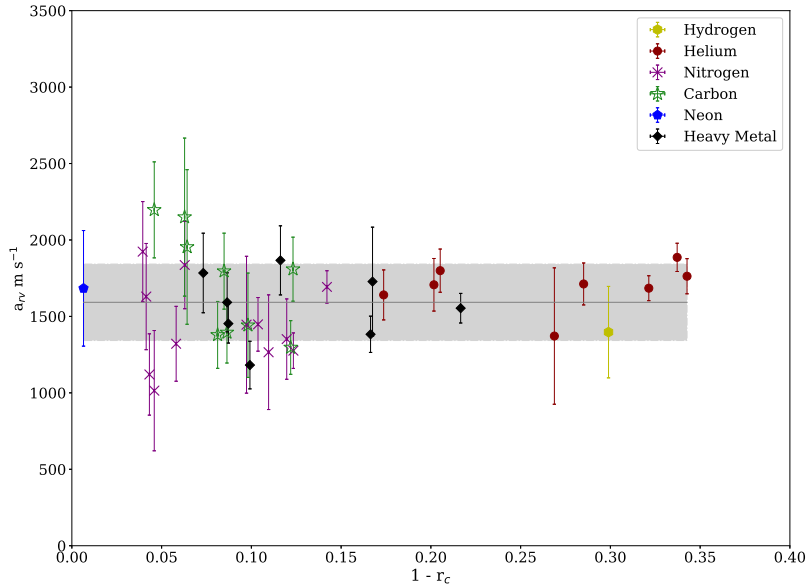
**Figure 3.8:** Pulsation amplitude versus residual intensity at line centre ($r_c$). Here "heavy metals" denote Zr, Y and Sr and Ge. The solid line is the mean amplitude of all data points and the shaded region represent $1\sigma$ about this line. The points displayed are those which have signal-to-noise $> 3$.

### 3.3.4 Line Intensity

Following the Fourier analysis we looked at the amplitude of the main pulsation period in different lines as a function of line intensity. Residual intensity at line centre ($r_c$) can be used as a model-independent proxy for the depth of formation in the photosphere. For p-modes, an increase in pulsation amplitude is often seen as the pulsation (wave) travels upwards through the photosphere into regions of lower density (Kurtz et al., 2005). In Fig 3.8 we see no significant change in amplitude with depth in the photosphere, all data points lie within $2\sigma$ of the mean.

Different parts of the spectral line are formed in different regions of the photosphere. The line bisector is a measure of the displacement of the centre of the red and blue wing from the core of the spectral line at each residual flux. If we measure the line bisector velocity at various depths of a line we could possibly get a fine resolution of the changing pulsation behaviour as a function of depth in the line–forming layer of
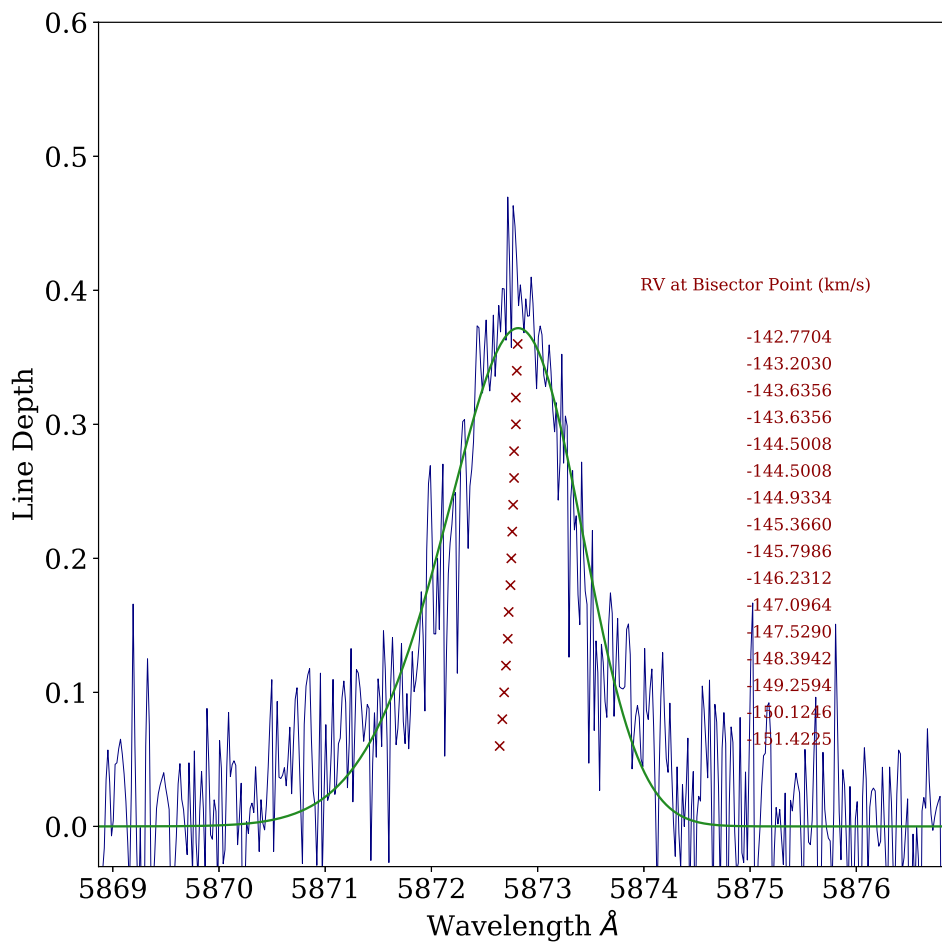
**Figure 3.9:** Skewed gaussian fit to a Helium absorption line, the red 'x' indicates the bisector points used for the radial velocity measurements shown to the right. The absorption line has been inverted to match the gaussian function.

that spectral line. This has been used to obtain a detailed vertical cross section of the roAp pulsation modes. The rapidly oscillating Ap stars (roAp) pulsate with low degree non-radial p-modes, thought to be driven by the $\kappa$-mechanism, they are an ideal class of pulsator to study the interaction between pulsations, rotation, chemical stratification and strong global magnetic fields

(Ryabchikova et al., 2007) have studied the velocity amplitudes of the pulsations of these stars to resolve the amplitude and phase of magnetoacoustic waves and their dependence on depth. Their results shown that, in general, pulsations waves are represented by a superposition of the running and standing wave components and are characterised by an increase in pulsation amplitude with line bisector depth.

To test whether this method could result in a similar outcome for g-modes, a skewed gaussian function[1] was fit to the individual spectra lines. The radial velocities were measured at the midpoints of the skewed gaussian at intervals of 0.05 in line depth (Fig. 3.9). This was done for the 355 spectra to get roughly 10 radial velocity curves per line. Only seven He I lines were used as they could be fitted well with this gaussian function; hydrogen is too broad and often blended with other lines and metal lines are too weak. Fourier analysis was used to get the amplitude of the main frequency. Figure 3.10 show the results of the amplitude of the radial velocity curves as a function of depth in the helium lines. These line bisector results agree with the individual lines, that there is no significant change in amplitude of the pulsation as a function of depth in the photosphere. This is perhaps due to the nature of g-modes in which the wave motion is predominantly transverse, unlike in p-modes.

---

[1]A skewed Gaussian is the sum of an independent Gaussian and exponential function.
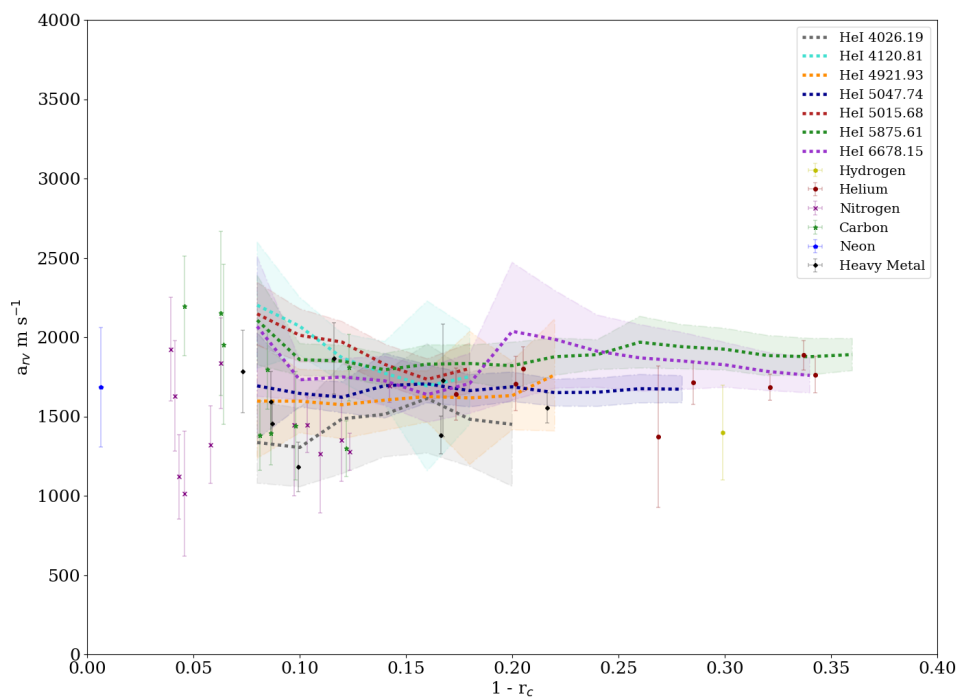
**Figure 3.10:** Pulsation amplitude as a function of line depth. Data points are as in Fig 3.8, the dotted lines represent the amplitude of the radial velocity curves at different depths of each Helium line. The shaded regions display the associated errors. The bisector depths do not directly coincide with the residual intensity at line centre as $r_c$ is a mean measurement whereas the bisector depth reaches as deep as possible in each of the line profiles.

## 3.4   Summary

We have performed a high-precision study of the radial velocity variability of LS IV$-$14°116, a curious pulsating hot subdwarf. We have found multiple periods in the radial velocity curve and have investigated the amplitude of the pulsation as a function of depth in the photosphere. We do see an increased dispersion of points at small values of (1–$r_c$), this is more likely due to noise than any physical effect. From measurements of the primary pulsation mode (0.5mHz), its amplitude does not appear to change with depth. This implies a standing wave behaviour.

The ratio of photometric amplitude to velocity amplitude could, perhaps, reveal some information on the degree of pulsation ($l$). For the primary pulsation mode we get $\delta V/\delta v \approx 2$. Taking the light amplitude variations from Green et al. (2011) for different frequencies their corresponding velocity amplitudes[1], all ratios are between 1 and 5.

Ryabchikova et al. (2007) give the radial velocity amplitudes for a number of the roAp stars and from Hubrig et al. (2004) we have the light amplitudes. For the stars common to each sample HD 101065, HD 137949 and HD 128898 we get a light-velocity amplitude of approximately 22, 6 and 13 respectively, these stars are known to be low degree modes ($l \leq 3$). Comparing this to LS IV$-$14°116's value of $\sim 2$ suggests that the g-modes in LS IV$-$14°116 are from a higher degree mode ($l \geq 3$) .

---

[1] The velocity amplitudes of other frequencies range between 400m/s and 1200m/s.

# Resolving Photospheric Pulsations of the Extreme Helium Star BX Cir

<div style="text-align:right; font-size:3em;">4</div>

BX Cir is an extreme helium (EHe) star and a B-type giant, with a nitrogen-rich carbon-poor surface, it pulsates with a period of 0.107d which is currently decreasing. Pulsations occur in many EHe stars. We use SALT HRS spectroscopy of the pulsating variable star BX Cir to perform line-by-line analysis of the entire pulsation cycle. We find no evidence of discontinuities or shocks in the radial velocity curves or line profiles of BX Cir.

The work done in this chapter is currently in prep. and will be submitted to MNRAS.

## 4.1   Introduction

In this chapter we explore the dynamics of the atmosphere of the pulsating star BX Cir, first classified as an extreme helium star by Heber et al. (1986), who found broad He I absorption lines and approximated the atmospheric parameters at $T_{eff} = 22\,000$K and $\log g = 3.2$. Saio (1993) predicted BX Cir would pulsate, due to the classical kappa mechanism and the iron opacity bump near $2{\times}10^5$K . Following this Kilkenny and Koen (1995) discovered BX Cir to be variable with a semi-amplitude of $\sim$0.01 mag in B with a period $\sim$0.107 d.

BX Cir shares many of its characteristics with the EHe star V652 Her, a star which also pulsates with a period of $\sim$0.11d. Both V652 Her and BX Cir have surface gravities too high to be CO+He white dwarf mergers, and their abundances are inconsistent with models for this evolutionary pathway; they may represent He+He white dwarf mergers (Zhang and Jeffery, 2012). Although the fact that one is nitrogen-rich and the other is carbon-rich still represents something of a mystery, the rates of period change (Kilkenny et al., 2005; Kilkenny and Worters, 2014) are consistent with the merger model.

In was recently demonstrated for V652Her using HDS on Subaru (Jeffery et al.,
2015b) that minimum radius coincides with a very strong outward acceleration through
the photosphere. The speed of the pulse running upwards through the photosphere is at
least 10 times the local sound speed meaning it must generate a shock wave. In BX Cir,
the acceleration phase is longer, although the pulsation periods and stellar dimensions
are very similar. One can surmise that the two stars represent a strong-shock and a
weak-shock pulsation, respectively. The objective of this chapter is to test if BX Cir
represents a weak shock pulsation.

### 4.1.1  Observations

Observations were made with the Southern African Large Telescope (SALT) between
the months of May and July 2015 (see section in Ch 2). In total, 275 spectra were
obtained with varying exposure times (Table 4.1) and an average signal-to-noise ratio
(SNR) of 11. The HRS spectrum was reduced to 1-dimension (total counts versus
wavelength) object and sky orders using the SALT HRS pipeline[1] (Crawford et al.,
2016). The orders were rectified, mapped onto a common wavelength grid, equally
spaced in log wavelength, and merged using an order-management tool written for
echelle spectra (Jeffery priv. comm).

As shown in Figure 4.1, the CCD of HRS contains a small defect which effects
many orders of the spectrograph. This results in sharp lines appearing at constant
wavelengths throughout the spectra. These defects were identified and masked in all
spectra, Figure 4.2 shows a spectra before any masks were applied and after the mask-
ing; we can see that the masks remove the defect adequately during different phases of
pulsation.

## 4.2  Phase folding

In order to optimise the SNR of the data, the spectra were phase folded into 38 bins,
these bins are not equally spaced in phase but chosen so as to contain approximately
7 spectra per bin, each phase bin is $\sim 0.027$ cycles. The spectra were co-added and

---

[1]PyHRS:$http://pysalt.salt.ac.za/$

**Table 4.1:** Observation log for BX Cir.

| Date | Number | Exp time (s) | Date | Number | Exp time (s) |
|---|---|---|---|---|---|
| 2015-05-07 | 1 | 300 | 2015-06-07 | 7 | 190 |
| | 4 | 190 | 2015-06-11 | 12 | 190 |
| 2015-05-08 | 12 | 190 | 2015-06-12 | 22 | 190 |
| | 1 | 1800 | 2015-06-13 | 16 | 200 |
| 2015-05-09 | 18 | 190 | 2015-06-14 | 24 | 190 |
| | 1 | 800 | 2015-06-23 | 1 | 2400 |
| 2015-05-13 | 12 | 190 | | 24 | 190 |
| 2015-05-16 | 11 | 190 | 2015-07-04 | 1 | 10 |
| 2015-05-17 | 12 | 190 | | 11 | 190 |
| 2015-05-25 | 35 | 190 | 2015-07-10 | 1 | 400 |
| 2015-05-27 | 14 | 190 | | 11 | 190 |
| 2015-05-28 | 21 | 190 | | | |
| | 2 | 1200 | | | |

weighted based on their SNR. The 17 nights of data were phased to the pulsation cycle using the ephemeris from Kilkenny and Worters (2014), where $T_0 = 2449\,477.4663$d and $P_0 = 0.106\,579\,94$d. Only spectra with an exposure time of 190 or 200 s were used to avoid line smearing or the addition of unnecessary noise, as would be the case of the spectra with an exposure time of 10s. The exposure time of 200s correspond to 0.0217 cycles. Figure 4.3 shows the number of spectra used per bin and the SNR of each phased spectra . The effect of phase folding the spectra increases our average SNR to 29.

## 4.3   Radial velocity measurements

As in section 3.2.1, we first need a model spectrum to identify lines suitable for radial velocity measurements. We used the highest SNR spectra (exp time $= 2400$s[1], SNR $=$ 65) to fit a model using the LTE code SPECTRUM (Jeffery et al., 2001b). Figure 4.4 shows our spectra fit to a model with with effective temperature $T_{\text{eff}} = 24\,800$ K, surface gravity $\log g/(\text{cm s}^{-2}) = 3.5$. The temperature is known to change throughout the pulsation cycle so this is not a difinative measurement of the atmospheric parameters; the goal was simply to identify lines. We have measured radial velocities for 72 lines,

---

[1]We expect velocity smearing of the order of $10\,\text{km s}^{-1}$ due to the exposure time corresponding to 0.26 cycles and the pulsation phase being 0.35 at the start of the exposure.
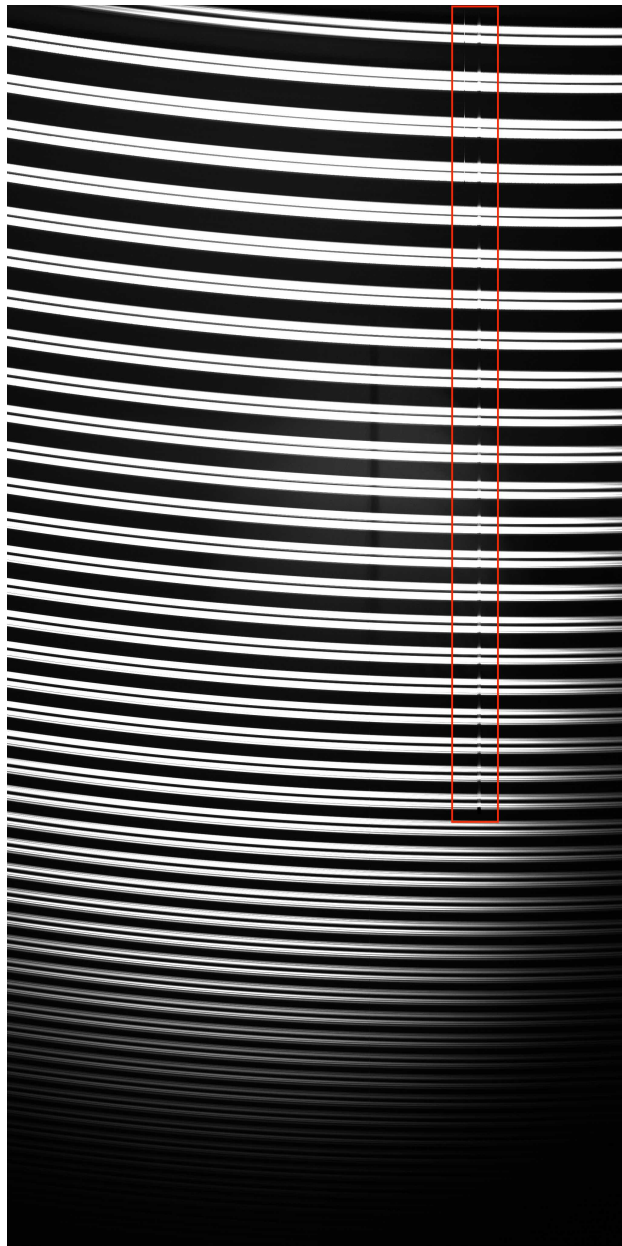
**Figure 4.1:** HRS master flat field frame showing the defect, highlighted in red.

these were measured line-by-line as described in section 3.2.1. Figure 4.5 shows the radial velocity curves for six lines. Table 4.2 lists all lines measured along with the mean line depth and equivalent width, Figures A.1 – A.2 in Appendix A show the radial velocity curves for all these lines. A mean line profile was created from the mean line depth, $r_c$, mean line position $\lambda$ and the mean FWHM , $\Gamma$. The equivalent width was calculated from this profile. Figure 4.6 shows the mean line profiles and an illustration
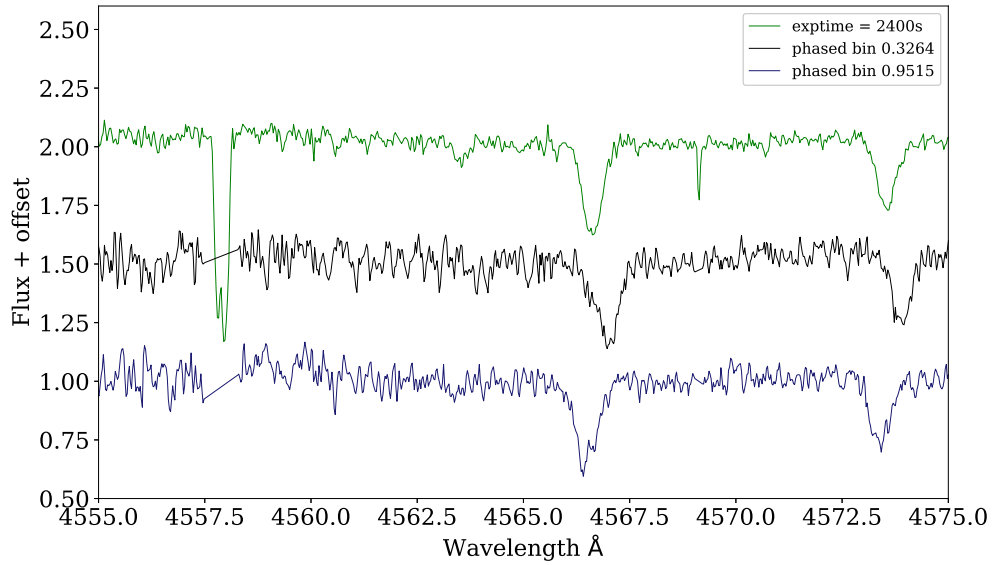
**Figure 4.2:** Comparison of three spectra in different pulsation phases, the topmost spectra has been used to identify the wavelengths at which the defects appear. The spectra below are shown after masks have been applied to those areas.
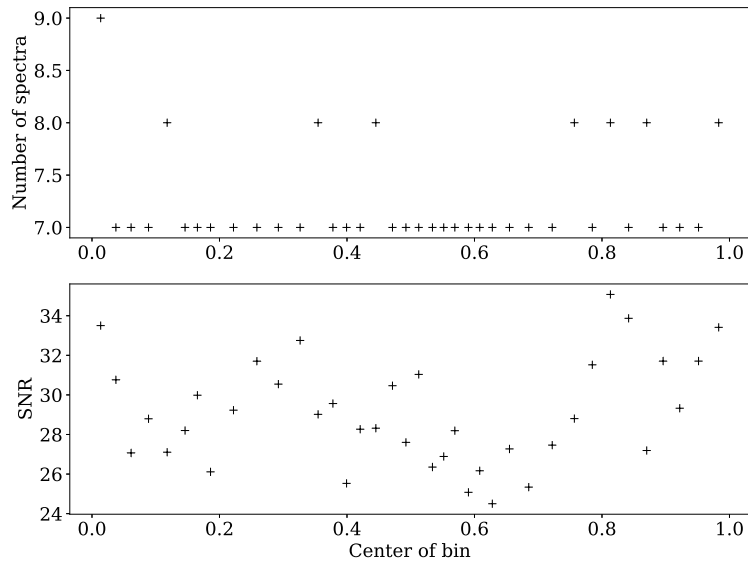


**Figure 4.3:** The number of spectra used per phase bin (top panel) and the SNR of each resulting co-added spectra (bottom).
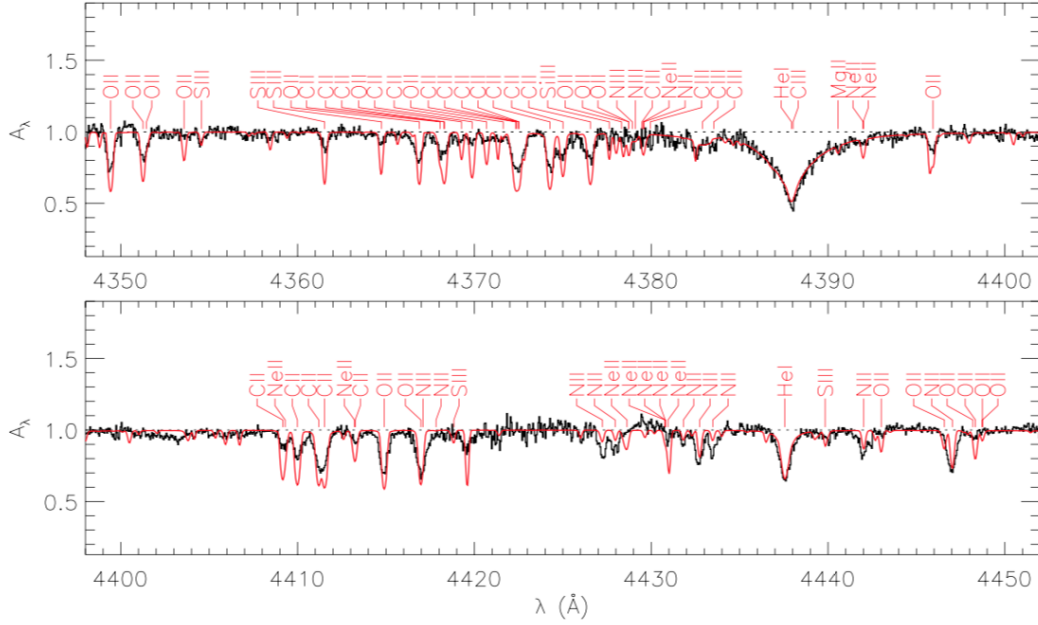
**Figure 4.4:** Fit of one spectrum to the synthetic spectrum used to locate lines suitable for radial velocity analysis. The model shown has $T_{eff} = 24,800$K and $\log g/(\text{cm s}^{-2}) = 3.5$.

of the equivalent width measured.

### 4.3.1 Errors

We have tested to see if the formal errors represent accurate uncertainties in the radial velocity measurements. Gaussian random noise was added in varying amounts to the model spectra in 1000 iterations. We use 10 different values for SNR approximately in the range seen in our phased spectra. The positions of seven lines of different species were measured and a standard deviation was recorded. Figure 4.7 show the standard deviation as a function of SNR. As expected the higher the SNR the lower the deviation from the mean. In addition the broad lines such as Helium show higher uncertainties and the measuring of radial velocities is more precise in sharp lines. We can see the uncertainties can vary up to $1.5\,\text{km s}^{-1}$ whereas the mean formal error in helium lines at low SNR is $0.12\,\text{km s}^{-1}$. This is a significant difference, therefore, in further plots we show the most pessimistic errors of $1.5\,\text{km s}^{-1}$.

**Table 4.2:** Line depth and equivalent width of each line measured.

| Line | <r$_c$> | $\sigma$ | <EW> | $\sigma$ | Line | <r$_c$> | $\sigma$ | <EW> | $\sigma$ |
|------|---------|----------|------|----------|------|---------|----------|------|----------|
| Al III 4512.54 | 0.20 | 0.04 | 0.10 | 0.04 | N II 4654.53 | 0.17 | 0.02 | 0.11 | 0.02 |
| C II 4267.02 | 0.48 | 0.05 | 0.65 | 0.20 | N II 4667.21 | 0.15 | 0.02 | 0.09 | 0.03 |
| C II 4317.26 | 0.29 | 0.03 | 0.29 | 0.08 | N II 4678.14 | 0.24 | 0.02 | 0.25 | 0.04 |
| C II 4372.33 | 0.32 | 0.05 | 0.42 | 0.10 | N II 4694.7 | 0.24 | 0.04 | 0.18 | 0.03 |
| C II 4411.52 | 0.31 | 0.05 | 0.38 | 0.11 | N II 4774.24 | 0.12 | 0.02 | 0.13 | 0.03 |
| C II 4625.64 | 0.16 | 0.02 | 0.24 | 0.03 | N II 4779.72 | 0.23 | 0.02 | 0.32 | 0.03 |
| C II 4638.92 | 0.29 | 0.03 | 0.33 | 0.05 | N II 4788.13 | 0.24 | 0.04 | 0.22 | 0.04 |
| C II 4802.7 | 0.28 | 0.02 | 0.38 | 0.02 | N II 4810.31 | 0.12 | 0.02 | 0.09 | 0.03 |
| C II 5032.13 | 0.22 | 0.03 | 0.28 | 0.04 | N II 5001.47 | 0.36 | 0.04 | 0.39 | 0.06 |
| C II 5121.83 | 0.24 | 0.03 | 0.30 | 0.06 | N II 5002.7 | 0.23 | 0.03 | 0.27 | 0.06 |
| C II 5133.28 | 0.41 | 0.04 | 0.43 | 0.07 | N II 5007.33 | 0.25 | 0.03 | 0.23 | 0.05 |
| C II 5139.17 | 0.21 | 0.03 | 0.23 | 0.05 | N II 5010.62 | 0.31 | 0.03 | 0.34 | 0.05 |
| C II 5143.49 | 0.30 | 0.03 | 0.30 | 0.06 | N II 5025.66 | 0.19 | 0.02 | 0.20 | 0.05 |
| C II 5145.16 | 0.37 | 0.04 | 0.39 | 0.05 | N II 5045.09 | 0.38 | 0.04 | 0.46 | 0.06 |
| C II 5151.09 | 0.31 | 0.04 | 0.38 | 0.07 | N II 5073.59 | 0.21 | 0.03 | 0.22 | 0.07 |
| C II 5342.38 | 0.20 | 0.03 | 0.25 | 0.05 | O II 4319.63 | 0.22 | 0.04 | 0.24 | 0.08 |
| He I 4437.55 | 0.38 | 0.03 | 0.40 | 0.08 | O II 4349.43 | 0.34 | 0.15 | 0.22 | 0.27 |
| He I 4713.14 | 0.48 | 0.02 | 0.61 | 0.04 | O II 4351.26 | 0.22 | 0.05 | 0.15 | 0.07 |
| He I 4921.93 | 0.45 | 0.01 | 2.27 | 0.16 | O II 4416.97 | 0.33 | 0.08 | 0.42 | 0.14 |
| He I 5015.68 | 0.46 | 0.02 | 0.81 | 0.09 | O II 4590.97 | 0.25 | 0.03 | 0.29 | 0.06 |
| He I 5047.74 | 0.41 | 0.03 | 0.59 | 0.06 | O II 4596.18 | 0.24 | 0.04 | 0.23 | 0.05 |
| Mg II 4481.33 | 0.37 | 0.04 | 0.33 | 0.04 | O II 4602.06 | 0.36 | 0.04 | 0.32 | 0.05 |
| N II 4236.93 | 0.36 | 0.14 | 0.32 | 0.12 | O II 4638.85 | 0.28 | 0.03 | 0.35 | 0.05 |
| N II 4237.05 | 0.36 | 0.15 | 0.33 | 0.13 | O II 4641.81 | 0.28 | 0.04 | 0.38 | 0.06 |
| N II 4241.78 | 0.35 | 0.06 | 0.50 | 0.14 | O II 4649.14 | 0.32 | 0.05 | 0.27 | 0.07 |
| N II 4432.74 | 0.26 | 0.13 | 0.38 | 0.21 | O II 4661.63 | 0.22 | 0.03 | 0.13 | 0.02 |
| N II 4442.02 | 0.20 | 0.03 | 0.19 | 0.06 | O II 4676.23 | 0.20 | 0.02 | 0.19 | 0.04 |
| N II 4447.03 | 0.34 | 0.15 | 0.30 | 0.08 | O II 4699.22 | 0.18 | 0.03 | 0.14 | 0.03 |
| N II 4530.4 | 0.27 | 0.03 | 0.26 | 0.07 | O II 4705.35 | 0.20 | 0.02 | 0.14 | 0.02 |
| N II 4552.53 | 0.44 | 0.04 | 0.39 | 0.04 | O II 4943.0 | 0.16 | 0.03 | 0.15 | 0.04 |
| N II 4601.48 | 0.36 | 0.04 | 0.32 | 0.06 | Si III 4552.62 | 0.44 | 0.04 | 0.40 | 0.05 |
| N II 4607.16 | 0.35 | 0.02 | 0.24 | 0.03 | Si III 4567.82 | 0.39 | 0.03 | 0.26 | 0.03 |
| N II 4613.87 | 0.33 | 0.03 | 0.23 | 0.03 | Si III 4574.76 | 0.30 | 0.03 | 0.17 | 0.03 |
| N II 4621.29 | 0.33 | 0.03 | 0.51 | 0.05 | Si III 4813.3 | 0.17 | 0.02 | 0.15 | 0.04 |
| N II 4630.54 | 0.47 | 0.03 | 0.47 | 0.04 | Si III 4819.72 | 0.21 | 0.02 | 0.18 | 0.04 |
| N II 4643.09 | 0.35 | 0.06 | 0.38 | 0.06 | Si III 4828.96 | 0.23 | 0.02 | 0.27 | 0.04 |
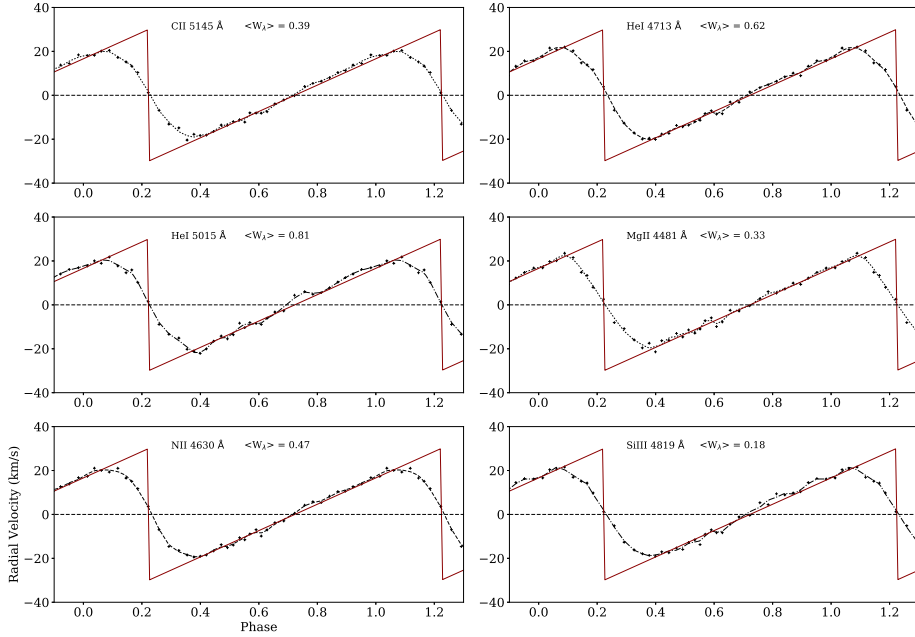
**Figure 4.5:** Six radial velocity curves, each '+' is a measurement and the dot dash line is the smoothed curve. The red lines are guides to represent infinite acceleration and uniform deceleration.

## 4.4 Analysis of radial velocity curves

In a highly compressed and possibly shocked material the accelerating atmosphere should show broader lines at minimum radius due to the higher surface gravity. There is also a possibility of seeing both the inward falling as well as the outward rising material in the same absorption line. This behaviour is seen clearly in the lines of V652 Her (Jeffery et al., 2015b). There is a jump discontinuity in the weak absorption line (deeper in the atmosphere) which is further evidence of a shock propagating in a highly compressed atmosphere.

Figure 4.8 shows the trailed spectra of a few absorption lines over the entire pulsation cycle. No discernible broadening, discontinuities or line profile asymmetries can be seen at all. The absorption shift in all lines appears to be a smooth transition from blueshift to redshift.

Next we take a closer look at the radial velocity curves. An initial inspection does not reveal any substantial difference in phase or amplitude The depth in the photosphere

**Figure 4.6:** Mean line profiles and representation of the equivalent width for each line shown in Fig. 4.5.

at which the core of a spectral line is formed is closely tied to the strength of the line; weak absorption lines are formed deeper, strong lines are formed farther out. Meaning that if we examine the measurements of lines formed deeper in the atmosphere we may detect a difference in the results in comparison with lines formed close to the surface. To that end, radial velocity measurements were then averaged from lines of similar
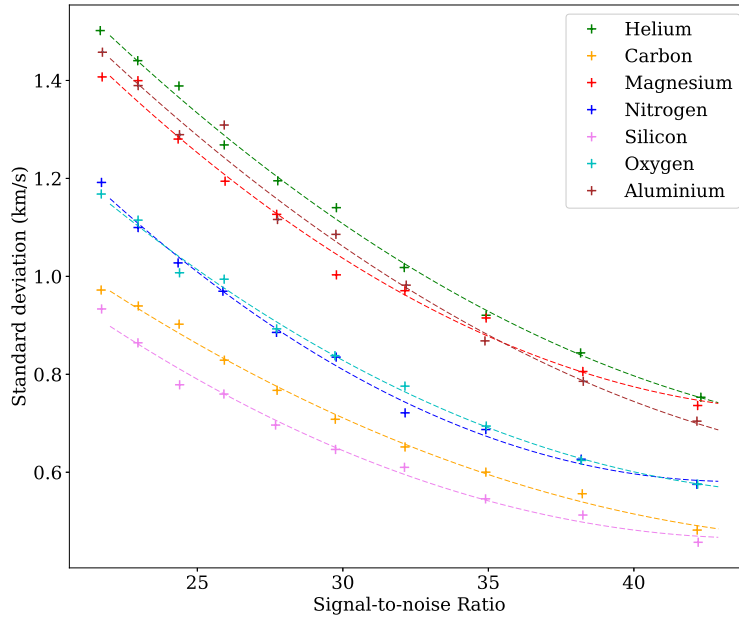
**Figure 4.7:** Standard deviation of the radial velocity measurement from a simulated spectrum versus the SNR of that spectrum, for seven elements.

strengths and are plotted in Figure 4.9. The range in line strength in which the lines were grouped together were chosen so that they each contain roughly equal numbers of lines. Again we find no discernible difference, the mean radial velocity curves are equivalent within errors.
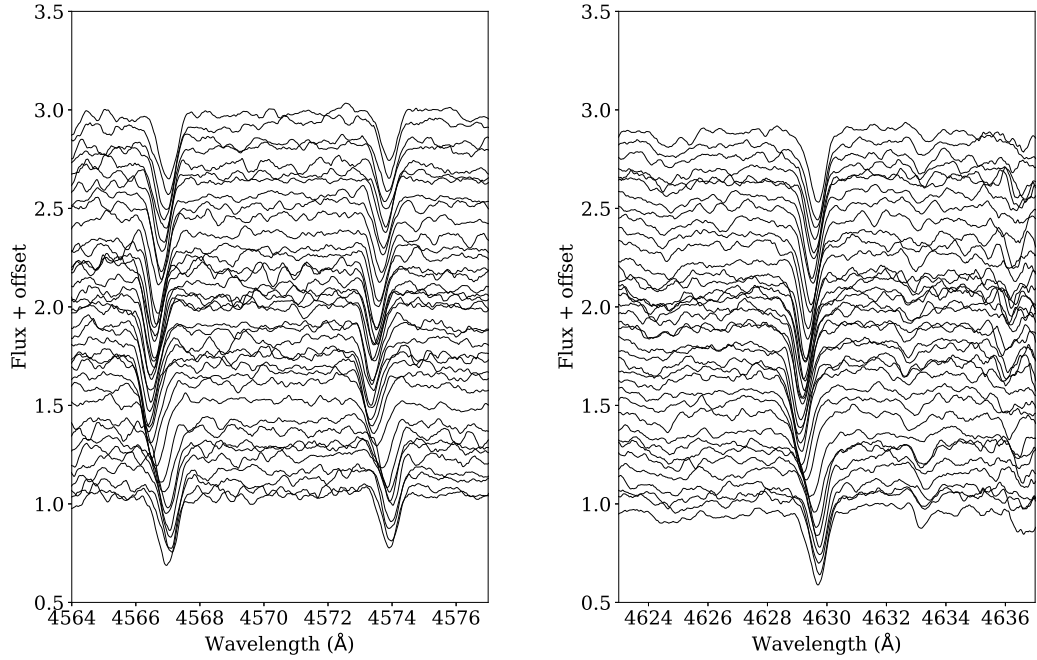
**Figure 4.8:** Line profile behaviour of two Si III lines (left) and one N II (right) line. The spectra are plotted with on offset which is proportional to their phase (cφ). The spectra have been smoothed used a savitzky golay filter, for clarity.
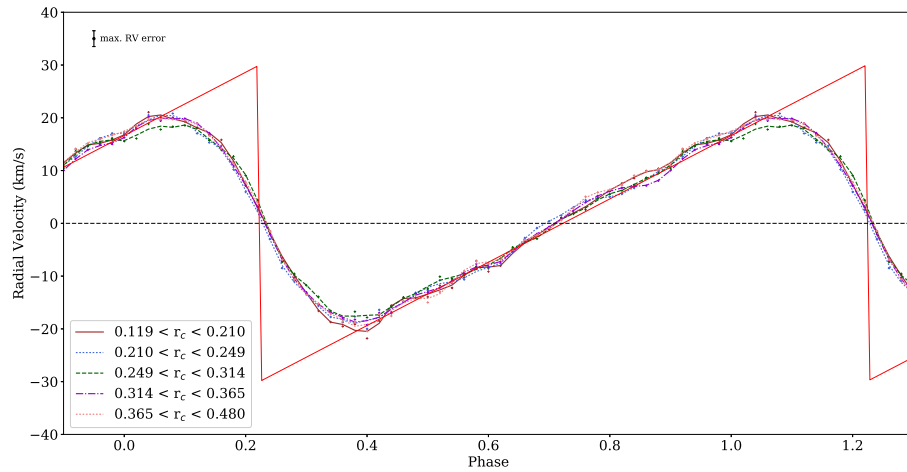


**Figure 4.9:** Comparison of the mean radial velocity curves. Each curve is the mean of all radial velocity curves in a particular line depth range.
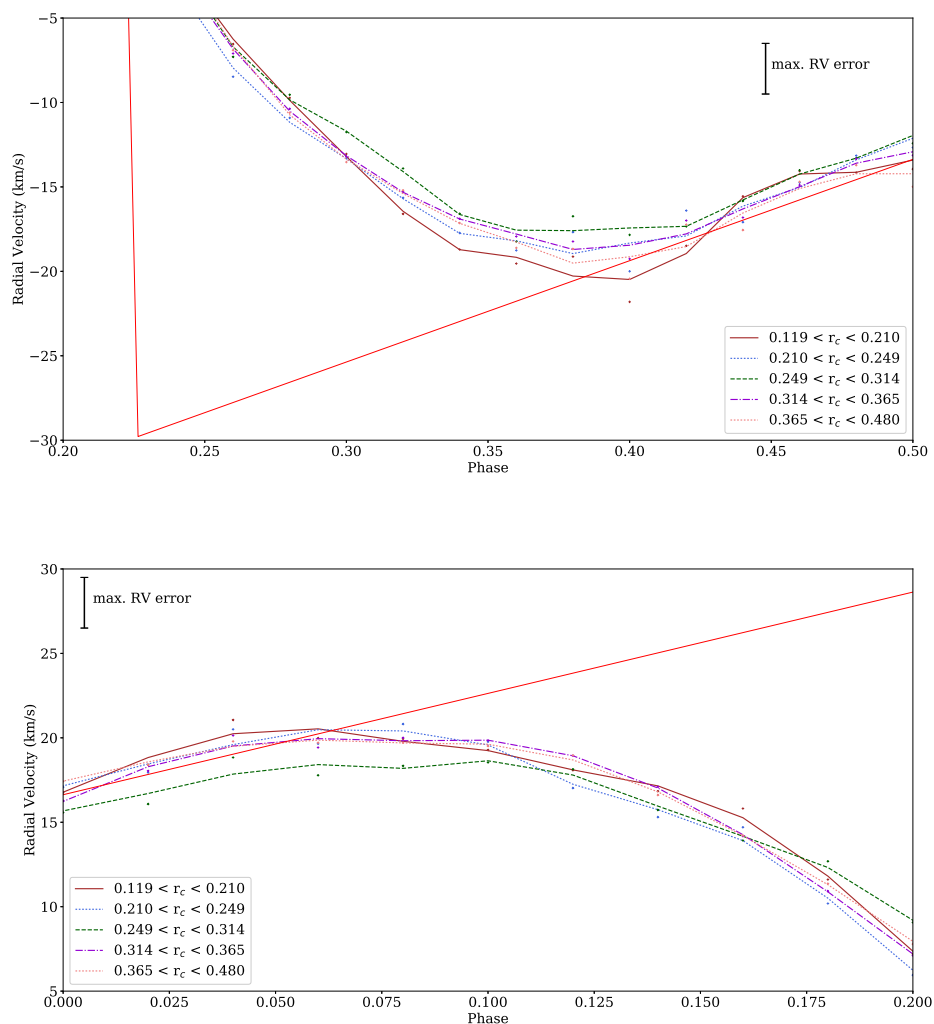
**Figure 4.10:** Zoomed in portions of mean radial velocity curves

## 4.5 Summary

We have analysed a time series of spectra for the pulsating Extreme Helium star, BX Cir. A line-by-line radial velocity analysis has been performed and radial velocity curves are presented for 72 lines. A comparison of the velocity curves by line and by depth in the photosphere has implied that the pulsation of this star is continuous, lacking any discontinuity or shock.

A closer inspection of the mean velocity curves at maximum and minimum radial

velocity (Fig. 4.10), does not reveal anything about the behaviour of the curves as a function of line depth. The difference in the amplitude and phase of the mean velocity curves are smaller than the measurement errors. Therefore we must conclude that the photosphere of BX Cir pulsates uniformly.

These results can be used as observational constraints for non-linear hydrodynamical pulsation models.

# Kinematics of Subluminous O and B Stars by Surface Helium Abundance

<span style="font-size:large">5</span>

The majority of hot subdwarf stars are low-mass core-helium-burning stars. Their atmospheres are generally helium deficient; however a minority have extremely helium-rich surfaces. An additional fraction have an intermediate surface-helium abundance, occasionally accompanied by peculiar abundances of other elements. We have identified a sample of 88 hot subdwarfs including 38 helium-deficient, 27 intermediate-helium and 23 extreme-helium stars for which radial-velocity and proper-motion measurements, together with distances, allow a calculation of Galactic space velocities. We have investigated the kinematics of these three groups to determine whether they belong to similar or different galactic populations. The majority of helium-deficient subdwarfs in our sample show a kinematic distribution similar to that of thick disk stars. Helium-rich sdBs show a more diverse kinematic distribution. Although the majority are probably disk stars, a minority show a much higher velocity dispersion consistent with membership of a Galactic halo population. Several of the halo subdwarfs are members of the class of "heavy-metal" subdwarfs discovered by Naslim et al. (2011, 2013).

This work has been published in MNRAS (Martin et al., 2017), co-authored by Nalsim N., who's initial radial velocity measurements sparked the idea for this project and V. Woolf who provided the HDS spectra which allowed for the radial velocity measurements of a further five stars.

## 5.1  Introduction

As the atmospheric abundance patterns of hot subdwarfs are governed by diffusion processes, they cannot be used to establish population membership. However, stars in the Milky Way formed at different epochs belong to different populations, which can be distinguished via kinematic criteria. Kinematical data gives us access to the

motions of the different populations of stars in the Galaxy. Some components of the Milky Way are rapidly rotating with little dispersion in the velocities of the members while others show only little rotation but high dispersions. Orbital eccentricity may also distinguish between younger and older stars as more gravitational interactions lead to larger deviations from originally circular orbits (if that is where the progenitors formed).

Members of the thin disk population are found close to the Galactic plane in low eccentricity orbits. Heliocentric velocities of thin disk stars in the solar neighbourhood are small. Stars of the thick disk population orbit around the Galactic centre on more eccentric orbits and are found at higher distances from the plane. Typically, velocities are larger, relative to the Local Standard of Rest, than for thin disk objects. Stars of the Galactic halo population (also known as population II stars) are often found at large distances from the galactic disc and their orbits are often highly eccentric. Halo stars as a population do not (or not much) participate in the galactic rotation. These stars include those with the highest heliocentric velocities.

Previous studies involving the kinematics of sdBs found that the majority are members of the disk, but that a minority are halo members (Altmann et al., 2004). Randall et al. (2015) have recently shown that the intermediate-helium sdB star LS IV$-14°116$ has halo kinematics. This raises the question of whether the helium-rich hot subdwarfs all belong to this halo minority and the "normal" sdO/Bs are a disk population. In this paper we collate radial velocities and proper motions for a significant sample of helium-deficient, intermediate-helium and extreme-helium subdwarfs, including a number of new measurements. From these we compute space velocities and galactic orbits in order to identify the parent populations. We discuss some of the implications of these results for interpreting the origin of, in particular, the chemically-peculiar intermediate-helium sdBs.

## 5.2   Data

We analysed a sample of 88 hot subdwarfs (sdO/B) including 38 helium deficient, 27 intermediate helium and 23 extreme helium stars. The criterion for inclusion was that

**Table 5.1:** Heliocentric radial velocities for 32 helium-rich hot subdwarfs.

| Star | Instrument | Date | RV ($\mathrm{km\ s^{-1}}$) | $\gamma$ | $\pm$ |
|---|---|---|---|---|---|
| HE 0001–2443 | UVES | 15/10/02 | 4.68 | 3.98 | 0.71 |
| | | 18/06/03 | 3.27 | | |
| HE 0111–1526 | UVES | 18/12/01 | 6.56 | –21.83 | 28.39 |
| | | 29/12/01 | –50.22 | | |
| HE 1135–1134 | UVES | 28/06/01 | 22.22 | 24.67 | 2.45 |
| | | 24/07/01 | 27.11 | | |
| HE 1136–2504 | UVES | 22/04/00 | 68.6 | 59.39 | 9.22 |
| | | 17/05/00 | 50.17 | | |
| HE 1238–1745 | UVES | 23/06/01 | –10.58 | –7.87 | 2.72 |
| | | 23/07/01 | –5.15 | | |
| HE 1256–2738 | UVES | 22/04/00 | 146.26 | 140.46 | 5.8 |
| | | 19/05/00 | 134.66 | | |
| HE 1258+0113 | UVES | 19/05/00 | –62.29 | –42.69 | 19.6 |
| | | 22/05/00 | –23.09 | | |
| HE 1310–2733 | UVES | 22/04/00 | 39.72 | 41.54 | 1.82 |
| | | 24/04/00 | 43.36 | | |
| HE 2218–2026 | UVES | 24/09/02 | –278.91 | –278.86 | 1.45 |
| | | 25/09/02 | –281.81 | | |
| HE 2359–2844 | UVES | 15/09/02 | –93.74 | –90.71 | 3.03 |
| | | 25/09/02 | –87.68 | | |
| UVO 0825 + 15 | HDS | 03/06/15 | 56.4 | | 0.5 |
| J092440.11+305013.16 | HDS | 03/06/15 | 2.7 | | 0.5 |
| J160131.30+044027.00 | HDS | 03/06/15 | –27.4 | | 0.9 |
| J175137.44+371952.37 | HDS | 03/06/15 | –73.6 | | 0.2 |
| J175548.50+501210.77 | HDS | 03/06/15 | –62.7 | | 0.2 |
| PG 2321+214 | HDS | 04/10/98 | –19.7 | | 3 |
| PG 0902+057 | UES | 06/05/95 | –15 | | 5 |
| PG 1615+413 | ISIS | 31/05/96 | –80 | | 5 |
| PG 1600+171 | ISIS | 31/05/96 | –78 | | 5 |
| PG 1658+273 | ISIS | 31/05/96 | –33 | | 5 |
| PG 1715+273 | ISIS | 31/05/96 | 31 | | 5 |
| HS 1844+637 | ISIS | 31/05/96 | 20 | | 10 |
| PG 1554+408 | ISIS | 31/05/96 | 73 | | 8 |
| PG 2258+155 | ISIS | 04/10/98 | 34 | | 5 |
| PG 1127+019 | IDS | 28/04/02 | 19 | | 2 |
| PG 1415+492 | IDS | 29/04/02 | 54 | | 1 |
| PG 2215+151 | ISIS | 31/05/96 | –13 | | 5 |
| HS 1000+471 | ISIS | 31/05/96 | 0 | | 10 |
| BPS CS 22956–0094 | UCLES | 27/08/05 | –4.1 | | 1 |
| BPS CS 29496–0010 | UCLES | 27/08/05 | –39.8 | | 0.1 |
| BPS CS 22940–0009 | UCLES | 26/08/05 | 47.8 | | 0.5 |
| LB 3229 | UCLES | 27/08/05 | 42.7 | | 1.0 |

each star should have measurements of radial velocity, helium abundance and proper motion; these are shown in appendix Tables B.1 – B.3.

## 5.2.1 Radial Velocities

Radial velocities for 63 stars were obtained from the literature, as described in Appendix Tables B.1–B.3. A small number of these have errors in excess of $30\,\mathrm{km\ s^{-1}}$; although large, the data were retained so as not to over-restrict the sample. The errors were propagated through the space motion calculations.

Radial velocities for 32 helium-rich hot subdwarfs were measured by us and are presented here (Table 5.1). Two spectra for 10 of these stars were obtained using the UVES instrument on the ESO VLT, as part of the ESO supernova progenitor survey between 2000 and 2003 (Napiwotzki et al., 2003). Pipeline reduced spectra were recovered from the ESO archive. Velocity shifts were measured by cross-correlation with an appropriately chosen model spectrum. Radial velocities for four stars observed in 2005 with the University College London Echelle Spectrograph (UCLES) on the Anglo-Australian Telescope (AAT), were measured by cross-correlation with theoretical spectra corresponding approximately to the solutions obtained by Naslim et al. (2010). The dates and heliocentric radial velocities measured for each observation are shown in Table 5.1. with a mean uncertainty of $\pm 4.6\,\mathrm{km\ s^{-1}}$. The mean velocity for each star is represented as $\gamma$, and the error represents half the difference between the two measurements. For HE 0111–1526 and HE 1258+0113, these differences are, respectively, more than 8 and 5 times the mean differences of the remainder, suggesting that one or both may be binaries. These stars have not been used in the kinematical analysis as the system velocity is unknown.

Five helium-rich sdO/B stars were observed with the HDS instrument on the *Subaru* telescope, operating in service mode on 2015 June 3. The data were reduced using standard IRAF procedures, the echelle orders were merged and wavelengths corrected for earth motion. Radial velocities of each star were measured by cross-correlation against a standard template. Two templates were used, being theoretical spectra for intermediate helium-rich hot subdwarfs and having effective temperatures of 34 000 and 40 000 K, the first being carbon-rich, the second nitrogen-rich. Two spectral windows

were used with each template, covering a part of both CCDs in the HDS instrument, and hence giving four independent measurements of velocity for each observation. The means and standard deviations are given in Table 1. The radial velocities for the other twelve stars reported in Table 1 were measured from the blue part of the spectrum (4165 – 4570 Å) published by Ahmad and Jeffery (2003), using cross-correlation as for the *Subaru* data. The template was an extremely helium-rich model with effective temperature 40 000 K and surface gravity $\log g = 5.4$.

Since binary companions affect the radial velocity of a star periodically, the system velocities, $\gamma$, were used for confirmed binary systems. We cannot exclude the possibility of unconfirmed binary systems which would affect the calculated Galactic velocities and orbits. Estimates of the binary fraction for EHB stars are between 50 and 60% (Maxted et al. 2001; Copperwheat et al. 2011).

This is a lower bound since the radial velocity variations of very long period systems are difficult to detect. All stars with single epoch radial velocity measurements and confirmed binary systems are flagged in Tables A.9 – A.11. These flagged stars should be considered as candidates for the thin disk, thick disk or halo populations until the radial velocities are confirmed.

### 5.2.2 Abundances

Subdwarf O and B stars can be further classified by their surface helium content. Based on the overall classification for hot subdwarfs developed by Drilling et al. (2013), extreme helium-rich subdwarfs are defined to have $n_{He} > 80\%$ by number, intermediate helium-rich subdwarfs have a helium abundance of $5\% < n_{He} < 80\%$ and helium-deficient subdwarfs have $n_{He} < 5\%$. Helium abundances for the current sample were obtained from Ahmad et al. (2007); Drilling et al. (2013); Edelmann (2003); Geier et al. (2015); Naslim et al. (2010, 2013) and Stroeer et al. (2007), and the sample subdivided according to the above criteria.

Six intermediate-helium sdBs have been found to have unusual and interesting surface chemistries.

Edelmann (2003) found PG 0909+276 and UVO 0512–08 to show surface helium abundances of roughly 20% by number, and extreme (3 – 4 dex) overabundances of
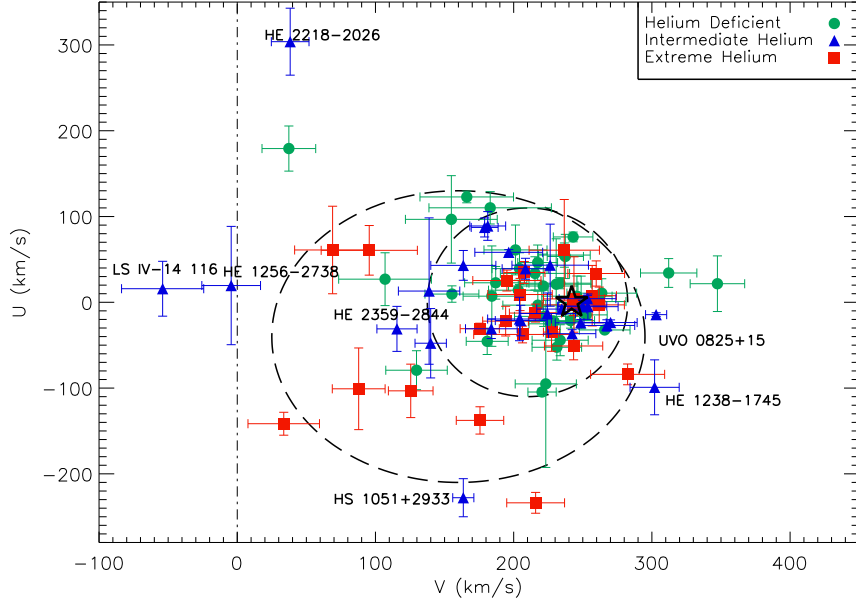
**Figure 5.1:** $U - V$- velocity diagram with 3-$\sigma$ (thin disk) and 3-$\sigma$ (thick disk) contours. Red squares are extremely helium rich subdwarfs, blue triangles are intermediate helium rich subdwarfs and the green data circles are the helium deficient stars. The black star represents the Local Standard of Rest (LSR). The dot-dash line at a Galactic rotational velocity of zero is to highlight stars with retrograde motion.
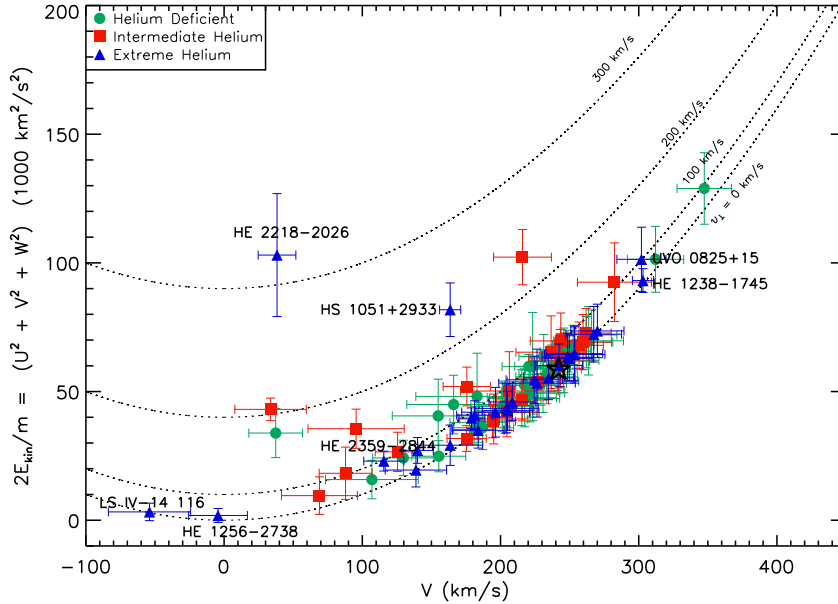


**Figure 5.2:** Galactic rotational velocity against the total kinetic energy. Symbols have the same meaning as above. The parabolic curves denote line of equal velocity $v_\perp = (U^2 + W^2)^{1/2}$.

74

scandium, titanium, vanadium, manganese, and nickel.

LS IV$-14°116$ has a gravity slightly lower than that of normal sdB stars ($\log g = 5.6$), and a surface helium abundance of about 16 per cent by number. It is slightly metal poor ($-0.8$ dex) relative to the Sun. What makes LS IV$-14°116$ distinct from any other hot subdwarf, whether helium rich or not, is the overabundance by 4 orders of magnitude of zirconium, yttrium and strontium and a 3 dex overabundance of germanium in the line-forming region of the photosphere (Naslim et al., 2011).

Two stars, HE 2359–2844 and HE 1256–2738, show optical absorption lines due to triply ionised lead (Pb IV) which have never previously been detected in any star (Naslim et al., 2013). The atmospheric abundance of lead is nearly 10 000 times that measured in the Sun. HE 2359–2844 also shows zirconium and yttrium abundances similar to those in the zirconium star LS IV$-14°116$. UVO 0825+15 has just been discovered to be a variable lead-rich hot subdwarf (Jeffery et al., 2017).

### 5.2.3 Proper Motions

The proper motions used in this work were taken from either the PPMXL or the NOMAD catalogues (Roeser et al., 2010; Zacharias et al., 2004), adopting the value with the smaller error wherever more than one value was available. Proper motions were obtained from *Gaia* DR1 (Arenou et al., 2017; Gaia Collaboration et al., 2016a,b; Lindegren et al., 2016) for JL 87 and SB 705. The mean error of the proper motions is $\pm 3.91$ mas/yr. Large catalogues such as PPMXL and NOMAD inevitably contain errors and extreme values due to outliers. For this reason the proper motions obtained for this paper were compared with the UCAC4 catalogues; all proper motions agree within errors where the catalogues overlap. A study of the problems of outliers is discussed in Ziegerer et al. (2015).

### 5.2.4 Distances and Reddening

Distances were estimated from photometry using the distance modulus

$$\mu = 5 \log_{10} d - 5 + A_{\mathrm{B}}, \tag{5.1}$$

where $\mu = m_{\mathrm{B}}$ - $M_{\mathrm{B}}$ and $A_{\mathrm{B}} = 4.1E_{\mathrm{B-V}}$. $M_{\mathrm{B}}$ is the absolute magnitude and $m_{\mathrm{B}}$ is the apparent magnitude in B. Values for $m_{\mathrm{B}}$ were taken from SIMBAD and those for $M_{\mathrm{B}}$ were taken from the literature (references in Appendix Tables B.1–B.3). Only 45% of stars in this sample had published values for $M_{\mathrm{B}}$, for the remainder estimates were made by assuming the means of these values, which are 4.14 mag for the helium-rich and 3.99 mag for the helium-deficient sdO/Bs. The reddening values ($A_{\mathrm{B}}$) were found using a dust extinction tool, hosted by the NASA/IPAC Infrared Science Archive, which gives the Galactic dust reddening for a line of sight, returning a reddening map that is a reprocessed composite of the COBE/DIRBE and IRAS/ISSA maps (Schlafly and Finkbeiner, 2011). The large reddening corrections to the KPD stars may be overestimated by this method due to their low Galactic latitudes. Hence their distances are likely underestimated.

Distances, from a variety of methods, were found in the literature. These were compared with the calculations performed here (Table 5.2). Out of the twenty distances compared there was a 95% agreement. Distances for JL 87 and SB 705 were taken from the Astraatmadja and Bailer-Jones (2016) catalogue which make use of the *Gaia* DR1 parallaxes.

## 5.3  Kinematics

### 5.3.1  Calculating Galactic Velocities

Using the observed values of right ascension, declination, distance, proper motion and radial velocity, the Galactic velocity components were calculated following the method outlined in Randall et al. (2015). The left-handed system for the velocity components is used here, where $U$ is the Galactic radial velocity, positive toward the Galactic centre, $V$ is the Galactic rotational velocity in the direction of the Galactic rotation and $W$ is the component positive toward the North Galactic Pole. This calculation assumes the distance of the Sun from the Galactic centre to be 8.4 kpc, its motion relative to the Local Standard of Rest (LSR) to have components $(v_x, v_y, v_z) = (11.1, 12.24, 7.25)$ km s$^{-1}$ and the velocity of the LSR to be $V_{LSR} = 242$ km s$^{-1}$ (Irrgang et al., 2013).

**Table 5.2:** Calculated distances in kpc compared with published values.

| Star | Calculated Distance | Published Distance |
|------|---------------------|--------------------|
| HE 0004–2737 | $0.62 \pm 0.09$ | $0.67^1$ |
| HE 0151–3919 | $1.07 \pm 0.27$ | $0.92^1$ |
| HS 0232+3155 | $1.95 \pm 0.27$ | $1.70^1$ |
| HS 0233+3037 | $1.23 \pm 0.17$ | $1.00^1$ |
| HE 0407–1956 | $0.86 \pm 0.12$ | $0.89^1$ |
| HS 0546+8009 | $1.10 \pm 0.15$ | $1.00^1$ |
| HS 0815+4243 | $2.60 \pm 0.35$ | $2.50^1$ |
| PG 1136–003 | $0.87 \pm 0.23$ | $1.3 \pm 0.2^2$ |
| HS 1236+4754 | $1.99 \pm 0.27$ | $2.10^1$ |
| HS 1320+2622 | $3.14 \pm 0.43$ | $3.40^1$ |
| HS 1739+5244 | $1.76 \pm 0.24$ | $1.80^1$ |
| HS 1741+2133 | $1.95 \pm 0.27$ | $1.80^1$ |
| HE 2135–3749 | $0.66 \pm 0.10$ | $0.71^1$ |
| HS 2156+2215 | $3.05 \pm 0.42$ | $2.80^1$ |
| HS 2201+2610 | $0.95 \pm 0.13$ | $0.90^1$ |
| HS 2208+2718 | $1.28 \pm 0.18$ | $1.20^1$ |
| HS 2242+3206 | $1.48 \pm 0.20$ | $1.30^1$ |
| HE 2337–2944 | $0.90 \pm 0.13$ | $0.96^1$ |
| CD–35°15910 | $0.22 \pm 0.06$ | $0.22 \pm 0.08^3$ |
| PG 2352+181 | $0.38 \pm 0.06$ | $0.90 \pm 0.32^4$ |

[1] Edelmann (2003), [2] Geier et al. (2015), [3] van Leeuwen (2007), [4] Colin et al. (1994)

**Table 5.3:** Mean values and standard deviations of the hot subdwarf helium classes. Results from Altmann et al. (2004) and Pauli et al. (2006) are also shown here.

| Subsample | N | $\overline{U}$ | $\sigma_U$ | $\overline{V}$ | $\sigma_V$ | $\overline{W}$ | $\sigma_W$ |
|-----------|---|-----|-----|-----|-----|-----|-----|
| All | 88 | –1.7 | 72.6 | 202.2 | 67.6 | 5.6 | 49.0 |
| Helium-Deficient | 38 | 14.1 | 56.7 | 215.0 | 52.9 | –4.4 | 39.8 |
| Intermediate-Helium | 27 | 3.1 | 83.3 | 190.2 | 84.7 | 13.4 | 35.5 |
| Extreme-Helium | 23 | –30.4 | 72.6 | 193.8 | 65.9 | 13.9 | 69.9 |
| Altmann | 114 | –8 | 74 | 198 | 79 | 12 | 64 |
| Pauli WD thin disk | 361 | ... | 34 | ... | 24 | ... | 18 |
| Pauli WD thick disk | 27 | ... | 79 | ... | 36 | ... | 46 |
| LSR | ... | 0 | ... | 242 | ... | 0 | ... |
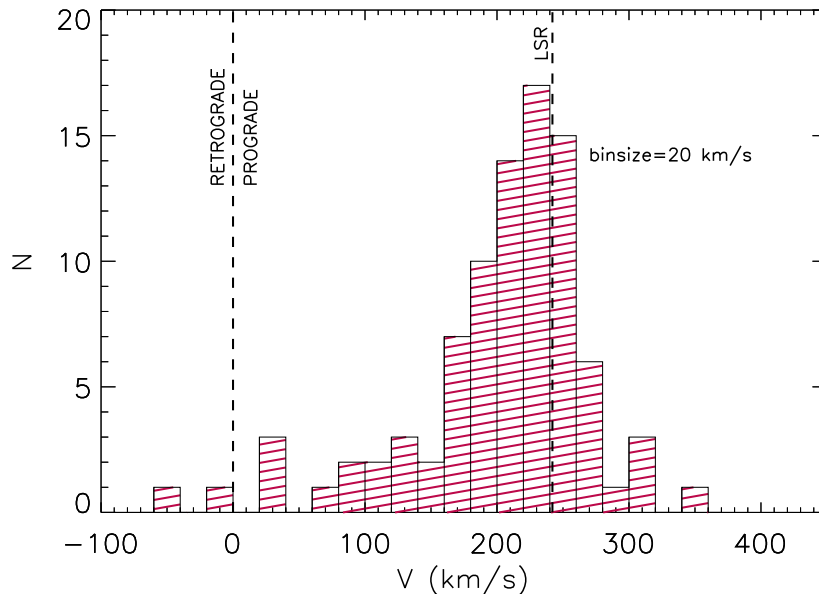
**Figure 5.3:** Histogram of the Galactic rotational velocities of all 88 stars of the sample.

## 5.3.2 Galactic velocities and velocity dispersions

Figure 5.3 shows the distribution of rotational velocity, $V$, for all 88 stars. A peak
can be seen at $220\,\mathrm{km\,s^{-1}}$, near the local standard of rest (LSR) where disk stars are
expected to be. This has also been found in (Pauli et al., 2006) for their white dwarf
sample. This distribution is similar to the sample of 114 sdBs analysed by Altmann
et al. (2004) who also found a similar peak and a tail of the distribution extending into
negative rotational velocities.

The kinematics of this sample were first investigated using a $U-V$ velocity diagram.
In Fig. 5.1, the Galactic radial velocity $U$ is plotted versus the Galactic rotational
velocity $V$. The dotted ellipses correspond to the $3\sigma$-thick and $3\sigma$-thin disk distributions
of white dwarfs as calculated by Pauli et al. (2006), who classified a sample of 398
white dwarfs based on their position in the $U - V$ diagram, the position in the $J_z$
– eccentricity diagram and the stars Galactic orbit combined with age information.
Pauli's classification scheme is based on a calibration using F and G main-sequence
(MS) stars. 137 MS stars were divided into populations with [Fe/H] and [Mg/Fe]
abundances. The halo stars have [Fe/H] < –1.2, the thick disk stars –1.1 ≤ [Fe/H]

$\leq$ –0.3 and [Mg/Fe] $\geq$ 0.3 and the thin disk stars [Fe/H] > –0.3 and [Mg/Fe] $\leq$ 0.2. Any overlap between thin and the thick disk were neglected to gain a clear distinction between the populations.

In the $U - V$ diagram (Fig. 5.1) the helium-deficient stars (green) are mostly clustered around the LSR (black star). The helium-rich stars (intermediate and extreme) are more widely distributed in this plot. Two of these stars have possible retrograde orbits, with their Galactic rotational velocities being negative, they are labelled in Fig. 5.1. HE 2218–2026 lies far outside the disk distributions with a high Galactic radial velocity of almost 300 km s$^{-1}$.

Another method of analysing the kinematics of stars is to look at their total velocity or kinetic energy. In Fig. 5.2 the kinetic energy $2E_{\mathrm{kin}}/m = U^2 + V^2 + W^2$ is plotted against the rotational velocity $V$. Included in this graph are contours showing the velocities perpendicular to Galactic rotation at certain values, where $v_\perp = (U^2 + W^2)^{1/2}$. The higher the value of $2E/m$ the more an object deviates from a circular orbit. For low values of $v_\perp$ the deviation from LSR gives information about the kinetic temperature. The clustering of values around $v_\perp = 0$ means that they are kinematically cool. A few stars are located further away from the $v_\perp = 0$ contour; these are the kinematically hot stars and likely to have a more eccentric orbit. Another reason for a large proportion of stars with low $v_\perp$ could be that they are near their orbital turning point. Table 5.3 shows the mean values and standard deviations of the galactic velocities for the hot subdwarf helium classes as compared with previous studies. The Galactic velocities and corresponding errors for individual stars are shown in appendix Tables B.4 – B.6.

## 5.4 Galactic Orbits

### 5.4.1 Calculating the orbits

In addition to Galactic velocities the orbits were calculated for the stars in this sample. This was achieved using `galpy`, a python package for Galactic-dynamic calculations (Bovy, 2015). The orbits were computed using the potential MWPotential2014, this model is fit to dynamical data of the Milky Way. Although this is not the best possible current model, it was chosen as it gives a realistic model of the Milky Way's gravitational

potential that is simple and easy to use. It consists of a bulge modelled as a power-law density profile that is exponentially cut off with a power-law exponent of –1.8 and a cut-off radius of 1.9 kpc, a Miyamoto-Nagai Potential disk (Miyamoto and Nagai, 1975), and a dark-matter halo described by a Navarro-Frenk-White potential (Navarro et al., 1996). The distance of the Sun from the Galactic centre is set to 8.4 kpc and the velocity of the LSR is $V_{\mathrm{LSR}} = 242\,\mathrm{km\ s^{-1}}$.

Extracted from these orbits, integrated over $\approx 3\mathrm{Gyrs}$, are the quantities apocentre, $R_{\mathrm{a}}$, pericentre, $R_{\mathrm{p}}$, eccentricity, $e$, maximum vertical amplitude, $z_{\mathrm{max}}$, and normalised z-extent, $z_{\mathrm{n}}$. The quantities $R_{\mathrm{a}}$ and $R_{\mathrm{p}}$ are the maximum and minimum distances from the Galactic centre attained during a revolution of $2\pi$ radians, measured on the Galactic plane. From these distances we find the eccentricity which is given by

$$e = \frac{R_{\mathrm{a}} - R_{\mathrm{p}}}{R_{\mathrm{a}} + R_{\mathrm{p}}} \tag{5.2}$$

The normalised z-extent of the orbit, which can be used as a measure for the inclination of an orbit, is given by

$$z_n = \frac{z_{\mathrm{max}}}{R(z_{\mathrm{max}})} \tag{5.3}$$

where $R$ is the galactocentric distance. These quantities are shown in appendix Tables B.4–B.6, along with the star's Galactic velocities. The mean values and standard deviations for the parameters $e$, $z_{\mathrm{n}}$ and $z_{\mathrm{max}}$ are shown in Table 5.4.

Two important orbital parameters are the z-component of the angular momentum $J_z$ and the eccentricity of the orbit. Fig. 5.4 shows a plot of $J_z$ versus eccentricity. This diagram can be used to distinguish different populations. The thin disk stars cluster in an area of low eccentricity and $J_z$ around 1800 kpc km s$^{-1}$. Pauli et al. (2003) call this Region 1. The thick disk stars possess higher eccentricities and lower angular momenta called Region 2. Those stars which lie outside these regions are halo candidate stars.

### 5.4.2   The orbits and orbit parameters

Fig. 5.7 shows histograms of the eccentricity distribution of the three helium classes. The He-deficient and total group of stars has a peak of $e \approx 0.2$, this region is mainly
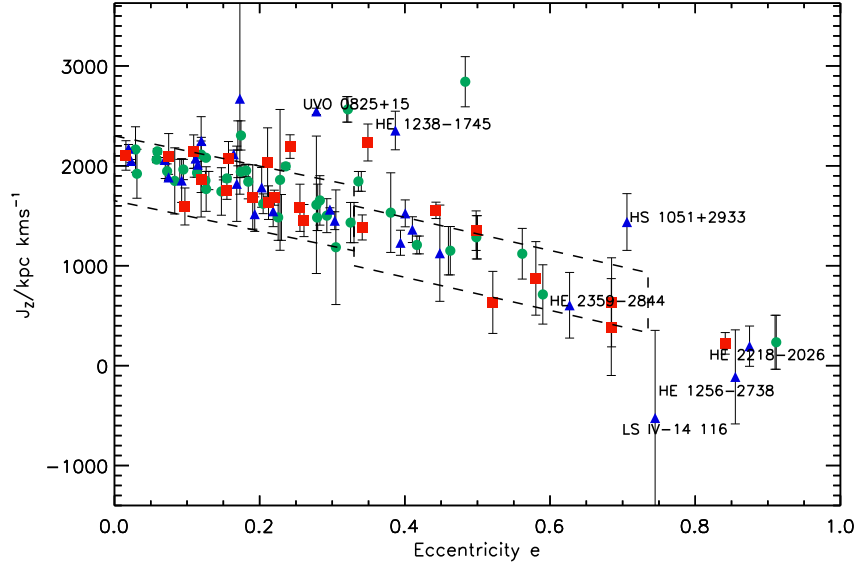
**Figure 5.4:** Z-component of the angular momentum versus eccentricity. Symbols have same meaning as previous plots. Eccentricity errors have been removed for clarity.
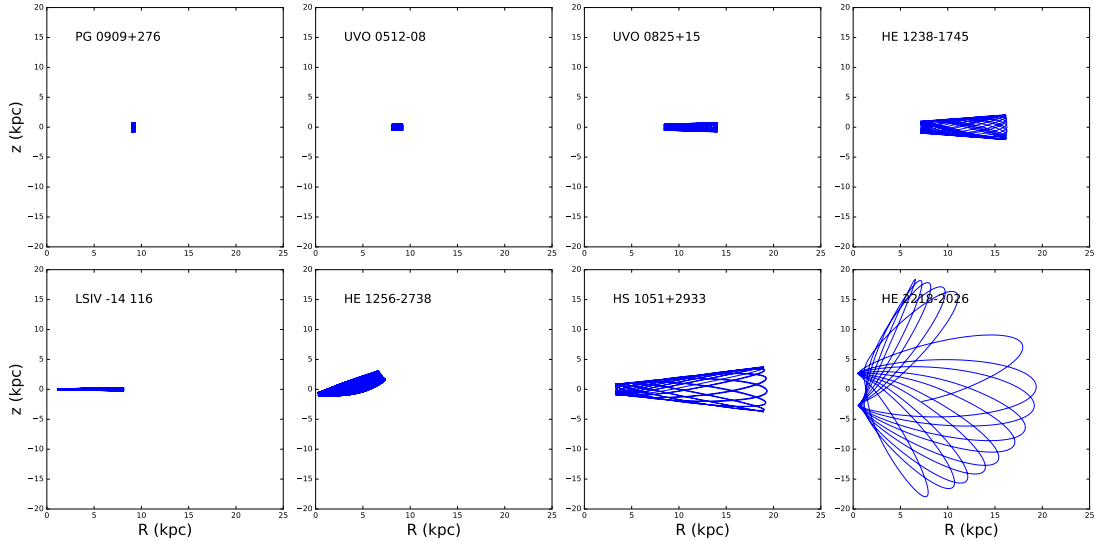


**Figure 5.5:** Meridional sections of the orbits of 8 stars. Columns 1−2 in row 1 are examples of probable thin disk stars and columns 2−4 include probable thick disk orbits. Row 2 contains probable halo orbits.
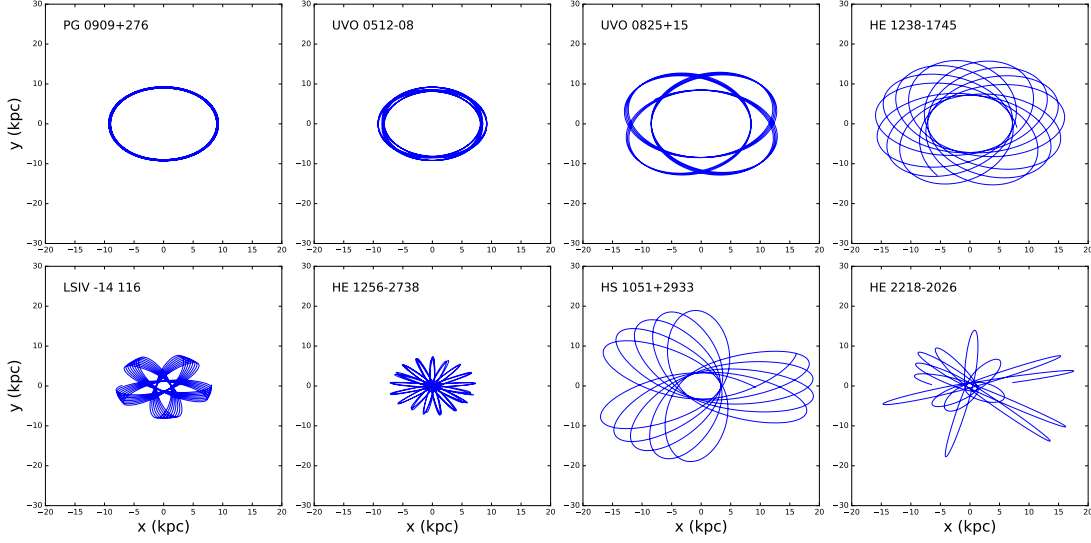
**Figure 5.6:** As Fig. 5.5, but projected on the x-y Galactic plane.

**Table 5.4:** Mean values and standard deviations of the orbital parameters eccentricity, maximum z–extent, maximum vertical amplitude, apocentre and pericentre, respectively.

| Subsample | N | $\overline{e}$ | $\sigma_e$ | $\overline{z_n}$ | $\sigma_{z_n}$ | $\overline{z_{max}}$ | $\sigma_{z_{max}}$ | $\overline{R_a}$ | $\sigma_{R_a}$ | $\overline{R_p}$ | $\sigma_{R_p}$ |
|---|---|---|---|---|---|---|---|---|---|---|---|
| All | 88 | 0.29 | 0.22 | 0.23 | 0.35 | 1.76 | 2.55 | 10.03 | 2.85 | 5.70 | 2.26 |
| Helium-Def | 38 | 0.26 | 0.18 | 0.16 | 0.17 | 1.19 | 1.18 | 9.91 | 2.75 | 5.99 | 1.97 |
| Inter-Helium | 27 | 0.32 | 0.23 | 0.27 | 0.41 | 1.92 | 3.02 | 10.31 | 2.78 | 5.49 | 2.39 |
| Ex-Helium | 23 | 0.32 | 0.23 | 0.31 | 0.34 | 2.53 | 2.78 | 9.91 | 2.57 | 5.44 | 2.44 |
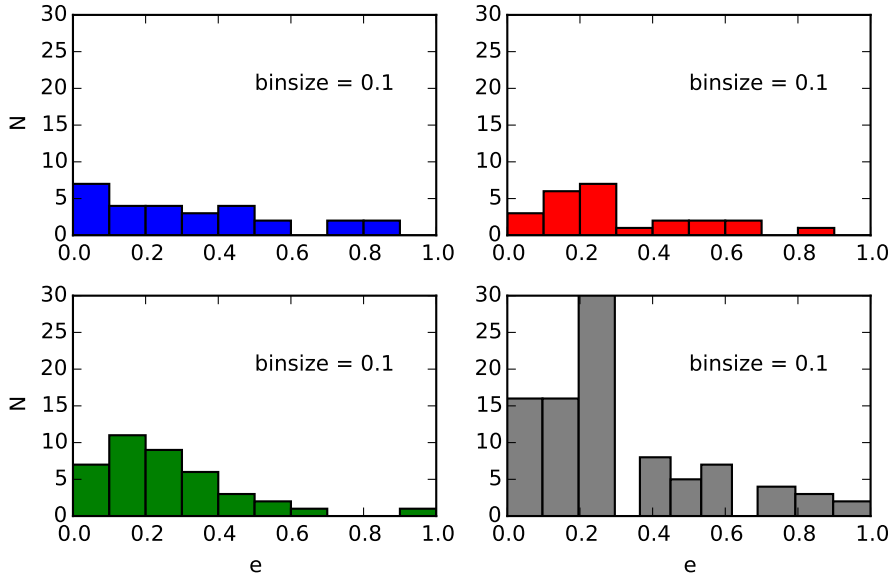


**Figure 5.7:** Histograms of the eccentricity distribution. Top left: intermediate-helium, top right: extreme-helium, bottom left: helium-deficient, bottom right: all.

populated by disk stars. The He-enriched stars, on the other hand, have a distribution widely spread over the whole range.

Our classification scheme has been adopted from Pauli et al. (2003, 2006). Ma et al. (2016) found a vertical scale height for the thick disk between 1 and 1.5 kpc, so here we have set 1.5 kpc as the cut-off height for the thin disk.

1. Stars whose orbits have low eccentricity and low inclination on the Galactic plane are referred to as the thin disk component. These stars must lie within region 1 in the $J_z - e$ diagram and within the $3\sigma$-thin disk contour and have $z_{\max} < 1.5$ kpc

2. Stars which lie in Region 2 and the $3\sigma$-thick disk contour have been classified as belonging to the thick disk.

3. Stars which have been classified as halo lie outside Regions 1, 2 and lie outside both $3\sigma$ contours and have a $z_{\max} > 1.5$ kpc.

   All orbits have also been visually inspected as part of the classification.

Table 5.5 shows the number of stars classified as halo, thin or thick disk stars. The thin and thick disk kinematically overlap one another in a way which makes it difficult to find selection criteria capable of distinguishing them from one another. It has been suggested by Bovy (2011) that there is actually no thin/thick disk dichotomy and that the transition between thin and thick disk is rather a continuum of disks.

There is a large variety of orbit morphologies in this sample. Fig. 5.5 shows the meridional sections of the orbits of 18 stars. Row 1 contains intermediate helium stars, row 2 contains extreme helium sdO/Bs and row 3 shows the orbits of the helium-deficient sdO/Bs. Columns 1–3 are examples of disk stars and columns 4–6 show halo orbits. The same layout applies to Fig. 6.9 which shows the orbits projected onto the $x - y$ Galactic plane.

## 5.5 Discussion

In general, hot subdwarfs show a much larger distribution in velocity than white dwarfs. Figure 5.1 shows that the helium-deficient subdwarfs are more clustered around the

## 5. KINEMATICS OF SUBLUMINOUS O AND B STARS BY SURFACE HELIUM ABUNDANCE

**Table 5.5:** Population classification

| Subsample | N | Thin Disk | Thick Disk | Halo |
|---|---|---|---|---|
| All | 88 | 45 | 36 | 7 |
| Helium-Deficient | 38 | 25 | 12 | 1* |
| Intermediate-Helium | 27 | 13 | 10 | 4 |
| Extreme-Helium | 23 | 7 | 14 | 2 |

The halo classification for the helium-deficient HS 2208+2718 should be considered provisional, as there is a non-zero probability that it is a radial velocity variable.

LSR which suggests that they are likely disk stars with some having possible thin disk kinematics. Two of the chemically–peculiar sdBs have a very low or even retrograde rotational velocity indicating that they have halo kinematics. The kinetic energy diagram (Fig. 5.2) shows a significant portion of the sample have kinematics that are solar-like suggesting membership of the thin disk. The mean values and standard deviations of the galactic velocities of the entire sample of sdO/Bs agree amiably with Altmann's study of 114 sdBs. Examining the helium-deficient velocity distribution alone (Table 5.3), it may be seen that the classical sdB stars fit closer to Pauli's white-dwarf thick-disk sample than to Altmann's sample. The helium-rich groups have much higher standard deviations (Table 5.3), suggesting that there is more of a halo contribution to these subgroups. Kawka et al. (2015) calculated the Galactic velocity components of all known hot subdwarf binary systems. They found that the population kinematics imply an old age and include a few likely halo population members and that the hot subdwarf binary population has a velocity dispersion between the thin and thick disk dispersions for white dwarfs.

Special attention has been paid to intermediate-helium stars with peculiar surface chemistries (Figs. 5.5 and 6.9).

**LS IV−14°116** (Zr, Y, Sr, Ge) initially appears to have a disk orbit due to its maximum vertical amplitude ($z_{\mathrm{max}} = 0.26$kpc), very low inclination and the shape of its meridional orbit (Fig. 5.5). But due to its high eccentricity ($e$=0.74) and retrograde velocity ($V = -54\,\mathrm{km\,s^{-1}}$) it clearly has a halo orbit; cf. Randall et al. (2015).

**HE 1256−2738** (Pb) immediately presented as a halo orbit. It has a very low galactic rotational velocity and a very high eccentricity of 0.86. It also has a very close approach to the galactic centre with a pericentre value of 0.59 kpc, which could account for its

deviation from a circular orbit.

**HE 2218–2026**, an intermediate-helium hot subdwarf, stands out as having a halo orbit with a large radial, low rotational velocity and a chaotic orbit (Fig. 5.5) which closely approaches the galactic centre. All of its orbital parameters are characteristic of the halo. At 18 kpc, it has the highest $z_{max}$ of any of the stars in this sample. The Galactic rest-frame velocity of 321 km s$^{-1}$ is not high enough to be classified as a hyper-velocity star, *i.e.* as having rest-frame velocity greater than that of the local Galactic escape velocity ($\approx 500$ km s$^{-1}$), cf. the review by Brown (2015).

UVO 0825–08 (Ca, Ge, Y, Pb), HE 1238–1745 and HS 1051+2933 are all marginally outside the thick disk $3\sigma$ contour and have $z_{max} = 0.86$, 2.08 and 3.76 kpc respectively. HS 1051+2933 is clearly a halo star, the other two are marginally halo/thick disk stars. We have been conservative in assigning stars to the lower energy population.

**PG 0909+276 and UVO 0512–08** (Sc, Ti, V, Mn, Ni), although chemically interesting intermediate-helium subdwarfs, appear to show typical thin disk orbits.

These results are helpful for interpreting the evolutionary origin of all types of hot subdwarfs. For the helium-deficient or "normal" sdB stars, an origin in a close binary system is considered likely for the majority; indeed, 15/38 of the sample are confirmed binaries. Whether these systems originate in one or more common-envelope ejection episodes, or in a stable Roche-lobe overflow episode, the age and mass of the progenitor are closely linked by the progenitor main-sequence lifetime. Models imply binary sdB progenitors may have masses in the range $0.8 < M_{MS}/M_{\odot} < 5$ or more (Han et al., 2002), implying possible ages anywhere between 0.2 and 10 Gyr, and hence an origin in either disk or halo. Significantly, the fractions for both classes of helium-rich subdwarfs are much lower, only one intermediate-helium subdwarf, CD–20°1123, is a confirmed close binary (Naslim et al., 2012).

For extreme-helium subdwarfs, Zhang and Jeffery (2012) argue for an origin in a merging double-helium white dwarf binary. Such systems require a significant delay between formation of the double white dwarf and the subsequent merger because, for these stars, orbital decay by gravitational radiation has a timescale $\geq 1$ Gyr. Binary star population synthesis studies show that double helium-white dwarf progenitor systems

# 5. KINEMATICS OF SUBLUMINOUS O AND B STARS BY SURFACE HELIUM ABUNDANCE

must have formed at least $2\,\mathrm{Gyr}$ ago, with 95% formed more than $4\,\mathrm{Gyr}$ ago (Yu and Jeffery, 2011; Zhang et al., 2014). One would therefore expect kinematics representative of an older population, as suggested by Table 5.5.

The intermediate-helium subdwarfs present more of a challenge. Naslim et al. (2011, 2013) have argued that the extreme surface abundances seen in $\mathrm{LS\,IV}-14°116$ and the lead stars $\mathrm{HE\,2359}$–2844 and $\mathrm{HE\,1256}$–2738 are proto-subdwarfs, evolving *onto* the extended horizontal branch. Their atmospheres should consequently represent a snapshot of an evolving surface chemistry in which radiative levitation and gravitational settling continually resort the surface layers as the star evolves and helium sinks out of the photosphere. For this to be true, the intermediate-helium subdwarfs should share the kinematical properties of the helium-deficient subdwarfs. If the fraction of halo stars in each subsample (Table 5.5) is representative of age, then the intermediate-helium subdwarfs (4 halo / 27 stars) would appear to be older than both the helium-deficient (1/38) and the extreme-helium subdwarfs (2/23). However, the statistics are at best small. Radial velocities have not been obtained in a uniform manner so that a high fraction of extreme-helium subdwarfs have only single epoch data, whilst the other groups are represented by multi-epoch data. Similarly, the sample space volumes are slightly different, with mean distances for the three groups being $\langle d \rangle = 1.13 \pm 0.89\,\mathrm{kpc}$ (intermediate), $\langle d \rangle = 1.39 \pm 0.90\,\mathrm{kpc}$ (extreme), and $\langle d \rangle = 1.07 \pm 0.79\,\mathrm{kpc}$ (helium-deficient). This could account for the slightly lower energy classification of the helium-deficient group with respect to the helium-rich groups. Moreover, our sample of helium-deficient subdwarfs omits a more distant sample of halo sdBs. Tillich et al. (2011) identified two distinct kinematic groups: normal halo subdwarfs with low Galactic rotation and extreme halo subdwarfs on highly-eccentric retrograde orbits. The presence of two distinct groups indicates different origins. The normal halo sdBs might have been ejected into the halo via the slingshot mechanism. The extreme halo stars might originate in the outskirts of the Galactic disc and not in the central bulge. It is therefore not unreasonable to suspect that the intermediate-helium subdwarfs equally show such a diverse range of kinematical properties.

However, it is puzzling that the two intermediate-helium subdwarfs with the most extreme chemistries are in halo orbits. An intriguing alternative is that these stars rep-

resent the ejecta from Type Ia supernovae, as suggested for the hyper-velocity compact helium star US 708 (Geier et al., 2013; Justham et al., 2009). A hot subdwarf having a massive white dwarf companion in a short-period orbit, such as CD$-30°11223$, will, towards the end of core helium burning, expand and transfer mass to its companion, potentially stripping the hydrogen layers from the subdwarf and leading to a thermonuclear explosion in the white dwarf. The explosion will have the consequences of i) contaminating the helium-rich subdwarf remnant with heavy-metal ejecta from the supernova, and ii) unbinding it with a velocity close to the orbital velocity at the time of explosion $\approx 300 - 500\,\mathrm{km\ s^{-1}}$ (Liu et al., 2013). The result is a chemically-peculiar helium-rich subdwarf in a halo-like orbit. Whether bound or unbound will depend on the subdwarf velocity vector relative to the Galactic potential at the time of explosion.

## 5.6   Summary

The space motions and Galactic orbits of 88 hot subdwarfs were computed from published proper motions, radial velocities and inferred distances. The orbital parameters were used to classify sample members as having disk or halo orbits. This study confirms that sdO/B stars are members of all Galactic populations. The sample was divided into helium-deficient (or *normal*), intermediate-helium and extreme-helium subdwarfs based on their surface helium abundances, in order to establish whether the different groups could be distinguished kinematically. Of the samples studied, helium-deficient sdO/Bs show the lowest standard deviations in all orbital parameters discussed here and are likely to be primarily disk stars. However at least one and possibly two populations of halo sdB stars are also known to exist (Tillich et al., 2011). Both samples of He-rich subdwarfs appear to have similar kinematics, primarily comprising disk stars with a small fraction of halo objects.

# Kinematics of Hydrogen Deficient post-AGB stars with *Gaia* DR2

<div style="text-align: right">6</div>

*Gaia* DR2 has provided us with a five-parameter astrometric solution for over 1.3 billion stars in our Galaxy. It equips us with more precise space motions and distances to stars to allow for the computation of Galactic velocities, positions and orbits of almost any type of star. We have studied the kinematics of a sample of ∼210 post-AGB stars with a variety of surface properties, with luminosities thought to lie roughly between 3 000 and 30 000 $L_\odot$, and effective temperatures between 4 000 and 200 000 K. The unifying feature is a severe absence of hydrogen, and usually some enrichment in carbon. Our main goal was to asses if these stars are linked kinematically, and not just by their unusual surface composition. I present a kinematical analysis of hydrogen-deficient supergiants (EHe, R CrB, HdC), hot-subdwarfs (sdO/B) and central stars of planetary nebulae (CSPNe).

A sample of work completed in this chapter and Chapter 7 is currently in prep. and will be submitted to MNRAS.

## 6.1   Introduction

In this chapter we utilise the methods outlined in Chapter 5 to analyse the kinematics of a sample of 209 post-AGB stars. These evolved low mass stars are all linked by their unusual surface composition and are thought to be connected by similar evolution channels, therefore we should see some similarities in their kinematic populations.

These stars have already been introduced in Chapter 1, but here I will briefly summarise their properties.

**Helium Hot Subdwarfs**   are extreme horizontal branch stars of spectra type O and B. Here we only examine the helium-rich subdwarfs as we are looking for links to other

classes of hydrogen deficient stars. As shown in the previous chapter, these stars are kinematically diverse, they are seen in the disk and the halo.

**Extreme helium (EHe) stars**   are low-mass supergiants of spectral types Ap and Bp, with Balmer lines being either exceptionally weak or totally absent and effectively replaced by neutral helium. The absence of hydrogen means that the metallic-line spectrum is much stronger than in a normal star. Nevertheless, carbon, nitrogen and, in some stars, oxygen are abnormally strong. Distribution on the sky and a large velocity dispersion indicates an old population strongly concentrated towards the Galactic Centre (Jeffery et al., 1986).

**R Coronae Borealis (R CrB) variables**   are a small group of carbon-rich supergiants which show irregular drops in brightness by up to 8 magnitudes that last from weeks to months (Clayton, 1996). Previous to this year, approximately 65 R CrB stars were known in the Galaxy and 25 in the Magellanic Clouds (Clayton, 2012). Thanks to a dedicated spectroscopic survey targeting R CrBs, 45 new stars have been reported (Tisserand et al., 2018).

**Hydrogen-deficient carbon (HdC) stars**   are carbon-rich red supergiants spectroscopically similar to RCB stars, but lacking large-amplitude light variations (Goswami et al., 2010; Tisserand, 2012; Warner, 1967).

**O(He) stars**   have higher effective temperatures and surface gravities than the EHe stars and are classified spectroscopically by an almost pure HeII optical absorption spectrum. There are 9 such objects known to date, they are found with and without nebulae.

**[WC]**   are the central stars of planetary nebulae (CSPNe) which share a spectroscopic appearance with the massive carbon-rich Wolf-Rayet stars. The only defining characteristic amongst these stars in the Milky Way is the presence of a bright nebula. They are seen in the disk, Magellanic clouds and in the bulge.

**PG1159** stars are dominated by absorption lines of highly ionised He, C and O (Wesemael et al., 1985). It is believed that the PG1159 stars are descendants of the Wolf-Rayet CSPNe and often co-exist in the same region of the HR diagram before travelling down the white dwarf cooling track. They are found with and without planetary nebulae.

Sect. 6.3.1 deals with the updated results from the previous chapter given the new astrometric data from Gaia Data Release 2. Following this, we add to this sample of helium-rich hot subdwarfs in 6.3.2. Section 6.4 deals with the helium-rich giants (EHe, R CrB, HdC) and in 6.5 we examine the central stars of planetary nebulae (O(He), [WC], PG1159).

## 6.2 Data Sources

### 6.2.1 *Gaia*

Gaia Data Release 2 was released on 25 April 2018, consisting of astrometry, photometry, radial velocities, and information on astrophysical parameters and variability, for sources brighter than magnitude 21. It is a major advance following the first data release, providing a high-precision parallax and proper motion catalogue for over 1 billion sources. Coordinates $(\alpha, \delta)$, proper motions $(\mu_\alpha, \mu_\delta)$ and parallaxes $(\pi)$ were obtained, for all stars presented here, from Gaia DR2 (Gaia Collaboration et al., 2016a,b). The parameters published by *Gaia* have not been derived independently from each other but as a result of a 5–parameter fit to a model, hence some correlation between the values is to be expected. These have not been used in the error propagation, hence errors on the subsequent calculations should be considered as lower limits.

Inverting a parallax to give a distance is only appropriate when we have no measurement errors. As we always have measurement errors, determining the distance given a parallax becomes an inference problem (Bailer-Jones, 2015; Luri et al., 2018). Once the fractional parallax error becomes larger than about 0.2 a simple inversion becomes noisy and gives an incorrect error estimate. We can improve on this by the use of a properly normalised prior. Here we adopt an Exponentially Decreasing Space Density Prior with only one free parameter, the length scale, which we set at a constant L =

1.35kpc (Luri et al., 2018). Even though a Bayesian approach can give distances esti-mates from even a negative parallax measurement the prior will always dominate when the fractional error in parallax ($f = \sigma/\pi$) is high. Due to this we limit our sample to stars which have parallax measurements with f $\leq$ 0.5. Our distance estimates, along with the astrometric data, are reported in the appendix tables C.2 – C.4, here we report are the 68.27% confidence intervals on the distance.

Radial velocities (RVs) published in DR2 are only measured for stars with effective temperatures in the region of 3550 to 6900 K. Only RCrB stars fall in this temperature range. The hot subdwarfs, Ehes and CSPNe certainly do not, so we must look elsewhere. In this situation we rely on spectroscopic surveys such as the Sloan Digital Sky Surveys (SDSS).

## 6.2.2   SDSS

Recently Geier et al. (2017) released a catalog of the known hot subdwarf stars, provid-ing spectroscopic classifications for 5055 hot subdwarfs, 540 of which are helium-rich. Radial velocities are provided for the 2122 stars with spectra in the SDSS archive. Those RVs have been measured automatically by cross-correlation with template spec-tra during the course of SDSS. This template library does not include very helium-rich stars such as He-sdOs, RVs of such stars can be incorrect by up to $100\,\mathrm{km\,s^{-1}}$ due to the confusion of the Pickering series of singly ionized helium and the hydrogen Balmer series. In order to gather accurate radial velocities we have obtained individual spectra for the 221 stars classified as helium-rich and contained in the SDSS archive (Gaensicke priv. comm). The signal-to-noise ratio (SNR) of the individual spectra ranges from about 10 to 75. Due to the large variation in SNR and the undetermined spectral pa-rameters of these stars we aim to measure the best radial velocities we can, en masse, without prior knowledge of the temperature or gravity. We choose a variety of SPECTRUM models of constant log$g$ = 4.5, varying $T_{\mathrm{eff}}$ and helium abundance, summarised in Ta-ble 6.1. Figure 6.1 shows the spectra of the He-sdO SDSSJ220429.51+211610.6 with a SPECTRUM model of $T_{\mathrm{eff}}$ = 50kK and a helium abundance of 95%. Each spectrum is first normalised to unity by a polynomial fit to the smoothed spectrum. Models were degraded to the resolution of the SDSS spectra then cross correlated in the wavelength

Table 6.1: Spectroscopic parameters for the models used in cross correlation.

| He | 99% | 95% | 90% | 70% |
|---|---|---|---|---|
| $T_{eff}$ | 25 | 26 | 26 | 26 |
| (kK) | 30 | 36 | 36 | 36 |
| | 40 | 50 | 45 | 45 |
| | 50 | | | |

region 3800Å − 7000Å. The mean radial velocity measurements and standard deviations are shown in Figure 6.2 against the velocities reported in Geier et al. (2017). Here we see a systematic offset of $+72\,\mathrm{km}\ \mathrm{s}^{-1}$ with only a few outliers. This justifies the need to remeasure all radial velocity measurement of the helium-rich hot subdwarfs. In table C.1 we report our mean radial velocity measurements and standard deviations.
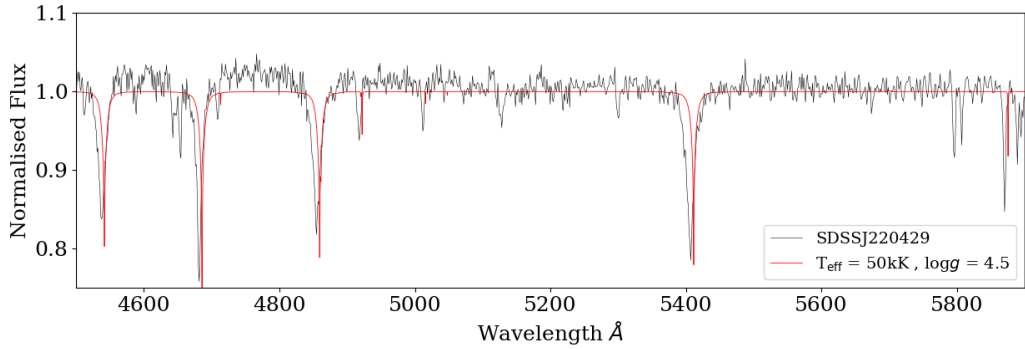


Figure 6.1: SDSS spectrum normalised (black) with model used for cross correlation (nHe = 95%) (red).

## 6.3 Helium–rich Hot subdwarfs

### 6.3.1 Updated results from Chapter 5

The work presented in this section is the recalculation of the Galactic velocities and orbital parameters of the helium-rich stars presented in chapter 5, with the astrometric solution provided by Gaia DR2. The results of this re-analysis are displayed and discussed in the following section. As described in Sect. 6.2.1 we have derived distances to all stars reported in this chapter. As we have also estimated the distances to the hot subdwarfs from photometry (Sect. 5.2.4) we compare these measurements
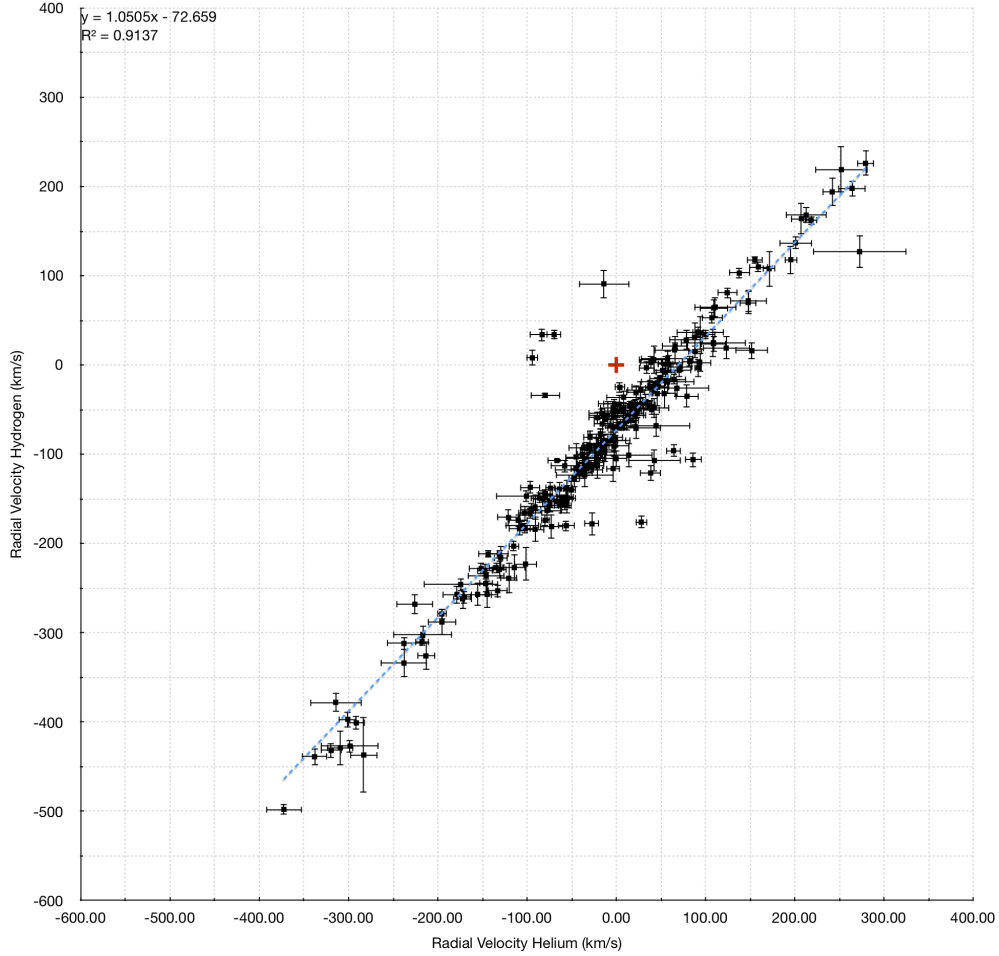
**Figure 6.2:** Comparison of radial velocity shifts measured with a hydrogen-rich template (Geier et al., 2017) and helium templates (this work), zero point is shown with a red cross.

in Fig. 6.3. Roughly half of the stars have distances which agree in both methods; we can also see that at distances greater than $\sim$ 2kpc the error bars become rather large. The photometric distances include an estimation of the interstellar reddening at the stars Galactic coordinates (as opposed to calculation from the stars spectrum). If this reddening has been overestimated (e.g if stars lie at low Galactic latitudes) this could account for the large amount of stars with have much larger astrometric distances.

When comparing the Galactic velocities and orbital parameters that we have re-calculated from chapter 5, we see clearly the added precision provided by *Gaia*, the errors are reduced by an average of 60%. Most notably the eccentricity errors have been reduced by 80% (Table C.5).
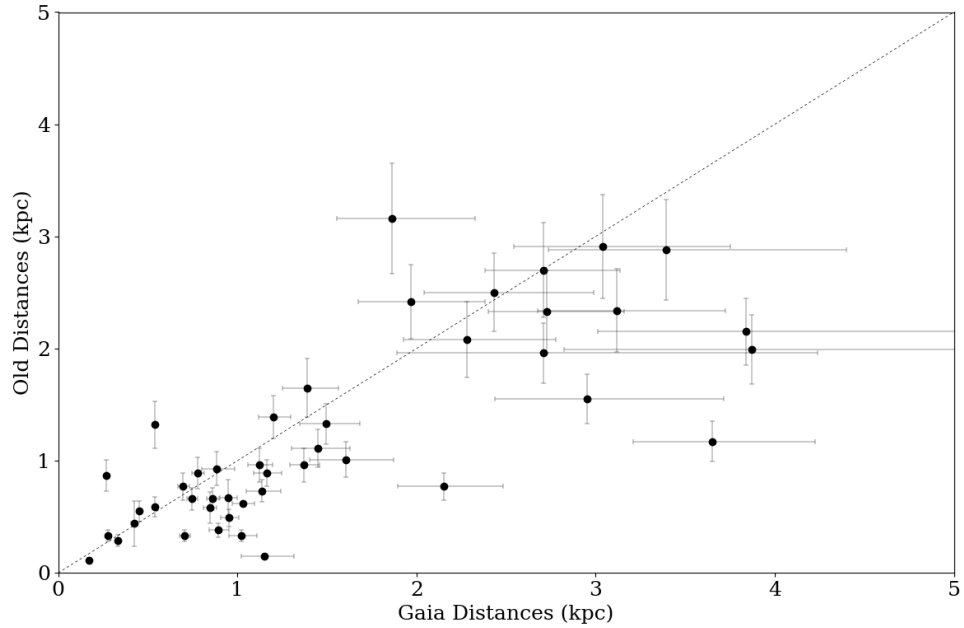
**Figure 6.3:** Comparison of distances estimated in Ch.5 and those estimated from the *Gaia* DR2 parallaxes.

### 6.3.2 Addition of new He-rich Hot subdwarfs

From 6.2.2 we can expand our sample of He-rich hot subdwarfs. Of the 221 stars for which we have measured radial velocities, only 76 are present in Gaia DR2 and have a fractional parallax error of less than 0.5. Even so, our total sample of helium-rich subdwarfs increases to 121 stars. We divide these stars based upon the helium classifications from Geier et al. (2017) and keep the labels of intermediate-helium and extreme-helium from the previous chapter. The reason for this is that we do not have sufficient information on the abundances of the new subdwarfs to assign them into the Inter-He or Ex-He groups. A label of He-sdB indicates HeI is present and possibly some hydrogen; He-sdOBs have He I and HeII with a possibility of hydrogen. Stars with the classification He-sdO have HeII and possibly He I and H.

### 6.3.3 Galactic and Orbital parameters

The Galactic velocities and orbital parameters were calculated as in Chapter 5, the results are tabulated in Table C.5. All of the Helium sdO/B classes show the same

trend in Galactic rotational velocity (Fig. 6.4*). They have a peak near the Local Standard of Rest (LSR) velocity ($242\,\mathrm{km\,s^{-1}}$) and a tail towards low velocities. The U–V velocity diagram shows that we are finding more of the halo subdwarfs, which is to be expected as we expand our sample to greater distances. One interesting trend that can be seen is that most of the stars which lie outside the thin and thick disk ellipses are found at negative Galactic radial (U) velocities. This could be a selection effect imposed on this sample due to the fact that we are only adding stars from SDSS which observes with an optical telescope based in the Northern Hemisphere.
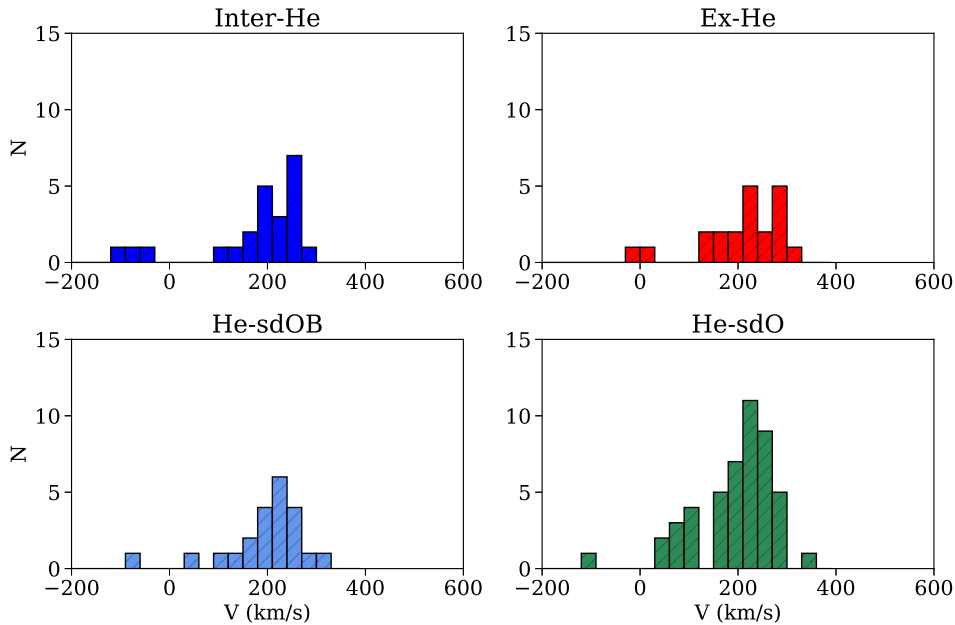


**Figure 6.4:** Galactic rotational velocity for all He-sdO/Bs.

One star stands out in the kinetic energy diagram (Fig. 6.6), PG1608+374, with a tangential velocity ($v_{\perp}$) of greater than $400\,\mathrm{km\,s^{-1}}$. The rest of the stars have a much lower kinetic energy and many of them cluster around the LSR, marked with a star.

Looking at the z-component of angular momentum versus eccentricity, Figure 6.7, we see the majority of stars clustered in and around regions 1 and 2 and a group of stars with high eccentricities and/or negative momentum. This tells us that these sdO and B stars are mainly part of the disk but also that there is a significant halo population. The eccentricity distribution (Fig. 6.8) shows us that all the sub-groups have stars in

*The He-sdB group only has 4 members so is not shown here.
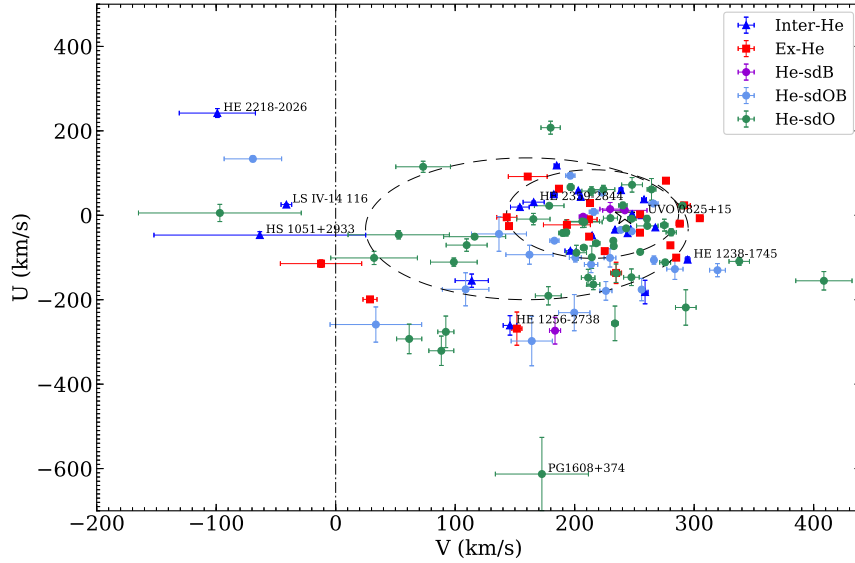
**Figure 6.5:** U – V- velocity diagram with $3\sigma$ (thick disk) and $3\sigma$ (thin disk) contours. The black star represents the local standard of rest (LSR). The dot–dashed line at a Galactic rotational velocity of zero is to highlight stars with retrograde motion.
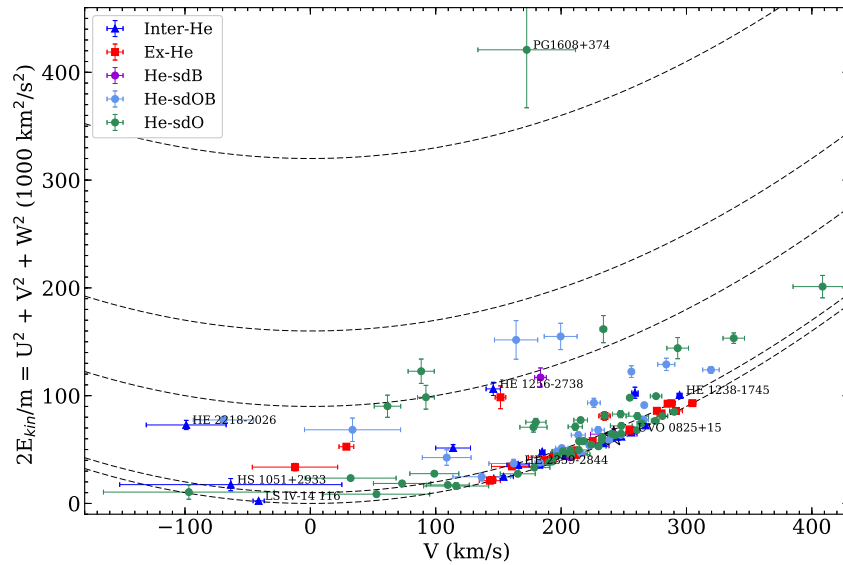


**Figure 6.6:** Galactic rotational velocity against the total kinetic energy. The parabolic curves denote line of equal velocity ($v_\perp = (U^2 + W^2)^{1/2}$) at 0, 100, 200 & 300 km s$^{-1}$ respectively.
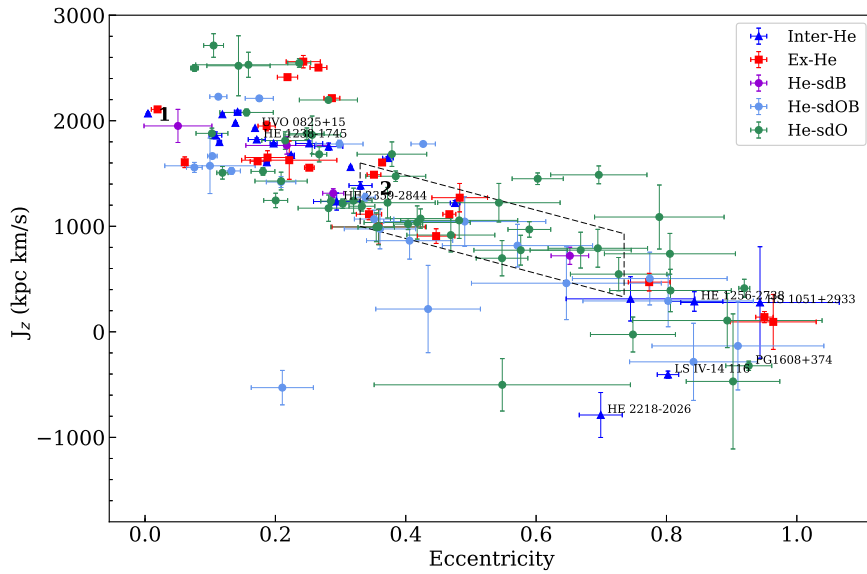
**Figure 6.7:** Z-component of angular momentum versus eccentricity. Regions 1 and 2 denote the thin and thick disk respectively.

the disk and halo but we are sampling a higher proportion of eccentric orbits with stars from the SDSS categories.
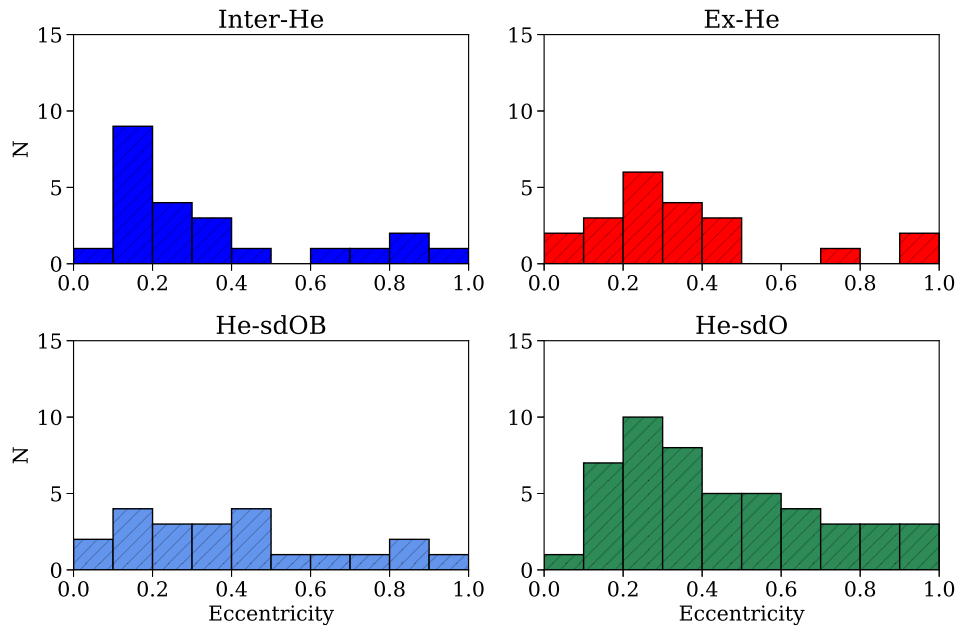


**Figure 6.8:** Histograms of the eccentricity distribution.

**Table 6.2:** Population classification.

| Subsample | N | Thin Disk | Thick Disk | Halo |
|-----------|-----|-----------|------------|------|
| He–sdB    | 4   | 1         | 2          | 1    |
| He–sdOB   | 23  | 2         | 15         | 6    |
| He–sdO    | 49  | 3         | 35         | 11   |
| Inter–He  | 23  | 14        | 4          | 5    |
| Ex–He     | 22  | 4         | 15         | 3    |
| All       | 121 | 24        | 71         | 26   |

### 6.3.4 Population Classification

Stars have been classified based on the scheme outlined in Sect.5.4.2 and the results are summarised in Table 6.2, with the individual classifications in the last column of Table C.5. We see that most of the stars in this sample are part of the thick disk with 20% in the thin disk and 22% in the halo. We increased our sample by 160% and our halo hot subdwarf population increased from 12% to $\sim 22\%$ We are currently limited by the parallax precision of *Gaia* DR2, we still have 136 hot subdwarfs which have radial velocities and proper motions but no reliable distance measurement.

### 6.3.5 Selection Effects

As mentioned earlier we do see the presence of a selection bias. Figures 6.9 and 6.10 show the positions of the stars in the Galactic $X - Y$ and $X - Z$ plane, respectively, where $X$ and $Y$ are distances from the Galactic Centre (GC) and $Z$ is the distance from the Galactic plane. We define the inner disk $R < 7$kpc, the Solar ring $7 < R < 11$kpc and the outer disk $R > 11$kpc from the GC.

Our sample does not extend to the southern hemisphere or in the direction of the Galactic centre. We did not expect a complete and unbiased sample as we rely on independent photometric and spectroscopic surveys to overlap in order to perform our Galactic dynamic calculations. However, we have expanded the sample to greater distances and into the halo.
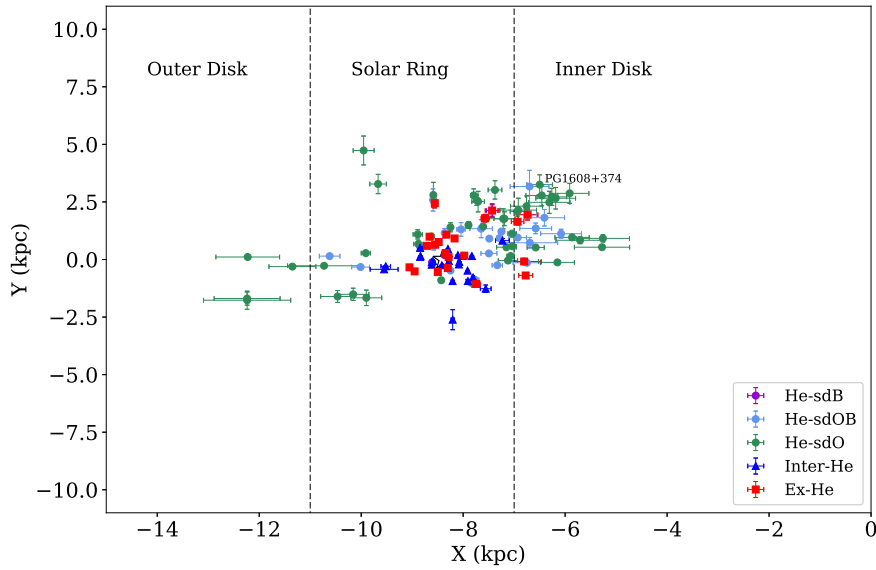
**Figure 6.9:** Distribution of sample in the Galactic $X - Y$ plane.
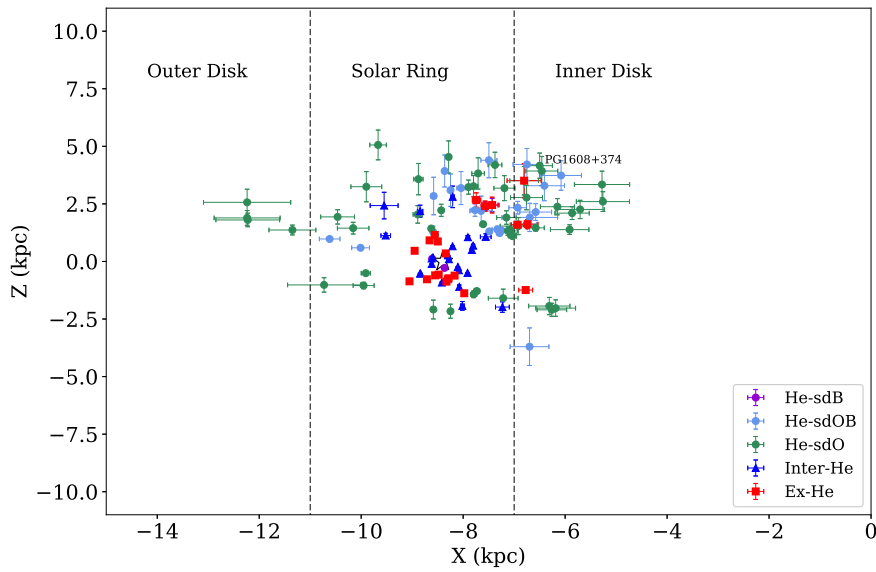


**Figure 6.10:** Distribution of sample in the Galactic $X - Z$ plane.

### 6.3.6   Discussion

**PG1608+374**: was originally classified as an sdO(C) star by Kilkenny et al. (1988a) who found a spectrum dominated by HeII absorption. This star stands out in Figures
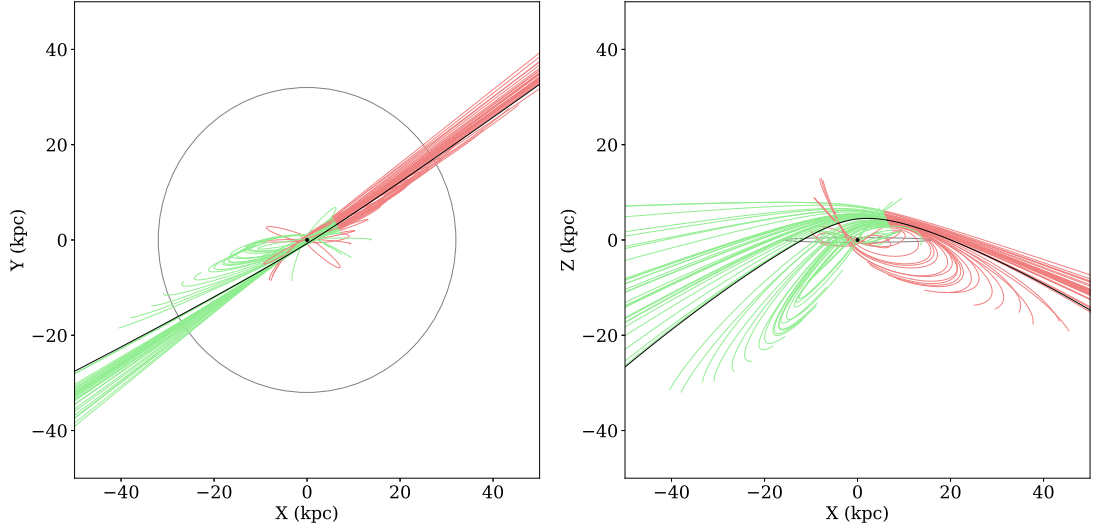
**Figure 6.11:** The orbit of PG1608+374. Left: x-y plane, grey is an estimate of the thin disk size. Right: x-z plane. The black line is the orbit of the star integrated $\sim 250$Myrs forward and backwards. The green lines are 50 randomly generated orbits integrated forward $\pm 1\sigma$ from the input parameters. The red lines represent the same orbits integrated backwards in time.

6.5 and 6.6 for its high velocity orbital parameters. Figure 6.11 shows the orbit of the star in black and 50 random orbits integrated within $\pm$ one sigma of the input parameters. The current orbit shows the star apparently entering from outside the galaxy. When the distance input is lower the star follows a highly eccentric orbit bound to the Galaxy. This star appears to be part of the outer halo, although it has the possibility of reaching the escape velocity of the Galaxy with a Galactic rest frame velocity of $v_{grf} = 648^{+81}_{-88}$ km s$^{-1}$. Estimates on the escape velocity of the Galaxy vary and Banik and Zhao (2018) give an estimate as high as 690 km s$^{-1}$ in the solar neighbourhood. As this star is currently residing in the inner disk, the escape velocity is expected to be somewhat higher. Nevertheless this star is an interesting one to follow up as a hypervelocity star (HVS) candidate. More precise astrometry is needed (principally to constrain the distance) to examine the star's origin.

**Heavy metal subdwarfs:** Are labelled in Figures 6.5 - 6.7 so as to be easily compared with figures from Chapter 5, these stars still do not seem to be found preferentially in any population.

**Ex-He stars:** There are no major changes in the Ex-He population classification.

**Inter-He:** *Gaia* DR2 has provided more precise astrometry for most of these stars but we have excluded four due to parallax precision. It is interesting that almost 60% of the stars classed as thin disk are part of the intermediate helium class. This could suggest that these stars are closer in kinematics to the He-deficient subdwarfs than the Ex-He subdwarfs.

## 6.4 Helium-rich Giants

### 6.4.1 Sample selection

This sample consists of 45 hydrogen-deficient giants including 22 EHe, 18 R CrB and 5 HdC stars. The criterion for inclusion was that each star should have measurements of radial velocity and be included in DR2 with $f < 0.5$.
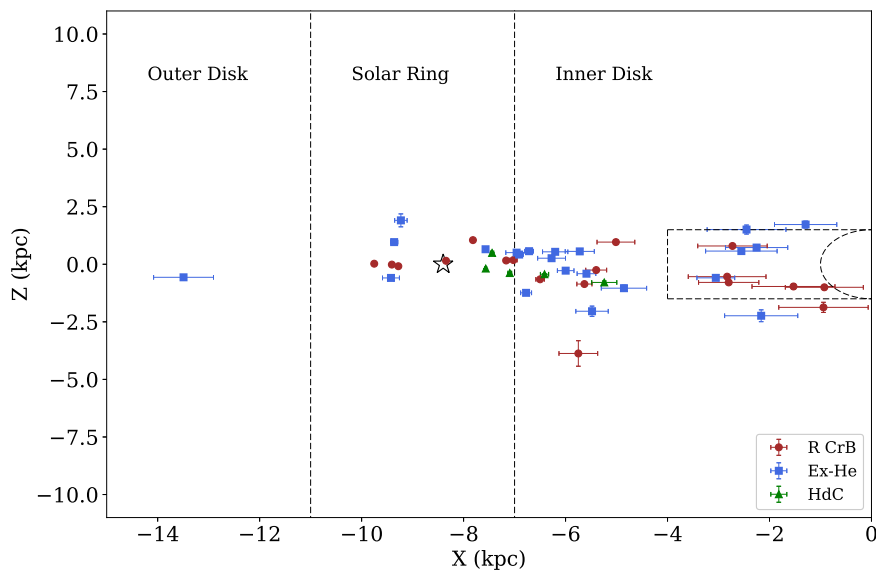


**Figure 6.12:** Distribution of sample in the Galactic X - Z plane. The dashed shapes show estimates of the location of the inner bulge (R $\sim$ 1.5kpc) and the bar (X = $\pm$4kpc , Y = $\pm$1.5kpc, Z = $\pm$ 1.5kpc).

### 6.4.2 Galactic and orbital parameters

Table C.6 contains the Galactic velocities and orbital parameters for all the stars mentioned in this section. Figure 6.12 shows the positions of the stars in the Galactic $X - Z$ plane, where $Z$ is the distance from the Galactic plane and $X$ from the Galactic Centre (GC). Here we label the inner disk at R < 7kpc, the solar ring at 7 < R < 11kpc and the outer disk past 11kpc from the GC. Estimates of the extent of the bulge and bar are also shown to highlight possible bulge members. The basic definition of the Galactic bulge is an over-density that swells up from the plane of the disk. A large fraction of

the bulge stars follow a rotating, barred, box/peanut shaped bulge with an exponential density distribution. In N-body models for disk galaxy evolution, box/peanut bulges are the inner three-dimensional parts of a longer, planar bar that formed through buckling out of the galaxy plane and/or orbits in vertical resonance. Thus the Milky Way is expected to have a thin bar component extending well outside the box/peanut bulge. There is much debate about the extent of this bar with estimates ranging from 3.1kpc to 5.0kpc (Bland-Hawthorn and Gerhard, 2016). We have adopted the values of R $\sim$ 1.5kpc for the inner bulge and X = $\pm$4kpc , Y = $\pm$1.5kpc, Z = $\pm$ 1.5kpc for the bar. Most of the stars in this sample lie between the Sun and the GC. Twelve stars are situated within or in close proximity to the bulge/bar region.
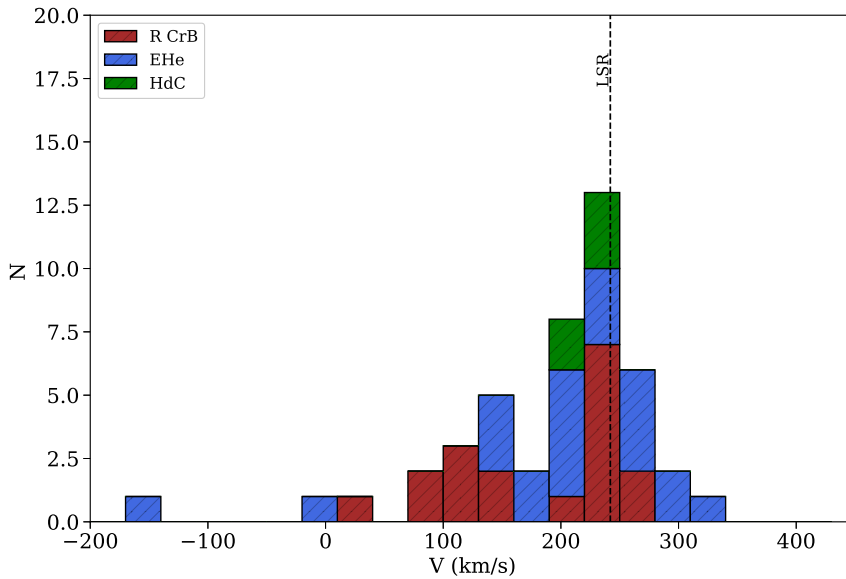


**Figure 6.13:** Stacked histogram of the Galactic rotational velocities of all 45 stars of the sample.

Figure 6.13 shows the distribution of rotational velocity, $V$, for all 45 stars. We see a peak at roughly the LSR as well as a tail towards lower velocities. This implies this sample is not a purely disk population but a there is a significant contribution from a population that does not participate in the Galactic rotation.

In the U–V velocity diagram (Fig. 6.14) we find that most of the stars lie within the disk distributions. Although if we look at their total velocity or kinetic energy (Fig.
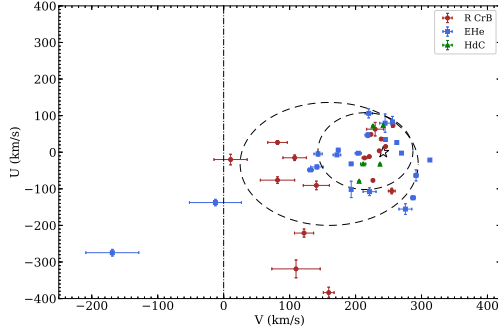
**Figure 6.14:** U – V- velocity diagram with $3\sigma$ (thick disk) and $3\sigma$ (thin disk) contours. The black star represents the local standard of rest (LSR).
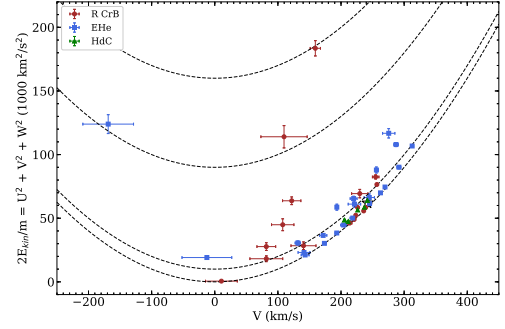


**Figure 6.15:** Galactic rotational velocity against the total kinetic energy. The parabolic curves denote line of equal velocity ($v_\perp = (U^2 + W^2)^{1/2}$) at 0, 100, 200 & 300 km s$^{-1}$ respectively.
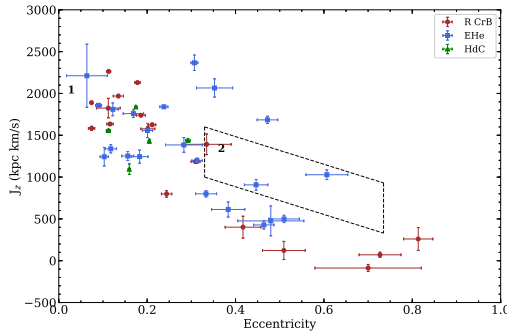


**Figure 6.16:** Z-component of angular momentum versus eccentricity. Regions 1 and 2 are the thin and thick disk respectively.
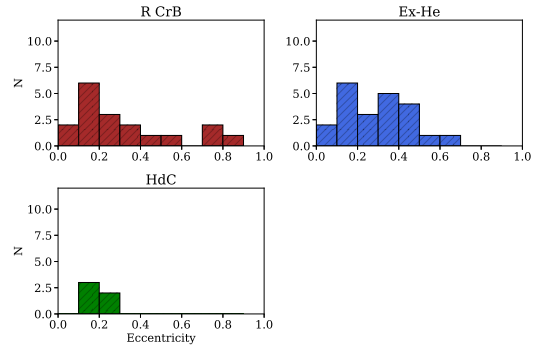


**Figure 6.17:** Histograms of the eccentricity distribution.

6.15) many of these stars have velocities that are inconsistent with disk kinematics, which would take them on higher energy orbits. Here the kinetic energy $2E_{\text{kin}}/m = U^2 + V^2 + W^2$ is plotted against the rotational velocity $V$, including contours showing the velocities perpendicular to Galactic rotation at certain values, where $v_\perp = (U^2 + W^2)^{1/2}$. This highlights the stars which do not belong in the disk population even if they appear in the $3\sigma$ disk contours.

Fig. 6.16 shows a plot of the z-component of the angular momentum, $J_z$, versus eccentricity. The thin disk stars cluster in an area of low eccentricity and $J_z$ around

1800 kpc km s$^{-1}$. Pauli et al. (2003) call this Region 1. The thick disk stars possess higher eccentricities and lower angular momenta called Region 2. Those stars which lie outside these regions we consider as halo and bulge candidate stars. We see a considerable number of stars populating the low momentum (below $\sim 1000$ kpc km s$^{-1}$) portion of the plot, including a star at a negative $J_z$ which is traveling retrograde to the Galactic rotation. Figure 6.17 shows the histogram of eccentricity of the four class of hydrogen deficient stars. The R CrB and EHe stars both have peaks at $\sim 0.2$ and tails extending somewhat to higher eccentricities.

### 6.4.3 Population classification

We use the population classification described in Sect. 5.4.2 with an added classification for the bulge. In short:

1. **Thin Disk (TH):** stars which lie near Region 1 in the angular momentum diagram and within the 3$\sigma$-thin disk contour and have $z_{\mathrm{max}} < 1.5$ kpc.

2. **Thick Disk (TK):** stars which lie in Region 2 and/or the 3$\sigma$-thick disk contour.

3. **Halo (H):** stars which lie outside Regions 1, 2 and outside both 3$\sigma$ contours and have $z_{\mathrm{max}} > 1.5$ kpc and $R_a > 10$.

4. **Bulge (B):** stars with low angular momentum, that come in close proximity to the Galactic Centre and stay in the inner disk, i.e. $J_z < 1000$ kpc km s$^{-1}$, $R_p < 3$ kpc and $R_a < 7$ kpc.

All orbits have also been visually inspected as part of the classification.

The leading difference between the Halo and bulge populations is the maximum distance from the Galactic Centre and the Galactic plane (i.e $R_a$ and $z_{\mathrm{max}}$).

DY Cen initially presents as a retrograde rotating star in Figures 6.14 and 6.15, suggesting a halo orbit. This is contradicted by the orbital parameters derived from `galpy`, where the star has a prograde orbit. This is due to the fact that the calculation of the Galactic velocities, U, V and W is Cartesian and so the V>0 criterion for prograde orbits is only valid in the solar neighbourhood. This is not a problem for the faint

**Table 6.3:** Population classification.

| Category | N | Thin Disk | Thick Disk | Halo | Bulge |
|----------|-----|-----------|------------|------|-------|
| HdC | 5 | 5 | 0 | 0 | 0 |
| R CrB | 18 | 8 | 3 | 1 | 6 |
| EHe | 22 | 6 | 11 | 0 | 5 |
| Total | 45 | 19 | 14 | 1 | 11 |

subdwarfs but is not necessarily valid for distant stars like DY Cen. In the case of the more distant stars, we classify the stars solely by the `galpy` outputs.

Fig. 6.18 shows the meridional sections and projections onto the $x - y$ Galactic plane of the orbits of four stars. Columns 1 and 2 show a thin and thick disk star respectively. These stars display roughly circular orbits which do not stray far from the Galactic plane. Column 3 shows the only star classified as a halo member, which extends greater than 6kpc from the plane and is in a more eccentric orbit than members of the disk. Lastly, column 4 shows a bulge candidate, this star remains close to the GC throughout its entire orbit.

### 6.4.4 Discussion

Table 6.3 shows the number of stars classified as halo, bulge, thin or thick disk stars. The thin and thick discs kinematically overlap one another in a way that makes it difficult to find selection criteria capable of distinguishing them. There should also be an overlap with the thick disk and the bulge.

R CrB and EHe stars are kinematically similar in terms of their velocity distributions, their higher eccentricities and orbital characteristics. They both consist of a disk population as well as an old bulge component. The R CrB stars have a higher percentage of stars in the young thin disk whereas the EHe stars are mainly found in the thick disk. The HdC stars are entirely found in the thin disk, although small number statistics dominate.
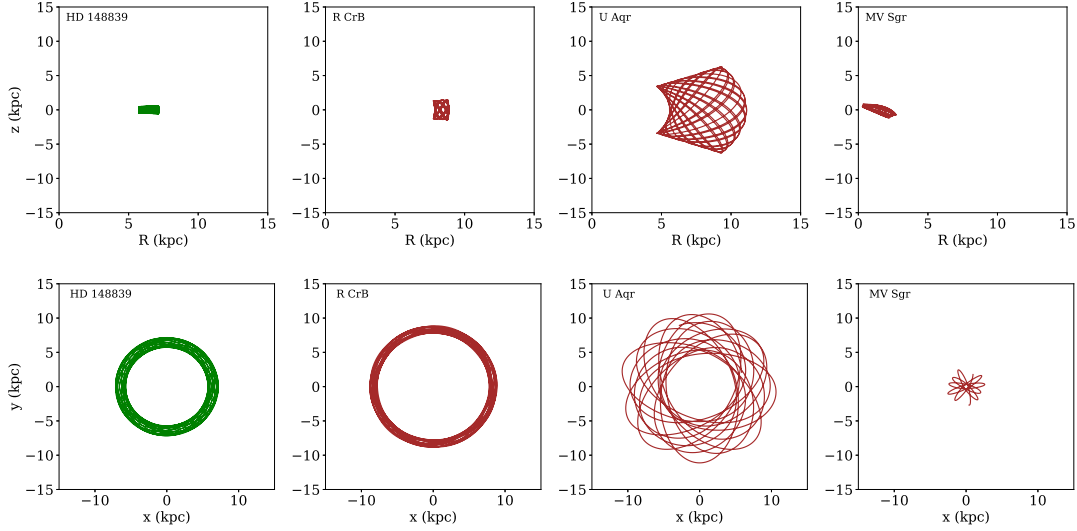
**Figure 6.18:** Top: Meridional sections of the orbits of 4 stars, examples of orbits from thin-disk, thick-disk , halo and bulge stars respectively. The colour of the orbit indicates the stars category, as in previous plots. The orbits in column 4 have been integrated over 300 Myrs in these figures, for clarity. Bottom: As above, but projected on the x-y Galactic plane

## 6.5 Central Stars of Planetary Nebulae

### 6.5.1 Sample selection

As in previous sections the selection criteria is that each star should have measurements of radial velocity and be included in DR2 with $f < 0.5$. This is especially limiting for the [WC] stars as many are found in the Magellanic clouds or are suspected to be members of the bulge population, hence at a low parallax.

### 6.5.2 Galactic and Orbital parameters

All Galactic and orbital quantities for the CSPNe are listed in Table C.7. All stars, bar two, lie within the thin/thick disk contours in the U-V velocity diagram (Fig. 6.19 ). This indicates an almost a pure disk population, as illustrated by the Galactic rotational velocity histogram (Fig. 6.20), where there is a peak at the LSR and just two stars at a rotational velocity of less than $100\,\mathrm{km\,s^{-1}}$. We see a few more outliers from the disk in the kinetic energy plot (Fig. 6.21), although there are no stars with a perpendicular velocity of $> 200\,\mathrm{km\,s^{-1}}$. Looking at the z-component of angular momentum, Figure

6.22 tells us much the same, most of the CSPNe appear to be part of the thin disk as they are clustered around region 1.
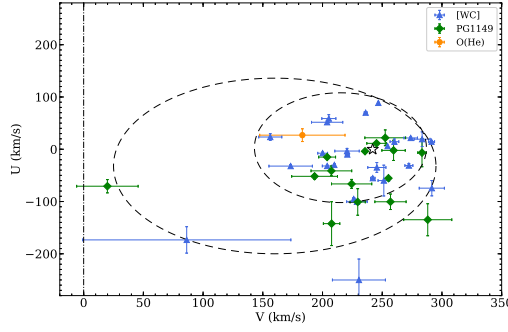


**Figure 6.19:** U – V- velocity diagram with $3\sigma$ (thick disk) and $3\sigma$ (thin disk) contours. The black star represents the local standard of rest (LSR).
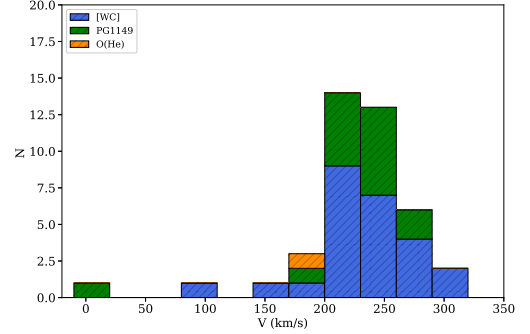


**Figure 6.20:** Stacked histogram of the Galactic rotational velocities of the CSPNe
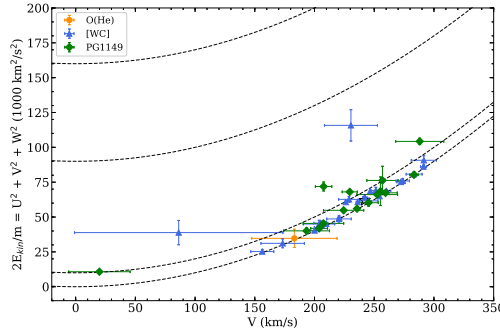


**Figure 6.21:** Galactic rotational velocity against the total kinetic energy. The parabolic curves denote line of equal velocity ($v_\perp = (U^2 + W^2)^{1/2}$) at 0, 100, 200 & 300 km s$^{-1}$ respectively.
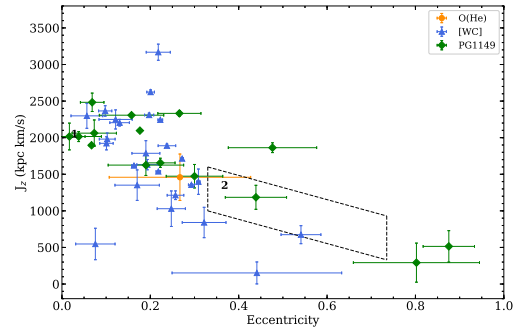


**Figure 6.22:** Z-component of angular momentum versus eccentricity. Regions 1 and 2 are the thin and thick disk respectively.

### 6.5.3 Population classification

Here we use the population criteria from section 6.4.3 as we expect some of these stars to reside in the bulge, Table 6.4 details the results.

For the [WC] stars, four stars are classified as bulge and the rest are thin disk star

**Table 6.4:** Population classification.

| Category | N | Thin Disk | Thick Disk | Halo | Bulge |
|----------|----|-----------|------------|------|-------|
| PG 1159  | 14 | 10        | 2          | 2    | 0     |
| [WC]     | 24 | 20        | 0          | 0    | 4     |
| O(He)    | 1  | 0         | 1          | 0    | 0     |
| Total    | 39 | 30        | 3          | 2    | 4     |

with none classified as part of the thick disk population. For the PG1159 stars 10 are thin disk, 3 are thick disk and 2 are halo. This sample does not extend to the bulge. There is only one O(He) star in our sample and therefore we cannot draw any conclusions. We are very limited by *Gaia* precision, for this group of stars. There are $\sim 40$ known PG 1159 stars and less than half have radial velocities and a sufficiently precise parallax.

## 6.6   Summary and Discussion

In this chapter the kinematics of 209 Hydrogen deficient stars have been examined, Figures 6.23 – 6.26 contain all stars mentioned in this chapter.

With the help of the SDSS radial velocities our sample of helium-rich hot subdwarfs has been increased from 50 to 121 stars. This has lead to the addition of many more halo hot subdwarfs, however the bulk of the population still resides in the thick disk. There are roughly the same number of stars classified as halo and as thin disk; interestingly 60% of the thin disk subdwarfs are the intermediate-helium stars. Could this suggest that these stars are closer in kinematics to the He-deficient subdwarfs than the Ex-He subdwarfs? The He-subdwarfs belong to all Galactic populations, however we do not find any bulge population. This is expected as these stars are intrinsically faint (with absolute magnitudes of $\sim 4$), and due to the selection effects outlined in Section 6.3.5.

From our analysis of helium-rich supergiants we have identified a small population of EHe and R CrB stars in the bulge, demonstrating the precision of *Gaia*'s second data release. The HdC stars, although they lie in the direction of the Galactic Centre, are members of the thin disk.

Our last sample consists of the central stars of planetary nebulae. The [WC] stars are mainly a thin disk population with a small number in the bulge but none in the thick disk. The PG1159 stars are also found mainly in the thin disk, although there are a few in the thick disk and halo. The PG 1159-type stars without planetary nebulae are too faint to be detected with sufficient parallax precision to be found in the bulge. Unfortunately the kinematical sample of O(He) stars consists only of one.

The majority of the CSPNe who's planetary nebula have already dispersed are quite faint (G > 16*), this is most likely the reason for our low numbers of PG1149 and O(He) stars. They could be perfect targets for the likes of The Large Synoptic Survey Telescope (LSST).

The CSPNe show a different kinematical behaviour to the supergiants and the hot-subdwarfs, they reside almost exclusively in the thin disk. Whereas the EHe and

---

*Gaia* G magnitude

Helium-rich subdwarfs[†] both have a majority in the thick disk.
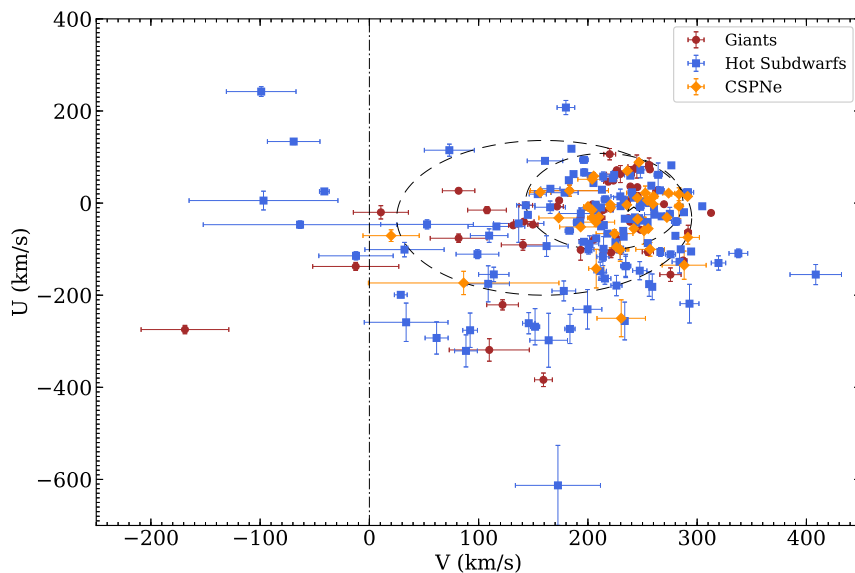


**Figure 6.23:** U – V- velocity diagram with $3\sigma$ (thick disk) and $3\sigma$ (thin disk) contours. The black star represents the local standard of rest (LSR).
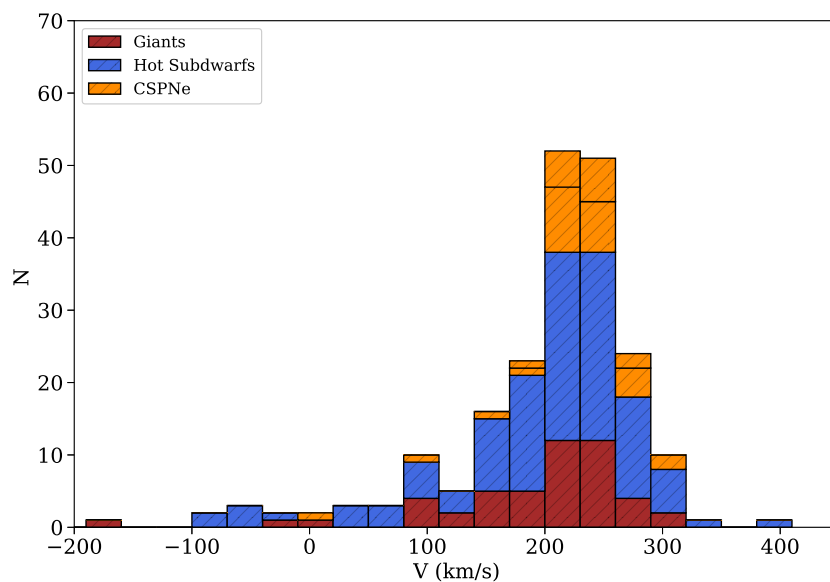


**Figure 6.24:** Stacked histogram of the Galactic rotational velocities of all groups of stars.

---

[†]excluding the Intermediate-helium sdO/Bs

112
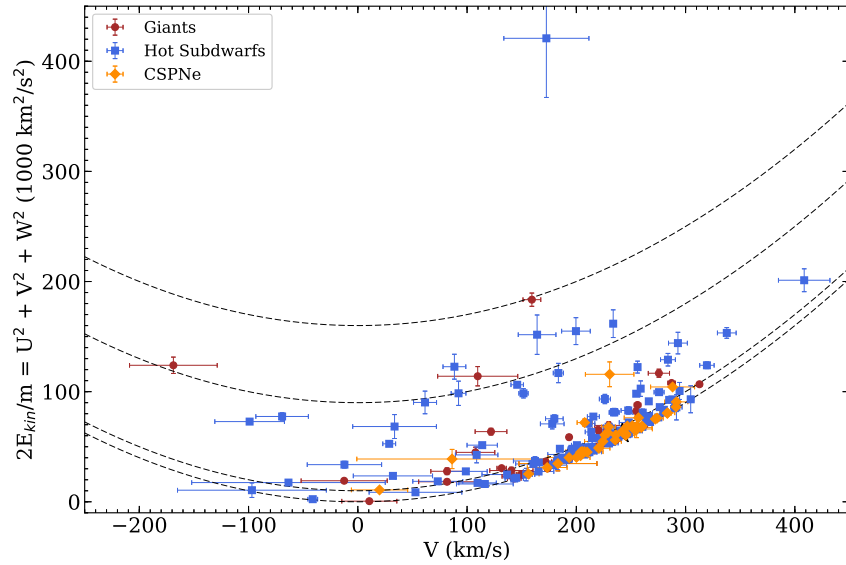
**Figure 6.25:** Galactic rotational velocity against the total kinetic energy. The parabolic curves denote line of equal velocity ($v_\perp = (U^2 + W^2)^{1/2}$) at 0, 100, 200 & 300 km s$^{-1}$ respectively.
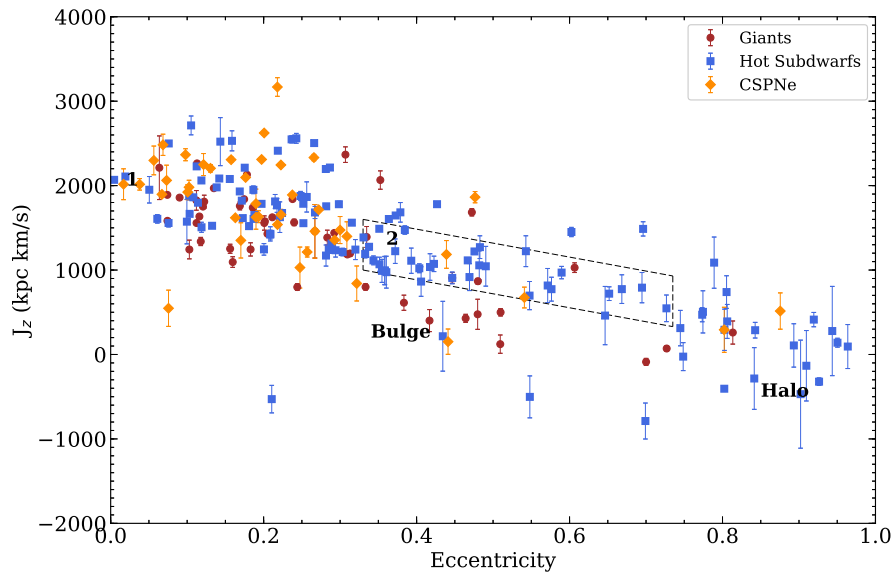


**Figure 6.26:** Z-component of angular momentum versus eccentricity. Regions 1 and 2 are the thin and thick disk respectively.

113

# 7

# Evolution of Hydrogen Deficient post-AGB stars with $Gaia$ DR2

Distances, and hence luminosities, are critical for explaining the origin and life histories of stars which possess so little surface hydrogen that, in several cases, their abundance cannot be detected. I will discuss several classes of star with luminosities thought to lie between 3 000 and 30 000 $L_\odot$, effective temperatures between 4 000 and 200 000 K and, consequently, radii between 0.01 and 100 $R_\odot$. The unifying feature is a severe absence of hydrogen, and, in most cases, enrichment of carbon (from $3\alpha$ burning), nitrogen (from CNO-processing), oxygen (from $\alpha$-capture on 14N ) and other elements as a consequence of neutron capture.

## 7.1 Introduction

Distances provided by $Gaia$ DR2 allow us to calculate luminosities and masses which provide vital clues to the origin and life histories of stars which cannot be explained by standard evolution channels.

The canonical evolution channels cannot reproduce the observed helium abundances found in these stars and in the case of the EHes the problem is to explain how hydrogen can be completely removed from such stars and for them to become supergiants without evidence of any binary companion. Regarding the hot subdwarfs, no canonical evolution tracks reach the extended horizontal branch. There are three leading theories for the evolution of these post-AGB stars, and are discussed in this chapter.

**Mergers:** In the merger scenario, we begin with a close binary of two helium white dwarfs (WD). The less massive WD is disrupted and part of the debris forms a hot corona, the remainder forms a disk which subsequently accretes onto the surviving WD. Off-centre ignition of helium is followed by expansion and evolution onto the helium

main sequence. Following the inward migration of the helium-burning shell the merged star is essentially a helium main sequence star. For lowest mass stars, following core helium exhaustion they will evolve directly to become CO/He WD. For M $\geq 1.0 M_\odot$, helium shell burning will ignite around the carbon/oxygen core and the star will become a giant. When the mass above the helium-burning shell becomes sufficiently small, the surface temperature begins to increase and the star evolves blueward nearly horizontally on the HR diagram.

**Helium flashes:** In general low mass stars undergo the helium core flash at the tip of the RGB. If there is sufficient mass loss on the RGB the star can depart from the RGB and experience the helium core flash (HeCF) while descending the hot white dwarf cooling track (Castellani and Castellani, 1993). There are three types of hot flashers.

1. Early hot flashers: HeCF during the stage of constant luminosity after leaving the RGB-tip. These become hot subdwarfs with standard H/He envelopes.

2. Late hot flashers with shallow mixing. Become He-enriched hot subdwarfs due to convection dilution of the envelope into deeper regions of the star.

3. Late hot flashers with deep mixing in which the H-rich envelope is engulfed and burned in the convective zone generated by the primary HeCF.

**Thermal Pulses (or "born-again" AGB stars):** The CSPNe stars can possibly be explained with the "born-again" scenario that definitely does not explain the R Coronae Borealis (R CrB) stars, extreme helium B stars, helium-rich subdwarf O stars, and the O(He) central stars. They all generally have helium-dominated atmospheres with abundances of carbon at $0.3 - 3\%$, in contrast to [WC] and PG1159 stars, which usually have high carbon abundances ($> 10\%$).

Thermal pulses also come three different flavours:

1. AGB final thermal pulse (AFTP): occurs when the star is still located on the AGB and the H-rich envelope is mixed with the helium rich inter-shell material. This results in a hydrogen mass fraction of $0.2 \, M_\odot$.

2. Late thermal pulse (LTP) : occurs when the final flash happens after the star leaves the AGB but before fusion is ceased. H is diluted by dredge up and the leaves a H mass fraction of $0.02\,\mathrm{M_\odot}$.

3. Very late thermal pulse (VLTP): the flash occurs when the star is already on the WD cooling track and the H envelope is totally consumed. During the flash the convection zone reaches the H-rich envelope which is carried into the hot C-rich interior and violently burned.

The work presented in the following sections is intended as a broad discussion of the evolutionary status of all stars mentioned in this thesis and not an in-depth analysis of the individual stars. In this chapter we calculate the luminosities, masses and radii and discuss the evolutionary histories of the groups of hydrogen-deficient stars introduced in Chapter 6. Section 7.2 details the methods used, sect. 7.3 deals with the helium hot subdwarfs, sect. 7.4 the supergiants and sect. 7.5 examines the CSPNe.

## 7.2 Methods

### 7.2.1 Masses, Radii and Luminosities

Gaia distances and magnitudes allow a calculation of a stars luminosity and, with the addition of published temperatures and surface gravities, mass and radius follow. Beginning with the absolute magnitude defined in terms of the apparent Gaia magnitude $G$,

$$M_{\mathrm{G}} = G - 5(\log_{10} d - 1) - 3.1 E_{\mathrm{B-V}} \tag{7.1}$$

where distance, $d$, is in pc. All extinction coefficients are taken from Schlafly and Finkbeiner (2011),unless published alongside the effective temperature of the individual stars. Adjusted for the bolometric correction,

$$M_{\mathrm{bol}} = M_{\mathrm{G}} + BC. \tag{7.2}$$

The bolometric correction was obtained from a cubic interpolation in Lang (1974) for temperatures up to $79\,000\,\mathrm{K}$. For the CSPNe, which can have temperatures $\gg 79,000\mathrm{K}$,

the BC has been extrapolated up to $200\,000$K using values from Weidemann and Bues (1967) (see Figure 7.1). [*]

The luminosity, mass and radius are given by:

$$L_\star = 10^{\frac{(M_{\text{bol},\odot} - M_{\text{bol},\star})}{2.5}} L_\odot, \tag{7.3}$$

$$R_\star = \sqrt{\frac{L_\star}{(T_{\text{eff}}/T_\odot)^4}} R_\odot \tag{7.4}$$

and

$$M_\star = \frac{gR_\star^2}{g_\odot} M_\odot. \tag{7.5}$$

In addition to $d$, the fundamental measurement in this analysis is $G$, which for Gaia DR2 is an average of all measurements made by the spacecraft. The number of photometric observations is included in the Tables C.1 - C.2, along with the inputs and outputs from these calculations.

### 7.2.1.1   Error propagation

Beginning with the asymmetric errors for surface gravity:

$$\Delta g_+ = 10^{\Delta \log g + \log g} - g \tag{7.6}$$

$$\Delta g_- = g - 10^{\log g - \Delta \log g} \tag{7.7}$$

and those of the distance create asymmetric errors in the absolute magnitude

$$\Delta M_{\text{G}+} = \sqrt{\Delta G^2 + \left(5\frac{\Delta d_+}{d * \log(10)}\right)^2 + (3.1\Delta E_{\text{B}-\text{V}})^2} \tag{7.8}$$

$$\Delta M_{\text{G}-} = \sqrt{\Delta G^2 + \left(5\frac{\Delta d_-}{d * \log(10)}\right)^2 + (3.1\Delta E_{\text{B}-\text{V}})^2} \tag{7.9}$$

---

[*]With the exception of the [WC] stars which is discussed in the following section

and hence luminosity mass and radius,

$$\Delta L_{\star+} = \frac{\log(10)}{2.5} L_\star \Delta M_{\text{bol}+} \tag{7.10}$$

$$\Delta L_{\star-} = \frac{\log(10)}{2.5} L_\star \Delta M_{\text{bol}-} \tag{7.11}$$

$$\Delta R_{\star+} = \frac{\sqrt{\left(\frac{\Delta L_{\star+}}{(T_{\text{eff}}/T_\odot)^4}\right)^2 + \left(\frac{4L_\star(T_{\text{eff}}/T_\odot)^4}{(T_{\text{eff}}/T_\odot)^5}\right)^2}}{2R_\odot} \tag{7.12}$$

$$\Delta R_{\star-} = \frac{\sqrt{\left(\frac{\Delta L_{\star-}}{(T_{\text{eff}}/T_\odot)^4}\right)^2 + \left(\frac{4L_\star(T_{\text{eff}}/T_\odot)^4}{(T_{\text{eff}}/T_\odot)^5}\right)^2}}{2R_\odot} \tag{7.13}$$

$$\Delta M_{\star+} = \sqrt{\left(\frac{\Delta g_+}{g_\odot} R_\star^2\right)^2 + \left(\frac{\Delta g_+}{g_\odot} \Delta R_{\star+} R_\star^2\right)^2} \tag{7.14}$$

$$\Delta M_{\star-} = \sqrt{\left(\frac{\Delta g_-}{g_\odot} R_\star^2\right)^2 + \left(\frac{\Delta g_-}{g_\odot} \Delta R_{\star-} R_\star^2\right)^2} \tag{7.15}$$

### 7.2.2 Bolometric correction

The bolometric correction is an important correction as it accounts for the star's radiation outside of the visible wavelength range. The bolometric correction is large both for early type stars and for late type stars. The former because they emit substantial radiation in the ultraviolet, the latter because a large part is in the infrared.

As the BC we use is taken from multiple sources we have compared to values in the literature for the EHe stars. (Heber and Schoenberner, 1981) publishes BC for nine of the EHe stars in our sample. Their BC matches with the one used here within 0.1. With regards to the [WC] stars we have assigned a bolometric correction based on the stars spectral class instead of the temperature. This is due to the fact that the BC is not just a function of temperature but of wind density. We use the values published in Table 1. from Crowther (2008b) and using the spectral classifications of Jeffery et al. (1996).
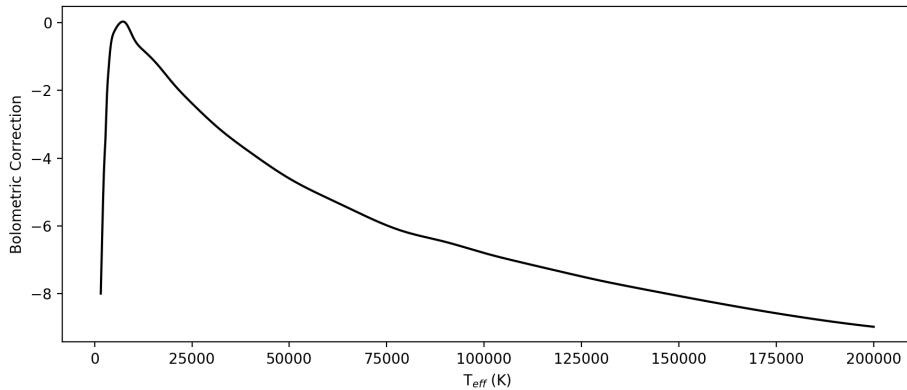
**Figure 7.1:** Bolometric corrections used in these calculations.

## 7.3    Hot Subdwarfs

This sample contains the intermediate and extreme helium subdwarfs from chapters 5 and 6 as well as the hot-subdwarfs listed in the catalog by Geier et al. (2017) with published temperatures and surface gravities. This is not the same sample of stars as in chapter 6, although there are 19 stars in common. Figure 7.2 show the H–R diagram for 108 helium-rich hot-subdwarfs. In this figure I have included two He+He WD merger channels of different masses (Zhang and Jeffery, 2012) and a late hot flasher model (Miller Bertolami et al., 2008).

The majority of stars lie close to the helium main sequence (HeMS) and are therefore currently in a core helium burning phase or are about to evolve onto or away from this phase.

The merger and hot-flasher scenario both explain the subdwarfs* well in terms of helium abundance and position on the HR digram; the question of which stars are part of a binary system would be the important distinction. For the hot flasher models a mass loss event must take place on the RGB so as to allow the helium core flash to occur later in the star's evolution. This can occur via common envelope ejection in a short binary system or stable RLOF resulting in a wide binary. However hot subdwarfs are found both in binaries and apparently single stars. The helium-rich subdwarfs match well with the merger scenario and those found in binaries are more likely the product

---

*Excluding the intermediate helium hot subdwarfs

of a late hot flasher. The "born-again" evolution channels, despite the similarity to the hot-flasher models, do not produce hot subdwarfs.

There are two ExHe stars well above the HeMS which could represent an earlier stage of evolution to the rest, these are PG 1415+492 and BPS CS 22940-0009.

The masses derived for these stars are largely unreliable, dominated by errors in the surface gravity measurements. The radii, on the other hand, are more precise with most of the measurements between 0.1 and $0.25R_\odot$ (Fig. 7.3). Figure 7.4 shows the mass distributions the all hot subdwarfs with derived masses where the mean mass error is less than 30%. The standard deviation on the mean mass is larger than the mean itself which highlights a problem with these measurements. A large portion of these masses are too low to be physical (i.e. the 11 stars with masses below $0.1M_\odot$)

### 7.3.1 Notes on individual stars

Three intermediate helium hot subdwarfs appear as outliers in the HR diagram, these are JL 87, PG 0229+064 and CPD-20° 1123

**CPD-20° 1123** is the first intermediate helium rich sdB star found in a short-period binary. It has a period of 2.3 d with a companion of either a low-mass main-sequence star or a white dwarf (Naslim et al., 2012). It is argued that all intermediate helium subdwarfs are very young "normal" sdBs and helium will eventually sink and reveal a hydrogen rich surface

Kupfer et al. (2015) give a spectroscopic distance which is twice the Gaia derived value, although significant for the mass and radius this does not hugely affect its position on the HR diagram.

**JL 87** has not shown any evidence of being in a binary system although long term monitoring is needed to test this.

**PG 0229+064** is the coolest of the subdwarfs and has a low surface gravity.Aznar Cuadrado and Jeffery (2002) found no evidence of a short binary system but there are no long term observations to rule out a long period binary
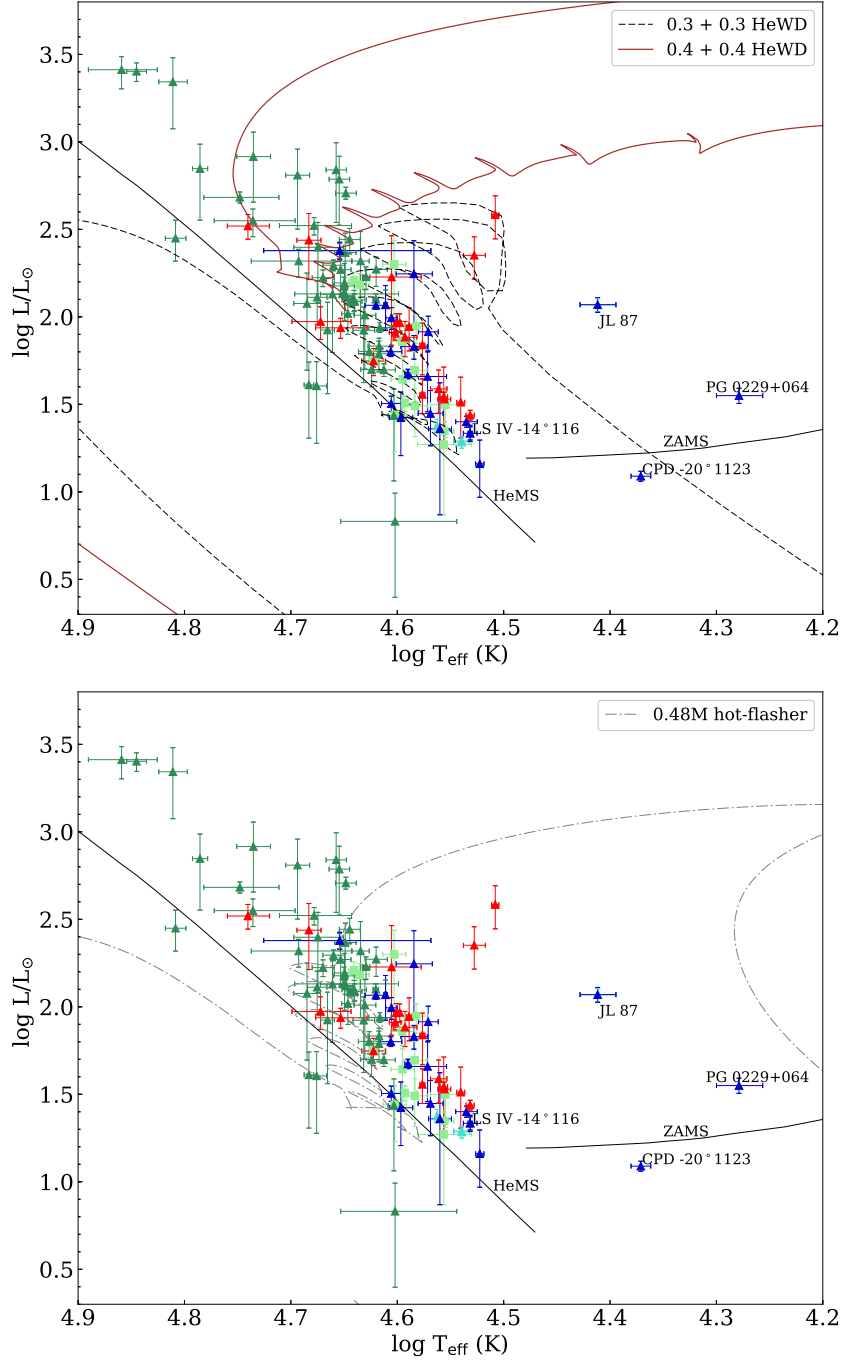
**Figure 7.2:** H–R diagrams for subgroups of hot subdwarfs. The post-merger evolution of a He+He WD merger (Zhang and Jeffery, 2012) (0.40+0.40 M$_\odot$) is shown as a brown solid line and the 0.30+0.30 M$_\odot$ merger is shown in the black dashed line (Top). The late hot flasher model (Miller Bertolami et al., 2008) is shown in the dark grey dot-dashed line. The ZAMS (Dorman et al., 1993) and HeMS are also shown (black solid lines, bottom).
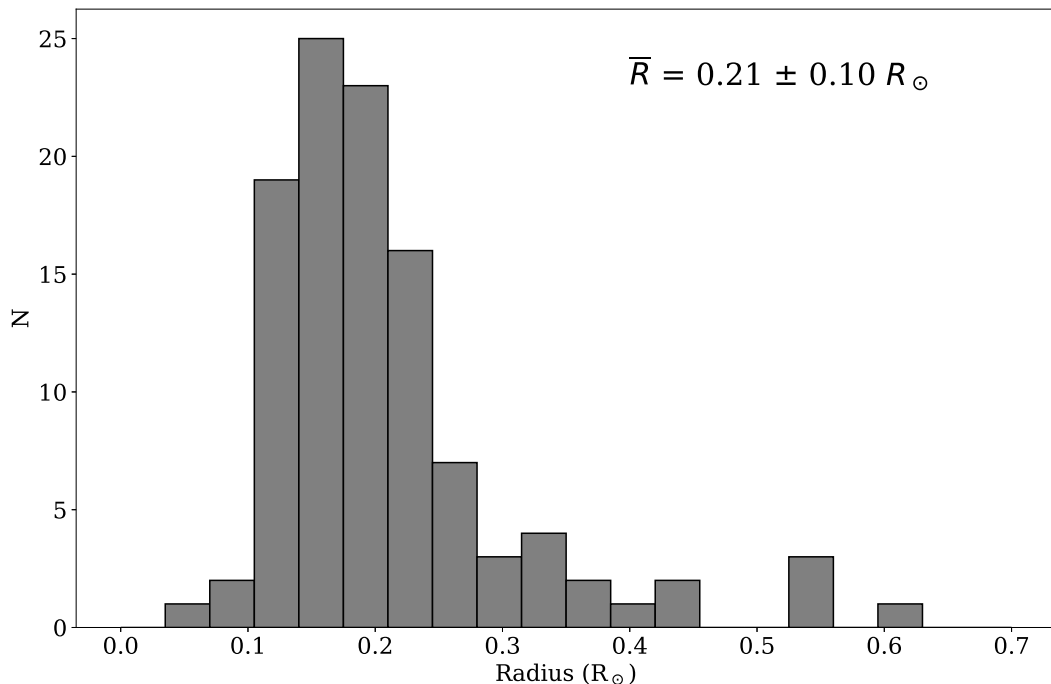
**Figure 7.3:** Histogram of the derived radius measurement for the hot subdwarfs.

**LS IV$-$14°116:** As discussed in chapter 1 has two differing measurements of $T_{eff}$ and $\log g$ depending on the choice of LTE or NLTE models, in this study we adopt the results from Naslim et al. (2011). This makes a negligable difference to the luminosity and radius but the mass estimate using the NLTE spectral parameters ($M = 0.551^{+0.09}_{-0.08}$) is closer to the canonical mass for hot subdwarfs.

The low luminosity of LS IV$-$14°116 seems to suggest that this star is on the HeMS. This disagrees with the theory that this star is settling to become a "normal" sdB. The lack of evidence for a companion make the hot flasher theory unlikely and the merger scenario cannot reproduce an intermediate helium surface abundance.

## 7.4   Giants

This sample consists of the helium-rich supergiants introduced in section 6.4 with published effective temperatures or gravities. We have also included the hot-sdO stars LSE 153, 263 and 259. These stars are thought to be successors of the R CrB and EHe
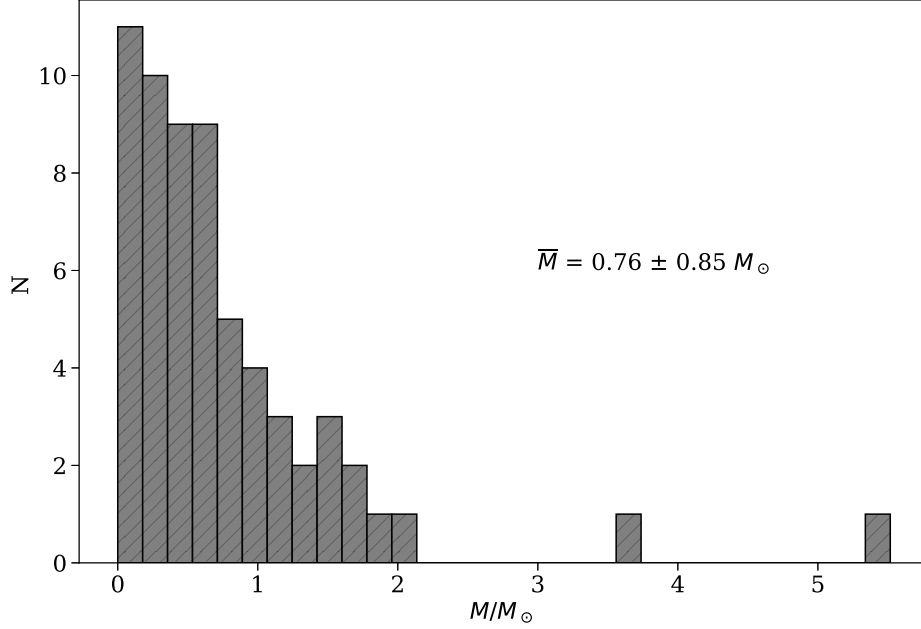
**Figure 7.4:** Histogram of the derived mass measurement for the hot subdwarfs where the average errors on the mass are less that 30%.

stars based on previous estimates of their luminosities ($\log L/L_\odot$=3.7–4.5 ), although LSE 263 displays too low of a carbon abundance to fit in with this evolution channel (Husfeld et al., 1989).

Both R CrB and EHe stars are known to be photometric variables, the former with very large amplitudes. Since the individual Gaia measurements are not available in DR2, the AAVSO database was interrogated for all stars in our sample having light curves during the period of Gaia observations (25 July 2014 and 23 May 2016). AAVSO light curves are available for all RCrB and HdC stars and for two EHe stars, indicated by the * in table C.3.

Four stars showed brightness changes of more than 1 magnitude. R CrB and S Aps show dips exceeding 4 magnitudes (Figs. 7.5). For these we adopt the estimates of $G$ from the Initial Gaia Source List (Smart and Nicastro, 2013) which combines data from Tycho2, LQRF, UCAC4, SDSS-DR9, PPMXL, GSC23, GEPC, OGLE, Sky2000 and 2MASS. These values were compared to the AAVSO light curves to ensure they correspond approximately to maximum light.

DY Per shows a slight dip in the AAVSO light curve of $\sim 1$ magnitude (Fig. 7.5(b)). The value of $G$ given by Gaia DR2 agrees well with the estimate from (Smart and Nicastro, 2013). Perhaps Gaia did not observe DY Per during the dip, or the number of observations at maximum light dominates the average. We adopt the Gaia DR2 measurement in this case.

As usual, errors on the mass are dominated by errors in the surface gravity. For example, NO Ser has $\log g(\mathrm{cms}^{-2}) = 2.3 \pm 0.4$ or $g = 199.5^{+301.7}_{-120.1}\mathrm{cms}^{-2}$, which translates to a mass error of $\approx^{+150\%}_{-60\%}$. Only 7 stars have a mean mass error of less than 50% (DY Cen, HD 144941, BX Cir, V652 Her, GALEX J184559.8-413827, LSIV+6 2 & BPS CS 22940-0009). All of these have relatively high surface gravities; consequently the helium lines have well-defined Stark wings, enabling surface gravities to be measured more precisely. The radius measurements are more precise because the main contributor to the error is the effective temperature which is more easily measured, 44 stars have a radius error less than 50%. Figure 7.6 shows the $L - T_{\mathrm{eff}}$ or Hertzsprung–Russell (HR) diagram for all hydrogen-deficient stars in Table C.3, with evolution tracks included. The most luminous EHes lie in the post-merger domain of a CO+He white dwarf binary. The lower luminosity EHe stars, on the other hand, lie in the region of the He+He mergers (solid brown line) or a late hot flasher with deep mixing (solid grey line). In the case of the R CrB and HdC stars, the CO+He WD merger track from Zhang & Jeffery (2014) passes through the domain of the HdC stars during the period of accretion before evolving towards the hotter RCrB stars with $L/L_{\odot} \sim 4.0$. This could suggest the HdC stars directly evolve to become R CrB stars and will show the same light decline event when they reach a higher luminosity (hence have a greater pulsational instability). One challenge to that theory is that the models predict the star will spend a greater amount of time at the turn off point ($\sim$53000yrs) before the star evolves at a constant luminosity reaching a temperature of 10 000K ($\sim$2000yrs). Hence we should expect to see many more HdC stars than RCrB stars.

### 7.4.1 Notes on individual stars

**BD+10°2179** lies in a region of the H–R diagram with MV Sgr and HD 12448, coinciding with the He+He WD merger tracks and late hot flasher model. Most of these

**(a)** R CrB



**(b)** DY Per



**(c)** S Aps
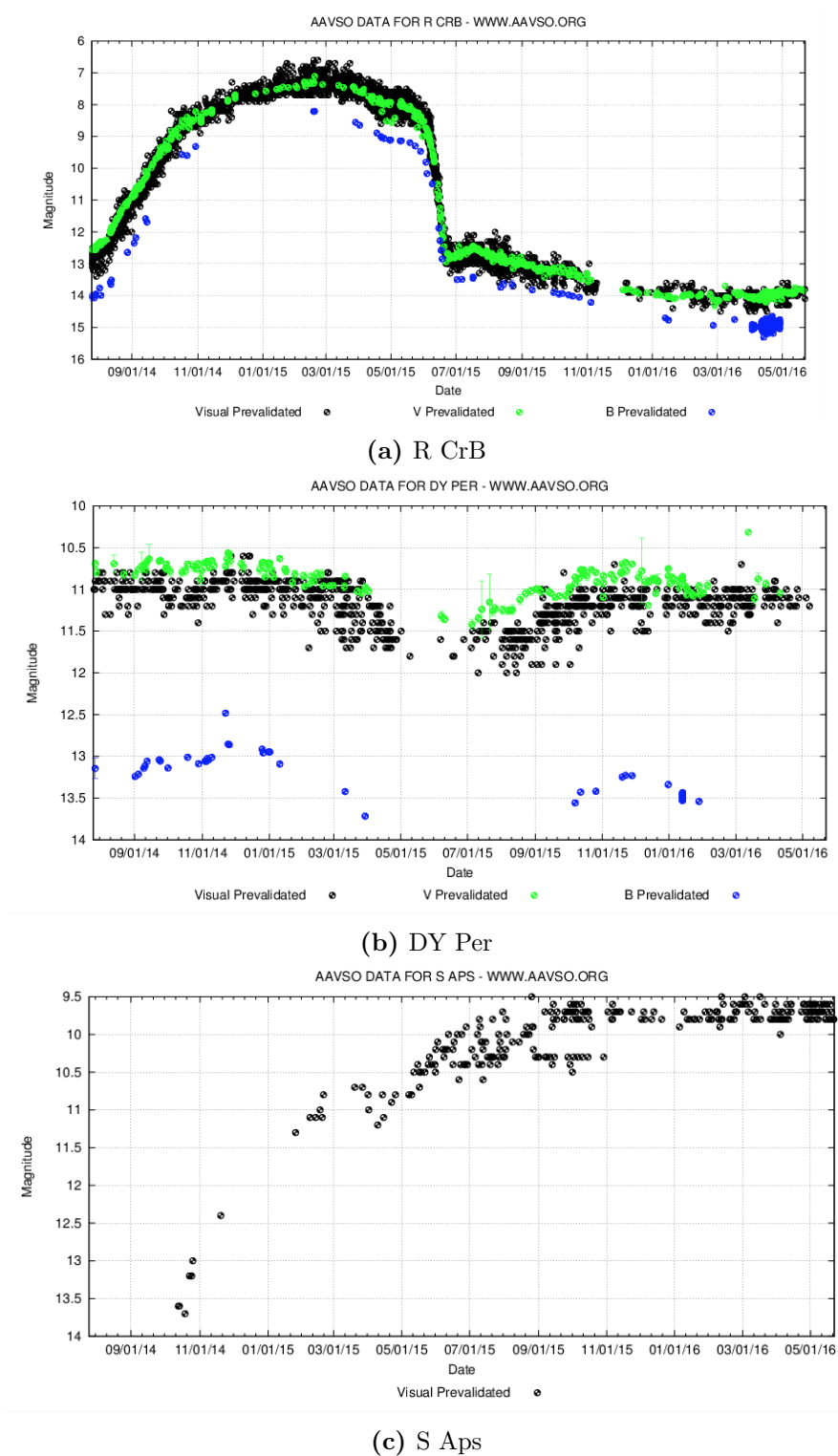
**Figure 7.5:** Light curves of the three stars which show significant brightness changes of the period of Gaia DR2 data acquisition
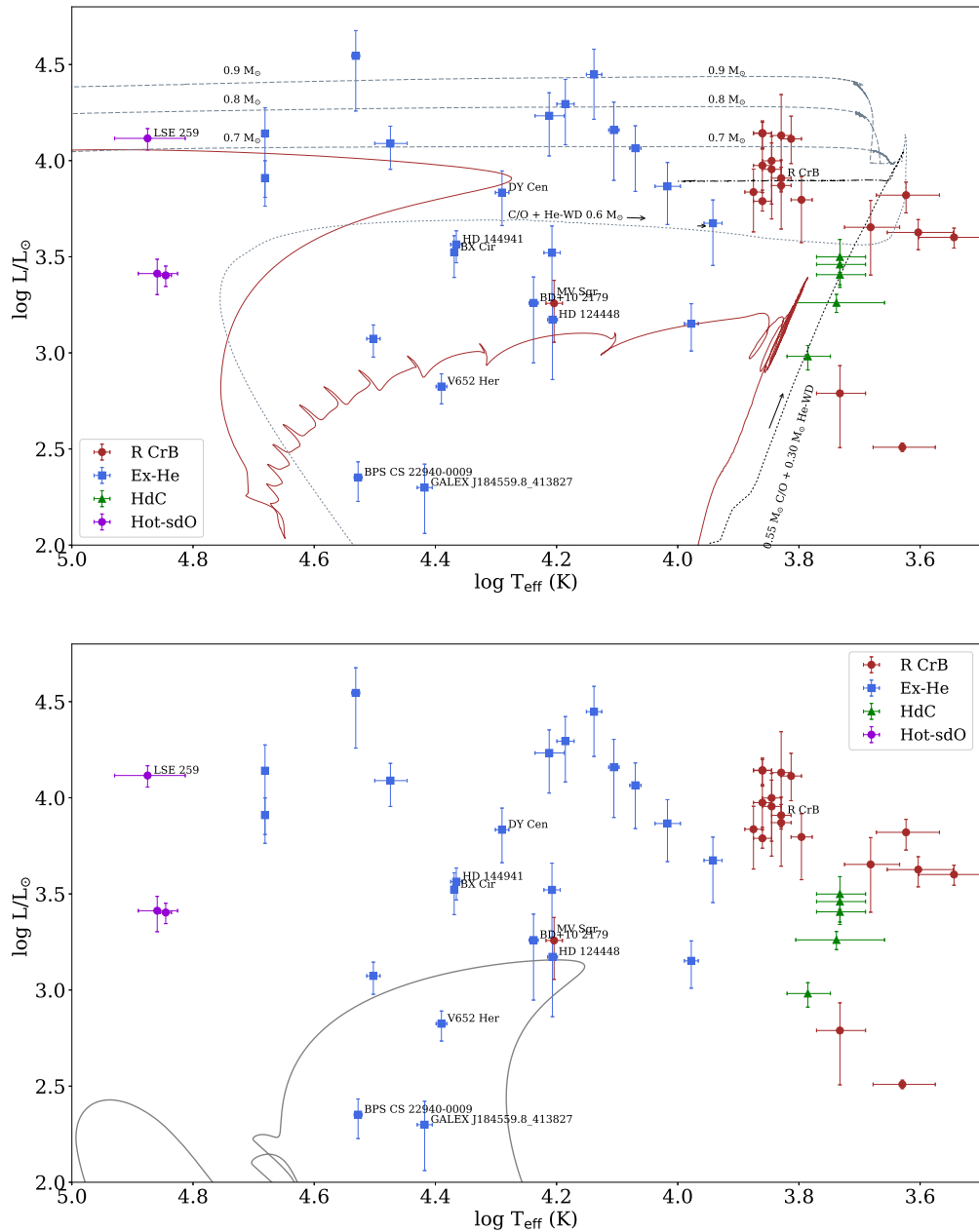
**Figure 7.6:** H–R diagram for subgroups of hydrogen-deficient star. Top: Including post-merger evolution tracks for models of CO+He WD mergers (Saio and Jeffery, 2002) (0.6+0.1, 0.6+0.2 and 0.6+0.3 $M_\odot$) are shown in light grey (pre-merger dotted, post-merger dashed). The post-merger evolution of a He+He WD merger (Zhang and Jeffery, 2012) (0.40+0.40 $M_\odot$) is shown as a brown solid line. The black line represents the $0.55 + 0.3 M_\odot$ CO+He WD merger calculation by Zhang et al. (2014). The dotted section denotes the accretion stage whereas the dash-dot line is the post-merger track. Bottom: The late hot flasher model (Miller Bertolami et al., 2008) is shown in dark grey.

hot flasher models predict too much carbon for the amount of hydrogen remaining on the surface of BD+10°2179 (Kupfer et al., 2017). This plus the lack of evidence for a companion to participate in a mass transfer event favours the merger scenario as a better fit.

**MV Sgr** is a curious case. It is classed here as a R CrB star as it was seen to decline at least twice (1930 and 1945) but since has not been seen to have a large decline (Hoffleit 1959). This could suggest that it has already evolved to become an EHe star, Studying the spectra of MV Sgr is difficult due to the emission lines from the high-density, hydrogen rich nebula surrounding the star. Although the star has a temperature and luminosity consistent with both the merger and hot flasher model, neither can explain this star adequately.

**GALEX J184559.8–413827** shares spectroscopic similarities with V652 Her and Jeffery (2017) argues that this star is also a post double helium white dwarf merger (Saio and Jeffery, 2002; Zhang and Jeffery, 2012). The star's position on the H–R diagram and a derived radius of 0.69R$_\odot$, however, suggest that this star is more likely to be an extreme helium hot subdwarf.

**BPS CS 22940-0009** is included in section 7.3 as an extreme helium hot subdwarf. We include this star in the EHe sample as it shows spectroscopic similarities with LS IV+6 2 and a recent re-analysis of the star's T$_{\text{eff}}$ and log$g$ suggest much lower values than previously measured (Jeffery priv. comm.). The luminosity, radius and mass derived here are all consistent with an extreme helium hot subdwarf star. These results are not changed significantly by a revision of the spectroscopically derived parameters, the distance to the star would have to be substantially decreased for this star to be classified as an extreme helium supergiant.

**HD 144941** was classified as an EHe star by Jeffery and Ramsay (2018) as the mass estimate of 1.2 ± 0.7M$_\odot$ ruled out the main-sequence star argument. In *Gaia* DR2, however, the distance has substantially increased and now, with such a high mass ($\sim$ 4M$_\odot$), HD 144941 is more likely to be a main-sequence Bp(He) star.

**BX Cir** shows a much higher luminosity than V652 Her, although it belongs to the same pulsation class, they may not share they same evolutionary history. The carbon-rich atmosphere of BX Cir does not match the He+He WD merger scenario

and is thought to be a product of a He + CO white dwarf merger. BX Cir does not match any of the post-merger tracks.

**Hot sdOs:** LSE 259 has a very high luminosity for a sdO star, coinciding with the both the He+He WD merger track and the CO+He WD merger tracks. This star could be a direct link to the EHe stars, possibly evolving to become an O(He) star. LSE153 and 259 on the other hand have luminosities lower than previous estimates and are more difficult to explain.

## 7.5 Central Stars of Planetary Nebulae

Here we present luminosities for a sample of CSPNe for which we could obtain temperatures and in some cases gravities. This sample contains 20 PG 1159 stars, 14 [WC] and 4 O(He) stars. Figure 7.7 shows the sample of CSPNe with four VLTP tracks (Miller Bertolami and Althaus, 2006) with initial masses of $1\,M_\odot$- $3.75\,M_\odot$ and post-thermal pulse masses of $0.53\,M_\odot$-$0.741\,M_\odot$. We include a LTP track and a He+He WD merger track (Zhang and Jeffery, 2012).

Miller Bertolami and Althaus (2006) found that the different nitrogen abundances observed on the surface may of the PG 1159 stars is an indication that the progenitors of these stars evolved through VLTP episodes, where most of the hydrogen content of the remnant is burnt, or late thermal pulses where hydrogen is not burnt but instead diluted to very low surface abundances. They also showed that this scenario provides a possible explanation for the existence of O(He) stars of low mass, linking them as the immediate ancestors of the He-enriched PG 1159.

Care needs to be taken when evaluating the [WC] stars, the bolometric correction was assigned based on spectra classification. This combined with the difficulty in measuring the temperatures of [WC] stars (due to the presence of optically thick winds) makes our luminosities largely unreliable.

All but one of the CSPNe with LogL > 3.4 have planetary nebulae (PN), stars with lower luminosities do not, presumably because the PN has already dispersed after passing the "knee" of the evolution channels.

PG1159 stars have been shown to have systematics in the determination of their
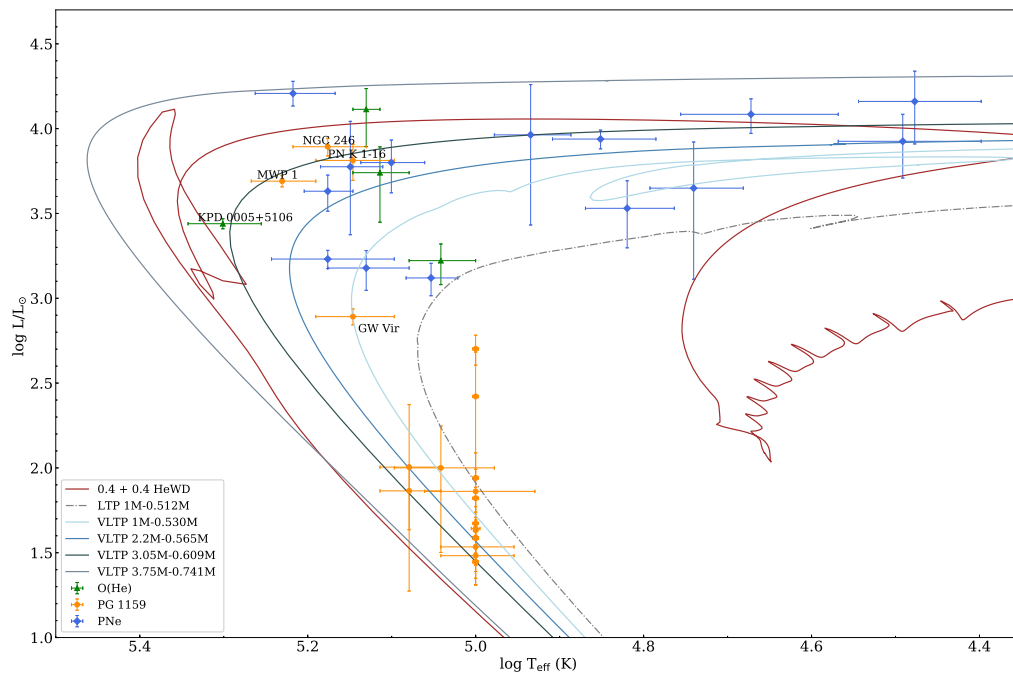
**Figure 7.7:** HR diagram with four VLTP tracks differing in mass, one LTP track (Miller Bertolami and Althaus, 2006) and one He+He WD merger track (Zhang and Jeffery, 2012). The PG1159 stars labelled have been detected to have PN, except in the case of GW Vir (==PG1159 +035) which is highlighted as it is the prototype of its class.

temperatures, these can be up to 30kK. Because of the difficulty with the temperature determinations of all of these stars and the bolometric correction problem no conclusions can be drawn from such a uncertain group of measurements. The only trend we can be sure of is that the low luminosity PG1159 stars without planetary nebulae have all begun their descend to the WD cooling track as expected.

# Conclusions and Future Work    8

## 8.1    Pulsation Analysis

We have measured radial velocities line-by-line over 355 spectra resulting in 57 radial velocity curves for 11 elements. We have found multiple periods in the radial velocity curve and have investigated the amplitude of the pulsation as a function of depth in the photosphere. From measurements of the primary pulsation mode, its amplitude does not appear to change with depth implying a standing wave behaviour. To learn more about LS IV$-14°116$ from these oscillations, theoretical models are needed to interpret the spectrum, incorporating the non-radial oscillations, chemical stratification, and including differential vertical motion. Obtaining spectrophotometry would allow an exploration of the extent of UV line-blanketing in the atmospheres of peculiar this subdwarf and to address the discrepancy between different measurements of its surface properties Green et al. (2011). The effective temperature measurement will be too high if there is more UV line opacity in the star than is accounted for in the models. UV observations will remove this uncertainty by quantifying the UV opacity, and potentially solve the pulsation problem. Since this star cannot be excited by iron-group opacities as seen in the hot subdwarf population we must look for alternative solutions. One suggestion is that pulsations are excited by the $\epsilon-$mechanism (Miller Bertolami et al., 2011), no stars have been proven to be excited by this mechanism to date. The question remains what is the driving mechanism of this star?

We have applied our methods to a time series of spectra for the pulsating Extreme Helium star BX Cir. A line-by-line radial velocity analysis has been performed and radial velocity curves are presented for 72 lines. A comparison of the velocity curves by line and by depth in the photosphere has shown that the pulsation of this star is

continuous, lacking any discontinuity or shock. The next step will be to compute a model atmosphere to find where in the photosphere the core of each line is formed and its emergent spectrum in order to resolve the vertical motion. Does BX Cir go through any phase of compression or does is pulsate as a slab i.e. a smooth contraction and expansion? By shifting and adding the spectra we can produce a high SNR spectra suitable for measuring abundances, specifically to derive detailed abundances and perhaps detect more exotic species.

**Table 8.1:** Comparison of the luminosity, radius and mass of V652 Her and BX Cir.

| | V652 Her | | BX Cir | |
|---|---|---|---|---|
| | Jeffery et al. (2001b) | This work | Woolf and Jeffery (2000, 2002) | This work |
| $L_\odot$ | $919 \pm 14$ | $668.15 \, ^{+96.68}_{-135.27}$ | $1412 \pm 300$ | $3333.80 \, ^{+646.18}_{-991.48}$ |
| $R_\odot$ | $2.32 \pm 0.02$ | $1.43 \, ^{+0.10}_{-0.14}$ | $2.31 \pm 0.10$ | $3.52 \, ^{+0.34}_{-0.52}$ |
| $M_\odot$ | $0.59 \pm 0.18$ | $0.36 \, ^{+0.07}_{-0.08}$ | $0.47 \pm 0.03$ | $1.08 \, ^{+0.22}_{-0.33}$ |

This star is often compared to the Extreme helium star V652 Her which has the same pulsation period and comparable surface properties. Table 8.1 compares the luminosities, masses and radii computed in this thesis published in the literature. The new measurements of the both stars are different than previously thought. The uncertainty of the masses is largely due to the error in the surface gravity and now the stars appear to have differing radii. They shares a pulsation class but perhaps have a different history? The carbon-rich atmosphere of BX Cir does not match the He+He WD merger scenario that can explain V652 Her. It is thought to be a product of a He + CO white dwarf merger, but does not match any of the post-merger tracks on the HR diagram. Do we need to investigate alternate evolutionary models or improve our observational constraints?

## 8.2   Kinematics

The space motions and Galactic orbits of 88 hot subdwarfs were computed from published proper motions, radial velocities and inferred distances. The orbital parameters were used to classify sample members as having disk or halo orbits. This study confirms that sdO/B stars are members of all Galactic populations. The primary limita-

tion of this study was the small sample size, particularly with regard to the extreme- and intermediate-helium subsamples. Following the second *Gaia* data release and the collection of SDSS spectra we have significantly increased our sample of helium-rich subdwarfs. This has lead to the addition of many more halo hot subdwarfs, however the bulk of the population still resides in the thick disk. Interestingly 60% of the thin disk subdwarfs are the intermediate-helium stars. Could this suggest that these stars are closer in kinematics to the He-deficient subdwarfs than the Ex-He subdwarfs?

In our examination of the Galactic orbits we have found one hyper-velocity star candidate, worthy of follow-up in future data releases of *Gaia* to put a more strict constraint the distance to the star. Three intermediate-helium stars, including two with peculiar surface chemistries, show quite extreme halo orbits, but their space velocities are insufficient for them to be *bona fide* hyper-velocity stars. The high velocities argue *against* a previously proposed connection between the chemically-peculiar and normal hot subdwarfs, but pose equally challenging questions concerning the origin of the former. The possibility that they are the polluted ejecta from Type Ia supernovae appears to be worth exploring further. High-resolution spectroscopy of the HVS candidate would allow us to determine if this star shares the property of a peculiar surface chemistry.

With the analysis of Helium-rich supergiants we have identified a small population of EHe and R CrB stars in the bulge, demonstrating the precision of *Gaia*'s second data release. The HdC stars, although they lie in the direction of the Galactic Centre, are members of the thin disk. Our last sample consists of the central stars of planetary nebulae. The [WC] stars are mainly a thin disk population with a small number in the bulge but none in the thick disk. The PG1159 stars are also found mainly in the thin disk, none can be seen in the bulge. We speculate that the PG 1159-type stars without planetary nebulae are too faint to be detected with sufficient parallax precision to be found in the bulge. The CSPNe show a different kinematical behaviour to the Supergiants and the Hot-subdwarfs. They reside almost exclusively in the thin disk whereas the EHe and Helium-rich subdwarfs* have a majority in the thick disk.

As we extend our kinematical sample to the halo and the bulge our stars become

---

*excluding the Intermediate-helium sdO/Bs

increasingly faint and the higher precision data expected from *Gaia* DR3 is vital. Although they are good candidates for new surveys such as LSST, multi-epoch radial velocities and accurate distances are still needed to calculate the 3D space velocities.

## 8.3   The H-def HR Diagram

Our aim was to create a HR diagram for the hydrogen-deficient low-mass stars. This HR diagram (Fig. 8.1) combines the observations of all 190 stars studied in Chapter 7.
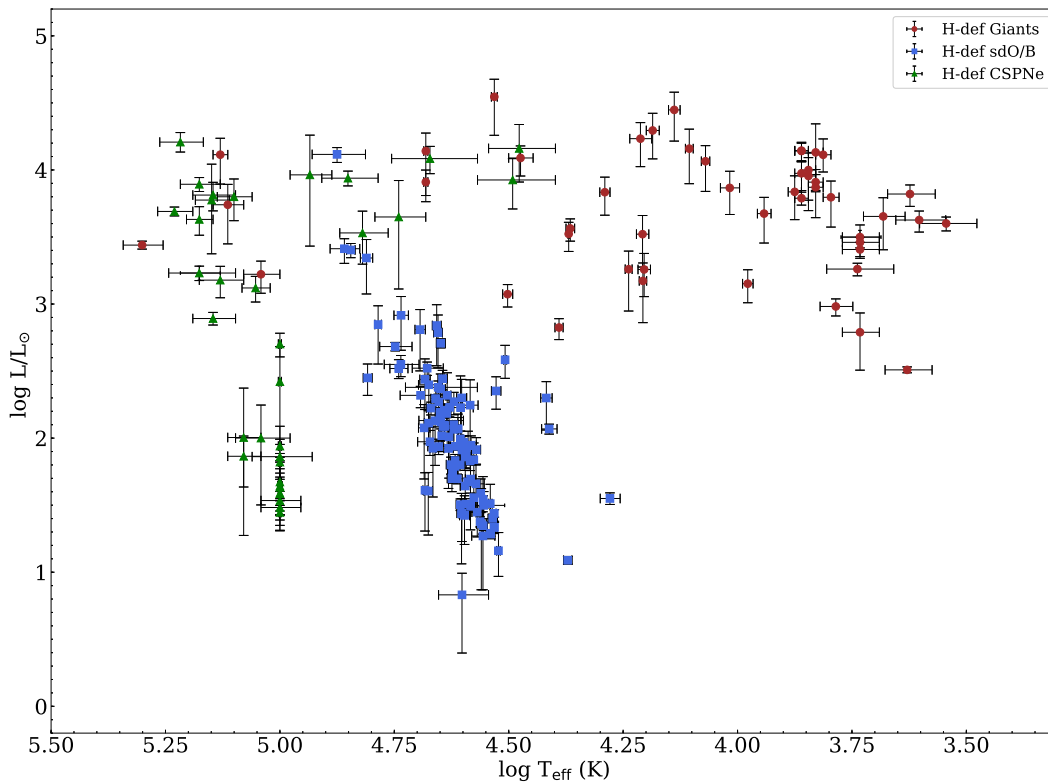


**Figure 8.1:** The hydrogen deficient HR diagram of all stars studied in Chapter 7.

We can compare or HR diagram that of Figure 8.2, a log $g$ – log $T_{eff}$ diagram for several classes of low-mass hydrogen-deficient stars (Jeffery, 2008). As *Gaia* delivers us more accurate distances we can transform our observational log $g$ – log $T_{eff}$ diagram to the theoretical HR diagram in addition to greatly increasing our sample sizes of these rare stars.

Even with a quick glance at Figure 8.1 one can see that a straightforward canonical
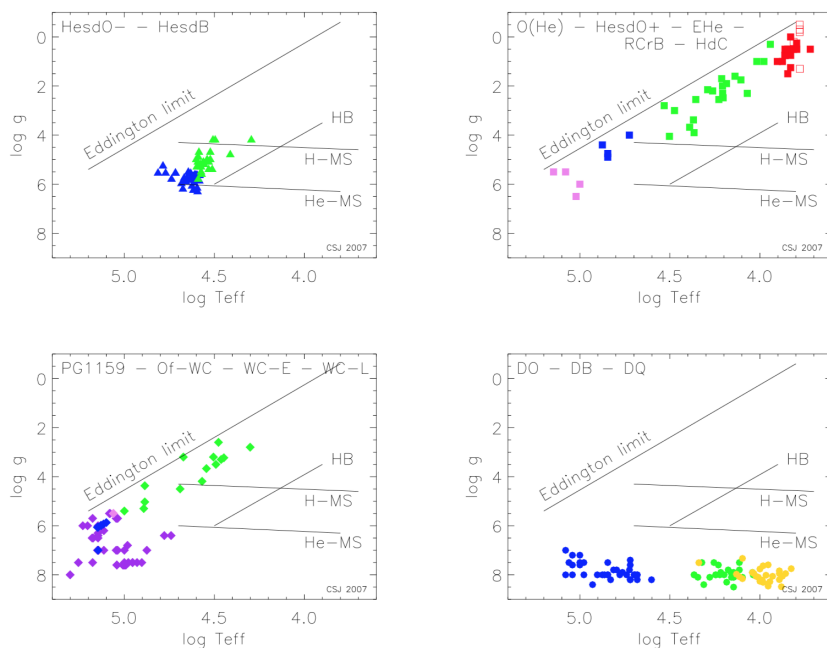
**Figure 8.2:** $\log g$ – $\log T_{\mathrm{eff}}$ diagram for several classes of low-mass hydrogen-deficient stars (Jeffery, 2008). Different panels identify contemporary evolutionary proposals, classes are separated by colour.

evolution track is not suitable to explain all of these hydrogen deficient stars. The supergiants (in red) can only be explained by the merging of two white dwarfs. We suggest that the evolution channel:

$$\mathrm{HdC} \to \mathrm{RCrB} \to \mathrm{Ehe} \to \text{hot-sdO} \to \mathrm{O(He)} \to \mathrm{DB}$$

Figure 8.3 illustrates that the merger of a CO and He-WD can explain the majority of the supergiants, although it does not allow for the formation of the Hot Subdwarfs.

Looking at Figure 8.4 and the evolution of two helium white dwarfs merging,

$$\text{He-WD} + \text{He-WD} \to \mathrm{EHe} \to \text{He-sdB} \to \mathrm{sdO} \to \mathrm{DB}$$

does well to connect the lower luminosity EHe stars with the extreme sdBs.

The hot subdwarfs (in blue) can also be explained by a merger, as long as they are single stars with a helium abundance of $\approx 99\%$. Analysis of the SDSS spectra with non-LTE model atmospheres (to give a first approximation of $T_{\mathrm{eff}}$ and $\log g$) would extend the number of helium-rich hot subdwarfs on the HR diagram and search for those stars which are in apparently short lived and/or rare stages of evolution such as the three Hot-sdOs .
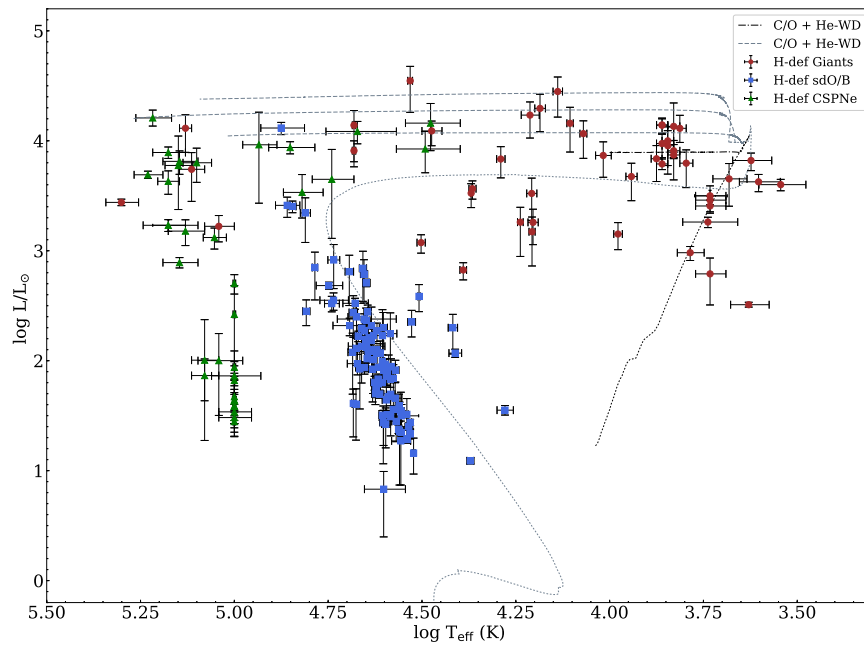
**Figure 8.3:** The hydrogen deficient HR diagram with the evolution track for CO and He-WD mergers.
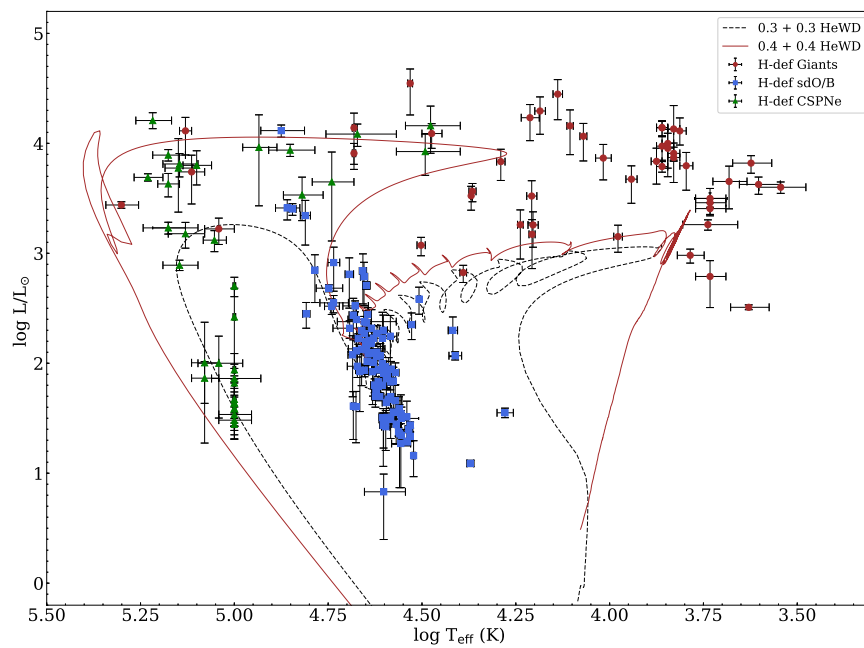


**Figure 8.4:** The hydrogen deficient HR diagram with the evolution track for He-Wd and He-WD mergers.

Figure 8.5 plots a late hot flasher model which can explain the hot subdwarfs that are seen in binary systems. For the CSPNe (in green) the (very) late thermal pulse is the favoured explanation, although the high uncertainties in the temperatures, and therfore luminosities, means we cannot infer too much from their position on this HR diagram.

This final chapter has been a first look and the nature of the hydrogen-deficient HR diagram, subsequent *Gaia* data releases and improved measurements of surface parameters methods will provide us with a better picture in the future.
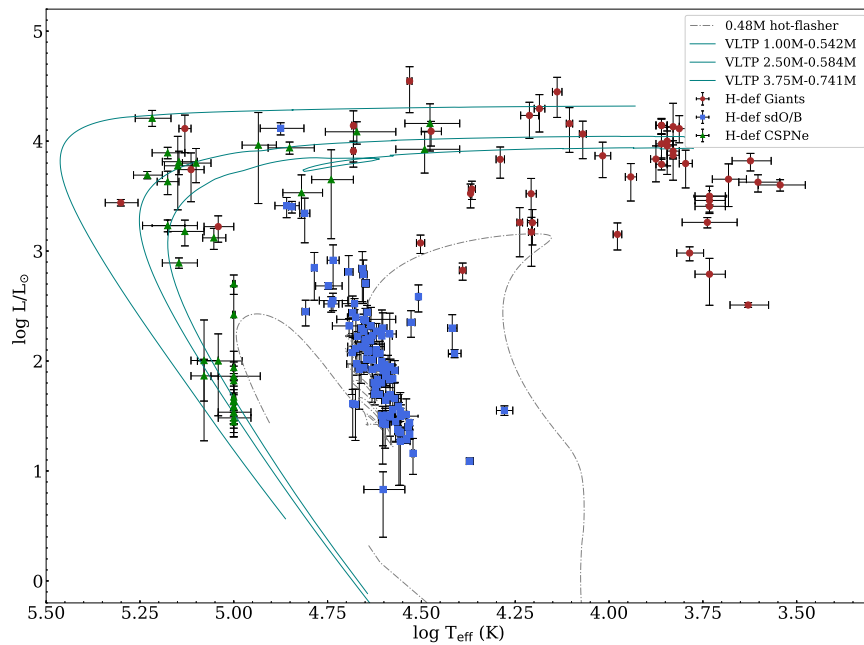


**Figure 8.5:** The hydrogen deficient HR diagram with the evolution tracks for the hot-flashers, and late thermal pulses.

# A

# Radial velocity curves for BX Cir

Presented here are radial velocity curves for the 72 lines measured in Chapter 4.
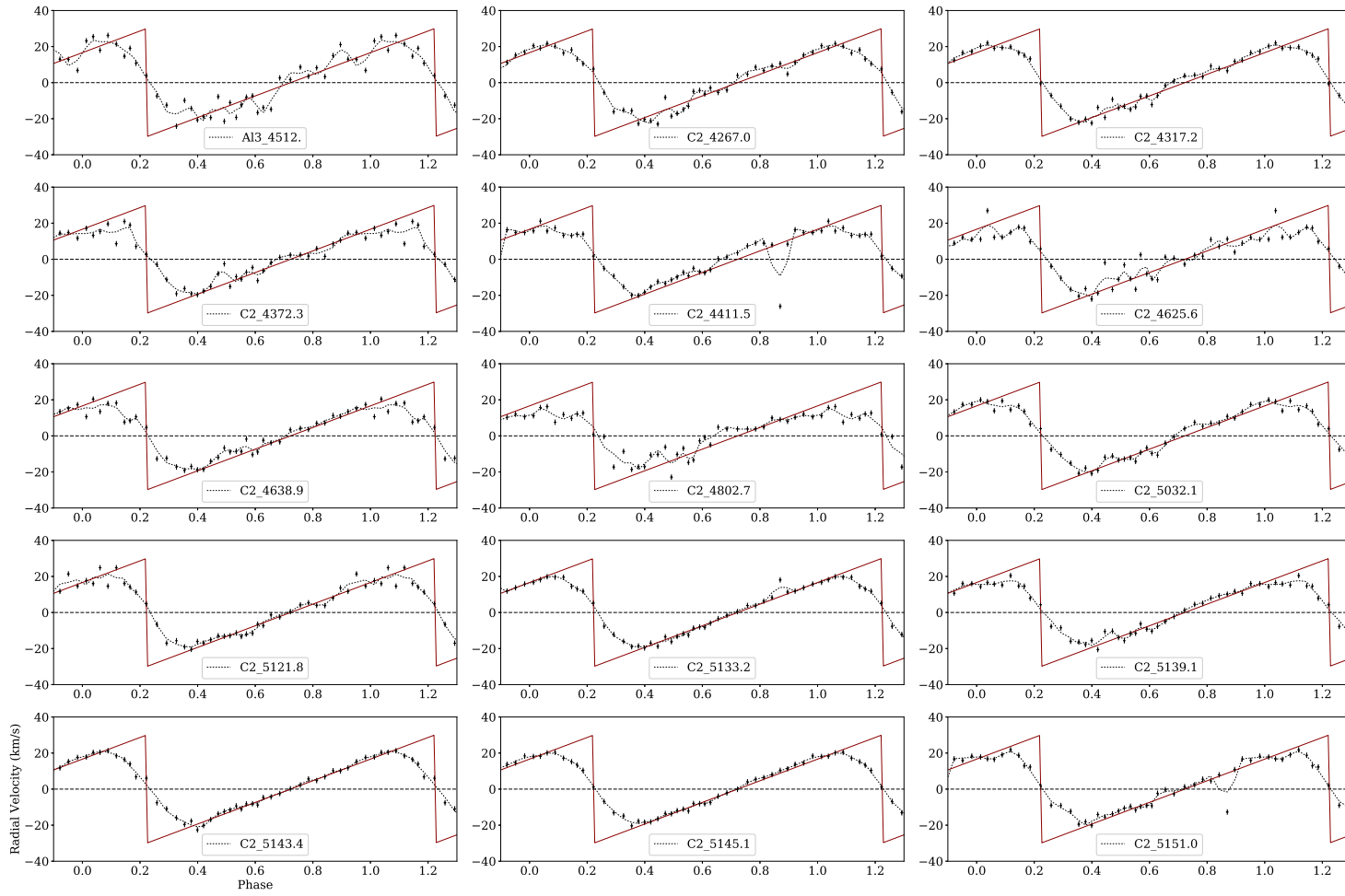
**Figure A.1:** Radial velocity curves for spectral lines in BX Cir
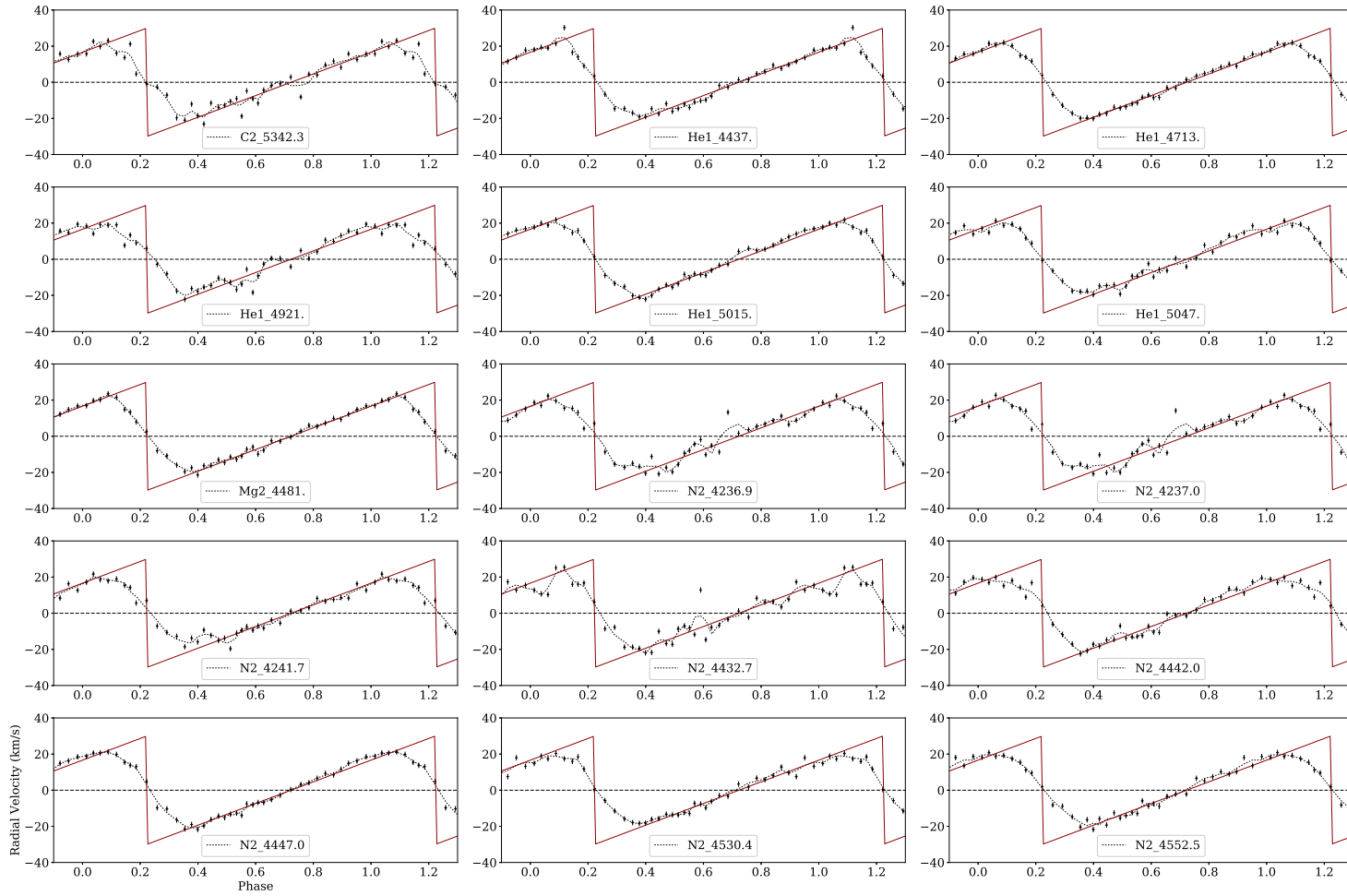
**Figure A.2:** Radial velocity curves cont.
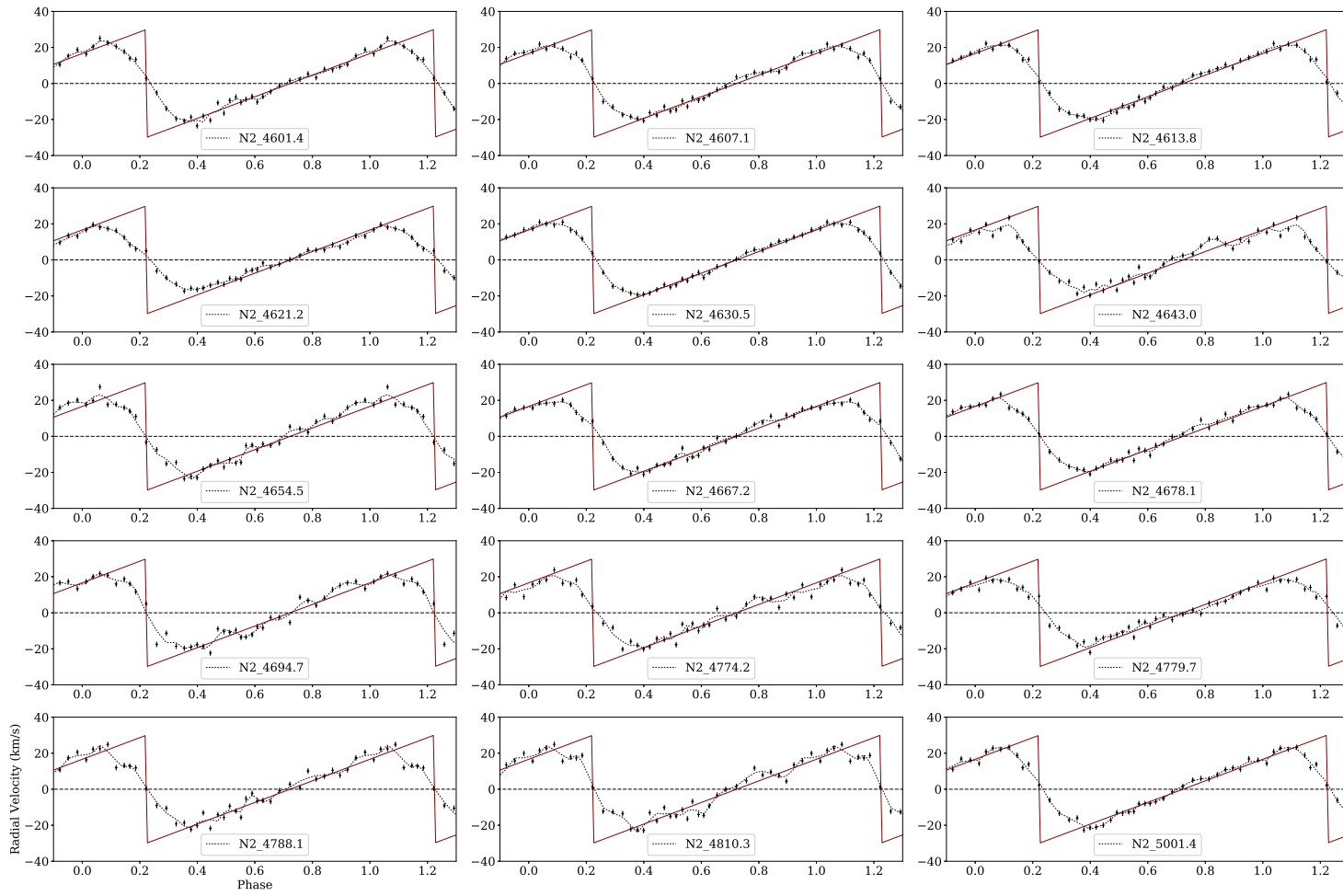
**Figure A.3:** Radial velocity curves cont.
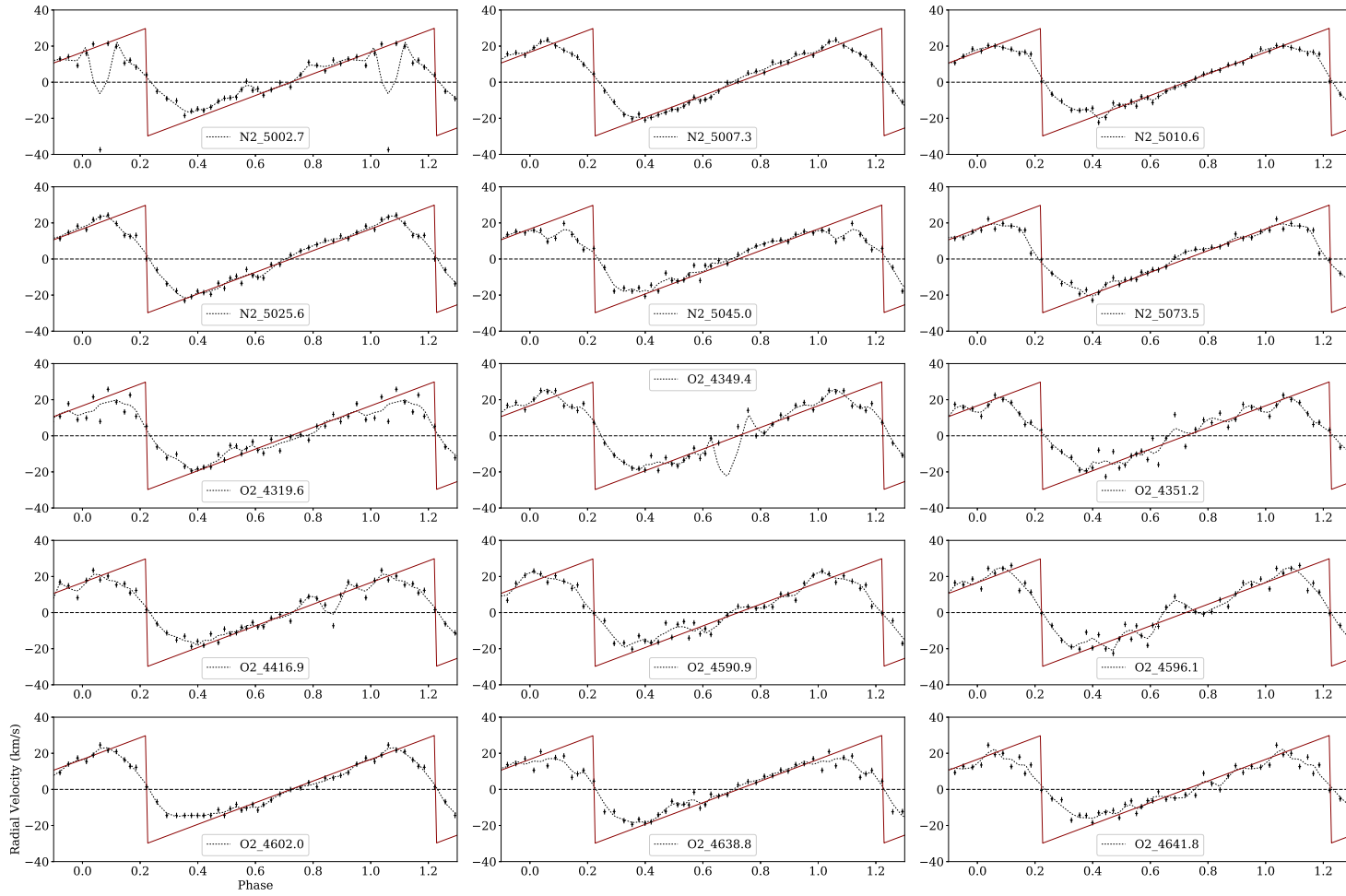
**Figure A.4:** Radial velocity curves cont.
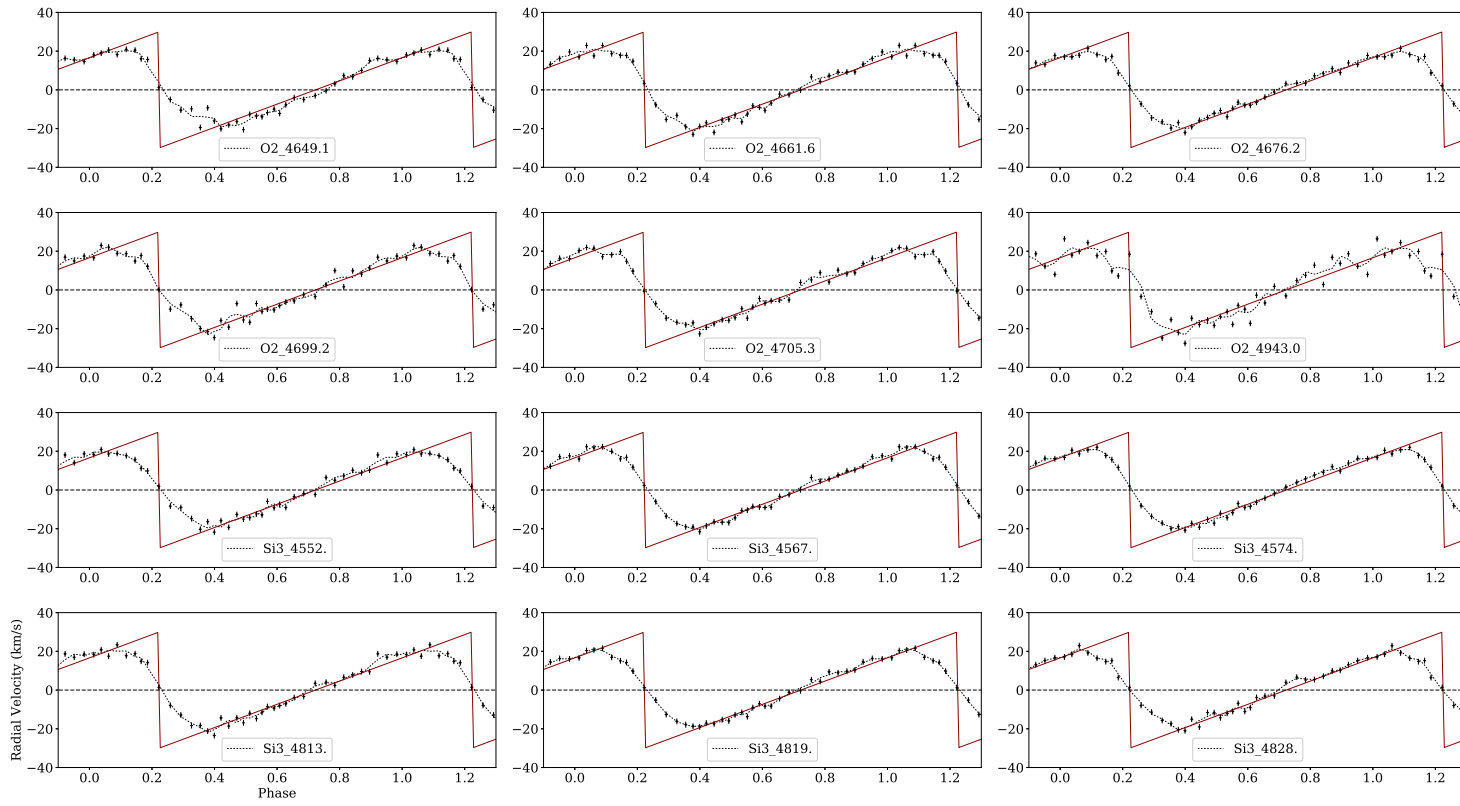
**Figure A.5:** Radial velocity curves cont.

# Kinematics Input and Outputs

B

The input data, including radial velocities, proper motions and inferred distances for each of the three subdwarf groups discussed in Chapter 5 are presented in Tables B.1 – B.3. The orbital parameters, space motions, and inferred population are presented in Tables B.4 – B.6. The table contents are described fully in the text.

# B. KINEMATICS INPUT AND OUTPUTS

**Table B.1:** Input data for the intermediate helium-rich stars. [2] highlights confirmed binary systems in which case the system velocity $\gamma$ is quoted. * corresponds to single epoch radial velocity measurements. [3] marks distances obtained from Astraatmadja and Bailer-Jones (2016).

| Star | RV km s$^{-1}$ | $\pm$ | ref | $\mu_\alpha$ mas yr$^{-1}$ | $\pm$ | $\mu_\delta$ mas yr$^{-1}$ | $\pm$ | ref | $M_B$ | $d$ kpc | $\pm$ |
|---|---|---|---|---|---|---|---|---|---|---|---|
| UVO 0512−08 | 11.0 | 3.3 | a | −28.5 | 1.3 | −24.0 | 2.9 | PPMXL | ... | 0.22 | 0.03 |
| BPS CS 22946−0005 | −57 | 10 | b | 3.2 | 4.1 | −3.5 | 4.1 | PPMXL | ... | 1.30 | 0.21 |
| BPS CS 22956−0094 | −21 | 10 | b, t | 37.3 | 2.8 | −27.5 | 2.8 | NOMAD | ... | 0.59 | 0.09 |
| CPD−20°1123[2] | −6.3 | 1.2 | c | 6.6 | 1.7 | −14.8 | 3.6 | NOMAD | ... | 0.29 | 0.05 |
| HD 127493 | 7 | 3 | de | −32.9 | 1.3 | −16.6 | 1.2 | PPMXL | ... | 0.11 | 0.02 |
| HE 1135−1134 | 24.67 | 2.45 | t | −9.4 | 6.0 | 2.3 | 6.0 | PPMXL | 3.88f | 2.15 | 0.30 |
| HE 1136-2504 | 59.39 | 9.22 | t | −5.1 | 3.0 | −6.6 | 2.8 | NOMAD | 4.25f | 0.89 | 0.12 |
| HE 1238-1745 | −7.87 | 2.72 | t | 12.4 | 5.0 | 3.1 | 5.0 | PPMXL | 3.83f | 1.33 | 0.18 |
| HE 1256-2738 | 140.46 | 5.6 | t | −11.3 | 6.6 | −10.6 | 6.6 | PPMXL | 4.04f | 3.16 | 0.49 |
| HE 1310−2733 | 41.54 | 1.82 | t | −6.5 | 4.6 | 0.6 | 4.6 | NOMAD | 3.76f | 1.39 | 0.19 |
| HE 2218−2026 | −278.86 | 1.45 | t | 20 | 4 | −4 | 1 | NOMAD | 4.40f | 2.50 | 0.35 |
| HE 2357−3940 | −18.38 | 14.15 | g | 15.8 | 1.2 | 3.7 | 1.2 | NOMAD | ... | 0.15 | 0.02 |
| HE 2359-2844 | −90.71 | 3.03 | t | 2 | 3 | −12 | 3 | NOMAD | 3.85f | 2.42 | 0.33 |
| HS 1051+2933 | −130 | 3 | h | 14 | 3 | −16 | 3 | NOMAD | 4.70h | 1.96 | 0.27 |
| JL 87 | −6.1 | 2.3 | i | −0.4 | 1.06 | 3.77 | 1.49 | GAIA | ... | 0.58 | 0.14[3] |
| LS IV−14°116 | −150 | 2 | j | 9.2 | 1.8 | −130.6 | 1.8 | PPMXL | ... | 0.44 | 0.20 |
| PG 0229+064 | 7.6 | 4.0 | k | −16.0 | 1.9 | −2.0 | 1.9 | PPMXL | ... | 0.33 | 0.05 |
| PG 0240+046 | 63.4 | 2.0 | k | 28.4 | 2.7 | −5.4 | 2.6 | PPMXL | ... | 0.77 | 0.12 |
| PG 0909+276 | 20.0 | 2 | h | 0.5 | 1.0 | 0.1 | 0.9 | NOMAD | ... | 0.87 | 0.14 |
| SB 705 | 4 | 12 | a | 10.36 | 0.53 | 9.84 | 0.61 | GAIA | ... | 0.67 | 0.16[3] |
| TON 107 | 28.5 | 2.8 | l | −2 | 6 | −14 | 5 | NOMAD | ... | 2.08 | 0.34 |
| UVO 0825+15 | 56.4* | 0.5 | t | −23.7 | 1.2 | −0.2 | 1.2 | NOMAD | ... | 0.33 | 0.05 |
| SDSSJ092440.11 +305013.16 | 2.7* | 0.5 | t | 0.2 | 4.5 | −10.4 | 4.5 | PPMXL | ... | 1.01 | 0.16 |
| SDSSJ160131.30 +044027.00 | -26.7* | 0.9 | t | −14.8 | 4.3 | 0.2 | 4.3 | PPMXL | ... | 0.89 | 0.14 |
| SDSSJ175137.44 +371952.37 | -73.6* | 0.2 | t | −9.3 | 4.2 | 0.5 | 4.2 | PPMXL | ... | 1.32 | 0.21 |
| SDSSJ175548.50 +501210.77 | -62.7* | 0.2 | t | −9.9 | 1.6 | 25.2 | 1.6 | PPMXL | ... | 0.42 | 0.07 |
| HS 1000+471 | 0* | 10 | t | −1.5 | 5.6 | −5.8 | 5.6 | PPMXL | ... | 4.14 | 0.65 |

*a*. Kilkenny and Muller (1989), *b*. Beers et al. (1992), *c*. Naslim et al. (2012), *d*. Bobylev et al. (2007), *e*. Kharchenko et al. (2007a), *f*. Stroeer et al. (2007), *g*. Kordopatis et al. (2013), *h*. Edelmann (2003), *i*. Ahmad et al. (2007), *j*. Randall et al. (2015), *k*. Aznar Cuadrado and Jeffery (2002), *l*. Luo et al. (2015), *t*. This paper: Table 1

**Table B.2:** Input data for the extreme helium–rich stars. Symbols as in A.6.

| Star | RV km s$^{-1}$ | $\pm$ | ref | $\mu_\alpha$ mas yr$^{-1}$ | $\pm$ | $\mu_\delta$ mas yr$^{-1}$ | $\pm$ | ref | $M_B$ | $d$ kpc | $\pm$ |
|---|---|---|---|---|---|---|---|---|---|---|---|
| BPS CS 22940−0009 | 37 | 10 | a, t | 2.8 | 5.2 | −14.4 | 5.2 | NOMAD | ... | 0.77 | 0.12 |
| BPS CS 29496−0010 | −39.8 | 0.1 | t | −19.0 | 4.3 | −1.2 | 4.3 | PPMXL | ... | 1.11 | 0.17 |
| HE 0001−2443 | 3.98 | 0.71 | t | 6 | 2 | −26 | 3 | NOMAD | 4.62i | 0.66 | 0.1 |
| HE 0342-1702 | −15* | 10 | a | −3.0 | 5.6 | −8.8 | 5.6 | PPMXL | ... | 0.73 | 0.10 |
| HE 1251+0159 | 3* | 24 | b | 8 | 2 | −18 | 3 | NOMAD | 4.47i | 1.55 | 0.22 |
| LB 3229 | 24 | 28 | c, t | 16.2 | 5.2 | −4.4 | 5.3 | NOMAD | ... | 0.66 | 0.10 |
| PG 0039+135 | −92* | 66 | d | −2.6 | 4.9 | 1.8 | 5.4 | NOMAD | ... | 0.33 | 0.05 |
| PG 1413+114 | 23.2 | 17 | e | −1.4 | 4.6 | −16.8 | 4.6 | PPMXL | ... | 1.99 | 0.31 |
| PG 1536+690 | −295 | 15 | f | 0 | 2 | −20 | 4 | NOMAD | ... | 0.96 | 0.15 |
| PG 2321+214 | −19.7* | 3 | t | 23.9 | 4.6 | −8.9 | 4.9 | NOMAD | ... | 0.49 | 0.08 |
| PG 2352+181 | −49* | 38 | d | 26.3 | 4.9 | −3.4 | 5.2 | NOMAD | ... | 0.38 | 0.06 |
| PG 0902+057 | −15* | 5 | t | −15.4 | 4.4 | −6.3 | 4.4 | PPMXL | ... | 0.93 | 0.15 |
| PG 1615+413 | −80* | 5 | t | −6.9 | 5.6 | −13.5 | 5.6 | PPMXL | ... | 2.88 | 0.45 |
| PG 1600+171 | −78* | 5 | t | −10.5 | 5.2 | −4.9 | 5.2 | PPMXL | ... | 3.14 | 0.47 |
| PG 1658+273 | −33* | 5 | t | −19.2 | 4.4 | −0.7 | 4.4 | PPMXL | ... | 2.33 | 0.37 |
| PG 1715+273 | 31* | 5 | t | −2.0 | 3 | −6.0 | 1 | NOMAD | ... | 2.91 | 0.46 |
| HS 1844+637 | 20* | 10 | t | −5.0 | 5.6 | 1.3 | 5.6 | PPMXL | ... | 2.7 | 0.42 |
| PG 1554+408 | 73* | 8 | t | −5.1 | 5.4 | −3.3 | 5.4 | PPMXL | ... | 2.34 | 0.37 |
| PG 2258+155 | 34* | 5 | t | 0.6 | 5.3 | −5.6 | 5.3 | PPMXL | ... | 1.65 | 0.26 |
| PG 1127+019 | 19* | 2 | t | −7.1 | 4.1 | −9.2 | 4.1 | PPMXL | ... | 0.62 | 0.01 |
| PG 1415+492 | 54* | 1 | t | −1.3 | 4 | −3.8 | 4 | PPMXL | ... | 1.17 | 0.18 |
| PG 2215+151 | −13* | 5 | t | 3.1 | 5.5 | 15.1 | 5.1 | NOMAD | ... | 0.96 | 0.15 |
| PG 1544+488[2] | −25.5 | 0.4 | t | −44 | 3 | 34 | 1 | NOMAD | ... | 0.55 | 0.09 |

*a*. Beers et al. (1992), *t*. This paper: Table 1, *b*. Adelman-McCarthy et al. (2008), *c*. Kilkenny and Muller (1989), *d*. Brown et al. (2008), *e*. Geier et al. (2015), *f*. Heber et al. (1996), *i*. Stroeer et al. (2007)

**Table B.3:** Input data for the helium–deficient stars. Symbols as in A.6 and A.7.

| Star | RV<br>km s$^{-1}$ | ± | ref | $\mu_\alpha$<br>mas yr$^{-1}$ | ± | $\mu_\delta$<br>mas yr$^{-1}$ | ± | ref | $M_{\rm B}$ | $d$<br>kpc | ± |
|---|---|---|---|---|---|---|---|---|---|---|---|
| CD −35°15910 | 25.7* | 2.8 | a | −21.4 | 1.8 | −6.2 | 1.5 | PPMXL | ... | 0.22 | 0.06 |
| Feige 65 | 53.5* | 2 | c | 4.1 | 1.3 | −11.9 | 1.3 | PPMXL | ... | 0.35 | 0.09 |
| HD 205805 | −71.0* | 4 | c | 76.7 | 1.1 | −10.2 | 0.8 | PPMXL | ... | 0.15 | 0.04 |
| HD 4539 | −4* | 2 | c | 5.09 | 1.50 | 25.19 | 1.00 | PPMXL | ... | 0.15 | 0.04 |
| HE 0004−2737 | 31.56§ | 28.91 | b | 17.5 | 3.0 | −11.5 | 2.8 | NOMAD | 4.8c | 0.62 | 0.09 |
| HE 0151−3919 | −48* | 15 | e | −9.2 | 9.4 | −41.4 | 9.4 | PPMXL | ... | 1.07 | 0.27 |
| HE 0407−1956 | 59* | 30 | d | 8.5 | 4.1 | 2.1 | 4.1 | PPMXL | 3.8c | 0.86 | 0.12 |
| HE 1318−2111[2] | 48.9 | 0.7 | f | 2.7 | 12.3 | −1.1 | 12.3 | NOMAD | 3.3c | 2.04 | 0.28 |
| HE 2135−3749[2] | 45.0 | 0.5 | i | 17.1 | 9.8 | −1.2 | 9.8 | PPMXL | 4.7c | 0.66 | 0.10 |
| HE 2337−2944 | 7 | 10 | d | 19.9 | 4.3 | −7.3 | 4.3 | PPMXL | 4.5c | 0.90 | 0.13 |
| HS 0232+3155 | −11* | 30 | c | 2.8 | 4.3 | −1.9 | 4.3 | PPMXL | 4.1c | 1.95 | 0.27 |
| HS 0233+3037 | −129 * | 30 | c | 8.2 | 4.3 | −11.4 | 4.3 | PPMXL | 4.3c | 1.23 | 0.17 |
| HS 0546+8009 | 7* | 30 | c | 6.5 | 4.1 | 1.2 | 4.1 | PPMXL | 4.1c | 1.10 | 0.15 |
| HS 0815+4243 | 41* | 30 | c | 4.2 | 5.4 | −5.2 | 5.4 | PPMXL | 4.6c | 2.60 | 0.35 |
| HS 1236+4754 | −46.6 | 1.1 | g | −14 | 1 | 2 | 6 | NOMAD | 4.1c | 1.99 | 0.27 |
| HS 1320+2622 | −110 * | 30 | c | −8.7 | 4.7 | −1.2 | 4.7 | PPMXL | 4.1c | 3.14 | 0.43 |
| HS 1739+5244 | −28* | 30 | c | −2 | 2 | −6 | 1 | NOMAD | 3.5c | 1.76 | 0.24 |
| HS 1741+2133 | −84* | 30 | c | −13.2 | 5.1 | −5.2 | 5.1 | PPMXL | 3.1c | 1.95 | 0.27 |
| HS 2156+2215 | −22* | 30 | c | −2.5 | 4.6 | −2.3 | 4.6 | NOMAD | 3.0c | 3.05 | 0.42 |
| HS 2201+2610 | −31* | 30 | c | −0.7 | 4.1 | −6.1 | 4.1 | PPMXL | 4.0c | 0.95 | 0.13 |
| HS 2208+2718 | 124* | 30 | c | 4.3 | 4.8 | −7.2 | 4.8 | PPMXL | 3.9c | 1.28 | 0.18 |
| HS 2242+3206 | −168* | 30 | c | 28.2 | 3.3 | 6.9 | 3.3 | PPMXL | 4.3c | 1.48 | 0.20 |
| KPD 0054+5406 | −35.5 | 5.0 | h | −2.0 | 0.4 | −0.4 | 0.4 | PPMXL | ... | 0.57 | 0.14 |
| KPD 2040+3955[2] | −16.4 | 1.0 | b | −8.9 | 5.6 | −10.2 | 5.6 | NOMAD | ... | 1.03 | 0.26 |
| KPD 2215+5037[2] | −7.2 | 1.0 | b | 16 | 12 | 18 | 4 | NOMAD | ... | 0.48 | 0.12 |
| KUV 16256+4034[2] | −90.9 | 0.9 | f | −19.3 | 0.8 | −13.2 | 0.6 | NOMAD | ... | 0.48 | 0.12 |
| PG 0004+133 | −1.88 | 3.9 | b | −0.5 | 5.0 | −20.7 | 5.2 | NOMAD | ... | 0.47 | 0.12 |
| PG 0005+179 | −15.99§ | 32.94 | b | 19.2 | 5.0 | −2.0 | 5.3 | NOMAD | ... | 0.83 | 0.21 |
| PG 0919+273[2] | −68.6 | 0.6 | b | 23.1 | 0.7 | −25.5 | 1.2 | NOMAD | ... | 0.44 | 0.11 |
| PG 0934+186[2] | 7.7 | 3.2 | b | −20.7 | 4.4 | −6.2 | 4.7 | NOMAD | ... | 0.55 | 0.14 |
| PG 1136-003[2] | 63 | 14 | f | −6.4 | 5.5 | −20.7 | 5.5 | NOMAD | ... | 0.87 | 0.23 |
| PG 1230+052[2] | 43.1 | 0.7 | b | −3.2 | 5.8 | −20.2 | 6.4 | NOMAD | ... | 0.69 | 0.17 |
| PG 1244+113[2] | 7.4 | 0.8 | b | 0.0 | 4.9 | −8.5 | 5.3 | NOMAD | ... | 0.34 | 0.09 |
| PG 1403+316[2] | −2.1 | 0.9 | b | −34.3 | 2.1 | 4.5 | 2.1 | NOMAD | ... | 0.98 | 0.25 |
| PG 1519+640[2] | 0.9 | 0.8 | b | 28.1 | 2.3 | 41.2 | 2.5 | NOMAD | ... | 0.39 | 0.10 |
| PG 1558-007[2] | −71.9 | 0.7 | b | −4.4 | 5.6 | −7.9 | 5.5 | NOMAD | ... | 0.99 | 0.25 |
| PG 1648+536[2] | −69.9 | 0.9 | f | −3.8 | 4.2 | 0.1 | 4.2 | PPMXL | ... | 1.19 | 0.30 |
| PG 2331+038[2] | −9.5 | 1.1 | b | −9.2 | 4.6 | 6.5 | 4.7 | PPMXL | ... | 0.84 | 0.21 |
| PHL 932 | 18 | 2 | c | 36.1 | 2.9 | 7 | 2 | NOMAD | ... | 0.35 | 0.09 |

*a*. Gontcharov (2006), *b*. Copperwheat et al. (2011), *c*. Edelmann (2003), *d*. Beers et al. (1992), *e*. Beers et al. (2001), *f*. Geier et al. (2015), *g*. Sperauskas and Bartkevicius (2002), *h*. Downes (1986), *i*. Karl et al. (2006) [0]

**Table B.4:** Orbital parameters, galactic velocities and 1–$\sigma$ errors for the intermediate helium–rich stars. The last column shows the Galactic population in which each star has been classified. TH = thin disk, TK = thick disk and H = halo.

| Star | $R_a$ kpc | $\pm$ | $R_p$ kpc | $\pm$ | $z_{max}$ kpc | $\pm$ | $e$ | $\pm$ | $J_z$ kpc km s$^{-1}$ | $\pm$ | $z_n$ | $\pm$ | $U$ km s$^{-1}$ | $\pm$ | $V$ km s$^{-1}$ | $\pm$ | $W$ km s$^{-1}$ | $\pm$ | pop |
|---|---|---|---|---|---|---|---|---|---|---|---|---|---|---|---|---|---|---|---|
| UVO 0512−08 | 9.22 | 0.20 | 8.03 | 0.12 | 0.54 | 0.12 | 0.07 | 0.01 | 2059.50 | 23.50 | 0.07 | 0.01 | −23.9 | 3.82 | 248.53 | 18.42 | −31.29 | 3.36 | TH |
| BPS CS 22946−0005 | 8.93 | 0.59 | 7.42 | 1.53 | 2.04 | 0.29 | 0.09 | 0.10 | 1853.26 | 219.21 | 0.27 | 0.07 | −13.06 | 23.90 | 224.38 | 20.36 | 63.67 | 3.61 | TK |
| BPS CS 22956−0094 | 9.11 | 0.28 | 3.85 | 0.57 | 0.43 | 0.08 | 0.41 | 0.07 | 1361.16 | 128.91 | 0.05 | 0.01 | 87.27 | 11.08 | 178.99 | 9.73 | -4.03 | 3.07 | TK |
| CPD−20°1123 | 9.47 | 0.09 | 7.48 | 0.26 | 0.16 | 0.04 | 0.12 | 0.02 | 2024.59 | 31.41 | 0.02 | 0.00 | −36.57 | 4.64 | 242.33 | 17.12 | 9.83 | 2.22 | TH |
| HD 127493 | 8.36 | 0.04 | 7.14 | 0.22 | 0.18 | 0.02 | 0.08 | 0.01 | 1878.41 | 30.77 | 0.02 | 0.00 | −7.92 | 2.76 | 234.80 | 18.07 | 11.27 | 3.85 | TH |
| HE 1135−1134 | 9.38 | 2.19 | 6.67 | 2.14 | 1.75 | 0.52 | 0.17 | 0.17 | 1820.26 | 376.82 | 0.20 | 0.10 | 43.25 | 47.84 | 226.41 | 27.68 | 12.20 | 9.35 | TK |
| HE 1136−2504 | 8.42 | 0.11 | 4.50 | 0.46 | 0.60 | 0.09 | 0.30 | 0.05 | 1450.76 | 89.45 | 0.09 | 0.01 | −30.86 | 11.37 | 183.83 | 18.69 | 13.59 | 4.94 | TH |
| HE 1238−1745 | 16.25 | 4.18 | 7.18 | 0.46 | 2.08 | 0.75 | 0.39 | 0.12 | 2353.45 | 192.97 | 0.17 | 0.09 | −99.14 | 32.01 | 301.97 | 17.78 | 19.34 | 7.72 | TK |
| HE 1256−2738 | 7.62 | 0.65 | 0.59 | 0.17 | 3.11 | 0.41 | 0.86 | 0.04 | −112.76 | 470.87 | 0.58 | 0.20 | 19.56 | 68.96 | −4.39 | 21.24 | −37.87 | 5.24 | H |
| HE 1310−2733 | 7.84 | 0.20 | 5.30 | 1.14 | 1.14 | 0.37 | 0.19 | 0.10 | 1516.45 | 172.76 | 0.20 | 0.07 | −19.49 | 25.31 | 204.22 | 23.06 | 37.22 | 3.34 | TH |
| HE 2218−2026 | 19.52 | 4.69 | 1.30 | 0.66 | 18.34 | 5.68 | 0.87 | 0.08 | 194.61 | 201.52 | 1.91 | 2.33 | 303.88 | 39.04 | 38.31 | 13.62 | 96.10 | 13.19 | H |
| HE 2357−3940 | 8.71 | 0.23 | 8.32 | 0.05 | 0.34 | 0.22 | 0.02 | 0.02 | 2049.08 | 14.24 | 0.04 | 0.03 | 4.24 | 3.79 | 253.41 | 20.50 | 22.22 | 8.09 | TH |
| HE 2359−2844 | 8.38 | 0.05 | 1.92 | 1.10 | 4.39 | 0.58 | 0.63 | 0.17 | 604.14 | 328.53 | 1.94 | 5.16 | −30.98 | 26.23 | 115.55 | 14.53 | 93.06 | 5.27 | TK |
| HS 1051+2933 | 19.33 | 3.26 | 3.33 | 0.86 | 3.76 | 0.54 | 0.71 | 0.08 | 1437.27 | 284.00 | 0.20 | 0.05 | −227.82 | 22.18 | 163.53 | 7.65 | −55.98 | 2.23 | H |
| JL 87 | 9.59 | 0.42 | 8.01 | 0.15 | 0.70 | 0.13 | 0.09 | 0.03 | 2084.43 | 35.84 | 0.08 | 0.02 | 28.63 | 10.31 | 257.23 | 20.95 | 3.86 | 6.08 | TH |
| LS IV−14°116 | 8.12 | 0.20 | 1.19 | 2.28 | 0.26 | 0.38 | 0.74 | 0.33 | −523.81 | 476.48 | 0.03 | 0.05 | 15.84 | 31.97 | −53.99 | 29.73 | −7.89 | 27.66 | H |
| PG 0229+064 | 10.69 | 0.41 | 8.40 | 0.06 | 0.31 | 0.07 | 0.12 | 0.02 | 2248.48 | 36.62 | 0.04 | 0.01 | −23.61 | 3.10 | 270.10 | 19.24 | −7.01 | 3.13 | TH |
| PG 0240+046 | 10.18 | 0.28 | 4.36 | 0.62 | 0.61 | 0.09 | 0.40 | 0.07 | 1524.02 | 134.50 | 0.06 | 0.01 | 88.99 | 16.76 | 181.23 | 12.97 | −8.31 | 3.28 | TK |
| PG 0909+276 | 9.36 | 0.35 | 9.00 | 0.10 | 0.80 | 0.12 | 0.02 | 0.02 | 2172.43 | 40.45 | 0.09 | 0.01 | −4.36 | 6.63 | 249.77 | 17.57 | 22.41 | 2.30 | TH |
| SB 705 | 10.52 | 0.98 | 7.87 | 0.26 | 0.39 | 0.07 | 0.14 | 0.06 | 2161.18 | 41.51 | 0.05 | 0.05 | −22.65 | 5.64 | 265.48 | 19.55 | 6.53 | 2.34 | TH |
| TON 107 | 9.28 | 0.69 | 3.54 | 1.92 | 3.32 | 1.86 | 0.45 | 0.21 | 1125.47 | 481.73 | 0.36 | 0.20 | −47.73 | 40.41 | 139.93 | 11.34 | 72.51 | 2.43 | TK |
| UVO 0825 + 15 | 14.93 | 0.58 | 8.44 | 0.01 | 0.86 | 0.06 | 0.28 | 0.02 | 2543.88 | 35.38 | 0.09 | 0.01 | −19.81 | 2.30 | 307.23 | 19.44 | −31.7 | 2.46 | TK |
| SDSS J092440.11 +305013.16 | 9.22 | 0.19 | 6.11 | 1.27 | 0.75 | 0.12 | 0.20 | 0.10 | 1783.13 | 199.25 | 0.09 | 0.02 | −20.87 | 17.95 | 205.01 | 17.50 | 4.70 | 2.31 | TH |
| SDSS J160131.30 +044027.00 | 8.10 | 0.26 | 5.21 | 0.81 | 0.81 | 0.21 | 0.22 | 0.07 | 1546.31 | 154.44 | 0.10 | 0.03 | 38.65 | 12.31 | 208.68 | 24.01 | 30.77 | 2.90 | TH |
| SDSS J175137.44 +371952.37 | 8.18 | 0.27 | 3.56 | 0.47 | 0.76 | 0.32 | 0.39 | 0.05 | 1229.67 | 127.13 | 0.10 | 0.04 | 43.05 | 17.60 | 163.55 | 25.19 | 23.15 | 4.71 | TK |
| SDSS J175548.50 +501210.77 | 8.91 | 0.18 | 4.83 | 0.17 | 0.24 | 0.03 | 0.30 | 0.02 | 1561.31 | 28.15 | 0.03 | 0.00 | 58.29 | 3.29 | 196.40 | 22.87 | −0.59 | 3.23 | TH |
| HS 1000+471 | 15.24 | 9.04 | 10.75 | 2.11 | 5.01 | 6.46 | 0.17 | 0.20 | 2672.06 | 956.10 | 0.37 | 0.58 | 13.11 | 85.32 | 138.81 | 12.14 | 7.36 | 11.62 | TK |

**Table B.5:** Orbital parameters and galactic velocities for the extreme helium–rich stars.

| Star | $R_a$ kpc | $\pm$ | $R_p$ kpc | $\pm$ | $z_{max}$ kpc | $\pm$ | $e$ | $\pm$ | $J_z$ kpc km s$^{-1}$ | $\pm$ | $z_n$ | $\pm$ | $U$ km s$^{-1}$ | $\pm$ | $V$ km s$^{-1}$ | $\pm$ | $W$ km s$^{-1}$ | $\pm$ | pop |
|---|---|---|---|---|---|---|---|---|---|---|---|---|---|---|---|---|---|---|---|
| BPS CS 22940−0009 | 7.90 | 0.15 | 4.68 | 0.85 | 0.53 | 0.19 | 0.26 | 0.08 | 1452.08 | 160.86 | 0.08 | 0.03 | -21.95 | 17.29 | 194.19 | 16.63 | -17.91 | 4.52 | TH |
| BPS CS 29496−0010 | 14.87 | 3.14 | 7.17 | 0.46 | 3.03 | 1.01 | 0.35 | 0.09 | 2233.39 | 184.77 | 0.21 | 0.09 | −84.03 | 12.11 | 282.43 | 26.78 | 75.28 | 2.78 | H |
| HE 0001−2443 | 8.46 | 0.06 | 4.16 | 0.58 | 0.65 | 0.10 | 0.34 | 0.06 | 1383.07 | 125.65 | 0.10 | 0.02 | −22.14 | 4.40 | 210.48 | 14.34 | −1.11 | 3.63 | TH |
| HE 0342−1702 | 10.26 | 0.93 | 7.48 | 0.85 | 0.59 | 0.10 | 0.16 | 0.05 | 2077.65 | 165.70 | 0.08 | 0.01 | −50.94 | 16.11 | 243.34 | 21.08 | 4.94 | 4.29 | TH |
| HE 1251+0159 | 11.10 | 0.92 | 3.72 | 0.72 | 2.09 | 0.62 | 0.50 | 0.09 | 1350.89 | 197.91 | 0.22 | 0.09 | −137.71 | 15.89 | 175.63 | 17.17 | −46.38 | 11.58 | TK |
| LB 3229 | 8.38 | 0.07 | 5.51 | 0.99 | 0.57 | 0.10 | 0.21 | 0.09 | 1630.99 | 168.18 | 0.07 | 0.01 | 9.08 | 18.79 | 204.59 | 23.30 | 1.14 | 12.97 | TH |
| PG 0039+135 | 8.97 | 0.24 | 6.10 | 1.36 | 1.89 | 0.95 | 0.19 | 0.12 | 1687.63 | 321.38 | 0.29 | 0.15 | −37.5 | 9.78 | 206.38 | 35.29 | 78.71 | 29.10 | TK |
| PG 1413+114 | 8.80 | 0.90 | 2.33 | 1.17 | 2.03 | 0.36 | 0.58 | 0.16 | 873.22 | 368.26 | 0.26 | 0.07 | −103.25 | 31.16 | 125.49 | 16.15 | −12.69 | 7.93 | TK |
| PG 1536+690 | 11.54 | 0.71 | 0.99 | 1.04 | 9.76 | 1.48 | 0.84 | 0.15 | 222.93 | 108.13 | 1.29 | 1.05 | −141.57 | 13.37 | 33.63 | 25.86 | −148 | 4.64 | H |
| PG 2321+214 | 8.74 | 0.19 | 5.59 | 0.46 | 0.35 | 0.14 | 0.22 | 0.04 | 1680.81 | 75.47 | 0.04 | 0.02 | 34.74 | 12.73 | 207.73 | 14.91 | −14.52 | 4.34 | TH |
| PG 2352+181 | 8.59 | 0.15 | 5.10 | 1.22 | 0.49 | 0.42 | 0.26 | 0.11 | 1579.87 | 236.22 | 0.06 | 0.05 | 25.36 | 12.19 | 195.09 | 24.67 | 25.45 | 14.90 | TH |
| PG 0902+057 | 9.25 | 0.99 | 8.96 | 0.41 | 1.61 | 0.60 | 0.02 | 0.04 | 2103.74 | 147.58 | 0.18 | 0.07 | −3.01 | 12.49 | 243.27 | 22.74 | −62.28 | 2.23 | TK |
| PG1615+413 | 9.03 | 1.61 | 1.69 | 1.57 | 3.18 | 0.53 | 0.68 | 0.27 | 633.66 | 445.89 | 0.44 | 0.16 | −100.82 | 47.61 | 87.85 | 19.11 | 18.77 | 4.74 | TK |
| PG1600+171 | 7.25 | 0.81 | 1.36 | 1.15 | 2.39 | 0.51 | 0.68 | 0.23 | 386.13 | 484.78 | 0.36 | 0.10 | 61.00 | 51.03 | 68.97 | 27.47 | 32.72 | 8.36 | TK |
| PG1658+273 | 8.35 | 1.02 | 2.63 | 0.33 | 5.76 | 2.44 | 0.52 | 0.03 | 632.82 | 310.84 | 1.24 | 3.28 | 60.61 | 28.90 | 95.49 | 34.81 | 150.84 | 4.03 | TK |
| PG1715+273 | 7.66 | 0.57 | 6.30 | 0.85 | 1.78 | 0.33 | 0.10 | 0.05 | 1593.18 | 185.26 | 0.27 | 0.06 | −34.72 | 22.37 | 227.38 | 5.85 | 30.17 | 7.88 | TK |
| HS1844+637 | 11.36 | 1.70 | 7.40 | 2.29 | 2.61 | 2.36 | 0.21 | 0.20 | 2037.64 | 342.34 | 0.25 | 0.25 | 60.76 | 59.10 | 236.59 | 25.46 | 74.93 | 10.65 | TK |
| PG1554+408 | 10.03 | 2.88 | 7.89 | 0.90 | 3.77 | 0.81 | 0.12 | 0.16 | 1867.92 | 380.46 | 0.47 | 0.25 | 3.93 | 49.11 | 243.61 | 22.08 | 101.52 | 6.73 | TK |
| PG2258+155 | 9.76 | 1.77 | 8.40 | 0.60 | 1.62 | 0.47 | 0.07 | 0.09 | 2094.75 | 228.02 | 0.17 | 0.05 | 7.70 | 35.24 | 256.79 | 17.59 | −44.41 | 6.27 | TK |
| PG1127+019 | 8.51 | 0.08 | 6.22 | 0.60 | 0.56 | 0.03 | 0.15 | 0.05 | 1751.48 | 87.32 | 0.07 | 0.01 | −12.56 | 10.43 | 215.77 | 18.88 | 5.11 | 2.29 | TH |
| PG1415+492 | 10.56 | 1.65 | 8.48 | 0.06 | 2.24 | 0.20 | 0.11 | 0.08 | 2142.10 | 167.49 | 0.21 | 0.04 | −3.01 | 20.76 | 261.89 | 18.19 | 64.48 | 4.48 | TK |
| PG2215+151 | 12.30 | 2.04 | 7.51 | 0.50 | 1.58 | 0.79 | 0.24 | 0.09 | 2192.41 | 117.95 | 0.13 | 0.07 | −233.78 | 12.14 | 215.86 | 20.93 | 31.20 | 16.51 | TK |
| PG1544+488 | 11.23 | 0.80 | 4.34 | 0.45 | 1.05 | 0.32 | 0.44 | 0.07 | 1554.39 | 81.96 | 0.09 | 0.03 | 33.56 | 14.72 | 259.72 | 20.51 | −24.84 | 6.21 | TK |

**Table B.6:** Orbital parameters and galactic velocities for the helium–deficient stars.

| Star | $R_\mathrm{a}$ kpc | $\pm$ | $R_\mathrm{p}$ kpc | $\pm$ | $z_\mathrm{max}$ kpc | $\pm$ | $e$ | $\pm$ | $J_z$ kpc km s$^{-1}$ | $\pm$ | $z_\mathrm{n}$ | $\pm$ | $U$ km s$^{-1}$ | $\pm$ | $V$ km s$^{-1}$ | $\pm$ | $W$ km s$^{-1}$ | $\pm$ | pop |
|---|---|---|---|---|---|---|---|---|---|---|---|---|---|---|---|---|---|---|---|
| CD −35°15910 | 9.87 | 0.26 | 7.66 | 0.13 | 0.29 | 0.05 | 0.13 | 0.02 | 2080.52 | 13.91 | 0.04 | 0.01 | −32.24 | 2.57 | 265.86 | 18.34 | −16.22 | 4.28 | TH |
| Feige 65 | 9.40 | 0.20 | 8.37 | 0.06 | 1.50 | 0.12 | 0.06 | 0.01 | 2061.68 | 29.80 | 0.17 | 0.01 | −14.71 | 5.48 | 252.57 | 15.06 | 64.24 | 3.82 | TH |
| HD 205805 | 10.75 | 0.25 | 6.64 | 0.32 | 0.44 | 0.18 | 0.24 | 0.03 | 1994.73 | 31.93 | 0.05 | 0.02 | 76.20 | 5.68 | 243.01 | 14.31 | 24.66 | 2.13 | TH |
| HD 4539 | 9.51 | 0.30 | 8.45 | 0.01 | 0.33 | 0.07 | 0.06 | 0.02 | 2145.20 | 27.70 | 0.04 | 0.01 | 0.85 | 4.73 | 262.19 | 19.06 | 21.12 | 2.22 | TH |
| HE 0004−2737 | 8.40 | 0.08 | 5.54 | 0.64 | 0.88 | 0.37 | 0.20 | 0.06 | 1620.18 | 98.79 | 0.11 | 0.05 | 18.14 | 11.70 | 201.24 | 21.91 | −4.7 | 15.62 | TH |
| HE 0407−1956 | 9.29 | 0.44 | 6.40 | 1.13 | 0.61 | 0.20 | 0.18 | 0.09 | 1841.28 | 171.99 | 0.07 | 0.02 | 33.66 | 19.40 | 215.41 | 25.04 | −8.82 | 12.76 | TH |
| HE 1318−2111 | 9.53 | 5.60 | 5.38 | 2.70 | 2.01 | 1.90 | 0.28 | 0.29 | 1609.83 | 688.11 | 0.25 | 0.37 | −95.15 | 97.41 | 223.22 | 22.12 | 28.68 | 21.34 | TK |
| HE 2135−3749 | 8.46 | 2.28 | 7.95 | 0.29 | 1.36 | 0.59 | 0.03 | 0.13 | 1920.73 | 244.94 | 0.16 | 0.08 | −0.18 | 30.72 | 248.84 | 16.15 | −61.42 | 8.68 | TH |
| HE 2337−2944 | 8.69 | 0.36 | 4.76 | 0.86 | 0.97 | 0.18 | 0.29 | 0.08 | 1501.14 | 170.00 | 0.12 | 0.02 | 46.28 | 21.90 | 217.37 | 18.81 | −55.94 | 9.91 | TH |
| HS 0232+3155 | 10.09 | 0.58 | 7.93 | 2.85 | 0.86 | 0.19 | 0.12 | 0.18 | 2112.29 | 379.73 | 0.09 | 0.02 | 18.99 | 37.19 | 221.40 | 25.13 | 7.12 | 9.79 | TH |
| HS 0233+3037 | 10.08 | 0.53 | 2.83 | 0.82 | 0.88 | 0.76 | 0.56 | 0.10 | 1119.88 | 253.56 | 0.19 | 0.28 | −79.21 | 22.73 | 129.70 | 22.24 | 33.28 | 14.04 | TK |
| HS 0546+8009 | 9.46 | 1.78 | 8.93 | 0.90 | 1.02 | 0.61 | 0.03 | 0.09 | 2163.23 | 227.46 | 0.11 | 0.07 | 7.14 | 23.50 | 245.75 | 25.45 | 40.98 | 11.09 | TH |
| HS 0815+4243 | 10.73 | 1.58 | 6.74 | 4.45 | 2.81 | 1.66 | 0.23 | 0.36 | 1858.99 | 704.73 | 0.42 | 1.64 | 7.17 | 58.53 | 184.18 | 20.76 | 63.79 | 6.19 | TK |
| HS 1236+4754 | 11.11 | 2.20 | 4.98 | 1.76 | 3.61 | 1.83 | 0.38 | 0.09 | 1531.28 | 398.46 | 0.71 | 0.45 | 110.13 | 18.86 | 183.01 | 44.30 | −49.97 | 14.57 | TK |
| HS 1320+2622 | 9.61 | 1.99 | 5.12 | 2.98 | 5.83 | 1.91 | 0.31 | 0.26 | 1185.05 | 573.89 | 0.73 | 0.51 | 96.67 | 50.97 | 154.91 | 33.21 | −84.9 | 5.15 | TK |
| HS 1739+5244 | 8.44 | 0.12 | 6.54 | 1.55 | 0.97 | 0.14 | 0.13 | 0.11 | 1767.63 | 223.17 | 0.13 | 0.03 | −16.44 | 11.67 | 221.73 | 21.14 | 3.42 | 16.42 | TH |
| HS 1741+2133 | 7.42 | 0.36 | 1.91 | 1.31 | 1.55 | 0.81 | 0.59 | 0.23 | 712.46 | 296.68 | 0.63 | 1.67 | 26.96 | 30.78 | 106.93 | 33.56 | 60.31 | 10.77 | TK |
| HS 2156+2215 | 8.58 | 1.18 | 7.26 | 2.71 | 1.37 | 0.57 | 0.08 | 0.21 | 1848.99 | 331.22 | 0.17 | 0.08 | 21.09 | 52.93 | 230.76 | 25.79 | 16.04 | 4.57 | TH |
| HS 2201+2610 | 8.34 | 0.04 | 6.20 | 1.68 | 0.35 | 0.05 | 0.15 | 0.13 | 1743.14 | 237.88 | 0.04 | 0.01 | −3.34 | 16.18 | 217.48 | 25.30 | 2.05 | 12.47 | TH |
| HS 2208+2718 | 23.93 | 7.25 | 8.34 | 0.09 | 4.52 | 2.16 | 0.48 | 0.12 | 2841.56 | 251.09 | 0.19 | 0.11 | 21.62 | 32.43 | 347.42 | 19.72 | −88.06 | 10.91 | H |
| HS 2242+3206 | 11.50 | 1.37 | 0.53 | 0.69 | 0.93 | 0.22 | 0.91 | 0.11 | 234.00 | 270.30 | 0.08 | 0.02 | 179.27 | 26.30 | 37.35 | 19.43 | 18.52 | 3.32 | TK |
| KPD 0054+5406 | 8.95 | 0.07 | 7.12 | 0.31 | 0.16 | 0.02 | 0.11 | 0.02 | 1930.35 | 44.49 | 0.02 | 0.00 | −22.44 | 3.32 | 229.16 | 18.52 | 11.34 | 4.03 | TH |
| KPD 2040+3955 | 9.07 | 0.77 | 6.64 | 0.51 | 0.15 | 0.41 | 0.15 | 0.08 | 1873.78 | 14.64 | 0.02 | 0.05 | −44.22 | 18.04 | 233.62 | 20.29 | 11.49 | 3.21 | TH |
| KPD 2215+5037 | 9.66 | 0.68 | 6.80 | 0.78 | 0.33 | 0.30 | 0.17 | 0.09 | 1940.89 | 59.13 | 0.04 | 0.03 | 53.44 | 25.75 | 237.36 | 13.11 | 20.98 | 5.95 | TH |
| KUV 16256+4034 | 8.27 | 0.04 | 3.41 | 0.37 | 0.57 | 0.05 | 0.42 | 0.04 | 1207.94 | 89.08 | 0.08 | 0.01 | 9.62 | 9.55 | 155.33 | 19.50 | −25.57 | 4.36 | TK |
| PG 0004+133 | 8.72 | 0.21 | 6.78 | 0.58 | 0.50 | 0.22 | 0.13 | 0.04 | 1852.57 | 91.01 | 0.06 | 0.03 | −25.13 | 9.38 | 226.44 | 15.36 | −20.8 | 3.50 | TH |
| PG 0005+179 | 9.36 | 0.73 | 5.23 | 1.28 | 0.59 | 0.17 | 0.28 | 0.11 | 1653.79 | 247.74 | 0.06 | 0.02 | 61.03 | 28.17 | 201.31 | 16.06 | −0.41 | 3.57 | TH |
| PG 0919+273 | 11.27 | 0.17 | 5.60 | 0.56 | 0.48 | 0.01 | 0.34 | 0.05 | 1844.09 | 99.11 | 0.07 | 0.00 | −104.6 | 4.37 | 220.52 | 10.22 | −15.73 | 4.92 | TK |
| PG 0934+186 | 9.03 | 0.37 | 7.47 | 0.63 | 0.68 | 0.34 | 0.09 | 0.04 | 1962.96 | 101.55 | 0.08 | 0.04 | 22.27 | 6.46 | 233.42 | 22.38 | −26.91 | 2.05 | TH |
| PG 1136−003 | 8.60 | 0.21 | 3.16 | 0.98 | 0.80 | 0.37 | 0.46 | 0.12 | 1150.28 | 242.10 | 0.14 | 0.09 | −52.42 | 14.98 | 231.22 | 17.93 | −86.17 | 8.78 | TK |
| PG 1230+052 | 8.62 | 0.26 | 4.39 | 1.00 | 0.84 | 0.13 | 0.33 | 0.10 | 1431.81 | 201.26 | 0.14 | 0.03 | −45.5 | 16.48 | 255.43 | 21.55 | 3.96 | 5.58 | TH |
| PG 1244+113 | 8.67 | 0.24 | 7.50 | 0.50 | 0.40 | 0.08 | 0.07 | 0.03 | 1946.10 | 73.24 | 0.05 | 0.01 | −21.4 | 8.78 | 241.18 | 17.36 | 10.60 | 2.46 | TH |
| PG 1403+316 | 10.42 | 0.93 | 3.49 | 0.87 | 1.58 | 0.30 | 0.50 | 0.12 | 1284.22 | 216.57 | 0.17 | 0.03 | 122.82 | 6.83 | 166.06 | 33.84 | 47.86 | 3.51 | TK |
| PG 1519+640 | 16.20 | 2.95 | 8.32 | 0.05 | 1.84 | 1.01 | 0.32 | 0.08 | 2565.16 | 127.65 | 0.13 | 0.08 | 34.15 | 16.78 | 312.14 | 20.38 | −52.7 | 8.42 | TK |
| PG 1558−007 | 7.92 | 0.38 | 5.01 | 1.24 | 1.03 | 0.41 | 0.23 | 0.11 | 1483.40 | 229.31 | 0.14 | 0.06 | 39.30 | 18.44 | 204.22 | 19.91 | −39.82 | 4.73 | TH |
| PG 1648+536 | 8.42 | 0.18 | 4.75 | 0.76 | 0.93 | 0.25 | 0.28 | 0.07 | 1482.03 | 129.92 | 0.12 | 0.04 | 22.73 | 19.05 | 187.00 | 22.50 | −21.23 | 6.37 | TH |
| PG 2331+038 | 11.91 | 2.12 | 8.37 | 0.12 | 1.32 | 0.59 | 0.17 | 0.09 | 2303.87 | 145.96 | 0.14 | 0.07 | 10.68 | 16.74 | 263.73 | 25.22 | 7.22 | 6.23 | TH |
| PHL 932 | 9.80 | 0.34 | 6.79 | 0.55 | 0.27 | 0.09 | 0.18 | 0.05 | 1952.07 | 62.56 | 0.03 | 0.01 | 55.02 | 14.12 | 236.66 | 18.74 | 5.29 | 9.70 | TH |

# Kinematics Input and Outputs for Gaia DR2

C

Table C.1 displays the radial velocities for SDSS spectra, stars marked with a †
are measurements of just one spectrum, all others are measurements from at least two
spectra.

Table C.2. lists the proper motions and distances for the hot subdwarfs from Chapter 6. In Table C.3 and C.4 the proper motions, distances and radial velocities from
the literature are displayed for the giants and CSPNe respectively.

**Table C.1:** Radial velocities for helium rich Hot Subdwarfs in the SDSS catalog.

| Star | RV<br>km s$^{-1}$ | $\sigma$<br>km s$^{-1}$ |
|---|---|---|
| SDSSJ114604.93+082934.9 | 279.15 | 9.95 |
| SDSSJ125551.61+043238.8 | 272.41 | 52.37 |
| †SDSSJ095613.20-030009.2 | 264.06 | 15.38 |
| †SDSSJ112855.25-061004.04 | 252.09 | 29.97 |
| †SDSSJ081640.05+305632.4 | 241.79 | 10.52 |
| PG1033+097 | 218.20 | 7.06 |
| †SDSSJ085727.65+424215.4 | 212.60 | 23.22 |
| SDSSJ121111.31+250105.9 | 207.26 | 11.71 |
| †SDSSJ101113.54-010626.2 | 200.72 | 18.15 |
| †SDSSJ121029.23+090553.9 | 195.46 | 7.26 |
| †SDSSJ154359.37+055842.6 | 171.18 | 7.10 |
| SDSSJ095911.47+220003.9 | 159.12 | 10.21 |
| PG0934+163 | 155.16 | 9.34 |
| SDSSJ145419.32+020323.7 | 151.80 | 18.36 |
| SDSSJ100019.98-003413.3 | 147.68 | 20.63 |
| SDSSJ135150.62+035718.0 | 147.58 | 9.76 |
| †SDSSJ073220.14+270408.5 | 137.73 | 11.90 |
| SDSSJ124552.82+175112.2 | 124.11 | 11.16 |
| †SDSSJ103424.78+155544.3 | 123.04 | 26.41 |
| †SDSSJ134352.14+394008.3 | 110.73 | 23.59 |
| SDSSJ153419.42+372557.2 | 109.03 | 15.75 |
| †SDSSJ173119.14+313831.1 | 108.87 | 13.94 |
| SDSSJ123821.49-021211.4 | 108.63 | 36.21 |
| †SDSSJ131224.00+273915.5 | 107.09 | 11.93 |
| SDSSJ133449.26+041014.8 | 100.22 | 10.53 |
| †SDSSJ134738.33+043426.9 | 94.20 | 26.31 |
| SDSSJ090902.40+161207.4 | 93.38 | 12.40 |
| †SDSSJ153701.00+182024.3 | 91.73 | 4.54 |
| †SDSSJ081304.04-071306.5 | 91.65 | 6.69 |

**Table** C.1: Radial velocities (continued)

| Star | RV | $\sigma$ |
| --- | --- | --- |
| | km s$^{-1}$ | km s$^{-1}$ |
| †PG1617+076 | 88.09 | 7.19 |
| SDSSJ115141.24+130200.2 | 87.54 | 9.73 |
| PG1441+407 | 85.91 | 9.22 |
| PG0912+119 | 82.27 | 9.05 |
| SDSSJ104242.84+181025.0 | 79.12 | 12.84 |
| SDSSJ110215.45+024034.1 | 78.28 | 18.80 |
| †SDSSJ165519.73+274945.5 | 71.56 | 13.88 |
| SDSSJ123808.65+053318.2 | 70.25 | 13.52 |
| SDSSJ082216.14+133822.6 | 67.77 | 35.74 |
| SDSSJ134621.23+224836.7 | 65.81 | 14.22 |
| SDSSJ150300.35-021947.3 | 65.23 | 23.01 |
| SDSSJ125738.33+181724.2 | 64.80 | 13.58 |
| †SDSSJ145803.55+043922.0 | 64.08 | 8.23 |
| †SDSSJ104054.47+112023.7 | 59.14 | 12.24 |
| SDSSJ012602.52-004834.5 | 57.42 | 29.73 |
| †SDSSJ145815.90+370017.4 | 57.37 | 29.33 |
| SDSSJ161014.87+045046.6 | 55.20 | 8.66 |
| †SDSSJ161804.93+204104.1 | 54.86 | 11.26 |
| SDSSJ140715.41+033147.5 | 53.61 | 13.02 |
| †SDSSJ112414.45+402637.1 | 51.77 | 9.89 |
| †SDSSJ161439.04+113049.1 | 48.79 | 12.37 |
| †SDSSJ180757.08+230133.0 | 45.96 | 4.14 |
| †PG1722+317 | 45.96 | 8.67 |
| †PG1251+019 | 45.88 | 10.34 |
| †SDSSJ233725.49+064603.0 | 45.82 | 6.80 |
| SDSSJ232404.68-001812.9 | 44.48 | 37.97 |
| PG1026+259 | 42.64 | 29.83 |
| SDSSJ095601.68+091137.8 | 42.33 | 17.30 |
| †SDSSJ044149.12+100821.7 | 41.94 | 16.55 |
| PG2110+001 | 41.11 | 6.71 |
| †SDSSJ163602.14+175401.6 | 39.50 | 9.58 |
| SDSSJ140803.07+242549.4 | 38.65 | 12.68 |
| †SDSSJ150150.76+383147.1 | 38.46 | 11.70 |
| †SDSSJ092227.66+322916.25 | 37.73 | 21.38 |
| PG1248+066 | 36.95 | 7.42 |
| †SDSSJ001908.56+242422.34 | 33.68 | 9.09 |
| SDSSJ152708.31+003308.3 | 33.15 | 6.91 |
| †SDSSJ183317.70+642737.0 | 28.90 | 5.68 |
| †SDSSJ142558.43+402257.8 | 27.85 | 6.69 |
| †SDSSJ164611.45+274752.4 | 27.45 | 15.41 |
| †PG1413+114 | 24.94 | 5.96 |
| SDSSJ074613.16+333307.6 | 23.11 | 8.11 |
| †PG1715+273 | 22.03 | 10.60 |
| SDSSJ155610.40+254640.2 | 22.01 | 28.20 |
| †SDSSJ041536.05+253857.11 | 20.94 | 6.88 |
| SDSSJ094856.95+334151.0 | 20.63 | 6.64 |
| †PG1432+108 | 20.58 | 12.90 |
| †SDSSJ204940.85+165003.6 | 19.85 | 6.52 |
| †SDSSJ184359.81+634651.7 | 18.39 | 5.46 |
| PG1610+043 | 17.85 | 8.84 |
| †SDSSJ103806.64+134412.0 | 16.82 | 8.87 |
| SDSSJ163702.78-011351.7 | 14.80 | 7.64 |
| SDSSJ142939.35+152623.6 | 13.84 | 27.01 |

**Table** C.1: Radial velocities (continued)

| Star | RV km s$^{-1}$ | σ km s$^{-1}$ |
|------|------|------|
| SDSSJ233541.47+000219.4 | 12.67 | 17.94 |
| †SDSSJ151628.36+340657.5 | 11.52 | 10.96 |
| †SDSSJ153251.11+050536.6 | 9.11 | 13.75 |
| †PG1552+464 | 8.17 | 19.87 |
| †SDSSJ163416.08+221141.0 | 7.64 | 21.25 |
| SDSSJ072824.72+414953.7 | 6.86 | 12.89 |
| PG2116+008 | 4.00 | 8.00 |
| SDSSJ153526.07+211441.0 | 3.98 | 6.32 |
| †PG1624+085 | 3.52 | 5.34 |
| †SDSSJ165131.40+274229.4 | 3.19 | 17.81 |
| †SDSSJ160325.51+341237.4 | 1.48 | 7.80 |
| †SDSSJJ141013.02+091938.9 | -0.28 | 12.73 |
| †SDSSJ164216.67+212117.0 | -0.93 | 16.36 |
| †SDSSJ101420.73-025228.1 | -1.25 | 9.30 |
| †PG1624+382 | -1.90 | 8.64 |
| †SDSSJ155202.72+261542.9 | -1.98 | 18.64 |
| SDSSJ075732.18+184329.3 | -2.63 | 17.39 |
| SDSSJ160233.32+361345.4 | -3.03 | 13.82 |
| SDSSJ140453.68+124428.5 | -3.27 | 12.35 |
| †KUV08102+3843 | -3.44 | 14.42 |
| SDSSJ092245.80+214239.0 | -3.65 | 7.82 |
| SDSSJ162435.66+150355.5 | -5.82 | 6.50 |
| †PG0135+242 | -8.45 | 5.72 |
| †GALEXJ17042+6451 | -9.99 | 21.18 |
| PG1258+012 | -12.86 | 13.08 |
| †SDSSJ080453.73+301607.2 | -13.14 | 11.09 |
| SDSSJ104312.02+180038.7 | -13.83 | 6.85 |
| †SDSSJJ145547.78+100044.8 | -14.01 | 28.31 |
| †SDSSJ211423.98-001034.7 | -15.07 | 13.99 |
| SDSSJJ153959.50+165108.0 | -15.89 | 9.00 |
| PG1425+590 | -16.13 | 14.63 |
| †SDSSJ082154.35+554048.06 | -16.77 | 6.12 |
| SDSSJ160715.22+094629.4 | -17.52 | 19.49 |
| PG1301+270 | -17.71 | 12.06 |
| †SDSSJ141323.33+170306.7 | -17.91 | 14.43 |
| †PG0016+151 | -20.01 | 4.79 |
| PG1539+442 | -20.37 | 9.21 |
| SDSSJ091512.06+191114.6 | -20.82 | 10.39 |
| †SDSSJ083747.22+194955.8 | -21.14 | 20.04 |
| †SDSSJ074843.87+325348.6 | -21.47 | 7.87 |
| †SDSSJ102241.20+203839.6 | -21.47 | 10.33 |
| SDSSJ170045.09+391830.3 | -21.63 | 10.27 |
| †SDSSJ153021.99+343423.6 | -22.19 | 10.10 |
| SDSSJ163027.19+180233.2 | -22.29 | 8.87 |
| PG1528+029 | -22.89 | 12.28 |
| SDSSJ082751.06+410925.8 | -22.97 | 15.08 |
| †SDSSJ144107.00+144233.3 | -27.29 | 8.23 |
| SDSSJ215631.55+121237.6 | -28.34 | 9.69 |
| PG1203+084 | -29.47 | 9.88 |
| SDSSJ213054.60-004117.3 | -29.47 | 7.83 |
| SDSSJ153935.00+133800.9 | -33.03 | 20.04 |
| †SDSSJ162626.25+333315.0 | -33.11 | 8.64 |
| †KUV16160+4120 | -33.11 | 7.72 |

**Table** C.1: Radial velocities (continued)

| Star | RV | σ |
|------|-----|---|
|  | km s$^{-1}$ | km s$^{-1}$ |
| †SDSSJ133805.38+395044.8 | -33.84 | 9.82 |
| SDSSJ141812.51-024426.9 | -35.28 | 32.00 |
| †SDSSJ132747.87+564040.14 | -35.53 | 21.11 |
| †PG1700+198 | -36.02 | 8.09 |
| †SDSSJ161624.36+265314.7 | -36.34 | 9.64 |
| †TON261 | -38.20 | 6.25 |
| †SDSSJ215553.90+202802.9 | -41.11 | 6.52 |
| SDSSJ073856.98+401942.0 | -41.65 | 26.80 |
| SDSSJ135210.12-015836.1 | -45.08 | 12.20 |
| SDSSJ233719.19+062504.0 | -45.28 | 5.47 |
| SDSSJ141505.46+020237.2 | -47.58 | 6.41 |
| SDSSJ133543.00+330558.4 | -50.33 | 5.22 |
| †SDSSJ100451.92+433653.2 | -54.78 | 9.16 |
| SDSSJ152208.01+342502.8 | -55.55 | 6.90 |
| †SDSSJ155155.11+092344.0 | -55.91 | 7.26 |
| PG1507-015 | -56.03 | 9.91 |
| †PG1554+408 | -57.12 | 9.24 |
| SBSS0803+510 | -57.50 | 7.39 |
| †SDSSJ094552.63+374533.9 | -57.85 | 16.33 |
| SDSSJ080833.76+180221.8 | -61.04 | 8.54 |
| SDSSJ102120.44+444636.9 | -61.81 | 8.87 |
| †SDSSJ161345.80+384950.7 | -63.91 | 5.28 |
| †SDSSJ163409.36+163715.1 | -66.42 | 9.82 |
| †SDSSJ161221.17+270945.0 | -66.57 | 11.03 |
| SDSSJ145817.52+022806.6 | -69.74 | 8.06 |
| SDSSJ113412.76+211514.5 | -72.54 | 12.53 |
| †SDSSJ174516.32+244348.3 | -73.70 | 5.25 |
| †SDSSJ152143.87+450022.5 | -74.43 | 6.06 |
| SDSSJ161507.08+105513.5 | -74.79 | 7.91 |
| †PG1614+378 | -77.73 | 15.88 |
| †PG1600+171 | -79.52 | 8.30 |
| †SDSSJ231726.22+205416.82 | -79.52 | 4.91 |
| †SDSSJ143729.14-021506.0 | -79.78 | 16.35 |
| SDSSJ160835.68+045345.2 | -81.94 | 11.56 |
| †GALEXJ14258-0432 | -83.16 | 13.84 |
| †SDSSJ090252.99+073533.9 | -86.07 | 9.34 |
| SDSSJ131218.11+381535.2 | -90.97 | 9.96 |
| †SDSSJ152538.14+134201.0 | -91.16 | 16.10 |
| SDSSJ150704.10+212257.5 | -94.11 | 6.72 |
| SDSSJ135707.34+010454.4 | -95.64 | 11.90 |
| †SDSSJ161938.64+252122.4 | -96.42 | 11.47 |
| SDSSJ153204.35+324152.7 | -96.74 | 13.86 |
| †SDSSJ232757.46+483755.2 | -100.73 | 33.85 |
| †SDSSJ224326.26+133904.09 | -101.81 | 12.56 |
| SDSSJ154641.88+062539.2 | -102.16 | 9.32 |
| †SDSSJ152046.66+180300.7 | -102.83 | 5.33 |
| †SDSSJ215827.55-000532.0 | -105.39 | 18.36 |
| SDSSJ153237.94+275636.9 | -108.55 | 12.03 |
| SDSSJ163605.36+130404.1 | -110.00 | 11.07 |
| †SDSSJ135505.63+114440.0 | -114.37 | 12.48 |
| †PG1608+374 | -115.01 | 5.67 |
| SDSSJ162411.53+312252.6 | -120.64 | 9.61 |
| SDSSJ160450.44+051909.2 | -120.81 | 13.23 |

**Table** C.1: Radial velocities (continued)

| Star | RV | $\sigma$ |
|------|----|----|
| | km s$^{-1}$ | km s$^{-1}$ |
| SDSSJ171142.45+380525.2 | -129.57 | 7.83 |
| †SDSSJ023532.60-063437.8 | -131.02 | 8.30 |
| †SDSSJ152136.25+162150.3 | -131.02 | 10.66 |
| SDSSJ154227.88+310601.9 | -132.94 | 11.24 |
| †SDSSJ214612.17+005110.0 | -134.66 | 8.50 |
| SBSS1034+496 | -143.64 | 11.16 |
| SDSSJ155344.97+124313.7 | -144.77 | 12.44 |
| †PG1348+606 | -145.89 | 20.87 |
| †SDSSJ162904.19+184639.7 | -146.36 | 7.50 |
| SDSSJ125301.62+394622.1 | -147.27 | 8.78 |
| SDSSJ022422.21+000313.5 | -151.40 | 13.78 |
| †SDSSJ002624.64+074113.8 | -155.44 | 16.36 |
| SDSSJ161059.80+053625.2 | -170.32 | 7.90 |
| †SDSSJ224739.96+071732.46 | -172.34 | 10.60 |
| †SDSSJ012905.14+133354.78 | -174.43 | 41.99 |
| SDSSJ104033.83+562206.4 | -178.54 | 16.28 |
| SDSSJ160240.56+444649.4 | -195.44 | 15.66 |
| SDSSJ000607.88-010320.8 | -195.54 | 5.39 |
| †SDSSJ163707.43+284240.2 | -213.42 | 10.05 |
| SDSSJ171916.97+365326.6 | -216.87 | 32.58 |
| SDSSJ220429.52+211610.8 | -217.67 | 8.11 |
| SDSSJ093521.38+482432.4 | -225.74 | 20.75 |
| SDSSJ204358.55-065025.8 | -237.95 | 19.15 |
| †SBSS1529+519 | -237.98 | 25.81 |
| †SDSSJ170035.84+374528.0 | -282.98 | 15.54 |
| †SDSSJ121703.12+454539.35 | -291.35 | 9.03 |
| †SDSSJ172854.34+361958.6 | -298.33 | 32.29 |
| SDSSJ170957.39+222745.0 | -300.89 | 9.71 |
| †SDSSJ165924.75+273244.4 | -309.26 | 14.30 |
| †SDSSJ180635.71+235908.4 | -314.45 | 28.96 |
| SDSSJ233913.99+134214.2 | -319.51 | 11.39 |
| †SDSSJ173034.09+272139.8 | -338.17 | 14.34 |
| SDSSJ222515.34-011157.0 | -372.49 | 20.25 |

**Table C.2:** Proper motions and distances derived from the *Gaia* parallaxes for the hot subdwarfs.

| Star | Category | $\mu_\alpha$ | $\pm$ | $\mu_\delta$ | $\pm$ | Distance |
|---|---|---|---|---|---|---|
| BPS CS 22940-0009 | Ex-He | 2.452 | 0.087 | -10.956 | 0.074 | $2.15^{+0.26}_{-0.33}$ |
| BPS CS 29496-0010 | Ex-He | 6.398 | 0.125 | -3.536 | 0.097 | $1.45^{+0.15}_{-0.18}$ |
| HE 0001-2443 | Ex-He | 11.803 | 0.130 | -30.018 | 0.061 | $0.75^{+0.03}_{-0.03}$ |
| HE 0342-1702 | Ex-He | -7.394 | 0.090 | -2.425 | 0.060 | $1.14^{+0.09}_{-0.11}$ |
| HE 1251+0159 | Ex-He | 3.823 | 0.156 | -22.047 | 0.087 | $2.95^{+0.51}_{-0.76}$ |
| HS 1844+637 | Ex-He | 1.744 | 0.125 | -4.566 | 0.112 | $2.71^{+0.33}_{-0.43}$ |
| LB 3229 | Ex-He | 10.897 | 0.060 | -3.671 | 0.068 | $0.86^{+0.03}_{-0.04}$ |
| PG 0039+135 | Ex-He | 1.691 | 0.133 | -1.779 | 0.062 | $1.02^{+0.07}_{-0.08}$ |
| PG 0902+057 | Ex-He | -14.896 | 0.212 | -6.177 | 0.280 | $0.88^{+0.08}_{-0.10}$ |
| PG 1127+019 | Ex-He | -9.117 | 0.098 | -9.732 | 0.082 | $1.03^{+0.06}_{-0.06}$ |
| PG 1413+114 | Ex-He | -5.567 | 0.171 | -2.304 | 0.134 | $3.87^{+1.05}_{-1.74}$ |
| PG 1415+492 | Ex-He | 1.036 | 0.055 | -6.635 | 0.057 | $3.65^{+0.44}_{-0.57}$ |
| PG 1536+690 | Ex-He | -1.752 | 0.082 | -23.707 | 0.078 | $1.37^{+0.08}_{-0.09}$ |
| PG 1544+488 | Ex-He | -44.236 | 0.074 | 31.119 | 0.098 | $0.45^{+0.01}_{-0.01}$ |
| PG 1554+408 | Ex-He | -2.492 | 0.090 | -2.357 | 0.118 | $3.12^{+0.44}_{-0.61}$ |
| PG 1615+413 | Ex-He | -6.835 | 0.111 | -16.612 | 0.132 | $3.39^{+0.66}_{-1.01}$ |
| PG 1658+273 | Ex-He | -5.154 | 0.073 | -4.863 | 0.084 | $2.73^{+0.33}_{-0.43}$ |
| PG 1715+273 | Ex-He | -1.785 | 0.098 | -5.206 | 0.103 | $3.04^{+0.50}_{-0.71}$ |
| PG 2215+151 | Ex-He | 3.342 | 0.077 | 14.925 | 0.082 | $1.12^{+0.06}_{-0.07}$ |
| PG 2258+155 | Ex-He | -7.144 | 0.152 | 1.946 | 0.094 | $1.39^{+0.14}_{-0.17}$ |
| PG 2321+214 | Ex-He | 20.556 | 0.080 | -7.608 | 0.060 | $0.95^{+0.05}_{-0.05}$ |
| PG 2352+181 | Ex-He | 28.964 | 0.113 | -1.291 | 0.068 | $0.89^{+0.05}_{-0.06}$ |
| BPS CS 22956-0094 | Inter-He | 43.733 | 0.059 | -37.365 | 0.070 | $0.54^{+0.01}_{-0.01}$ |
| CPD-20 1123 | Inter-He | 6.429 | 0.080 | -17.327 | 0.136 | $0.33^{+0.01}_{-0.01}$ |
| HD 127493 | Inter-He | -31.882 | 0.155 | -17.724 | 0.133 | $0.17^{+0.00}_{-0.00}$ |
| HE 1135-1134 | Inter-He | -6.012 | 0.131 | 1.171 | 0.079 | $3.84^{+0.83}_{-1.30}$ |
| HE 1136-2504 | Inter-He | -5.716 | 0.108 | -6.270 | 0.062 | $1.16^{+0.07}_{-0.08}$ |
| HE 1238-1745 | Inter-He | -12.410 | 0.139 | 4.218 | 0.074 | $1.50^{+0.15}_{-0.18}$ |
| HE 1256-2738 | Inter-He | -21.336 | 0.188 | -4.602 | 0.145 | $1.86^{+0.31}_{-0.46}$ |
| HE 1310-2733 | Inter-He | 2.066 | 0.108 | -2.225 | 0.093 | $1.20^{+0.08}_{-0.10}$ |
| HE 2218-2026 | Inter-He | 20.590 | 0.138 | -17.513 | 0.130 | $2.43^{+0.39}_{-0.56}$ |
| HE 2357-3940 | Inter-He | 17.139 | 0.207 | 2.732 | 0.141 | $1.15^{+0.13}_{-0.16}$ |
| HE 2359-2844 | Inter-He | 6.918 | 0.127 | -6.793 | 0.105 | $1.97^{+0.29}_{-0.41}$ |
| HS 1051+2933 | Inter-He | 10.919 | 0.201 | -21.852 | 0.233 | $2.71^{+0.82}_{-1.53}$ |
| JL 87 | Inter-He | -0.349 | 0.074 | 3.481 | 0.078 | $0.85^{+0.03}_{-0.04}$ |

**Table** C.2: (continued)

| Star | Category | $\mu_\alpha$ | $\pm$ | $\mu_\delta$ | $\pm$ | Distance |
|---|---|---|---|---|---|---|
| LS IV−14°116 | Inter-He | 7.490 | 0.130 | -127.992 | 0.084 | $0.42^{+0.01}_{-0.02}$ |
| PG 0229+064 | Inter-He | 17.835 | 0.125 | -2.622 | 0.099 | $0.70^{+0.03}_{-0.03}$ |
| PG 0240+046 | Inter-He | 31.120 | 0.109 | -0.147 | 0.105 | $0.70^{+0.03}_{-0.03}$ |
| PG 0909+276 | Inter-He | 1.224 | 0.160 | -0.186 | 0.103 | $0.27^{+0.01}_{-0.01}$ |
| SB 705 | Inter-He | 10.478 | 0.052 | 8.872 | 0.067 | $0.95^{+0.05}_{-0.05}$ |
| SDSS J092440.11+305013.16 | Inter-He | 7.716 | 0.108 | -8.143 | 0.079 | $1.61^{+0.20}_{-0.26}$ |
| SDSS J160131.30+044027.00 | Inter-He | -13.315 | 0.084 | -1.055 | 0.073 | $0.78^{+0.03}_{-0.04}$ |
| SDSS J175548.50+501210.77 | Inter-He | -7.529 | 0.074 | 23.366 | 0.080 | $0.54^{+0.01}_{-0.01}$ |
| TON 107 | Inter-He | -7.841 | 0.084 | -19.681 | 0.109 | $2.28^{+0.35}_{-0.50}$ |
| UVO 0825+15 | Inter-He | -26.451 | 0.116 | -1.855 | 0.081 | $0.28^{+0.01}_{-0.01}$ |
| KUV16160+4120 | He-sdB | -6.835 | 0.111 | -16.612 | 0.132 | $3.39^{+0.48}_{-0.98}$ |
| PG1554+408 | He-sdB | -2.492 | 0.090 | -2.357 | 0.118 | $3.12^{+0.33}_{-0.56}$ |
| SDSSJ082216.14+133822.6 | He-sdB | -18.918 | 0.416 | -12.719 | 0.269 | $0.27^{+0.01}_{-0.02}$ |
| SDSSJ232404.68-001812.9 | He-sdB | 29.619 | 0.606 | -23.402 | 0.476 | $0.34^{+0.03}_{-0.05}$ |
| PG0912+119 | He-sdO | -3.148 | 0.196 | -9.870 | 0.221 | $3.24^{+0.53}_{-1.21}$ |
| PG1203+084 | He-sdO | 0.236 | 0.216 | -16.534 | 0.088 | $2.40^{+0.32}_{-0.64}$ |
| PG1248+066 | He-sdO | -6.817 | 0.159 | -5.926 | 0.097 | $3.50^{+0.52}_{-1.09}$ |
| PG1301+270 | He-sdO | -12.254 | 0.128 | 4.940 | 0.135 | $4.54^{+0.77}_{-1.61}$ |
| PG1348+606 | He-sdO | -4.903 | 0.101 | -10.462 | 0.080 | $6.15^{+0.98}_{-1.84}$ |
| PG1413+114 | He-sdO | -5.567 | 0.171 | -2.304 | 0.134 | $3.87^{+0.74}_{-1.70}$ |
| PG1425+590 | He-sdO | -22.914 | 0.105 | -3.098 | 0.095 | $1.76^{+0.12}_{-0.17}$ |
| PG1441+407 | He-sdO | -5.652 | 0.078 | -20.242 | 0.088 | $3.60^{+0.44}_{-0.81}$ |
| PG1507-015 | He-sdO | -5.630 | 0.175 | 1.027 | 0.191 | $3.29^{+0.55}_{-1.26}$ |
| PG1528+029 | He-sdO | -7.193 | 0.098 | -3.451 | 0.090 | $1.92^{+0.15}_{-0.21}$ |
| PG1539+442 | He-sdO | -2.384 | 0.097 | -8.009 | 0.126 | $5.28^{+0.84}_{-1.65}$ |
| PG1608+374 | He-sdO | -8.433 | 0.108 | -21.495 | 0.125 | $5.63^{+0.91}_{-1.75}$ |
| PG1610+043 | He-sdO | -4.270 | 0.107 | -3.761 | 0.062 | $2.40^{+0.26}_{-0.46}$ |
| PG1617+076 | He-sdO | -3.179 | 0.101 | -7.840 | 0.066 | $3.45^{+0.53}_{-1.12}$ |
| PG1624+085 | He-sdO | -4.434 | 0.079 | -8.623 | 0.058 | $1.85^{+0.15}_{-0.22}$ |
| PG1624+382 | He-sdO | -5.051 | 0.079 | -2.668 | 0.099 | $2.31^{+0.19}_{-0.28}$ |
| PG1700+198 | He-sdO | -9.809 | 0.075 | -3.806 | 0.079 | $2.12^{+0.19}_{-0.29}$ |
| PG1722+317 | He-sdO | -6.412 | 0.107 | -6.675 | 0.106 | $3.02^{+0.36}_{-0.66}$ |
| PG2110+001 | He-sdO | -6.935 | 0.172 | -8.948 | 0.149 | $4.00^{+0.74}_{-1.66}$ |
| PG2116+008 | He-sdO | 0.315 | 0.119 | -2.643 | 0.096 | $4.04^{+0.62}_{-1.29}$ |
| SDSSJ041536.05+253857.11 | He-sdO | -0.327 | 0.141 | 0.767 | 0.104 | $1.62^{+0.13}_{-0.20}$ |
| SDSSJ044149.12+100821.7 | He-sdO | -1.233 | 0.723 | -5.993 | 0.321 | $2.57^{+0.74}_{-2.11}$ |

**Table** C.2: (continued)

| Star | Category | $\mu_\alpha$ | $\pm$ | $\mu_\delta$ | $\pm$ | Distance |
|---|---|---|---|---|---|---|
| SDSSJ073856.98+401942.0 | He-sdO | 2.246 | 0.137 | -2.784 | 0.084 | $4.21\,^{+0.76}_{-1.66}$ |
| SDSSJ074613.16+333307.6 | He-sdO | -4.012 | 0.124 | -1.348 | 0.080 | $3.25\,^{+0.53}_{-1.18}$ |
| SDSSJ080833.76+180221.8 | He-sdO | 6.887 | 0.170 | -12.742 | 0.109 | $4.58\,^{+0.91}_{-1.93}$ |
| SDSSJ090252.99+073533.9 | He-sdO | 9.368 | 0.190 | -14.078 | 0.126 | $2.72\,^{+0.47}_{-1.17}$ |
| SDSSJ103806.64+134412.0 | He-sdO | 1.522 | 0.231 | -6.633 | 0.168 | $3.93\,^{+0.81}_{-1.84}$ |
| SDSSJ125301.62+394622.1 | He-sdO | 3.936 | 0.141 | -13.254 | 0.152 | $3.66\,^{+0.71}_{-1.66}$ |
| SDSSJ132747.87+564040.14 | He-sdO | -1.222 | 0.209 | -1.511 | 0.223 | $2.36\,^{+0.43}_{-1.18}$ |
| SDSSJ151415.66-012925.2 | He-sdO | -10.021 | 0.367 | -9.010 | 0.505 | $1.85\,^{+0.27}_{-0.65}$ |
| SDSSJ152136.25+162150.3 | He-sdO | -16.802 | 0.168 | -2.683 | 0.231 | $2.35\,^{+0.37}_{-0.89}$ |
| SDSSJ152143.87+450022.5 | He-sdO | -2.577 | 0.172 | -3.414 | 0.228 | $4.63\,^{+0.90}_{-1.90}$ |
| SDSSJ153021.99+343423.6 | He-sdO | -4.441 | 0.136 | -0.210 | 0.219 | $3.85\,^{+0.74}_{-1.70}$ |
| SDSSJ153251.11+050536.6 | He-sdO | -11.235 | 0.173 | -3.496 | 0.163 | $4.63\,^{+0.89}_{-1.88}$ |
| SDSSJ160325.51+341237.4 | He-sdO | -4.381 | 0.119 | -1.544 | 0.148 | $5.21\,^{+0.91}_{-1.83}$ |
| SDSSJ161014.87+045046.6 | He-sdO | 3.630 | 0.196 | 0.268 | 0.150 | $4.20\,^{+0.83}_{-1.84}$ |
| SDSSJ161059.80+053625.2 | He-sdO | -4.566 | 0.138 | -0.798 | 0.081 | $3.63\,^{+0.66}_{-1.52}$ |
| SDSSJ162626.25+333315.0 | He-sdO | -5.195 | 0.244 | 0.968 | 0.294 | $3.98\,^{+0.84}_{-1.92}$ |
| SDSSJ173119.14+313831.1 | He-sdO | -7.897 | 0.289 | -4.232 | 0.334 | $3.03\,^{+0.65}_{-1.68}$ |
| SDSSJ180757.08+230133.0 | He-sdO | 3.450 | 0.093 | -3.956 | 0.139 | $4.05\,^{+0.67}_{-1.43}$ |
| SDSSJ184359.81+634651.7 | He-sdO | 1.744 | 0.125 | -4.566 | 0.112 | $2.71\,^{+0.25}_{-0.39}$ |
| SDSSJ211423.98-001034.7 | He-sdO | 0.178 | 0.168 | -5.215 | 0.154 | $3.77\,^{+0.70}_{-1.61}$ |
| SDSSJ214612.17+005110.0 | He-sdO | 7.137 | 0.255 | -5.622 | 0.230 | $2.65\,^{+0.55}_{-1.54}$ |
| SDSSJ215553.90+202802.9 | He-sdO | 8.392 | 0.090 | 5.348 | 0.089 | $2.95\,^{+0.31}_{-0.53}$ |
| SDSSJ220429.52+211610.8 | He-sdO | -12.422 | 0.098 | -19.412 | 0.098 | $3.18\,^{+0.39}_{-0.74}$ |
| SDSSJ231726.22+205416.82 | He-sdO | -3.237 | 0.249 | -4.848 | 0.164 | $3.50\,^{+0.76}_{-1.85}$ |
| SDSSJ232757.46+483755.2 | He-sdO | -4.106 | 0.091 | -0.515 | 0.089 | $5.09\,^{+0.80}_{-1.57}$ |
| SDSSJ233541.47+000219.4 | He-sdO | 3.974 | 0.236 | -1.325 | 0.110 | $2.58\,^{+0.40}_{-0.91}$ |
| SDSSJJ083747.22+194955.8 | He-sdO | -7.008 | 0.685 | -3.232 | 0.423 | $4.92\,^{+1.33}_{-2.48}$ |
| PG1258+012 | He-sdOB | -10.519 | 0.200 | 4.087 | 0.125 | $2.49\,^{+0.33}_{-0.66}$ |
| PG1715+273 | He-sdOB | -1.785 | 0.098 | -5.206 | 0.103 | $3.04\,^{+0.37}_{-0.68}$ |
| SDSSJ072824.72+414953.7 | He-sdOB | 0.526 | 0.123 | -3.142 | 0.083 | $2.42\,^{+0.28}_{-0.50}$ |
| SDSSJ073220.14+270408.5 | He-sdOB | -2.011 | 0.189 | -6.379 | 0.160 | $1.74\,^{+0.22}_{-0.43}$ |
| SDSSJ124552.82+175112.2 | He-sdOB | -15.505 | 0.330 | -10.187 | 0.184 | $3.14\,^{+0.67}_{-1.72}$ |
| SDSSJ131218.11+381535.2 | He-sdOB | -2.653 | 0.426 | -8.015 | 0.349 | $2.90\,^{+0.79}_{-2.10}$ |
| SDSSJ134352.14+394008.3 | He-sdOB | -9.368 | 0.127 | -9.774 | 0.159 | $4.09\,^{+0.84}_{-1.89}$ |
| SDSSJ134621.23+224836.7 | He-sdOB | -7.596 | 0.166 | -2.204 | 0.104 | $4.51\,^{+0.83}_{-1.76}$ |
| SDSSJ140453.68+124428.5 | He-sdOB | -4.136 | 0.191 | -13.867 | 0.165 | $4.54\,^{+0.89}_{-1.90}$ |

**Table** C.2: (continued)

| Star | Category | $\mu_\alpha$ | ± | $\mu_\delta$ | ± | Distance |
|---|---|---|---|---|---|---|
| SDSSJ142558.43+402257.8 | He-sdOB | -2.673 | 0.191 | -13.413 | 0.236 | $3.47\ ^{+0.77}_{-1.87}$ |
| SDSSJ143729.14-021506.0 | He-sdOB | -10.472 | 0.136 | 1.300 | 0.144 | $1.78\ ^{+0.21}_{-0.38}$ |
| SDSSJ152046.66+180300.7 | He-sdOB | -8.527 | 0.190 | -1.769 | 0.195 | $4.56\ ^{+0.87}_{-1.85}$ |
| SDSSJ153419.42+372557.2 | He-sdOB | -7.251 | 0.376 | -6.427 | 0.545 | $2.68\ ^{+0.69}_{-1.94}$ |
| SDSSJ153526.07+211441.0 | He-sdOB | -3.392 | 0.118 | -7.547 | 0.082 | $2.93\ ^{+0.39}_{-0.78}$ |
| SDSSJ154641.88+062539.2 | He-sdOB | -6.325 | 0.253 | -0.588 | 0.212 | $2.49\ ^{+0.46}_{-1.21}$ |
| SDSSJ155202.72+261542.9 | He-sdOB | -4.041 | 0.138 | -6.106 | 0.203 | $4.27\ ^{+0.86}_{-1.89}$ |
| SDSSJ155344.97+124313.7 | He-sdOB | -5.780 | 0.507 | -9.405 | 0.403 | $2.68\ ^{+0.81}_{-2.19}$ |
| SDSSJ161804.93+204104.1 | He-sdOB | -6.081 | 0.143 | -9.386 | 0.144 | $3.14\ ^{+0.55}_{-1.33}$ |
| SDSSJ163416.08+221141.0 | He-sdOB | -3.561 | 0.062 | -3.778 | 0.072 | $1.91\ ^{+0.13}_{-0.17}$ |
| SDSSJ183317.70+642737.0 | He-sdOB | -4.639 | 0.216 | -1.118 | 0.251 | $2.90\ ^{+0.51}_{-1.26}$ |
| SDSSJ222515.34-011157.0 | He-sdOB | 2.297 | 0.489 | -0.948 | 0.566 | $5.15\ ^{+1.36}_{-2.50}$ |
| SDSSJJ161624.36+265314.7 | He-sdOB | -0.883 | 0.074 | -12.014 | 0.090 | $1.84\ ^{+0.12}_{-0.16}$ |
| TON261 | He-sdOB | 1.850 | 0.079 | -1.022 | 0.109 | $2.15\ ^{+0.17}_{-0.24}$ |

**Table C.3:** Proper motions, distances derived from the *Gaia* parallaxes and published radial velocities for the giants.

| Star | Category | $\mu_\alpha$ | $\pm$ | $\mu_\delta$ | $\pm$ | v | $\pm$ | Distance |
|---|---|---|---|---|---|---|---|---|
| BD+10 2179 | EHe | -10.42 | 0.16 | -4.81 | 0.15 | $155.20^a$ | 2.80 | $2.36\,^{+0.50}_{-0.83}$ |
| BD+37 1977 | EHe | 10.91 | 0.14 | -11.69 | 0.13 | $-97.63^b$ | 9.88 | $1.36\,^{+0.18}_{-0.24}$ |
| BD+37 442 | EHe | -9.99 | 0.19 | -7.49 | 0.18 | $-99.40^b$ | 25.00 | $1.55\,^{+0.33}_{-0.56}$ |
| BPS CS 22940-0009 | EHe | 2.45 | 0.09 | -10.96 | 0.07 | $37.00^c$ | 10.00 | $2.15\,^{+0.26}_{-0.33}$ |
| BX Cir | EHe | -8.29 | 0.04 | 2.22 | 0.05 | $-89.00^d$ | 9.43 | $3.79\,^{+0.47}_{-0.61}$ |
| Cod-48 10153 | EHe | -6.05 | 0.07 | -6.46 | 0.06 | $-4.47^{e,f}$ | 2.47 | $7.25\,^{+1.25}_{-1.72}$ |
| DY Cen | EHe | -5.94 | 0.04 | -0.29 | 0.04 | $33.00^g$ | 3.00 | $11.90\,^{+1.98}_{-2.57}$ |
| FQ Aqr | EHe | -0.68 | 0.08 | -5.97 | 0.04 | $23.72^h$ | 1.41 | $4.88\,^{+0.89}_{-1.29}$ |
| GALEX J184559.8-413827 | EHe | 0.27 | 0.10 | -0.10 | 0.09 | $-57.60^g$ | 6.10 | $3.71\,^{+0.70}_{-1.05}$ |
| HD 124448 | EHe | -6.89 | 0.15 | -0.09 | 0.20 | $-65.00^f$ | 3.00 | $2.04\,^{+0.43}_{-0.71}$ |
| HD 144941 | EHe | -6.66 | 0.12 | 8.15 | 0.09 | $-52.60^i$ | 2.50 | $1.82\,^{+0.17}_{-0.21}$ |
| LS IV-14 109 | EHe | -0.42 | 0.08 | -0.32 | 0.06 | $-7.30^e$ | 2.70 | $3.02\,^{+0.37}_{-0.48}$ |
| LS IV+6 2 | EHe | -2.95 | 0.10 | -8.83 | 0.09 | $-24.00^f$ | 4.00 | $1.83\,^{+0.17}_{-0.21}$ |
| LSS 4357 | EHe | -3.55 | 0.09 | 1.53 | 0.07 | $-99.00^f$ | 10.00 | $5.93\,^{+1.19}_{-1.73}$ |
| LSS 5121 | EHe | -2.08 | 0.05 | 0.44 | 0.04 | $-62.00^f$ | 6.00 | $5.56\,^{+0.71}_{-0.92}$ |
| LSS 99 | EHe | 0.20 | 0.06 | -0.62 | 0.07 | $109.00^f$ | 3.00 | $6.92\,^{+1.26}_{-1.76}$ |
| NO Ser | EHe | 0.22 | 0.10 | -2.03 | 0.09 | $-21.10^e$ | 4.59 | $3.04\,^{+0.54}_{-0.81}$ |
| PV Tel | EHe | -1.09 | 0.07 | -7.71 | 0.07 | $-170.87^{a,f}$ | 2.30 | $7.08\,^{+1.43}_{-2.03}$ |
| V1920 Cyg | EHe | -0.02 | 0.07 | -6.05 | 0.07 | $-89.90^e$ | 1.90 | $5.98\,^{+1.07}_{-1.52}$ |
| V2076 Oph | EHe | -6.48 | 0.13 | 2.46 | 0.11 | $76.77^{a,f}$ | 2.57 | $2.17\,^{+0.44}_{-0.70}$ |
| V2244 Oph | EHe | -0.28 | 0.08 | -8.18 | 0.08 | $-8.30^e$ | 2.88 | $6.69\,^{+1.49}_{-2.15}$ |
| V652 Her | EHe | -4.65 | 0.12 | 4.11 | 0.10 | $2.00^j$ | 0.50 | $1.17\,^{+0.11}_{-0.13}$ |
| HD 137613 | HdC | -1.22 | 0.10 | -7.92 | 0.08 | $56.92^h$ | 0.60 | $1.13\,^{+0.08}_{-0.09}$ |
| HD 148839 | HdC | -5.95 | 0.03 | -3.25 | 0.06 | $-20.11^h$ | 0.26 | $1.70\,^{+0.09}_{-0.10}$ |
| HD 173409 | HdC | 1.96 | 0.08 | -2.86 | 0.06 | $-64.46^h$ | 0.31 | $2.03\,^{+0.15}_{-0.18}$ |
| HD 175893 | HdC | 0.93 | 0.09 | -3.66 | 0.08 | $47.17^h$ | 0.63 | $3.27\,^{+0.44}_{-0.58}$ |
| HD 182040 | HdC | 7.03 | 0.09 | 2.53 | 0.08 | $-44.99^h$ | 0.62 | $0.95\,^{+0.04}_{-0.04}$ |
| DY Per | RCrB | 2.34 | 0.09 | -0.83 | 0.09 | $-38.50^{e,k}$ | 6.20 | $1.22\,^{+0.07}_{-0.08}$ |
| LT Dra | RCrB | -3.24 | 0.05 | 3.28 | 0.04 | $-19.24^h$ | 0.16 | $0.38\,^{+0.00}_{-0.00}$ |
| MV Sgr | RCrB | -4.72 | 0.06 | -7.69 | 0.05 | $-92.25^{f,d}$ | 2.80 | $7.72\,^{+1.40}_{-1.94}$ |
| R CrB | RCrB | -2.45 | 0.14 | -11.81 | 0.34 | $27.83^b$ | 0.77 | $1.34\,^{+0.10}_{-0.12}$ |
| RS Tel | RCrB | -2.72 | 0.09 | -6.67 | 0.07 | $-1.02^h$ | 2.10 | $7.86\,^{+1.59}_{-2.21}$ |
| RT Nor | RCrB | -3.21 | 0.06 | -5.57 | 0.05 | $-43.90^l$ | 5.50 | $6.74\,^{+1.31}_{-1.86}$ |
| RY Sgr | RCrB | 8.89 | 0.08 | -0.47 | 0.08 | $-16.02^a$ | 4.68 | $2.01\,^{+0.17}_{-0.20}$ |
| S Aps | RCrB | -6.51 | 0.04 | -2.10 | 0.04 | $-82.13^l$ | 0.71 | $4.16\,^{+0.40}_{-0.48}$ |

**Table** C.3: (continued)

| Star | Category | $\mu_\alpha$ | $\pm$ | $\mu_\delta$ | $\pm$ | v | $\pm$ | Distance |
|------|----------|--------------|-------|--------------|-------|---|-------|----------|
| SV Sge | RCrB | -2.76 | 0.06 | -1.14 | 0.06 | -4.58[h] | 0.81 | $2.15\,^{+0.20}_{-0.24}$ |
| U Aqr | RCrB | 2.69 | 0.09 | -1.93 | 0.09 | 89.49[h] | 1.54 | $5.11\,^{+1.15}_{-1.74}$ |
| UV Cas | RCrB | -0.01 | 0.04 | 0.00 | 0.05 | -28.02[h] | 0.80 | $3.11\,^{+0.24}_{-0.28}$ |
| UW Cen | RCrB | -7.84 | 0.04 | -1.80 | 0.04 | -28.37[h] | 0.68 | $6.66\,^{+1.21}_{-1.69}$ |
| V2552 Oph | RCrB | 3.28 | 0.10 | -7.08 | 0.07 | 65.08[h] | 0.99 | $5.74\,^{+1.09}_{-1.56}$ |
| V482 Cyg | RCrB | -1.99 | 0.04 | -5.98 | 0.05 | -40.00[b] | 6.32 | $3.59\,^{+0.30}_{-0.36}$ |
| VZ Sgr | RCrB | -6.51 | 0.10 | -4.65 | 0.09 | 248.86[h] | 1.67 | $5.59\,^{+1.18}_{-1.75}$ |
| WX CrA | RCrB | 1.33 | 0.10 | -6.91 | 0.09 | -3.80[m] | 2.10 | $6.96\,^{+1.49}_{-2.13}$ |
| XX Cam | RCrB | 1.97 | 0.06 | -2.62 | 0.05 | 15.75[a,f] | 3.00 | $1.57\,^{+0.08}_{-0.09}$ |
| Y Mus | RCrB | -7.08 | 0.04 | -2.76 | 0.04 | 32.74[h] | 1.04 | $5.39\,^{+0.66}_{-0.86}$ |

*a*. Gontcharov (2006) , *b*. de Bruijne and Eilers (2012), *c*. Martin et al. (2017), *d*. Barbier-Brossat and Figon (2000), *e*. Kharchenko et al. (2007b), *f*. Jeffery et al. (1987), *g*. Jeffery priv. comm, *h*. *Gaia*, *i*. Hunger and Kaufmann (1973), *j*. Jeffery et al. (2015b),*k*.Liu and Zhu (2010),*l*. Bobylev (2006),*m*. Clayton et al. (2013)

# C. KINEMATICS INPUT AND OUTPUTS FOR GAIA DR2

**Table C.4:** Proper motions, distances derived from the *Gaia* parallaxes and published radial velocities for the CSPNe.

| Star | Category | $\mu_\alpha$ | $\pm$ | $\mu_\delta$ | $\pm$ | v | $\pm$ | Distance |
|---|---|---|---|---|---|---|---|---|
| FBS 1342+673 | PG1159 | -13.84 | 0.15 | -1.53 | 0.15 | $-75.0^a$ | 57.0 | $0.68^{+0.04}_{-0.04}$ |
| KUV 03467-0108 | PG1159 | 4.64 | 0.25 | -13.68 | 0.22 | $-156.0^a$ | 93.0 | $0.93^{+0.10}_{-0.13}$ |
| KUV 07523+4017 | PG1159 | -9.98 | 0.29 | -1.86 | 0.17 | $39.0^a$ | 51.0 | $1.04^{+0.18}_{-0.28}$ |
| NGC 246 | PG1159 | -16.96 | 0.21 | -8.99 | 0.13 | $-15.7^b$ | 9.9 | $0.52^{+0.03}_{-0.03}$ |
| PG 1424+535 | PG1159 | 0.41 | 0.08 | 14.01 | 0.08 | $-42.0^a$ | 60.0 | $0.55^{+0.02}_{-0.80}$ |
| PN K 1-16 | PG1159 | -3.27 | 0.13 | -3.05 | 0.11 | $-58.6^c$ | 15.0 | $2.21^{+0.23}_{-0.29}$ |
| SBSS 1446+575 | PG1159 | -12.12 | 0.26 | -3.58 | 0.22 | $-84.0^a$ | 57.0 | $1.22^{+0.17}_{-0.23}$ |
| SDSS J055905.02+633448.4 | PG1159 | -0.33 | 0.22 | 1.07 | 0.25 | $-9.0^d$ | 36.0 | $1.79^{+0.50}_{-1.02}$ |
| SDSS J075415.11+085232.1 | PG1159 | 1.12 | 0.58 | -2.93 | 0.33 | $-33.0^d$ | 3.0 | $2.48^{+1.05}_{-2.09}$ |
| SDSS J085422.39+013650.9 | PG1159 | 6.46 | 0.10 | -17.88 | 0.06 | $-30.0^a$ | 30.0 | $2.73^{+0.38}_{-0.51}$ |
| SDSS J093546.53+110529.0 | PG1159 | -15.62 | 0.31 | -7.84 | 0.32 | $-36.0^a$ | 72.0 | $1.12^{+0.24}_{-0.43}$ |
| SDSS J121523.08+120300.7 | PG1159 | -11.19 | 0.33 | -5.63 | 0.20 | $-30.0^a$ | 75.0 | $1.32^{+0.28}_{-0.49}$ |
| SDSS J152046.67+180300.7 | PG1159 | -8.53 | 0.19 | -1.77 | 0.20 | $-103.0^e$ | 5.0 | $4.56^{+1.22}_{-1.93}$ |
| SDSS J191845.01+624343.7 | PG1159 | 1.39 | 0.20 | -0.79 | 0.18 | $-12.0^d$ | 15.0 | $0.88^{+0.06}_{-0.07}$ |
| IR Peg | PG1159 | -9.28 | 0.67 | -4.33 | 0.61 | $-24.0^d$ | 3.0 | $0.11^{+0.01}_{-0.01}$ |
| NGC 6369 | [WC4] | -0.24 | 0.09 | -0.85 | 0.07 | $-100.9^f$ | 1.6 | $1.16^{+0.08}_{-0.09}$ |
| PN Hb 4 | [WC3-4] | 0.14 | 0.37 | -3.75 | 0.30 | $-60.0^f$ | 1.5 | $3.13^{+1.06}_{-1.91}$ |
| PN M 3-15 | [WC4-6] | 0.57 | 0.46 | -4.63 | 0.39 | $97.2^f$ | 0.7 | $2.19^{+0.67}_{-1.35}$ |
| PN M 2-34 | [WC4-5] | -2.14 | 0.13 | -1.36 | 0.12 | $66.7^f$ | 9.4 | $6.00^{+1.40}_{-2.07}$ |
| NGC 6578 | [WC]early | -2.38 | 0.12 | -6.50 | 0.10 | $4.4^f$ | 1.8 | $1.93^{+0.23}_{-0.30}$ |
| PN M 1-32 | [WC4-5] | -4.40 | 0.15 | -6.81 | 0.12 | $-90.6^f$ | 7.6 | $2.75^{+0.48}_{-0.72}$ |
| PN M 1-51 | [WC4-6] | -1.24 | 0.40 | -4.04 | 0.41 | $-6.7^f$ | 8.8 | $2.04^{+0.75}_{-1.64}$ |
| NGC 6905 | [WC3] | -6.94 | 0.08 | -5.53 | 0.08 | $-8.4^f$ | 1.7 | $2.57^{+0.27}_{-0.34}$ |
| HD 184738 | [WC9] | -2.24 | 0.10 | -8.84 | 0.08 | $-31.4^f$ | 0.8 | $1.76^{+0.18}_{-0.22}$ |
| PN A66 78 | Of-WR(C) | -3.11 | 0.10 | 0.35 | 0.10 | $17.0^f$ | 10.0 | $1.63^{+0.16}_{-0.19}$ |
| NGC 40 | [WC8] | -7.25 | 0.06 | -1.81 | 0.04 | $-20.4^f$ | 0.9 | $2.00^{+0.11}_{-0.12}$ |
| IC 1747 | [WC4] | -0.88 | 0.05 | 1.25 | 0.07 | $-66.5^f$ | 3.3 | $3.38^{+0.49}_{-0.68}$ |
| NGC 1501 | [WC4] | 2.20 | 0.04 | -5.20 | 0.04 | $36.2^f$ | 1.4 | $1.77^{+0.08}_{-0.08}$ |
| PN M 4-18 | [WC11] | 0.67 | 0.04 | -0.65 | 0.04 | $-17.0^f$ | 12.0 | $8.30^{+1.50}_{-2.05}$ |
| NGC 2371 | [WC3] | -1.31 | 0.11 | -7.07 | 0.10 | $20.8^f$ | 3.2 | $1.96^{+0.23}_{-0.29}$ |
| NGC 2452 | [WC3] | -2.47 | 0.18 | 3.53 | 0.18 | $62.0^f$ | 2.8 | $2.93^{+0.72}_{-1.24}$ |
| Hen 2-55 | [WC3] | -6.28 | 0.12 | 1.19 | 0.12 | $-21.0^f$ | 0.3 | $5.29^{+1.31}_{-2.00}$ |

**Table** C.4: (continued)

| Star | Category | $\mu_\alpha$ | ± | $\mu_\delta$ | ± | v | ± | Distance |
|------|----------|------|------|------|------|------|------|----------|
| PN Vo 1 | [WC11] | -0.76 | 0.59 | 9.42 | 0.70 | $-55.9^f$ | 4.0 | $0.73 \,^{+0.15}_{-0.26}$ |
| NGC 5189 | [WC2] | -12.69 | 0.05 | -3.43 | 0.06 | $14.0^f$ | 1.0 | $1.70 \,^{+0.09}_{-0.10}$ |
| PN PM 1-89 | [WC4] | -1.15 | 0.08 | -0.28 | 0.06 | $-81.0^f$ | 20.0 | $3.78 \,^{+0.44}_{-0.57}$ |
| Hen 2-142 | [WC9] | -3.87 | 0.26 | -4.61 | 0.24 | $-94.5^f$ | 0.3 | $2.01 \,^{+0.64}_{-1.33}$ |
| PN PC 14 | [WC4] | -9.14 | 1.13 | -4.53 | 1.04 | $-46.0^f$ | 7.2 | $0.55 \,^{+0.15}_{-0.40}$ |
| PN K 2-16 | [WC11] | -2.54 | 0.08 | -2.75 | 0.04 | $5.2^f$ | 12.0 | $7.31 \,^{+1.49}_{-2.10}$ |
| IC 1297 | [WC4] | -1.73 | 0.20 | -5.08 | 0.20 | $10.3^f$ | 1.5 | $3.37 \,^{+0.91}_{-1.55}$ |
| PN K 1-27 | O(He) | 1.13 | 0.08 | 5.95 | 0.09 | $75.0^f$ | 75.0 | $5.40 \,^{+0.99}_{-1.43}$ |

*a.* Adelman-McCarthy et al. (2008) , *b.* Bobylev (2006), *c.* Yuan and Liu (2013), *d.* Ahn et al. (2012), *e.* This work, *f.* Durand et al. (1998)

**Table C.5:** Orbital parameters and galactic velocities, sorted by category. The last column shows which Galactic population each star has been classified into where TH = thin disk, TK = thick disk and H = halo.

| Star | Cat. | U km s$^{-1}$ | ± | V km s$^{-1}$ | ± | W km s$^{-1}$ | ± | $J_z$ kpc km s$^{-1}$ | ± | $e$ | ± | $R_a$ kpc | ± | $R_p$ kpc | ± | $z_{max}$ kpc | ± | pop |
|------|------|------|------|------|------|------|------|------|------|------|------|------|------|------|------|------|------|------|
| BPS CS 22940-0009 | Ex-He | -4.68 | 5.63 | 143.16 | 6.72 | -24.19 | 3.48 | 974.81 | 60.91 | 0.45 | 0.03 | 6.94 | 0.11 | 2.66 | 0.25 | 1.33 | 0.10 | TK |
| BPS CS 29496-0010 | Ex-He | 29.02 | 1.83 | 212.84 | 2.44 | 33.12 | 0.80 | 1698.51 | 25.22 | 0.17 | 0.01 | 8.35 | 0.01 | 5.89 | 0.13 | 1.67 | 0.10 | TK |
| HE 0001-2443 | Ex-He | -25.60 | 0.42 | 145.05 | 2.56 | -9.59 | 0.53 | 1201.84 | 21.60 | 0.47 | 0.01 | 8.38 | 0.00 | 3.05 | 0.09 | 0.76 | 0.00 | TK |
| HE 0342-1702 | Ex-He | -71.08 | 4.21 | 280.10 | 1.90 | -5.23 | 4.45 | 2537.49 | 23.13 | 0.22 | 0.01 | 13.16 | 0.35 | 8.44 | 0.05 | 1.22 | 0.10 | TH |
| HE 1251+0159 | Ex-He | -114.52 | 9.54 | -12.26 | 36.13 | -143.03 | 22.12 | -95.81 | 283.33 | 0.96 | 0.07 | 14.62 | 2.08 | 0.27 | 0.44 | 5.92 | 1.60 | H |
| HS 1844+637 | Ex-He | 23.58 | 3.24 | 291.61 | 5.08 | -14.86 | 3.89 | 2595.13 | 52.56 | 0.24 | 0.02 | 14.64 | 0.75 | 8.92 | 0.07 | 1.89 | 0.20 | TK |
| LB 3229 | Ex-He | -9.46 | 1.63 | 211.95 | 7.30 | 3.19 | 15.10 | 1761.15 | 60.67 | 0.19 | 0.03 | 8.36 | 0.00 | 5.71 | 0.38 | 0.75 | 0.10 | TH |
| PG 0039+135 | Ex-He | -22.67 | 13.65 | 193.51 | 22.25 | 70.75 | 30.18 | 1689.39 | 193.93 | 0.22 | 0.07 | 9.01 | 0.20 | 5.74 | 0.81 | 2.02 | 1.00 | TK |
| PG 0902+057 | Ex-He | -100.36 | 5.08 | 284.97 | 1.87 | -35.30 | 2.52 | 2555.12 | 23.52 | 0.02 | 0.01 | 9.25 | 0.17 | 8.90 | 0.06 | 1.45 | 0.20 | TH |
| PG 1127+019 | Ex-He | -84.91 | 2.63 | 225.17 | 1.04 | 7.10 | 1.07 | 1917.25 | 8.02 | 0.25 | 0.01 | 8.54 | 0.01 | 5.10 | 0.08 | 0.93 | 0.00 | TH |
| PG 1413+114 | Ex-He | -136.53 | 22.16 | 234.66 | 3.94 | 85.86 | 13.82 | 1596.68 | 97.21 | 0.36 | 0.09 | 7.84 | 0.12 | 3.70 | 0.74 | 3.79 | 0.80 | TK |
| PG 1415+492 | Ex-He | -38.58 | 3.39 | 219.79 | 4.11 | 81.59 | 2.01 | 1900.51 | 28.34 | 0.14 | 0.01 | 11.72 | 0.29 | 8.84 | 0.10 | 5.64 | 0.50 | TK |
| PG 1536+690 | Ex-He | -199.20 | 5.53 | 28.72 | 6.48 | -110.15 | 6.90 | 250.32 | 56.45 | 0.95 | 0.02 | 13.40 | 0.35 | 0.34 | 0.11 | 6.36 | 0.70 | H |
| PG 1544+488 | Ex-He | 2.15 | 0.18 | 254.75 | 0.23 | 56.02 | 0.78 | 2126.01 | 1.81 | 0.36 | 0.00 | 10.20 | 0.03 | 4.76 | 0.03 | 0.75 | 0.00 | TK |
| PG 1554+408 | Ex-He | -19.86 | 1.92 | 287.95 | 2.91 | 98.38 | 4.41 | 2240.00 | 27.70 | 0.19 | 0.02 | 11.36 | 0.37 | 7.79 | 0.08 | 4.32 | 0.40 | TK |
| PG 1615+413 | Ex-He | -268.50 | 42.26 | 151.63 | 5.25 | 58.51 | 16.11 | 1172.08 | 33.90 | 0.77 | 0.03 | 10.95 | 1.16 | 1.40 | 0.12 | 5.39 | 2.30 | H |
| PG 1658+273 | Ex-He | -50.57 | 4.39 | 212.09 | 1.88 | 42.18 | 4.57 | 1510.89 | 22.56 | 0.34 | 0.02 | 7.30 | 0.06 | 3.57 | 0.19 | 1.71 | 0.20 | TK |
| PG 1715+273 | Ex-He | -41.15 | 1.43 | 254.64 | 2.25 | 32.44 | 1.76 | 1785.42 | 38.78 | 0.06 | 0.00 | 7.46 | 0.18 | 6.60 | 0.16 | 1.79 | 0.20 | TK |
| PG 2215+151 | Ex-He | 81.97 | 3.33 | 276.39 | 2.59 | 53.33 | 2.21 | 2271.65 | 20.96 | 0.29 | 0.01 | 13.27 | 0.31 | 7.35 | 0.05 | 1.98 | 0.10 | TK |
| PG 2258+155 | Ex-He | -6.91 | 0.76 | 304.69 | 2.91 | 13.71 | 2.46 | 2558.84 | 25.37 | 0.27 | 0.01 | 14.58 | 0.38 | 8.45 | 0.01 | 1.41 | 0.10 | TK |

**Table** C.5: Orbital parameters and galactic velocities (continued)

| Star | Cat. | U<br>km s$^{-1}$ | ± | V<br>km s$^{-1}$ | ± | W<br>km s$^{-1}$ | ± | $J_z$<br>kpc km s$^{-1}$ | ± | $e$ | ± | $R_a$<br>kpc | ± | $R_p$<br>kpc | ± | $z_{max}$<br>kpc | ± | pop |
|---|---|---|---|---|---|---|---|---|---|---|---|---|---|---|---|---|---|---|
| PG 2321+214 | Ex-He | 62.95 | 2.23 | 186.84 | 2.11 | -35.85 | 2.11 | 1590.80 | 17.27 | 0.35 | 0.01 | 9.33 | 0.05 | 4.48 | 0.10 | 0.95 | 0.10 | TK |
| PG 2352+181 | Ex-He | 91.69 | 5.65 | 160.72 | 15.16 | 10.38 | 14.06 | 1377.95 | 129.73 | 0.48 | 0.04 | 9.75 | 0.31 | 3.40 | 0.48 | 0.72 | 0.20 | TK |
| BPS CS 22956-0094 | Inter-He | 49.73 | 3.52 | 182.54 | 2.66 | 10.98 | 4.15 | 1476.21 | 21.86 | 0.48 | 0.01 | 9.18 | 0.10 | 3.26 | 0.08 | 0.40 | 0.00 | TH |
| CPD-20 1123 | Inter-He | -33.96 | 0.52 | 233.78 | 0.58 | 6.22 | 0.24 | 2015.01 | 4.66 | 0.14 | 0.00 | 9.45 | 0.03 | 7.15 | 0.02 | 0.13 | 0.00 | TH |
| HD 127493 | Inter-He | -42.42 | 1.15 | 244.30 | 0.67 | 19.35 | 0.93 | 2022.78 | 5.54 | 0.11 | 0.00 | 8.28 | 0.00 | 6.59 | 0.04 | 0.18 | 0.00 | TH |
| HE 1135-1134 | Inter-He | -181.83 | 26.17 | 258.90 | 2.47 | 51.43 | 4.16 | 2229.59 | 12.56 | 0.11 | 0.01 | 9.54 | 0.47 | 7.68 | 0.25 | 3.00 | 0.60 | TK |
| HE 1136-2504 | Inter-He | -84.07 | 2.47 | 196.42 | 4.60 | 17.79 | 3.16 | 1622.55 | 38.13 | 0.33 | 0.02 | 8.37 | 0.00 | 4.21 | 0.17 | 0.71 | 0.00 | TH |
| HE 1238-1745 | Inter-He | -105.10 | 5.88 | 294.49 | 1.84 | 53.41 | 3.07 | 2344.86 | 9.82 | 0.17 | 0.01 | 9.25 | 0.11 | 6.54 | 0.11 | 1.26 | 0.10 | TH |
| HE 1256-2738 | Inter-He | -260.84 | 22.85 | 145.87 | 5.68 | 130.13 | 5.54 | 1117.80 | 54.00 | 0.84 | 0.04 | 8.09 | 0.10 | 0.69 | 0.19 | 1.77 | 0.70 | H |
| HE 1310-2733 | Inter-He | -47.71 | 0.90 | 214.58 | 0.92 | 15.43 | 0.90 | 1683.00 | 10.59 | 0.22 | 0.00 | 8.91 | 0.02 | 5.65 | 0.05 | 0.93 | 0.00 | TH |
| HE 2218-2026 | Inter-He | 242.11 | 10.41 | -99.03 | 30.67 | 66.29 | 18.75 | -720.57 | 213.91 | 0.70 | 0.03 | 13.70 | 0.97 | 2.43 | 0.46 | 7.85 | 0.70 | H |
| HE 2357-3940 | Inter-He | 59.54 | 5.49 | 238.76 | 1.39 | 7.21 | 6.81 | 1928.62 | 16.20 | 0.25 | 0.02 | 9.96 | 0.19 | 5.96 | 0.17 | 1.31 | 0.10 | TH |
| HE 2359-2844 | Inter-He | 31.10 | 2.63 | 165.67 | 9.11 | 85.63 | 2.04 | 1328.11 | 80.19 | 0.29 | 0.03 | 8.41 | 0.02 | 4.59 | 0.33 | 3.56 | 0.20 | TK |
| HS 1051+2933 | Inter-He | -46.88 | 7.53 | -63.47 | 82.17 | -105.93 | 1.66 | -606.76 | 776.95 | 0.94 | 0.14 | 21.99 | 5.86 | 0.64 | 1.16 | 4.20 | 3.40 | H |
| JL 87 | Inter-He | -28.77 | 0.96 | 267.50 | 0.90 | 4.78 | 0.89 | 2120.80 | 7.09 | 0.12 | 0.00 | 9.74 | 0.05 | 7.67 | 0.03 | 0.56 | 0.00 | TH |
| LS IV−14°116 | Inter-He | 25.33 | 1.70 | -41.25 | 4.11 | -4.53 | 1.94 | -334.38 | 33.09 | 0.80 | 0.02 | 8.14 | 0.01 | 0.89 | 0.09 | 0.22 | 0.00 | H |
| PG 0229+064 | Inter-He | 43.54 | 1.77 | 205.11 | 1.23 | 16.24 | 1.73 | 1812.63 | 9.06 | 0.20 | 0.01 | 9.14 | 0.03 | 6.12 | 0.06 | 0.66 | 0.00 | TH |
| PG 0240+046 | Inter-He | 117.99 | 2.47 | 184.93 | 2.24 | -3.77 | 1.39 | 1635.63 | 17.55 | 0.37 | 0.01 | 10.56 | 0.05 | 4.83 | 0.08 | 0.58 | 0.00 | TK |
| PG 0909+276 | Inter-He | 2.49 | 0.84 | 248.07 | 0.30 | 21.02 | 0.77 | 2131.70 | 2.57 | 0.00 | 0.00 | 8.64 | 0.01 | 8.57 | 0.02 | 0.39 | 0.00 | TH |
| SB 705 | Inter-He | 37.76 | 1.38 | 258.06 | 1.68 | 6.09 | 6.10 | 2173.39 | 14.24 | 0.14 | 0.01 | 10.24 | 0.13 | 7.70 | 0.08 | 1.07 | 0.10 | TH |
| SDSS J092440.11+305013.16 | Inter-He | 19.46 | 2.50 | 154.12 | 7.56 | 23.48 | 1.13 | 1467.62 | 58.35 | 0.28 | 0.02 | 10.44 | 0.17 | 5.85 | 0.17 | 2.07 | 0.30 | TK |
| SDSS J160131.30+044027.00 | Inter-He | -32.73 | 1.14 | 246.89 | 0.16 | 35.19 | 1.23 | 1933.17 | 3.86 | 0.19 | 0.00 | 8.07 | 0.01 | 5.53 | 0.05 | 0.62 | 0.00 | TH |

**Table** C.5: Orbital parameters and galactic velocities (continued)

| Star | Cat. | U km s$^{-1}$ | ± | V km s$^{-1}$ | ± | W km s$^{-1}$ | ± | $J_z$ kpc km s$^{-1}$ | ± | $e$ | ± | $R_a$ kpc | ± | $R_p$ kpc | ± | $z_{max}$ kpc | ± | pop |
|---|---|---|---|---|---|---|---|---|---|---|---|---|---|---|---|---|---|---|
| SDSS J175548.50+501210.77 | Inter-He | 58.83 | 0.70 | 203.00 | 0.11 | 2.55 | 0.32 | 1687.14 | 0.94 | 0.32 | 0.00 | 9.15 | 0.02 | 4.76 | 0.01 | 0.31 | 0.00 | TH |
| TON 107 | Inter-He | -154.87 | 16.63 | 113.86 | 14.73 | 120.31 | 9.50 | 1008.62 | 124.29 | 0.74 | 0.09 | 9.21 | 0.14 | 1.35 | 0.53 | 6.50 | 1.40 | H |
| UVO 0825+15 | Inter-He | 0.10 | 0.41 | 256.02 | 0.32 | 15.50 | 0.23 | 2206.39 | 3.26 | 0.17 | 0.00 | 9.53 | 0.01 | 6.77 | 0.01 | 0.18 | 0.00 | TH |
| KUV16160+4120 | He-sdB | -273.29 | 34.87 | 183.57 | 4.84 | 92.37 | 14.37 | 1418.91 | 31.44 | 0.65 | 0.03 | 11.53 | 0.98 | 2.43 | 0.14 | 7.16 | 1.77 | H |
| PG1554+408 | He-sdB | -3.41 | 1.38 | 207.07 | 3.47 | -1.85 | 5.33 | 1610.86 | 28.55 | 0.29 | 0.02 | 8.22 | 0.04 | 4.54 | 0.16 | 2.41 | 0.19 | TK |
| SDSSJ082216.14 +133822.6 | He-sdB | 14.64 | 15.77 | 229.67 | 8.72 | 18.90 | 8.62 | 1977.50 | 75.04 | 0.22 | 0.06 | 9.17 | 0.26 | 5.89 | 0.60 | 0.22 | 0.11 | TH |
| SDSSJ232404.68 -001812.9 | He-sdB | 11.68 | 3.39 | 241.99 | 18.24 | -74.77 | 27.06 | 2024.51 | 152.64 | 0.05 | 0.05 | 8.88 | 1.44 | 8.03 | 0.83 | 1.68 | 1.05 | TK |
| PG0912+119 | He-sdO | -70.61 | 15.11 | 109.60 | 17.94 | -12.55 | 10.93 | 1160.17 | 143.66 | 0.69 | 0.08 | 10.73 | 0.40 | 1.93 | 0.54 | 2.49 | 0.72 | TK |
| PG1203+084 | He-sdO | -110.90 | 10.05 | 98.89 | 20.92 | -74.44 | 8.70 | 838.34 | 175.58 | 0.67 | 0.07 | 10.52 | 0.34 | 2.09 | 0.50 | 3.44 | 0.49 | TK |
| PG1248+066 | He-sdO | -190.72 | 22.60 | 177.95 | 11.57 | 51.94 | 4.18 | 1400.29 | 102.94 | 0.58 | 0.07 | 8.48 | 0.09 | 2.28 | 0.47 | 3.30 | 0.39 | TK |
| PG1301+270 | He-sdO | -155.19 | 20.82 | 408.55 | 22.73 | 100.82 | 17.76 | 3385.05 | 181.99 | 0.70 | 0.08 | 27.17 | 7.11 | 4.87 | 0.15 | 17.15 | 7.39 | H |
| PG1348+607 | He-sdO | -276.10 | 37.48 | 92.19 | 6.58 | 117.39 | 32.65 | 941.14 | 55.31 | 0.55 | 0.20 | 13.49 | 1.37 | 3.94 | 2.19 | 12.38 | 2.12 | H |
| PG1413+114 | He-sdO | -137.25 | 17.89 | 234.61 | 3.33 | 87.44 | 8.88 | 1596.35 | 81.55 | 0.36 | 0.08 | 7.85 | 0.08 | 3.70 | 0.66 | 3.81 | 0.65 | TK |
| PG1425+590 | He-sdO | -86.82 | 4.02 | 254.81 | 2.16 | 160.16 | 7.94 | 2212.80 | 19.69 | 0.59 | 0.03 | 11.04 | 0.20 | 2.85 | 0.22 | 4.63 | 0.36 | TK |
| PG1441+407 | He-sdO | -320.92 | 32.33 | 88.40 | 9.09 | 108.84 | 13.37 | 710.35 | 75.25 | 0.75 | 0.06 | 13.27 | 1.46 | 1.91 | 0.71 | 13.09 | 2.33 | H |
| PG1507-015 | He-sdO | -23.38 | 12.14 | 274.99 | 2.47 | 20.63 | 12.56 | 1691.93 | 73.91 | 0.32 | 0.03 | 8.48 | 0.17 | 4.37 | 0.37 | 3.17 | 0.54 | TK |
| PG1528+029 | He-sdO | -60.39 | 5.64 | 232.33 | 1.20 | 31.39 | 4.99 | 1642.39 | 24.69 | 0.29 | 0.01 | 7.31 | 0.06 | 4.07 | 0.15 | 1.40 | 0.07 | TH |
| PG1539+442 | He-sdO | -147.75 | 18.90 | 211.27 | 5.17 | 68.37 | 10.17 | 1683.89 | 44.08 | 0.33 | 0.02 | 10.05 | 0.58 | 5.03 | 0.37 | 6.11 | 1.20 | TK |
| PG1608+374 | He-sdO | -612.92 | 78.14 | 172.57 | 34.43 | 124.11 | 24.77 | 1254.03 | 244.58 | 0.93 | 0.03 | 116.92 | 92.41 | 4.48 | 1.51 | 66.91 | 28.22 | H |
| PG1610+043 | He-sdO | -72.98 | 5.46 | 232.73 | 2.10 | 47.80 | 4.03 | 1535.52 | 47.64 | 0.20 | 0.02 | 6.76 | 0.14 | 4.50 | 0.27 | 1.64 | 0.14 | TK |
| PG1617+077 | He-sdO | -163.79 | 12.34 | 215.58 | 5.98 | 63.67 | 2.78 | 1280.83 | 109.39 | 0.35 | 0.03 | 7.38 | 0.33 | 3.52 | 0.39 | 3.10 | 0.43 | TK |
| PG1624+085 | He-sdO | -76.64 | 4.33 | 207.60 | 2.41 | 19.94 | 2.01 | 1465.06 | 31.23 | 0.30 | 0.02 | 7.25 | 0.07 | 3.88 | 0.17 | 1.15 | 0.07 | TH |

**Table** C.5: Orbital parameters and galactic velocities (continued)

| Star | Cat. | U $\mathrm{km\,s^{-1}}$ | ± | V $\mathrm{km\,s^{-1}}$ | ± | W $\mathrm{km\,s^{-1}}$ | ± | $J_z$ kpc $\mathrm{km\,s^{-1}}$ | ± | $e$ | ± | $R_a$ kpc | ± | $R_p$ kpc | ± | $z_{max}$ kpc | ± | pop |
|---|---|---|---|---|---|---|---|---|---|---|---|---|---|---|---|---|---|---|
| PG1624+382 | He-sdO | -31.00 | 1.72 | 243.10 | 3.04 | 57.52 | 4.33 | 1882.03 | 25.07 | 0.18 | 0.02 | 8.07 | 0.02 | 5.59 | 0.25 | 1.96 | 0.13 | TK |
| PG1700+198 | He-sdO | -66.24 | 5.54 | 218.01 | 3.15 | 77.68 | 6.37 | 1554.02 | 27.93 | 0.40 | 0.02 | 7.33 | 0.06 | 3.12 | 0.17 | 1.66 | 0.15 | TK |
| PG1722+317 | He-sdO | -111.43 | 7.27 | 275.73 | 4.83 | 105.35 | 7.94 | 1996.84 | 29.34 | 0.12 | 0.01 | 7.98 | 0.15 | 6.29 | 0.20 | 2.95 | 0.30 | TK |
| PG2110+001 | He-sdO | -146.78 | 18.31 | 247.48 | 6.75 | 11.28 | 4.77 | 1666.25 | 32.38 | 0.38 | 0.05 | 10.49 | 0.75 | 4.66 | 0.25 | 2.33 | 0.72 | TK |
| PG2116+008 | He-sdO | 57.47 | 9.69 | 214.05 | 8.22 | -22.71 | 4.18 | 1461.05 | 82.98 | 0.21 | 0.04 | 8.00 | 0.13 | 5.24 | 0.37 | 2.18 | 0.32 | TK |
| SDSSJ041536.05 +253857.11 | He-sdO | -8.38 | 8.55 | 260.47 | 1.43 | 10.69 | 2.88 | 2582.15 | 29.76 | 0.08 | 0.01 | 11.53 | 0.18 | 9.90 | 0.13 | 0.58 | 0.04 | TH |
| SDSSJ044149.12 +100821.7 | He-sdO | -14.41 | 16.23 | 206.40 | 13.29 | -57.09 | 14.15 | 2214.93 | 45.11 | 0.16 | 0.04 | 10.81 | 0.71 | 7.89 | 0.30 | 2.36 | 0.86 | TK |
| SDSSJ073856.98 +401942.0 | He-sdO | -9.02 | 13.49 | 165.43 | 15.27 | 5.66 | 6.33 | 2022.48 | 64.64 | 0.28 | 0.04 | 13.17 | 0.75 | 7.39 | 0.28 | 2.29 | 0.45 | TK |
| SDSSJ074613.16 +333307.6 | He-sdO | -40.21 | 7.44 | 280.76 | 4.09 | -25.46 | 6.06 | 3187.46 | 165.16 | 0.11 | 0.01 | 13.54 | 0.83 | 10.96 | 0.45 | 2.52 | 0.57 | TK |
| SDSSJ080833.76 +180221.8 | He-sdO | 5.48 | 19.79 | -96.92 | 65.29 | -33.19 | 3.60 | -1197.32 | 825.38 | 0.90 | 0.07 | 18.63 | 2.83 | 0.96 | 0.83 | 3.45 | 2.01 | H |
| SDSSJ083747.22 +194955.8 | He-sdO | -218.38 | 41.57 | 293.00 | 9.02 | -102.75 | 22.84 | 3622.71 | 318.66 | 0.16 | 0.07 | 17.27 | 3.39 | 12.54 | 0.97 | 9.84 | 3.40 | H |
| SDSSJ090252.99 +073533.9 | He-sdO | -46.23 | 9.17 | 52.76 | 42.59 | -60.77 | 5.23 | 541.86 | 399.54 | 0.79 | 0.10 | 19.49 | 1.80 | 2.30 | 0.91 | 2.78 | 0.62 | TK |
| SDSSJ103806.64 +134412.0 | He-sdO | -50.71 | 5.90 | 116.27 | 24.46 | -8.80 | 7.11 | 1167.13 | 199.03 | 0.54 | 0.10 | 11.87 | 0.80 | 3.52 | 0.77 | 4.04 | 0.93 | TK |
| SDSSJ125301.62 +394622.1 | He-sdO | -101.03 | 15.39 | 32.13 | 35.64 | -110.73 | 7.31 | 286.09 | 309.52 | 0.81 | 0.10 | 16.16 | 2.16 | 1.74 | 0.70 | 5.97 | 1.01 | H |
| SDSSJ132747.87 +564040.14 | He-sdO | -6.69 | 3.44 | 229.94 | 5.81 | -9.39 | 10.32 | 2059.67 | 45.71 | 0.10 | 0.02 | 9.18 | 0.21 | 7.47 | 0.31 | 2.08 | 0.40 | TK |
| SDSSJ151415.66 -012925.2 | He-sdO | -88.71 | 17.68 | 201.45 | 8.18 | 4.58 | 7.36 | 1434.69 | 96.55 | 0.47 | 0.07 | 7.34 | 0.18 | 2.65 | 0.57 | 1.53 | 0.20 | TK |

**Table** C.5: Orbital parameters and galactic velocities (continued)

| Star | Cat. | U km s$^{-1}$ | ± | V km s$^{-1}$ | ± | W km s$^{-1}$ | ± | J$_z$ kpc km s$^{-1}$ | ± | e | ± | R$_a$ kpc | ± | R$_p$ kpc | ± | z$_{max}$ kpc | ± | pop |
|---|---|---|---|---|---|---|---|---|---|---|---|---|---|---|---|---|---|---|
| SDSSJ152136.25 +162150.3 | He-sdO | -99.34 | 23.57 | 214.34 | 1.90 | 44.50 | 22.33 | 1537.22 | 38.19 | 0.81 | 0.09 | 9.01 | 0.09 | 0.97 | 0.52 | 3.52 | 0.64 | H |
| SDSSJ152143.87 +450022.5 | He-sdO | -40.30 | 6.85 | 192.96 | 2.28 | 4.93 | 9.68 | 1564.23 | 19.23 | 0.42 | 0.05 | 8.93 | 0.26 | 3.62 | 0.33 | 3.86 | 0.61 | TK |
| SDSSJ153021.99 +343423.6 | He-sdO | -8.16 | 2.58 | 247.78 | 3.57 | 57.90 | 13.04 | 1834.93 | 32.91 | 0.37 | 0.06 | 9.11 | 0.28 | 4.17 | 0.52 | 3.56 | 0.66 | TK |
| SDSSJ153251.11 +050536.6 | He-sdO | -256.04 | 37.98 | 233.74 | 2.50 | 203.80 | 31.30 | 1239.61 | 113.81 | 0.89 | 0.14 | 7.38 | 0.23 | 0.42 | 0.67 | 4.75 | 1.06 | H |
| SDSSJ160325.51 +341237.4 | He-sdO | -25.18 | 3.35 | 260.78 | 8.00 | 110.97 | 16.84 | 1833.57 | 55.55 | 0.42 | 0.08 | 9.22 | 0.43 | 3.79 | 0.60 | 4.81 | 0.79 | TK |
| SDSSJ161014.87 +045046.6 | He-sdO | 61.37 | 23.51 | 264.30 | 3.58 | -26.27 | 12.67 | 1410.89 | 159.14 | 0.38 | 0.05 | 12.83 | 0.82 | 5.78 | 0.33 | 5.21 | 1.31 | TK |
| SDSSJ161059.80 +053625.2 | He-sdO | 66.66 | 8.66 | 196.61 | 2.98 | -28.08 | 14.16 | 1133.88 | 110.92 | 0.55 | 0.04 | 8.03 | 0.44 | 2.35 | 0.39 | 4.19 | 0.43 | TK |
| SDSSJ162626.25 +333315.0 | He-sdO | 23.38 | 6.75 | 240.34 | 4.12 | 79.75 | 19.47 | 1716.77 | 37.12 | 0.48 | 0.09 | 9.29 | 0.42 | 3.25 | 0.63 | 3.37 | 0.76 | TK |
| SDSSJ173119.14 +313831.1 | He-sdO | -109.17 | 8.79 | 337.71 | 8.68 | 165.39 | 22.58 | 2446.15 | 55.70 | 0.26 | 0.04 | 12.46 | 1.28 | 7.38 | 0.10 | 5.63 | 0.93 | TK |
| SDSSJ180757.08 +230133.0 | He-sdO | 72.15 | 19.63 | 248.02 | 10.31 | -72.88 | 15.54 | 1629.96 | 115.56 | 0.25 | 0.02 | 11.03 | 0.33 | 6.64 | 0.16 | 2.77 | 0.58 | TK |
| SDSSJ184359.81 +634651.7 | He-sdO | 23.09 | 2.83 | 290.24 | 2.78 | -15.55 | 2.80 | 2582.91 | 35.19 | 0.24 | 0.01 | 14.45 | 0.49 | 8.92 | 0.06 | 1.88 | 0.17 | TK |
| SDSSJ211423.98 -001034.7 | He-sdO | 22.55 | 4.67 | 178.69 | 12.48 | -29.43 | 8.35 | 1211.75 | 120.75 | 0.28 | 0.05 | 7.22 | 0.09 | 4.05 | 0.48 | 2.06 | 0.41 | TK |
| SDSSJ214612.17 +005110.0 | He-sdO | 114.85 | 12.74 | 73.18 | 22.26 | -5.25 | 20.71 | 543.60 | 187.03 | 0.73 | 0.09 | 8.46 | 0.05 | 1.34 | 0.53 | 1.75 | 0.19 | H |
| SDSSJ215553.90 +202802.9 | He-sdO | 207.49 | 16.76 | 179.87 | 8.45 | -1.16 | 2.94 | 1465.95 | 66.75 | 0.60 | 0.04 | 14.68 | 0.89 | 3.64 | 0.27 | 2.45 | 0.35 | TK |
| SDSSJ220429.52 +211610.8 | He-sdO | -292.87 | 31.83 | 61.52 | 10.94 | 25.48 | 8.31 | 509.11 | 92.09 | 0.92 | 0.01 | 19.90 | 3.79 | 0.84 | 0.17 | 2.97 | 0.89 | H |

**Table** C.5: Orbital parameters and galactic velocities (continued)

| Star | Cat. | U km s$^{-1}$ | $\pm$ | V km s$^{-1}$ | $\pm$ | W km s$^{-1}$ | $\pm$ | J$_z$ kpc km s$^{-1}$ | $\pm$ | $e$ | $\pm$ | R$_a$ kpc | $\pm$ | R$_p$ kpc | $\pm$ | z$_{max}$ kpc | $\pm$ | pop |
|---|---|---|---|---|---|---|---|---|---|---|---|---|---|---|---|---|---|---|
| SDSSJ231726.22 +205416.82 | He-sdO | -41.93 | 7.05 | 190.02 | 3.70 | 16.38 | 8.90 | 1715.90 | 68.42 | 0.27 | 0.01 | 9.88 | 0.47 | 5.72 | 0.37 | 2.19 | 0.41 | TK |
| SDSSJ232757.46 +483755.2 | He-sdO | -15.98 | 13.10 | 208.07 | 15.94 | 41.83 | 4.36 | 2293.17 | 224.41 | 0.14 | 0.05 | 12.88 | 1.32 | 9.65 | 1.28 | 2.03 | 0.35 | TK |
| SDSSJ233541.47 +000219.4 | He-sdO | 60.90 | 9.49 | 224.03 | 10.26 | -25.56 | 12.06 | 1874.26 | 84.44 | 0.22 | 0.04 | 10.12 | 0.46 | 6.54 | 0.44 | 2.27 | 0.34 | TK |
| PG1258+012 | He-sdOB | -130.02 | 14.41 | 319.52 | 6.29 | 70.27 | 9.84 | 2497.85 | 33.72 | 0.30 | 0.03 | 11.17 | 0.52 | 6.04 | 0.19 | 2.41 | 0.33 | TK |
| PG1715+273 | He-sdOB | -38.03 | 2.66 | 247.76 | 4.97 | 27.66 | 3.63 | 1737.18 | 47.13 | 0.08 | 0.01 | 7.32 | 0.13 | 6.29 | 0.25 | 1.73 | 0.16 | TK |
| SDSSJ072824.72 +414953.7 | He-sdOB | 8.01 | 7.03 | 215.84 | 3.21 | 4.94 | 3.13 | 2292.19 | 10.45 | 0.11 | 0.01 | 10.65 | 0.21 | 8.50 | 0.08 | 1.04 | 0.09 | TH |
| SDSSJ073220.14 +270408.5 | He-sdOB | 93.88 | 6.46 | 196.35 | 3.70 | 26.34 | 3.67 | 1966.89 | 15.14 | 0.43 | 0.02 | 12.56 | 0.32 | 5.05 | 0.15 | 0.88 | 0.08 | TK |
| SDSSJ124552.82 +175112.2 | He-sdOB | -297.87 | 61.71 | 164.09 | 18.50 | 189.92 | 15.15 | 1355.69 | 158.23 | 0.91 | 0.14 | 10.36 | 0.69 | 0.49 | 0.79 | 5.11 | 0.50 | H |
| SDSSJ131218.11 +381535.2 | He-sdOB | -93.39 | 22.54 | 162.18 | 20.10 | -45.27 | 11.48 | 1394.36 | 161.59 | 0.49 | 0.12 | 9.41 | 0.32 | 3.22 | 1.02 | 3.54 | 0.60 | TK |
| SDSSJ134352.14 +394008.3 | He-sdOB | -230.63 | 41.86 | 199.65 | 12.11 | 248.82 | 28.10 | 1685.18 | 98.67 | 0.43 | 0.06 | 10.73 | 0.87 | 4.23 | 0.65 | 10.58 | 1.84 | H |
| SDSSJ134621.23 +224836.7 | He-sdOB | -175.92 | 25.05 | 256.05 | 1.20 | 160.56 | 16.74 | 1920.28 | 35.98 | 0.57 | 0.11 | 10.23 | 0.56 | 2.79 | 0.77 | 5.89 | 0.83 | TK |
| SDSSJ140453.68 +124428.5 | He-sdOB | -258.81 | 46.07 | 33.63 | 42.56 | -14.66 | 8.42 | 227.01 | 313.28 | 0.84 | 0.10 | 9.28 | 0.57 | 0.80 | 0.58 | 5.04 | 1.15 | H |
| SDSSJ142558.43 +402257.8 | He-sdOB | -175.31 | 41.73 | 108.75 | 21.11 | 0.18 | 17.40 | 886.05 | 177.72 | 0.77 | 0.12 | 10.14 | 0.72 | 1.29 | 0.73 | 4.13 | 1.38 | H |
| SDSSJ143729.14 -021506.0 | He-sdOB | -106.13 | 9.49 | 266.32 | 1.74 | 95.05 | 9.30 | 1953.47 | 21.33 | 0.21 | 0.02 | 7.84 | 0.05 | 5.14 | 0.24 | 2.04 | 0.21 | TK |
| SDSSJ152046.66 +180300.7 | He-sdOB | -100.91 | 21.94 | 229.55 | 5.05 | 72.35 | 24.80 | 1419.02 | 52.27 | 0.80 | 0.13 | 8.26 | 0.17 | 0.90 | 0.69 | 4.84 | 0.96 | H |

**Table** C.5: Orbital parameters and galactic velocities (continued)

| Star | Cat. | U km s$^{-1}$ | ± | V km s$^{-1}$ | ± | W km s$^{-1}$ | ± | J$_z$ kpc km s$^{-1}$ | ± | e | ± | R$_a$ kpc | ± | R$_p$ kpc | ± | z$_{max}$ kpc | ± | pop |
|---|---|---|---|---|---|---|---|---|---|---|---|---|---|---|---|---|---|---|
| SDSSJ153419.42 +372557.2 | He-sdOB | -127.51 | 24.24 | 283.87 | 6.14 | 179.33 | 24.45 | 2203.67 | 84.59 | 0.10 | 0.07 | 9.76 | 1.66 | 7.99 | 0.10 | 5.76 | 0.85 | TK |
| SDSSJ153526.07 +211441.0 | He-sdOB | -100.34 | 10.69 | 200.56 | 4.96 | 33.44 | 4.13 | 1403.06 | 66.78 | 0.35 | 0.04 | 7.50 | 0.06 | 3.60 | 0.33 | 2.38 | 0.28 | TK |
| SDSSJ155202.72 +261542.9 | He-sdOB | -116.54 | 19.66 | 213.73 | 5.85 | 64.57 | 14.03 | 1423.12 | 74.20 | 0.41 | 0.07 | 7.45 | 0.04 | 3.15 | 0.56 | 3.72 | 0.74 | TK |
| SDSSJ155344.97 +124313.7 | He-sdOB | -44.18 | 44.10 | 136.66 | 24.59 | -64.07 | 12.34 | 920.06 | 265.89 | 0.65 | 0.15 | 7.08 | 0.62 | 1.52 | 1.15 | 3.80 | 0.54 | TK |
| SDSSJ161624.36 +265314.7 | He-sdOB | -60.17 | 3.94 | 183.03 | 3.54 | -26.92 | 3.87 | 1380.49 | 30.90 | 0.34 | 0.02 | 8.07 | 0.04 | 3.99 | 0.15 | 1.48 | 0.08 | TK |
| SDSSJ161804.93 +204104.1 | He-sdOB | -179.10 | 24.56 | 226.14 | 5.06 | 100.50 | 11.19 | 1518.44 | 90.80 | 0.36 | 0.05 | 7.67 | 0.18 | 3.61 | 0.57 | 3.68 | 0.73 | TK |
| SDSSJ163416.08 +221141.0 | He-sdOB | -34.64 | 2.61 | 238.55 | 2.46 | 32.35 | 3.14 | 1752.21 | 21.56 | 0.13 | 0.01 | 7.44 | 0.04 | 5.70 | 0.18 | 1.33 | 0.07 | TH |
| SDSSJ183317.70 +642737.0 | He-sdOB | 27.76 | 5.46 | 265.95 | 3.49 | 77.94 | 10.42 | 2385.79 | 34.39 | 0.18 | 0.02 | 11.96 | 0.57 | 8.39 | 0.06 | 2.78 | 0.57 | TK |
| SDSSJ222515.34 -011157.0 | He-sdOB | 133.64 | 7.52 | -69.29 | 23.70 | 234.11 | 12.82 | -513.43 | 173.58 | 0.21 | 0.05 | 12.85 | 1.36 | 8.38 | 0.47 | 12.42 | 1.27 | H |
| TON261 | He-sdOB | 53.75 | 3.06 | 222.72 | 2.35 | -37.48 | 2.39 | 1636.86 | 23.87 | 0.10 | 0.01 | 8.00 | 0.02 | 6.50 | 0.10 | 1.68 | 0.10 | TK |
| SDSSJ154641.88 +062539.2 | He-sdOB* | 4.07 | 10.70 | 232.88 | 1.56 | 2.33 | 12.96 | 1559.29 | 72.25 | 0.39 | 0.05 | 8.02 | 0.27 | 3.49 | 0.53 | 2.25 | 0.28 | TK |

**Table C.6:** Orbital parameters and galactic velocities, sorted by category. The last column shows which Galactic population each star has been classified into where TH = thin disk, TK = thick disk, H = halo and B = bulge.

| Star | Category | U km s$^{-1}$ | ± | V km s$^{-1}$ | ± | W km s$^{-1}$ | ± | J$_z$ kpc km s$^{-1}$ | ± | e | ± | R$_a$ kpc | ± | R$_p$ kpc | ± | z$_{max}$ kpc | ± | pop |
|------|----------|------|---|------|---|------|---|------|---|---|---|------|---|------|---|------|---|-----|
| HD 137613 | HdC | -79.44 | 0.89 | 205.38 | 1.33 | 7.87 | 0.98 | 1439.58 | 18.09 | 0.29 | 0.00 | 8.22 | 0.04 | 4.50 | 0.07 | 0.57 | 0.01 | TH |
| HD 175893 | HdC | -32.03 | 2.38 | 211.49 | 3.68 | -40.37 | 2.87 | 1094.67 | 62.95 | 0.16 | 0.00 | 5.53 | 0.27 | 4.01 | 0.21 | 1.00 | 0.07 | TH |
| HD 182040 | HdC | 73.29 | 1.15 | 241.89 | 0.24 | -10.77 | 0.70 | 1839.11 | 2.76 | 0.17 | 0.00 | 9.10 | 0.02 | 6.39 | 0.02 | 0.21 | 0.01 | TH |
| HD 148839 | HdC | -32.67 | 1.08 | 237.03 | 0.93 | 37.38 | 0.70 | 1556.97 | 15.33 | 0.11 | 0.00 | 7.18 | 0.03 | 5.73 | 0.07 | 0.56 | 0.01 | TH |
| HD 173409 | HdC | 71.52 | 0.90 | 226.42 | 1.08 | -9.24 | 1.30 | 1429.55 | 23.27 | 0.20 | 0.00 | 7.29 | 0.09 | 4.81 | 0.08 | 0.47 | 0.02 | TH |
| DY Per | RCrB | -11.85 | 2.88 | 220.78 | 2.38 | 11.27 | 0.41 | 1969.21 | 19.25 | 0.13 | 0.01 | 9.36 | 0.03 | 7.14 | 0.16 | 0.16 | 0.01 | TH |
| SV Sge | RCrB | 15.63 | 1.63 | 245.55 | 0.46 | 30.23 | 1.27 | 1634.51 | 17.68 | 0.12 | 0.01 | 7.53 | 0.02 | 5.96 | 0.11 | 0.37 | 0.02 | TH |
| S Aps | RCrB | -106.07 | 7.78 | 254.89 | 5.21 | 78.77 | 2.81 | 1583.10 | 24.30 | 0.07 | 0.01 | 7.28 | 0.14 | 6.27 | 0.13 | 0.16 | 0.04 | TH |
| LT Dra | RCrB | 3.81 | 0.06 | 235.93 | 0.08 | 6.62 | 0.07 | 1890.26 | 0.72 | 0.07 | 0.00 | 8.38 | 0.00 | 7.22 | 0.21 | 1.19 | 0.17 | TH |
| WX CrA | RCrB | 26.77 | 6.45 | 81.66 | 15.51 | -142.53 | 21.17 | 122.48 | 108.35 | 0.51 | 0.05 | 2.14 | 0.59 | 0.70 | 0.32 | 1.51 | 0.11 | B |
| U Aqr | RCrB | 63.03 | 16.61 | 229.72 | 11.72 | -112.20 | 6.91 | 1391.82 | 123.84 | 0.33 | 0.06 | 11.24 | 0.49 | 5.60 | 0.59 | 6.27 | 0.89 | H |
| V482 Cyg | RCrB | -15.50 | 0.84 | 213.71 | 3.64 | -16.02 | 0.99 | 1576.94 | 29.81 | 0.20 | 0.02 | 7.99 | 0.02 | 5.31 | 0.18 | 0.31 | 0.02 | TH |
| R CrB | RCrB | -76.98 | 2.54 | 226.35 | 1.64 | 35.73 | 0.64 | 1624.78 | 19.44 | 0.21 | 0.01 | 8.68 | 0.02 | 5.65 | 0.15 | 2.10 | 0.28 | TK |
| V2552 Oph | RCrB | -15.22 | 6.63 | 107.66 | 15.71 | -181.81 | 20.72 | 401.22 | 130.47 | 0.42 | 0.04 | 3.83 | 0.55 | 1.57 | 0.41 | 1.84 | 0.12 | B |
| RS Tel | RCrB | -20.02 | 14.43 | 10.51 | 23.24 | 6.88 | 1.89 | 70.64 | 31.02 | 0.73 | 0.05 | 2.76 | 0.33 | 0.44 | 0.11 | 0.91 | 0.12 | B |
| RT Nor | RCrB | -90.74 | 11.21 | 140.55 | 19.85 | -19.62 | 3.64 | 798.43 | 39.44 | 0.24 | 0.01 | 4.64 | 0.13 | 2.82 | 0.09 | 1.47 | 0.09 | B |
| VZ Sgr | RCrB | -383.71 | 14.78 | 159.31 | 7.87 | 104.46 | 15.71 | 259.84 | 136.90 | 0.81 | 0.03 | 6.15 | 1.22 | 0.63 | 0.28 | 0.94 | 0.09 | B |
| XX Cam | RCrB | 36.09 | 1.68 | 238.88 | 1.12 | 2.43 | 0.29 | 2263.29 | 7.65 | 0.11 | 0.00 | 10.67 | 0.09 | 8.50 | 0.02 | 0.07 | 0.00 | TK |
| Y Mus | RCrB | -220.96 | 11.62 | 121.89 | 15.29 | -4.74 | 1.02 | 1184.32 | 21.28 | 0.31 | 0.01 | 7.04 | 0.06 | 3.71 | 0.12 | 0.85 | 0.10 | TK |
| RY Sgr | RCrB | 73.16 | 3.34 | 256.80 | 0.45 | -72.05 | 3.76 | 1739.22 | 16.28 | 0.19 | 0.01 | 9.03 | 0.06 | 6.20 | 0.03 | 1.36 | 0.05 | TH |
| UV Cas | RCrB | 48.76 | 2.20 | 223.36 | 0.63 | 7.46 | 0.33 | 2130.25 | 12.67 | 0.18 | 0.01 | 10.73 | 0.14 | 7.49 | 0.02 | 0.12 | 0.01 | TH |
| UW Cen | RCrB | -318.87 | 23.31 | 109.73 | 35.06 | 16.92 | 1.59 | 1825.11 | 116.33 | 0.11 | 0.03 | 8.91 | 0.91 | 7.12 | 0.37 | 1.89 | 0.38 | TK |
| MV Sgr | RCrB | -76.32 | 9.94 | 81.67 | 24.49 | 75.27 | 6.18 | -87.47 | 41.20 | 0.70 | 0.12 | 2.83 | 0.21 | 0.50 | 0.11 | 1.45 | 0.06 | B |
| FQ Aqr | EHe | -2.78 | 2.15 | 204.14 | 4.80 | -54.27 | 5.71 | 1252.06 | 53.77 | 0.16 | 0.01 | 6.86 | 0.03 | 5.01 | 0.14 | 2.43 | 0.27 | TK |
| LS IV-14 109 | EHe | 34.66 | 4.15 | 245.29 | 1.13 | 12.43 | 0.75 | 1338.23 | 48.72 | 0.12 | 0.01 | 6.18 | 0.13 | 4.88 | 0.22 | 0.47 | 0.03 | TH |
| Cod-48 10153 | EHe | -137.57 | 7.35 | -12.50 | 35.97 | 3.94 | 1.50 | 499.43 | 43.41 | 0.51 | 0.03 | 4.69 | 0.08 | 1.52 | 0.15 | 0.95 | 0.13 | B |
| NO Ser | EHe | 46.61 | 6.24 | 218.58 | 3.99 | -13.36 | 2.20 | 1244.44 | 78.34 | 0.18 | 0.02 | 6.24 | 0.22 | 4.31 | 0.31 | 0.61 | 0.07 | TH |
| V2244 Oph | EHe | -48.36 | 3.41 | 131.61 | 4.11 | -104.35 | 15.92 | 427.95 | 47.84 | 0.46 | 0.02 | 4.34 | 0.19 | 1.59 | 0.14 | 2.08 | 0.30 | B |
| PV Tel | EHe | 79.40 | 26.31 | 244.79 | 8.32 | 6.79 | 7.00 | 799.88 | 36.73 | 0.33 | 0.02 | 6.39 | 0.18 | 3.20 | 0.13 | 3.38 | 0.38 | B |
| LSS 99 | EHe | 5.71 | 4.12 | 173.69 | 2.52 | -6.45 | 1.07 | 2366.78 | 92.16 | 0.31 | 0.01 | 14.26 | 0.64 | 7.56 | 0.30 | 0.49 | 0.06 | TK |

**Table** C.6: Orbital parameters and galactic velocities (continued)

| Star | Category | U | ± | V | ± | W | ± | $J_z$ | ± | $e$ | ± | $R_a$ | ± | $R_p$ | ± | $z_{max}$ | ± | pop |
|---|---|---|---|---|---|---|---|---|---|---|---|---|---|---|---|---|---|---|
| | | km s$^{-1}$ | | km s$^{-1}$ | | km s$^{-1}$ | | kpc km s$^{-1}$ | | | | kpc | | kpc | | kpc | | |
| HD 124448 | EHe | -63.33 | 14.70 | 291.71 | 2.75 | 31.67 | 5.83 | 1810.10 | 76.39 | 0.12 | 0.01 | 8.51 | 0.45 | 6.65 | 0.20 | 0.62 | 0.08 | TH |
| LSS 4357 | EHe | 82.91 | 17.67 | 256.02 | 3.81 | 124.37 | 15.20 | 475.99 | 178.23 | 0.48 | 0.07 | 4.36 | 0.56 | 1.53 | 0.51 | 1.04 | 0.11 | B |
| V1920 Cyg | EHe | -7.41 | 2.69 | 171.75 | 6.10 | -83.44 | 8.74 | 1384.39 | 87.88 | 0.28 | 0.04 | 8.47 | 0.22 | 4.73 | 0.50 | 2.32 | 0.33 | TK |
| BD+10 2179 | EHe | -101.68 | 21.36 | 193.37 | 1.14 | 104.62 | 4.15 | 1028.07 | 57.41 | 0.61 | 0.05 | 11.00 | 0.39 | 2.69 | 0.31 | 2.85 | 0.10 | TK |
| DY Cen | EHe | -274.61 | 8.57 | -168.81 | 39.80 | 141.56 | 12.18 | 2211.67 | 376.94 | 0.06 | 0.04 | 10.42 | 2.01 | 9.18 | 1.48 | 2.18 | 0.36 | TK |
| HD 144941 | EHe | -21.33 | 3.51 | 312.71 | 2.25 | 92.14 | 5.08 | 1840.42 | 18.04 | 0.24 | 0.01 | 10.29 | 0.07 | 6.34 | 0.08 | 1.85 | 0.14 | TK |
| BX Cir | EHe | -155.42 | 13.98 | 275.57 | 9.12 | 128.99 | 7.78 | 1758.90 | 46.24 | 0.17 | 0.02 | 9.12 | 0.42 | 6.49 | 0.05 | 1.89 | 0.15 | TK |
| V652 Her | EHe | -2.42 | 0.73 | 269.68 | 0.72 | 42.27 | 1.74 | 1858.05 | 11.47 | 0.09 | 0.01 | 8.55 | 0.03 | 7.14 | 0.07 | 0.97 | 0.05 | TH |
| GALEXJ184559.8 -413827 | EHe | 26.52 | 4.30 | 262.48 | 1.23 | 18.02 | 1.33 | 1243.42 | 110.83 | 0.10 | 0.01 | 5.93 | 0.43 | 4.82 | 0.34 | 1.23 | 0.15 | TH |
| LSS 5121 | EHe | 106.21 | 13.68 | 219.96 | 6.39 | 75.90 | 4.55 | 612.91 | 89.70 | 0.38 | 0.04 | 4.58 | 0.22 | 2.04 | 0.27 | 1.09 | 0.07 | B |
| LS IV+6 2 | EHe | -31.82 | 2.90 | 193.27 | 2.29 | -4.01 | 0.84 | 1196.05 | 31.00 | 0.31 | 0.01 | 7.02 | 0.06 | 3.67 | 0.14 | 0.44 | 0.02 | TH |
| BPS CS 22940-0009 | EHe | -4.68 | 4.75 | 143.17 | 6.48 | -24.19 | 3.24 | 907.05 | 64.26 | 0.45 | 0.03 | 6.94 | 0.09 | 2.66 | 0.21 | 1.33 | 0.09 | TK |
| V2076 Oph | EHe | -124.58 | 4.81 | 287.18 | 3.60 | 99.48 | 11.62 | 1556.88 | 84.63 | 0.20 | 0.01 | 8.27 | 0.44 | 5.51 | 0.18 | 1.56 | 0.14 | TK |
| BD+37 442 | EHe | -107.82 | 11.88 | 221.24 | 9.75 | -22.30 | 11.48 | 2065.81 | 108.82 | 0.35 | 0.04 | 13.22 | 0.84 | 6.33 | 0.58 | 1.15 | 0.39 | TK |
| BD+37 1977 | EHe | -40.21 | 5.03 | 141.38 | 8.46 | -38.67 | 4.39 | 1684.14 | 43.09 | 0.47 | 0.02 | 12.89 | 0.26 | 4.62 | 0.19 | 1.33 | 0.09 | TK |

**Table C.7:** Orbital parameters and galactic velocities, sorted by category. The last column shows which Galactic population each star has been classified into where TH = thin disk, TK = thick disk, H = halo and B = bulge.

| Star | Catagory | U | ± | V | ± | W | ± | $J_z$ | ± | $e$ | ± | $R_a$ | ± | $R_p$ | ± | $z_{max}$ | ± | pop |
|---|---|---|---|---|---|---|---|---|---|---|---|---|---|---|---|---|---|---|
| | | km s$^{-1}$ | | km s$^{-1}$ | | km s$^{-1}$ | | kpc km s$^{-1}$ | | | | kpc | | kpc | | kpc | | |
| NGC 6369 | [WC4] | 88.71 | 0.91 | 246.73 | 0.27 | -4.97 | 0.34 | 1788.98 | 13.53 | 0.27 | 0.00 | 9.51 | 0.08 | 5.44 | 0.05 | 0.19 | 0.01 | TH |
| PN Hb 4 | [WC3-4] | 51.65 | 2.71 | 203.86 | 12.98 | -27.67 | 8.60 | 1076.37 | 248.30 | 0.25 | 0.03 | 5.57 | 0.96 | 3.36 | 0.86 | 0.31 | 0.07 | TH |
| PN M 3-15 | [WC4-6] | -100.39 | 3.21 | 228.82 | 9.46 | -15.95 | 9.10 | 1425.85 | 199.83 | 0.31 | 0.00 | 8.09 | 1.15 | 4.27 | 0.60 | 0.27 | 0.08 | TH |
| PN M 2-34 | [WC4-5] | -59.91 | 31.01 | 251.33 | 4.90 | 48.74 | 7.99 | 644.51 | 215.71 | 0.08 | 0.05 | 2.77 | 0.95 | 2.38 | 0.56 | 0.44 | 0.07 | B |
| NGC 6578 | [WC]early | -32.03 | 1.81 | 203.90 | 4.05 | 1.83 | 0.88 | 1326.79 | 57.24 | 0.26 | 0.02 | 6.54 | 0.16 | 3.87 | 0.26 | 0.05 | 0.01 | TH |
| PN M 1-32 | [WC4-5] | 23.43 | 8.14 | 156.25 | 9.48 | 16.39 | 2.52 | 896.32 | 107.81 | 0.54 | 0.05 | 6.04 | 0.42 | 1.80 | 0.38 | 0.23 | 0.03 | B |
| PN M 1-51 | [WC4-6] | -3.42 | 5.56 | 220.52 | 10.26 | 2.04 | 2.90 | 1439.01 | 209.41 | 0.17 | 0.06 | 6.54 | 0.66 | 4.64 | 1.21 | 0.02 | 0.02 | TH |
| NGC 6905 | [WC3] | -55.35 | 2.71 | 242.09 | 1.76 | 47.61 | 2.55 | 1813.87 | 7.76 | 0.16 | 0.01 | 7.97 | 0.02 | 5.73 | 0.06 | 0.77 | 0.06 | TH |
| HD 184738 | [WC9] | -30.02 | 2.31 | 209.90 | 0.57 | -12.39 | 1.36 | 1637.05 | 9.79 | 0.22 | 0.00 | 7.93 | 0.01 | 5.09 | 0.06 | 0.26 | 0.02 | TH |
| PN A66 78 | Of-WR(C) | 21.60 | 2.27 | 273.87 | 6.28 | 21.19 | 1.90 | 2268.85 | 52.10 | 0.13 | 0.02 | 10.65 | 0.48 | 8.19 | 0.03 | 0.63 | 0.04 | TH |
| NGC 40 | [WC8] | 6.00 | 0.86 | 254.49 | 0.68 | -11.92 | 0.58 | 2425.02 | 16.41 | 0.20 | 0.01 | 13.99 | 0.34 | 9.31 | 0.05 | 0.51 | 0.03 | TH |
| IC 1747 | [WC4] | -10.08 | 3.52 | 220.76 | 1.62 | 20.38 | 1.52 | 2400.12 | 70.78 | 0.10 | 0.02 | 11.07 | 0.25 | 9.10 | 0.48 | 0.46 | 0.06 | TH |
| NGC 1501 | [WC4] | 69.99 | 1.49 | 236.13 | 1.09 | -8.60 | 0.59 | 2333.21 | 3.74 | 0.22 | 0.00 | 12.03 | 0.07 | 7.65 | 0.03 | 0.34 | 0.01 | TH |
| PN M 4-18 | [WC11] | 58.71 | 8.62 | 205.28 | 5.99 | 5.39 | 1.26 | 3269.53 | 119.11 | 0.22 | 0.03 | 17.79 | 1.32 | 11.42 | 0.24 | 1.24 | 0.17 | TH |
| NGC 2371 | [WC3] | -7.56 | 1.92 | 200.10 | 4.28 | -15.30 | 2.39 | 2048.53 | 15.05 | 0.24 | 0.02 | 10.25 | 0.14 | 6.32 | 0.15 | 0.86 | 0.10 | TH |
| NGC 2452 | [WC3] | -34.85 | 9.83 | 245.48 | 8.18 | 9.91 | 1.30 | 2475.78 | 166.61 | 0.06 | 0.03 | 10.21 | 0.47 | 9.12 | 0.98 | 0.03 | 0.01 | TH |
| Hen 2-55 | [WC3] | -250.12 | 40.50 | 230.49 | 22.32 | 9.09 | 1.40 | 1989.13 | 121.64 | 0.12 | 0.04 | 10.83 | 1.13 | 8.49 | 0.28 | 0.88 | 0.29 | TH |
| PN Vo 1 | [WC11] | 14.52 | 2.06 | 291.27 | 2.51 | 33.38 | 1.40 | 2384.09 | 27.38 | 0.20 | 0.01 | 12.14 | 0.30 | 8.14 | 0.04 | 0.84 | 0.07 | TH |
| NGC 5189 | [WC2] | -95.19 | 2.45 | 226.16 | 1.06 | 22.72 | 0.56 | 1699.28 | 12.81 | 0.29 | 0.01 | 7.65 | 0.01 | 4.19 | 0.07 | 0.10 | 0.01 | TH |
| PN PM 1-89 | [WC4] | -74.45 | 13.71 | 291.53 | 9.70 | 13.91 | 1.44 | 1698.23 | 82.43 | 0.19 | 0.02 | 8.20 | 0.54 | 5.55 | 0.27 | 0.34 | 0.03 | TH |
| Hen 2-142 | [WC9] | 19.25 | 15.20 | 283.40 | 7.30 | 8.95 | 1.51 | 1931.53 | 176.10 | 0.19 | 0.03 | 8.96 | 1.44 | 6.10 | 0.48 | 0.07 | 0.02 | TH |
| PN PC 14 | [WC4] | 14.47 | 6.23 | 260.20 | 4.59 | 28.42 | 4.96 | 2057.38 | 74.37 | 0.10 | 0.01 | 8.81 | 0.49 | 7.20 | 0.30 | 0.35 | 0.05 | TH |
| PN K 2-16 | [WC11] | -173.42 | 26.80 | 86.28 | 78.37 | 36.38 | 4.28 | 141.34 | 202.98 | 0.44 | 0.18 | 2.23 | 0.49 | 0.87 | 0.53 | 1.54 | 0.28 | B |
| IC 1297 | [WC4] | -32.23 | 2.84 | 173.34 | 16.42 | 6.69 | 2.04 | 909.39 | 204.77 | 0.32 | 0.05 | 5.45 | 0.60 | 2.80 | 0.70 | 1.23 | 0.26 | B |

**Table** C.7: Orbital parameters and galactic velocities (continued)

| Star | Catagory | U | ± | V | ± | W | ± | $J_z$ | ± | $e$ | ± | $R_a$ | ± | $R_p$ | ± | $z_{max}$ | ± | pop |
|---|---|---|---|---|---|---|---|---|---|---|---|---|---|---|---|---|---|---|
| | | km s$^{-1}$ | | km s$^{-1}$ | | km s$^{-1}$ | | kpc km s$^{-1}$ | | | | kpc | | kpc | | kpc | | |
| FBS 1342+673 | PG1159 | -41.36 | 11.01 | 207.42 | 20.35 | -26.27 | 26.84 | 1784.44 | 175.05 | 0.30 | 0.07 | 8.63 | 0.04 | 4.65 | 0.71 | 0.99 | 0.58 | TH |
| KUV 03467-0108 | PG1159 | -142.30 | 37.83 | 207.60 | 6.78 | 92.53 | 32.84 | 1887.99 | 54.59 | 0.48 | 0.10 | 15.42 | 4.62 | 5.47 | 0.15 | 3.90 | 2.95 | TK |
| KUV 07523+4017 | PG1159 | -6.53 | 26.62 | 283.29 | 3.77 | -5.29 | 14.47 | 2640.81 | 67.87 | 0.16 | 0.07 | 11.58 | 0.98 | 8.43 | 0.55 | 0.81 | 0.20 | TH |
| NGC 246 | PG1159 | -55.40 | 1.37 | 255.21 | 1.34 | 17.71 | 5.40 | 2158.10 | 11.38 | 0.18 | 0.01 | 10.61 | 0.07 | 7.43 | 0.05 | 0.64 | 0.05 | TH |
| PG 1424+535 | PG1159 | 21.92 | 15.78 | 252.51 | 19.03 | -43.30 | 28.35 | 2130.74 | 161.91 | 0.07 | 0.05 | 9.42 | 0.58 | 8.14 | 0.78 | 1.09 | 0.62 | TH |
| PN K 1-16 | PG1159 | -14.95 | 2.44 | 203.87 | 7.43 | 9.67 | 4.75 | 1785.22 | 66.29 | 0.22 | 0.03 | 8.83 | 0.04 | 5.61 | 0.38 | 1.06 | 0.08 | TH |
| SBSS 1446+575 | PG1159 | -51.79 | 5.31 | 193.35 | 19.22 | -4.19 | 26.91 | 1648.54 | 163.57 | 0.44 | 0.07 | 8.62 | 0.05 | 3.36 | 0.61 | 1.18 | 0.45 | TH |
| SDSSJ055905.02 +633448.4 | PG1159 | -2.16 | 18.54 | 259.49 | 9.58 | 5.77 | 6.72 | 2570.72 | 143.28 | 0.07 | 0.03 | 11.37 | 1.04 | 9.92 | 0.50 | 0.68 | 0.19 | TH |
| SDSSJ075415.11 +085232.1 | PG1159 | -66.32 | 8.57 | 224.37 | 16.78 | -9.54 | 3.11 | 2356.70 | 41.75 | 0.27 | 0.05 | 13.38 | 1.05 | 7.76 | 0.23 | 0.99 | 0.36 | TH |
| SDSSJ085422.39 +013650.9 | PG1159 | -70.71 | 12.77 | 19.87 | 26.39 | -73.32 | 9.47 | 203.63 | 265.18 | 0.88 | 0.07 | 15.67 | 1.42 | 1.04 | 0.57 | 2.21 | 0.50 | H |
| SDSSJ093546.53 +110529.0 | PG1159 | -134.84 | 32.15 | 288.10 | 20.65 | -55.51 | 29.86 | 2610.23 | 193.78 | 0.02 | 0.07 | 9.23 | 1.88 | 8.93 | 1.03 | 2.54 | 1.38 | TK |
| SDSSJ121523.08 +120300.7 | PG1159 | -100.49 | 16.35 | 256.91 | 13.57 | -12.43 | 42.34 | 2164.17 | 114.03 | 0.19 | 0.09 | 8.59 | 0.20 | 5.85 | 1.20 | 1.74 | 0.67 | TK |
| SDSSJ152046.67 +180300.7 | PG1159 | -100.84 | 23.04 | 229.49 | 5.80 | 72.21 | 26.34 | 1418.67 | 56.35 | 0.80 | 0.13 | 8.26 | 0.18 | 0.91 | 0.68 | 4.85 | 1.01 | H |
| SDSSJ191845.01 +624343.7 | PG1159 | 11.30 | 1.52 | 245.23 | 7.77 | -3.28 | 2.97 | 2082.17 | 65.85 | 0.04 | 0.01 | 8.68 | 0.28 | 8.05 | 0.35 | 0.35 | 0.02 | TH |
| IR Peg | PG1159 | -3.86 | 0.78 | 235.60 | 1.31 | 21.86 | 0.89 | 1968.14 | 10.91 | 0.07 | 0.01 | 8.36 | 0.00 | 7.31 | 0.08 | 0.30 | 0.01 | TH |
| PN K 1-27 | O(He) | 26.96 | 12.40 | 183.12 | 38.11 | -21.41 | 22.45 | 1459.17 | 317.07 | 0.27 | 0.16 | 8.96 | 0.34 | 5.18 | 1.88 | 2.70 | 0.34 | TK |

# Luminosities, Radii and Masses: Input and Outputs

D

**Table C.1:** Atmospheric parameters, extinction, G magnitudes and distances used in the calculation of Luminosities, Radii and Masses presented here.

| Star | Catagory | $T_{\rm eff}$ (K) | ± | $\log g$ (cm s$^{-2}$) | ± | $E_{(B-V)}$ | ± | G (mag) | # | Luminosity (L$_\odot$) | Radius (R$_\odot$) | Mass (M$_\odot$) | Distance (kpc) |
|---|---|---|---|---|---|---|---|---|---|---|---|---|---|
| CD-5111879 | He-sdO | 72300 | 5380 | 5.49 | 0.11 | 0.059 | 0.002 | 11.66 | 268 | $2585.11^{+13.79}_{-20.52}$ | $0.32^{+0.03}_{-0.03}$ | $1.18^{+0.34}_{-0.26}$ | $0.76^{+0.06}_{-0.09}$ |
| LSE153 | He-sdO | 70000 | 1500 | 4.75 | 0.15 | 0.106 | 0.002 | 11.29 | 150 | $2530.78^{+8.46}_{-10.43}$ | $0.34^{+0.00}_{-0.00}$ | $0.24^{+0.10}_{-0.07}$ | $0.63^{+0.03}_{-0.04}$ |
| SDSSJ232757.46+483755.2 | He-sdO | 64700 | 2000 | 5.40 | 0.08 | 0.137 | 0.002 | 15.80 | 332 | $2205.04^{+26.01}_{-51.02}$ | $0.37^{+0.00}_{-0.00}$ | $1.28^{+0.26}_{-0.22}$ | $5.09^{+0.80}_{-1.57}$ |
| SDSSJ041536.05+253857.11 | He-sdO | 64329 | 1429 | 6.12 | 0.07 | 0.406 | 0.058 | 16.36 | 298 | $281.29^{+19.37}_{-24.58}$ | $0.14^{+0.00}_{-0.00}$ | $0.88^{+0.15}_{-0.13}$ | $1.62^{+0.13}_{-0.20}$ |
| PG1430-082 | He-sdO | 61011 | 1000 | 5.26 | 0.10 | 0.053 | 0.001 | 15.96 | 127 | $703.57^{+26.34}_{-56.05}$ | $0.24^{+0.00}_{-0.00}$ | $0.37^{+0.10}_{-0.08}$ | $3.83^{+0.61}_{-1.30}$ |
| GALEXJ19111-1406 | He-sdO | 55970 | 4540 | 5.69 | 0.71 | 0.174 | 0.004 | 11.89 | 137 | $481.89^{+4.47}_{-4.88}$ | $0.23^{+0.01}_{-0.01}$ | $0.97^{+4.02}_{-0.78}$ | $0.47^{+0.01}_{-0.01}$ |
| PG0113+259 | He-sdO | 54410 | 4750 | 5.89 | 0.24 | 0.070 | 0.004 | 14.42 | 115 | $354.49^{+12.11}_{-16.95}$ | $0.21^{+0.01}_{-0.01}$ | $1.27^{+0.94}_{-0.54}$ | $1.55^{+0.21}_{-0.16}$ |
| PG1348+606 | He-sdO | 54360 | 1980 | 5.45 | 0.25 | 0.013 | 0.000 | 16.32 | 302 | $823.86^{+26.44}_{-49.50}$ | $0.32^{+0.00}_{-0.00}$ | $1.08^{+0.84}_{-0.47}$ | $6.15^{+0.98}_{-1.84}$ |
| PG1301+270 | He-sdO | 49400 | 1280 | 6.54 | 0.18 | 0.010 | 0.001 | 15.60 | 559 | $645.05^{+28.16}_{-58.61}$ | $0.35^{+0.01}_{-0.01}$ | $15.20^{+7.81}_{-5.16}$ | $4.54^{+0.77}_{-1.61}$ |
| GALEXJ07525+1616 | He-sdO | 49280 | 5320 | 6.08 | 0.36 | 0.024 | 0.001 | 14.46 | 304 | $208.45^{+12.19}_{-17.16}$ | $0.20^{+0.01}_{-0.01}$ | $1.72^{+2.22}_{-0.97}$ | $1.50^{+0.11}_{-0.16}$ |
| SDSSJ161014.87+045046.6 | He-sdO | 48400 | 1400 | 6.31 | 0.09 | 0.046 | 0.001 | 17.30 | 301 | $119.30^{+32.86}_{-72.55}$ | $0.16^{+0.01}_{-0.01}$ | $1.80^{+0.41}_{-0.34}$ | $4.20^{+0.83}_{-1.84}$ |
| SDSSJ151415.66-012925.2 | He-sdO | 48200 | 500 | 5.85 | 0.08 | 0.135 | 0.003 | 16.95 | 94 | $40.83^{+24.62}_{-57.83}$ | $0.09^{+0.01}_{-0.01}$ | $0.22^{+0.04}_{-0.04}$ | $1.85^{+0.27}_{-0.65}$ |
| PG0838+132 | He-sdO | 47660 | 3710 | 5.68 | 0.29 | 0.045 | 0.002 | 13.61 | 460 | $332.39^{+7.84}_{-9.55}$ | $0.27^{+0.01}_{-0.01}$ | $1.25^{+1.19}_{-0.61}$ | $1.31^{+0.06}_{-0.07}$ |
| SDSSJ152136.25+162150.3 | He-sdO | 47400 | 1000 | 5.81 | 0.08 | 0.030 | 0.000 | 17.10 | 172 | $40.29^{+26.15}_{-62.38}$ | $0.09^{+0.01}_{-0.01}$ | $0.21^{+0.04}_{-0.04}$ | $2.35^{+0.37}_{-0.89}$ |
| HE2203-2210 | He-sdO | 47343 | 1000 | 6.20 | 0.10 | 0.032 | 0.001 | 15.20 | 92 | $129.38^{+17.18}_{-29.18}$ | $0.17^{+0.00}_{-0.01}$ | $1.65^{+0.43}_{-0.34}$ | $1.75^{+0.18}_{-0.31}$ |
| SDSSJ074613.16+333307.6 | He-sdO | 47270 | 2530 | 5.77 | 0.25 | 0.042 | 0.002 | 15.85 | 254 | $249.84^{+26.83}_{-60.26}$ | $0.24^{+0.01}_{-0.01}$ | $1.19^{+0.93}_{-0.52}$ | $3.25^{+0.53}_{-1.18}$ |
| PG1020+694 | He-sdO | 46750 | 1110 | 5.63 | 0.43 | 0.018 | 0.001 | 14.57 | 333 | $167.51^{+7.48}_{-9.03}$ | $0.20^{+0.00}_{-0.00}$ | $0.61^{+1.02}_{-0.38}$ | $1.55^{+0.07}_{-0.08}$ |
| SDSSJ161059.80+053625.2 | He-sdO | 46300 | 700 | 6.22 | 0.10 | 0.042 | 0.001 | 17.20 | 390 | $84.04^{+30.12}_{-69.18}$ | $0.14^{+0.01}_{-0.02}$ | $1.23^{+0.32}_{-0.25}$ | $3.63^{+0.66}_{-1.52}$ |
| PG1507-015 | He-sdO | 45800 | 1210 | 6.25 | 0.26 | 0.069 | 0.001 | 16.52 | 125 | $134.72^{+27.74}_{-63.31}$ | $0.18^{+0.01}_{-0.02}$ | $2.20^{+1.81}_{-0.99}$ | $3.29^{+0.55}_{-1.26}$ |
| LSIV+109 | He-sdO | 45700 | 1070 | 6.08 | 0.24 | 0.070 | 0.001 | 11.97 | 272 | $197.29^{+4.29}_{-4.70}$ | $0.22^{+0.00}_{-0.00}$ | $2.20^{+1.62}_{-0.93}$ | $0.49^{+0.01}_{-0.01}$ |
| PG1203-108 | He-sdO | 45439 | 1000 | 5.91 | 0.10 | 0.073 | 0.003 | 15.90 | 342 | $691.73^{+29.31}_{-57.09}$ | $0.42^{+0.01}_{-0.01}$ | $5.34^{+1.38}_{-1.10}$ | $5.65^{+1.00}_{-1.95}$ |
| PG0914-037 | He-sdO | 45136 | 1000 | 5.79 | 0.10 | 0.031 | 0.001 | 15.22 | 156 | $612.20^{+24.73}_{-49.97}$ | $0.40^{+0.01}_{-0.01}$ | $3.68^{+0.95}_{-0.76}$ | $4.16^{+0.62}_{-1.25}$ |
| SB705 | He-sdO | 45090 | 8070 | 5.64 | 0.58 | 0.011 | 0.001 | 12.97 | 646 | $239.13^{+6.58}_{-7.72}$ | $0.25^{+0.13}_{-0.13}$ | $1.02^{+2.88}_{-0.79}$ | $0.95^{+0.04}_{-0.04}$ |
| EC14466-1058 | He-sdO | 45000 | 1000 | 5.76 | 0.10 | 0.081 | 0.003 | 15.17 | 141 | $186.32^{+17.54}_{-30.01}$ | $0.22^{+0.00}_{-0.01}$ | $1.06^{+0.27}_{-0.22}$ | $2.10^{+0.22}_{-0.38}$ |
| BD+393226 | He-sdO | 44700 | 5000 | 5.50 | 0.50 | 0.033 | 0.002 | 10.14 | 249 | $135.24^{+1.87}_{-1.67}$ | $0.19^{+0.01}_{-0.01}$ | $0.43^{+0.94}_{-0.30}$ | $0.19^{+0.00}_{-0.00}$ |
| GALEXJ04155-5421 | He-sdO | 44678 | 1000 | 5.76 | 0.10 | 0.009 | 0.001 | 14.87 | 165 | $150.38^{+8.62}_{-10.78}$ | $0.20^{+0.00}_{-0.00}$ | $0.88^{+0.23}_{-0.18}$ | $1.84^{+0.09}_{-0.12}$ |

**Table** C.1: (continued)

| Star | Catagory | $T_{\rm eff}$ (K) | $\pm$ | $\log g$ (cm s$^{-2}$) | $\pm$ | $E_{(B-V)}$ | $\pm$ | G (mag) | # | Luminosity ($L_\odot$) | Radius ($R_\odot$) | Mass ($M_\odot$) | Distance (kpc) |
|---|---|---|---|---|---|---|---|---|---|---|---|---|---|
| BPSCS22955-0024 | He-sdO | 44622 | 1000 | 5.80 | 0.10 | 0.063 | 0.002 | 15.68 | 243 | $156.15\,^{+20.90}_{-40.46}$ | $0.21\,^{+0.01}_{-0.01}$ | $1.01\,^{+0.26}_{-0.21}$ | $2.53\,^{+0.32}_{-0.62}$ |
| PG1318+062 | He-sdO | 44560 | 1040 | 5.79 | 0.21 | 0.031 | 0.001 | 14.74 | 201 | $232.87\,^{+20.84}_{-40.90}$ | $0.26\,^{+0.01}_{-0.01}$ | $1.47\,^{+0.92}_{-0.57}$ | $2.11\,^{+0.26}_{-0.52}$ |
| LSS1274 | He-sdO | 44500 | 1000 | 5.55 | 0.15 | 0.486 | 0.014 | 12.86 | 348 | $509.68\,^{+5.14}_{-5.40}$ | $0.38\,^{+0.00}_{-0.00}$ | $1.87\,^{+0.77}_{-0.55}$ | $0.69\,^{+0.02}_{-0.02}$ |
| GALEXJ21106+1425 | He-sdO | 44470 | 650 | 6.23 | 0.18 | 0.091 | 0.002 | 14.19 | 216 | $132.18\,^{+7.63}_{-9.24}$ | $0.19\,^{+0.00}_{-0.00}$ | $2.32\,^{+1.19}_{-0.79}$ | $1.13\,^{+0.05}_{-0.06}$ |
| PG1700+198 | He-sdO | 44300 | 600 | 5.79 | 0.11 | 0.067 | 0.002 | 15.72 | 336 | $104.23\,^{+14.58}_{-22.29}$ | $0.17\,^{+0.00}_{-0.01}$ | $0.68\,^{+0.19}_{-0.15}$ | $2.12\,^{+0.19}_{-0.28}$ |
| PG0958-119 | He-sdO | 44125 | 1000 | 5.51 | 0.10 | 0.053 | 0.001 | 14.01 | 150 | $277.33\,^{+11.27}_{-15.36}$ | $0.28\,^{+0.00}_{-0.00}$ | $0.96\,^{+0.25}_{-0.20}$ | $1.61\,^{+0.11}_{-0.15}$ |
| UVO0832-01 | He-sdO | 44000 | 250 | 5.64 | 0.05 | 0.025 | 0.001 | 11.38 | 281 | $122.15\,^{+4.01}_{-4.35}$ | $0.19\,^{+0.00}_{-0.00}$ | $0.58\,^{+0.07}_{-0.06}$ | $0.33\,^{+0.01}_{-0.01}$ |
| GALEXJ01194+4901 | He-sdOB | 43720 | 510 | 5.86 | 0.21 | 0.162 | 0.003 | 13.37 | 245 | $161.53\,^{+8.20}_{-10.10}$ | $0.22\,^{+0.00}_{-0.00}$ | $1.30\,^{+0.81}_{-0.50}$ | $0.80\,^{+0.04}_{-0.05}$ |
| GALEXJ17534+6910 | He-sdO | 43710 | 1160 | 5.81 | 0.41 | 0.025 | 0.001 | 15.12 | 258 | $125.10\,^{+9.50}_{-12.22}$ | $0.20\,^{+0.00}_{-0.00}$ | $0.90\,^{+1.41}_{-0.55}$ | $1.91\,^{+0.11}_{-0.14}$ |
| PG1127+019 | He-sdO | 43650 | 680 | 5.94 | 0.19 | 0.024 | 0.001 | 13.79 | 200 | $122.25\,^{+7.52}_{-9.09}$ | $0.19\,^{+0.00}_{-0.00}$ | $1.19\,^{+0.65}_{-0.42}$ | $1.03\,^{+0.05}_{-0.06}$ |
| GALEXJ07163+7502 | He-sdOB | 43200 | 880 | 5.55 | 0.53 | 0.030 | 0.001 | 14.90 | 301 | $152.64\,^{+11.63}_{-16.04}$ | $0.22\,^{+0.00}_{-0.01}$ | $0.63\,^{+1.50}_{-0.44}$ | $1.93\,^{+0.13}_{-0.19}$ |
| PG1413+114 | He-sdO | 43100 | 800 | 5.81 | 0.17 | 0.019 | 0.000 | 16.03 | 112 | $208.44\,^{+31.86}_{-72.52}$ | $0.26\,^{+0.01}_{-0.02}$ | $1.58\,^{+0.76}_{-0.51}$ | $3.87\,^{+0.74}_{-1.70}$ |
| HE1316-1834 | He-sdO | 42811 | 1000 | 5.56 | 0.10 | 0.063 | 0.001 | 16.30 | 125 | $83.75\,^{+25.19}_{-56.75}$ | $0.17\,^{+0.01}_{-0.02}$ | $0.37\,^{+0.09}_{-0.08}$ | $2.63\,^{+0.40}_{-0.90}$ |
| SDSSJ180757.08+230133.0 | He-sdO | 42700 | 1000 | 6.04 | 0.21 | 0.090 | 0.003 | 17.09 | 401 | $102.26\,^{+27.45}_{-58.61}$ | $0.18\,^{+0.01}_{-0.02}$ | $1.37\,^{+0.85}_{-0.52}$ | $4.05\,^{+0.67}_{-1.43}$ |
| KUV02445+3633 | He-sdO | 42590 | 340 | 5.67 | 0.10 | 0.065 | 0.003 | 12.98 | 151 | $169.52\,^{+9.99}_{-13.05}$ | $0.24\,^{+0.00}_{-0.00}$ | $0.98\,^{+0.25}_{-0.20}$ | $0.82\,^{+0.05}_{-0.06}$ |
| PG1511-110 | He-sdO | 42298 | 1000 | 5.68 | 0.10 | 0.093 | 0.001 | 14.95 | 140 | $63.44\,^{+9.91}_{-12.93}$ | $0.15\,^{+0.00}_{-0.00}$ | $0.38\,^{+0.10}_{-0.08}$ | $1.20\,^{+0.07}_{-0.09}$ |
| PG2258+155 | He-sdO | 42084 | 1000 | 6.08 | 0.10 | 0.047 | 0.002 | 15.36 | 173 | $49.98\,^{+12.75}_{-18.31}$ | $0.13\,^{+0.00}_{-0.01}$ | $0.78\,^{+0.20}_{-0.16}$ | $1.39\,^{+0.11}_{-0.15}$ |
| GALEXJ03449-1652 | He-sdOB | 41914 | 1000 | 5.78 | 0.10 | 0.070 | 0.005 | 14.87 | 533 | $56.02\,^{+10.30}_{-13.54}$ | $0.14\,^{+0.00}_{-0.00}$ | $0.44\,^{+0.11}_{-0.09}$ | $1.14\,^{+0.07}_{-0.09}$ |
| CD-249052 | He-sdO | 41700 | 250 | 5.49 | 0.05 | 0.044 | 0.001 | 11.72 | 275 | $125.98\,^{+4.43}_{-4.87}$ | $0.22\,^{+0.00}_{-0.00}$ | $0.52\,^{+0.06}_{-0.06}$ | $0.42\,^{+0.01}_{-0.01}$ |
| MCT0016-3212 | He-sdO | 41674 | 1000 | 5.70 | 0.10 | 0.012 | 0.000 | 14.39 | 200 | $186.97\,^{+12.72}_{-18.23}$ | $0.26\,^{+0.00}_{-0.01}$ | $1.26\,^{+0.33}_{-0.26}$ | $1.83\,^{+0.14}_{-0.20}$ |
| HE0031-5607 | He-sdO | 41423 | 1000 | 6.25 | 0.10 | 0.010 | 0.001 | 15.70 | 269 | $61.53\,^{+13.27}_{-19.37}$ | $0.15\,^{+0.01}_{-0.01}$ | $1.50\,^{+0.39}_{-0.31}$ | $1.94\,^{+0.15}_{-0.23}$ |
| MCT0155-3710 | He-sdO | 41405 | 1000 | 5.77 | 0.10 | 0.012 | 0.000 | 14.75 | 722 | $68.05\,^{+7.73}_{-9.41}$ | $0.16\,^{+0.00}_{-0.00}$ | $0.55\,^{+0.14}_{-0.11}$ | $1.32\,^{+0.06}_{-0.07}$ |
| HZ1 | He-sdO | 41344 | 1000 | 5.68 | 0.10 | 0.386 | 0.007 | 12.59 | 244 | $86.93\,^{+3.64}_{-3.80}$ | $0.18\,^{+0.00}_{-0.00}$ | $0.58\,^{+0.15}_{-0.12}$ | $0.32\,^{+0.01}_{-0.01}$ |
| MCT0001-2443 | He-sdO | 40975 | 1000 | 5.94 | 0.10 | 0.017 | 0.000 | 13.83 | 228 | $49.75\,^{+5.37}_{-6.07}$ | $0.14\,^{+0.00}_{-0.00}$ | $0.62\,^{+0.16}_{-0.13}$ | $0.75\,^{+0.02}_{-0.03}$ |
| PG0921+311 | He-sdO | 40830 | 160 | 5.84 | 0.15 | 0.022 | 0.001 | 14.57 | 208 | $117.19\,^{+15.70}_{-25.17}$ | $0.22\,^{+0.01}_{-0.01}$ | $1.18\,^{+0.49}_{-0.34}$ | $1.61\,^{+0.15}_{-0.24}$ |
| SDSSJ090252.99+073533.9 | He-sdO | 40100 | 500 | 5.91 | 0.19 | 0.052 | 0.005 | 17.33 | 346 | $27.27\,^{+28.74}_{-71.04}$ | $0.11\,^{+0.01}_{-0.03}$ | $0.35\,^{+0.19}_{-0.13}$ | $2.72\,^{+0.47}_{-1.17}$ |

**Table** C.1: (continued)

| Star | Catagory | $T_{\text{eff}}$ (K) | ± | $\log g$ (cm s$^{-2}$) | ± | $E_{(B-V)}$ | ± | G (mag) | # | Luminosity ($L_\odot$) | Radius ($R_\odot$) | Mass ($M_\odot$) | Distance (kpc) |
|---|---|---|---|---|---|---|---|---|---|---|---|---|---|
| PG1135-116 | He-sdOB | 40079 | 1000 | 5.68 | 0.10 | 0.023 | 0.001 | 15.83 | 559 | $199.58^{+26.00}_{-54.92}$ | $0.29^{+0.01}_{-0.02}$ | $1.50^{+0.39}_{-0.31}$ | $3.84^{+0.60}_{-1.27}$ |
| EC12563-2738 | He-sdOB | 40029 | 1000 | 5.68 | 0.10 | 0.060 | 0.001 | 16.52 | 122 | $27.50^{+20.49}_{-39.94}$ | $0.11^{+0.01}_{-0.02}$ | $0.21^{+0.05}_{-0.04}$ | $1.86^{+0.23}_{-0.45}$ |
| SDSSJ132747.87+564040.14 | He-sdO | 40000 | 5000 | 5.00 | 0.10 | 0.009 | 0.001 | 18.40 | 282 | $6.78^{+30.46}_{-82.60}$ | $0.05^{+0.00}_{-0.04}$ | $0.01^{+0.00}_{-0.00}$ | $2.36^{+0.43}_{-1.18}$ |
| SDSSJ163416.08+221141.0 | He-sdOB | 39384 | 1000 | 6.16 | 0.10 | 0.041 | 0.001 | 15.42 | 328 | $72.25^{+11.04}_{-14.93}$ | $0.18^{+0.01}_{-0.01}$ | $1.76^{+0.45}_{-0.36}$ | $1.91^{+0.13}_{-0.17}$ |
| PG1258+012 | He-sdOB | 39359 | 1000 | 5.64 | 0.10 | 0.022 | 0.000 | 16.47 | 217 | $43.94^{+21.87}_{-44.05}$ | $0.14^{+0.01}_{-0.02}$ | $0.32^{+0.08}_{-0.07}$ | $2.49^{+0.33}_{-0.66}$ |
| MCT0111-1526 | He-sdOB | 39152 | 1000 | 6.31 | 0.10 | 0.023 | 0.001 | 14.83 | 354 | $32.19^{+6.04}_{-7.84}$ | $0.12^{+0.00}_{-0.00}$ | $1.13^{+0.29}_{-0.23}$ | $1.01^{+0.04}_{-0.05}$ |
| HE2218-2026 | He-sdOB | 38330 | 1000 | 5.87 | 0.10 | 0.027 | 0.001 | 16.22 | 104 | $49.52^{+19.70}_{-36.51}$ | $0.16^{+0.01}_{-0.01}$ | $0.69^{+0.18}_{-0.14}$ | $2.43^{+0.29}_{-0.54}$ |
| MCT2359-2844 | He-sdOB | 38325 | 1000 | 5.65 | 0.10 | 0.017 | 0.001 | 16.23 | 246 | $30.96^{+18.51}_{-33.09}$ | $0.13^{+0.01}_{-0.02}$ | $0.26^{+0.07}_{-0.05}$ | $1.97^{+0.22}_{-0.39}$ |
| EC12383-1745 | He-sdOB | 38219 | 1000 | 5.64 | 0.10 | 0.035 | 0.001 | 14.55 | 278 | $88.51^{+12.73}_{-18.27}$ | $0.21^{+0.01}_{-0.01}$ | $0.73^{+0.19}_{-0.15}$ | $1.50^{+0.11}_{-0.16}$ |
| PG1559+048 | He-sdB | 36520 | 20 | 5.40 | 0.00 | 0.058 | 0.002 | 14.48 | 272 | $23.83^{+5.72}_{-6.53}$ | $0.12^{+0.00}_{-0.00}$ | $0.14^{+0.00}_{-0.00}$ | $0.78^{+0.03}_{-0.03}$ |
| SDSSJ134352.14+394008.3 | He-sdOB | 36000 | 2100 | 4.78 | 0.30 | 0.006 | 0.000 | 18.15 | 569 | $18.64^{+34.13}_{-76.40}$ | $0.11^{+0.02}_{-0.05}$ | $0.03^{+0.03}_{-0.01}$ | $4.09^{+0.84}_{-1.89}$ |
| PG2218+051 | He-sdOB | 35950 | 740 | 5.92 | 0.15 | 0.097 | 0.002 | 15.28 | 131 | $22.23^{+9.09}_{-11.54}$ | $0.12^{+0.01}_{-0.01}$ | $0.45^{+0.18}_{-0.13}$ | $1.05^{+0.06}_{-0.07}$ |
| SDSSJ143729.14-021506.0 | He-sdOB | 35870 | 1180 | 5.70 | 0.13 | 0.044 | 0.001 | 15.88 | 109 | $31.51^{+19.26}_{-35.68}$ | $0.15^{+0.01}_{-0.02}$ | $0.39^{+0.13}_{-0.10}$ | $1.78^{+0.21}_{-0.38}$ |
| GALEXJ160011.80-643330.35 | He-sdB | 34640 | 590 | 6.02 | 0.11 | 0.131 | 0.004 | 11.98 | 305 | $19.53^{+2.11}_{-1.85}$ | $0.12^{+0.00}_{-0.00}$ | $0.57^{+0.17}_{-0.13}$ | $0.22^{+0.00}_{-0.00}$ |
| FBS1749+373 | He-sdB | 34630 | 600 | 5.89 | 0.12 | 0.028 | 0.001 | 14.52 | 245 | $19.24^{+4.83}_{-5.37}$ | $0.12^{+0.00}_{-0.00}$ | $0.42^{+0.13}_{-0.10}$ | $0.80^{+0.02}_{-0.02}$ |
| PG 0039+135 | Ex-He | 55000[a] | 2500 | 5.80 | 0.30 | 0.081 | 0.002 | 13.67 | 286 | $330.46^{+11.94}_{-13.80}$ | $0.20^{+0.00}_{-0.00}$ | $0.92^{+0.92}_{-0.46}$ | $1.02^{+0.07}_{-0.06}$ |
| HE 1251+0159 | Ex-He | 48208[b] | 1253 | 5.98 | 0.10 | 0.017 | 0.001 | 15.53 | 358 | $274.15^{+28.87}_{-42.69}$ | $0.24^{+0.01}_{-0.01}$ | $1.96^{+0.49}_{-0.39}$ | $2.95^{+0.51}_{-0.76}$ |
| PG 0902+057 | Ex-He | 47000[c] | 3000 | 6.00 | 0.50 | 0.040 | 0.002 | 14.06 | 130 | $93.96^{+15.62}_{-19.08}$ | $0.15^{+0.00}_{-0.00}$ | $0.78^{+1.69}_{-0.53}$ | $0.88^{+0.08}_{-0.10}$ |
| PG 2215+151 | Ex-He | 45000[a] | 2500 | 5.90 | 0.30 | 0.044 | 0.000 | 14.53 | 121 | $86.56^{+9.63}_{-10.77}$ | $0.15^{+0.00}_{-0.00}$ | $0.68^{+0.68}_{-0.34}$ | $1.12^{+0.06}_{-0.07}$ |
| HE 0342-1702 | Ex-He | 41914[b] | 1090 | 5.78 | 0.10 | 0.069 | 0.005 | 14.87 | 533 | $55.90^{+13.15}_{-15.44}$ | $0.14^{+0.00}_{-0.01}$ | $0.44^{+0.11}_{-0.09}$ | $1.14^{+0.09}_{-0.11}$ |
| PG 1413+114 | Ex-He | 40300[c] | 2500 | 5.50 | 0.50 | 0.019 | 0.000 | 16.03 | 112 | $168.94^{+44.85}_{-74.23}$ | $0.27^{+0.02}_{-0.03}$ | $0.82^{+1.77}_{-0.56}$ | $3.87^{+1.05}_{-1.74}$ |
| LB 3229 | Ex-He | 40000[d] | 500 | 5.15 | 0.20 | 0.019 | 0.001 | 13.54 | 379 | $81.49^{+6.89}_{-7.42}$ | $0.19^{+0.00}_{-0.00}$ | $0.18^{+0.11}_{-0.07}$ | $0.86^{+0.03}_{-0.04}$ |
| PG 1127+019 | Ex-He | 39900[c] | 200 | 5.00 | 0.10 | 0.023 | 0.001 | 13.79 | 200 | $92.26^{+9.46}_{-10.56}$ | $0.20^{+0.00}_{-0.00}$ | $0.15^{+0.04}_{-0.03}$ | $1.03^{+0.06}_{-0.06}$ |
| PG 2321+214 | Ex-He | 39600[c] | 150 | 5.30 | 0.10 | 0.068 | 0.002 | 13.74 | 292 | $92.82^{+8.54}_{-9.40}$ | $0.20^{+0.00}_{-0.00}$ | $0.30^{+0.08}_{-0.06}$ | $0.95^{+0.05}_{-0.05}$ |
| BPS CS 29496-0010 | Ex-He | 39150[d] | 1000 | 5.65 | 0.20 | 0.018 | 0.000 | 14.66 | 116 | $76.46^{+16.75}_{-20.78}$ | $0.19^{+0.01}_{-0.01}$ | $0.59^{+0.34}_{-0.22}$ | $1.45^{+0.15}_{-0.18}$ |
| PG 1658+273 | Ex-He | 38800[c] | 200 | 4.90 | 0.10 | 0.062 | 0.001 | 15.99 | 316 | $87.90^{+20.10}_{-26.14}$ | $0.21^{+0.01}_{-0.01}$ | $0.12^{+0.03}_{-0.03}$ | $2.73^{+0.33}_{-0.43}$ |

**Table** C.1: (continued)

| Star | Catagory | $T_{\rm eff}$ (K) | ± | $\log g$ (cm s$^{-2}$) | ± | $E_{\rm (B-V)}$ | ± | G (mag) | # | Luminosity ($L_\odot$) | Radius ($R_\odot$) | Mass ($M_\odot$) | Distance (kpc) |
|---|---|---|---|---|---|---|---|---|---|---|---|---|---|
| PG 2258+155 | Ex-He | $37700^c$ | 200 | 5.20 | 0.10 | 0.048 | 0.002 | 15.36 | 173 | $36.02\,^{+16.55}_{-20.48}$ | $0.14\,^{+0.01}_{-0.01}$ | $0.11\,^{+0.03}_{-0.02}$ | $1.39\,^{+0.14}_{-0.17}$ |
| PG 1554+408 | Ex-He | $37700^c$ | 200 | 5.20 | 0.10 | 0.014 | 0.000 | 16.30 | 302 | $68.99\,^{+23.56}_{-32.18}$ | $0.19\,^{+0.01}_{-0.02}$ | $0.22\,^{+0.06}_{-0.05}$ | $3.12\,^{+0.44}_{-0.61}$ |
| HS 1844+637 | Ex-He | $36400^c$ | 650 | 5.10 | 0.20 | 0.048 | 0.002 | 16.62 | 259 | $38.76\,^{+20.09}_{-26.12}$ | $0.16\,^{+0.01}_{-0.02}$ | $0.11\,^{+0.07}_{-0.04}$ | $2.71\,^{+0.33}_{-0.43}$ |
| PG 1615+413 | Ex-He | $36000^c$ | 300 | 5.20 | 0.10 | 0.007 | 0.000 | 17.06 | 297 | $34.93\,^{+32.11}_{-49.09}$ | $0.15\,^{+0.02}_{-0.03}$ | $0.13\,^{+0.03}_{-0.03}$ | $3.39\,^{+0.66}_{-1.01}$ |
| HE 0001-2443 | Ex-He | $35960^d$ | 500 | 5.40 | 0.20 | 0.017 | 0.000 | 13.83 | 228 | $33.84\,^{+6.64}_{-7.12}$ | $0.15\,^{+0.00}_{-0.00}$ | $0.21\,^{+0.12}_{-0.08}$ | $0.75\,^{+0.03}_{-0.03}$ |
| PG 1715+273 | Ex-He | $34700^c$ | 300 | 5.00 | 0.10 | 0.060 | 0.007 | 16.95 | 325 | $32.49\,^{+27.12}_{-38.98}$ | $0.16\,^{+0.02}_{-0.03}$ | $0.09\,^{+0.02}_{-0.02}$ | $3.04\,^{+0.50}_{-0.71}$ |
| PG 1544+488 | Ex-He | $34000^c$ | 300 | 5.10 | 0.10 | 0.014 | 0.000 | 12.79 | 253 | $27.43\,^{+3.66}_{-3.77}$ | $0.15\,^{+0.00}_{-0.00}$ | $0.10\,^{+0.03}_{-0.02}$ | $0.45\,^{+0.01}_{-0.01}$ |
| BPS CS 22940-0009 | Ex-He | $33700^d$ | 800 | 4.70 | 0.20 | 0.051 | 0.001 | 13.98 | 500 | $224.80\,^{+19.79}_{-25.68}$ | $0.44\,^{+0.02}_{-0.02}$ | $0.35\,^{+0.21}_{-0.13}$ | $2.15\,^{+0.26}_{-0.33}$ |
| PG 1415+492 | Ex-He | $32200^c$ | 250 | 4.20 | 0.10 | 0.011 | 0.001 | 14.29 | 454 | $383.95\,^{+20.15}_{-26.11}$ | $0.63\,^{+0.02}_{-0.03}$ | $0.23\,^{+0.06}_{-0.05}$ | $3.65\,^{+0.44}_{-0.57}$ |
| SB 705 | Inter-He | $45090^e$ | 8070 | 5.64 | 0.58 | 0.011 | 0.001 | 12.97 | 646 | $239.13\,^{+8.22}_{-9.01}$ | $0.25\,^{+0.13}_{-0.13}$ | $1.02\,^{+2.88}_{-0.79}$ | $0.95\,^{+0.05}_{-0.05}$ |
| HD 127493 | Inter-He | $41687^f$ | 1000 | 5.70 | 0.50 | 0.083 | 0.002 | 9.96 | 166 | $116.44\,^{+2.45}_{-2.00}$ | $0.21\,^{+0.00}_{-0.00}$ | $0.78\,^{+1.69}_{-0.53}$ | $0.17\,^{+0.00}_{-0.00}$ |
| SDSS J092440.11+305013.16 | Inter-He | $40830^e$ | 160 | 5.84 | 0.15 | 0.021 | 0.001 | 14.57 | 208 | $117.08\,^{+20.71}_{-27.35}$ | $0.22\,^{+0.01}_{-0.01}$ | $1.18\,^{+0.49}_{-0.34}$ | $1.61\,^{+0.20}_{-0.26}$ |
| SDSS J175548.50+501210.77 | Inter-He | $40370^e$ | 940 | 5.96 | 0.15 | 0.037 | 0.001 | 12.88 | 266 | $63.21\,^{+3.69}_{-3.69}$ | $0.16\,^{+0.00}_{-0.00}$ | $0.88\,^{+0.36}_{-0.26}$ | $0.54\,^{+0.01}_{-0.01}$ |
| SDSS J160131.30+044027.00 | Inter-He | $40330^e$ | 860 | 6.16 | 0.18 | 0.058 | 0.002 | 14.48 | 272 | $31.95\,^{+7.09}_{-7.64}$ | $0.12\,^{+0.00}_{-0.00}$ | $0.71\,^{+0.36}_{-0.24}$ | $0.78\,^{+0.03}_{-0.04}$ |
| HE 1136-2504 | Inter-He | $40320^g$ | 500 | 5.65 | 0.05 | 0.040 | 0.001 | 14.07 | 355 | $98.70\,^{+10.48}_{-11.86}$ | $0.20\,^{+0.00}_{-0.00}$ | $0.68\,^{+0.08}_{-0.07}$ | $1.16\,^{+0.07}_{-0.07}$ |
| HE 1256-2738 | Inter-He | $39500^g$ | 1000 | 5.66 | 0.10 | 0.061 | 0.001 | 16.52 | 122 | $26.51\,^{+27.71}_{-41.04}$ | $0.11\,^{+0.01}_{-0.02}$ | $0.20\,^{+0.05}_{-0.04}$ | $1.86\,^{+0.31}_{-0.46}$ |
| UVO 0825+15 | Inter-He | $38900^h$ | 270 | 5.97 | 0.11 | 0.034 | 0.001 | 11.64 | 234 | $47.17\,^{+3.39}_{-3.47}$ | $0.15\,^{+0.00}_{-0.00}$ | $0.78\,^{+0.22}_{-0.17}$ | $0.28\,^{+0.01}_{-0.01}$ |
| HE 1310-2733 | Inter-He | $38400^g$ | 1100 | 5.48 | 0.15 | 0.059 | 0.002 | 14.45 | 118 | $176.11\,^{+35.85}_{-56.21}$ | $0.30\,^{+0.02}_{-0.03}$ | $1.46\,^{+0.38}_{-0.30}$ | $1.20\,^{+0.08}_{-0.10}$ |
| HE 1135-1134 | Inter-He | $38400^g$ | 1500 | 5.65 | 0.10 | 0.024 | 0.001 | 15.83 | 559 | $67.62\,^{+11.48}_{-13.18}$ | $0.19\,^{+0.01}_{-0.01}$ | $0.38\,^{+0.16}_{-0.11}$ | $3.84\,^{+0.83}_{-1.30}$ |
| HE 2218-2026 | Inter-He | $37280^g$ | 1500 | 5.80 | 0.10 | 0.026 | 0.001 | 16.22 | 104 | $45.61\,^{+26.51}_{-38.15}$ | $0.16\,^{+0.02}_{-0.02}$ | $0.60\,^{+0.16}_{-0.12}$ | $2.43\,^{+0.39}_{-0.56}$ |
| HE 1238-1745 | Inter-He | $37230^g$ | 800 | 5.57 | 0.20 | 0.036 | 0.001 | 14.55 | 278 | $82.14\,^{+16.52}_{-20.43}$ | $0.22\,^{+0.01}_{-0.01}$ | $0.64\,^{+0.38}_{-0.24}$ | $1.50\,^{+0.15}_{-0.18}$ |
| HE 2359-2844 | Inter-He | $37050^g$ | 1000 | 5.57 | 0.15 | 0.016 | 0.001 | 16.23 | 246 | $28.01\,^{+24.78}_{-34.88}$ | $0.13\,^{+0.01}_{-0.02}$ | $0.22\,^{+0.09}_{-0.07}$ | $1.97\,^{+0.29}_{-0.41}$ |
| HS 1051+2933 | Inter-He | $36300^i$ | 900 | 5.95 | 0.10 | 0.016 | 0.001 | 17.08 | 121 | $22.90\,^{+50.05}_{-93.48}$ | $0.12\,^{+0.03}_{-0.06}$ | $0.48\,^{+0.13}_{-0.15}$ | $2.71\,^{+0.82}_{-1.53}$ |
| BPS CS 22956-0094 | Inter-He | $34280^d$ | 800 | 5.63 | 0.20 | 0.023 | 0.001 | 13.32 | 316 | $25.16\,^{+4.64}_{-4.64}$ | $0.14\,^{+0.00}_{-0.00}$ | $0.31\,^{+0.18}_{-0.12}$ | $0.54\,^{+0.01}_{-0.01}$ |
| LS IV$-14°116$ | Inter-He | $34000^j$ | 500 | 5.60 | 0.10 | 0.038 | 0.003 | 12.98 | 202 | $21.60\,^{+5.84}_{-6.19}$ | $0.13\,^{+0.00}_{-0.01}$ | $0.26\,^{+0.07}_{-0.05}$ | $0.42\,^{+0.01}_{-0.02}$ |
| PG 0240+046 | Inter-He | $34000^c$ | 150 | 5.40 | 0.10 | 0.047 | 0.003 | 14.09 | 128 | $21.65\,^{+7.55}_{-8.19}$ | $0.13\,^{+0.01}_{-0.01}$ | $0.16\,^{+0.04}_{-0.03}$ | $0.70\,^{+0.03}_{-0.03}$ |

**Table** C.1: (continued)

| Star | Catagory | $T_{eff}$ (K) | ± | $\log g$ (cm s$^{-2}$) | ± | $E_{(B-V)}$ | ± | G (mag) | # | Luminosity ($L_\odot$) | Radius ($R_\odot$) | Mass ($M_\odot$) | Distance (kpc) |
|---|---|---|---|---|---|---|---|---|---|---|---|---|---|
| TON 107 | Inter-He | 33300[c] | 300 | 5.00 | 0.10 | 0.017 | 0.001 | 16.94 | 706 | $14.46^{+25.54}_{-36.27}$ | $0.11^{+0.02}_{-0.03}$ | $0.05^{+0.01}_{-0.01}$ | $2.28^{+0.35}_{-0.50}$ |
| JL 87 | Inter-He | 25800[k] | 1000 | 4.80 | 0.30 | 0.105 | 0.002 | 12.01 | 232 | $117.37^{+6.85}_{-7.36}$ | $0.54^{+0.02}_{-0.02}$ | $0.68^{+0.67}_{-0.34}$ | $0.85^{+0.03}_{-0.04}$ |
| CPD-20 1123 | Inter-He | 23500[l] | 500 | 4.90 | 0.10 | 0.068 | 0.001 | 12.06 | 561 | $12.28^{+3.77}_{-3.88}$ | $0.21^{+0.01}_{-0.01}$ | $0.13^{+0.03}_{-0.03}$ | $0.33^{+0.01}_{-0.01}$ |
| PG 0229+064 | Inter-He | 19000[m] | 950 | 4.55 | 0.10 | 0.057 | 0.004 | 11.92 | 151 | $35.46^{+7.04}_{-7.58}$ | $0.55^{+0.06}_{-0.06}$ | $0.39^{+0.10}_{-0.08}$ | $0.70^{+0.03}_{-0.03}$ |

a Thejll et al. (1994) ,b Stroeer et al. (2007),c Ahmad and Jeffery (2003),d Naslim et al. (2010),e Németh et al. (2012),f Kilkenny et al. (1988b),g Naslim et al. (2013),h Jeffery et al. (2017), i Edelmann (2003),j Naslim et al. (2011),k Ahmad et al. (2007),l Naslim et al. (2012),m Ramspeck et al. (2001)

**Table C.2:** Atmospheric parameters, extinction, G magnitudes and distances used in the calculation of Luminosities, Radii and Masses presented here. For stars without a published $T_{eff}$ error we adopt the square root of the temperature (in kK).

| Star | Catagory | $T_{eff}$ (kK) | ± | $\log g$ (cm s$^{-2}$) | ± | $E_{(B-V)}$ | ± | G (mag) | # | Luminosity (L$_\odot$) | Radius (R$_\odot$) | Mass (M$_\odot$) | Distance (kpc) |
|---|---|---|---|---|---|---|---|---|---|---|---|---|---|
| FBS 1342+673 | PG1159 | $100^a$ | 10 | - | - | 0.020 | 0.010 | 17.16 | 248 | $1.45\,^{+0.05}_{-0.06}$ | $0.02\,^{+0.00}_{-0.00}$ | - | $0.68\,^{+0.04}_{-0.04}$ |
| GW Vir | PG1159 | $140^b$ | 15 | 7.00 | 0.30 | 0.195 | 0.010 | 14.70 | 360 | $2.89\,^{+0.05}_{-0.05}$ | $0.05\,^{+0.18}_{-0.18}$ | $0.82\,^{+6.23}_{-6.19}$ | $0.56\,^{+0.02}_{-0.03}$ |
| KUV 03467-0108 | PG1159 | $100^a$ | 10 | - | - | 0.195 | 0.010 | 17.82 | 445 | $1.67\,^{+0.10}_{-0.12}$ | $0.02\,^{+0.00}_{-0.00}$ | - | $0.93\,^{+0.10}_{-0.13}$ |
| KUV 07523+4017 | PG1159 | $100^a$ | 10 | - | - | 0.050 | 0.010 | 17.83 | 164 | $1.59\,^{+0.15}_{-0.24}$ | $0.02\,^{+0.00}_{-0.01}$ | - | $1.04\,^{+0.18}_{-0.28}$ |
| MWP 1 | PG1159 | $170^c$ | 15 | 6.00 | 0.30 | 0.170 | 0.010 | 13.05 | 373 | $3.69\,^{+0.03}_{-0.03}$ | $0.08\,^{+0.25}_{-0.25}$ | $0.24\,^{+1.49}_{-1.48}$ | $0.50\,^{+0.01}_{-0.01}$ |
| NGC 246 | PG1159 | $150^b$ | 15 | 5.70 | 0.30 | 0.050 | 0.010 | 11.81 | 518 | $3.89\,^{+0.05}_{-0.05}$ | $0.13\,^{+0.46}_{-0.46}$ | $0.31\,^{+2.22}_{-2.21}$ | $0.52\,^{+0.03}_{-0.03}$ |
| PG 1144+005 | PG1159 | $100^a$ | 10 | - | - | 0.030 | 0.010 | 15.17 | 198 | $2.70\,^{+0.08}_{-0.10}$ | $0.07\,^{+0.01}_{-0.01}$ | $0.02\,^{+0.00}_{-0.00}$ | $1.14\,^{+0.10}_{-0.12}$ |
| PG 1424+535 | PG1159 | $100^a$ | 10 | - | - | 0.060 | 0.010 | 15.89 | 351 | $1.82\,^{+0.04}_{-0.13}$ | - | - | $0.55\,^{+0.02}_{-25.80}$ |
| PG 1707+427 | PG1159 | $100^a$ | 10 | - | - | 0.170 | 0.010 | 16.68 | 232 | $1.94\,^{+0.05}_{-0.05}$ | - | - | $0.78\,^{+0.04}_{-0.04}$ |
| PN K 1-16 | PG1159 | $140^b$ | 15 | 6.40 | 0.30 | 0.063 | 0.010 | 14.99 | 193 | $3.81\,^{+0.10}_{-0.12}$ | $0.14\,^{+0.52}_{-0.52}$ | $1.72\,^{+13.05}_{-12.97}$ | $2.21\,^{+0.23}_{-0.29}$ |
| SBSS 1020+541 | PG1159 | $100^a$ | 10 | - | - | 0.010 | 0.010 | 17.95 | 265 | $2.42\,^{+0.26}_{-0.47}$ | $0.05\,^{+0.02}_{-0.03}$ | $0.01\,^{+0.01}_{-0.01}$ | $3.06\,^{+0.92}_{-1.65}$ |
| SBSS 1446+575 | PG1159 | $100^a$ | 10 | - | - | 0.020 | 0.010 | 18.07 | 332 | $1.59\,^{+0.12}_{-0.16}$ | $0.02\,^{+0.00}_{-0.00}$ | - | $1.22\,^{+0.17}_{-0.23}$ |
| SDSS J055905.02+633448.4 | PG1159 | $110^d$ | 15 | 7.50 | 0.50 | 0.170 | 0.010 | 18.63 | 306 | $2.00\,^{+0.25}_{-0.50}$ | $0.03\,^{+0.13}_{-0.13}$ | $0.87\,^{+8.60}_{-8.46}$ | $1.79\,^{+0.50}_{-1.02}$ |
| SDSS J075415.11+085232.1 | PG1159 | $120^d$ | 10 | 7.00 | 0.30 | 0.020 | 0.010 | 19.14 | 333 | $2.00\,^{+0.37}_{-0.73}$ | $0.02\,^{+0.02}_{-0.03}$ | $0.20\,^{+0.43}_{-0.49}$ | $2.48\,^{+1.05}_{-2.09}$ |
| SDSS J093546.53+110529.0 | PG1159 | $100^a$ | 1 | - | - | 0.030 | 0.010 | 17.79 | 122 | $1.64\,^{+0.19}_{-0.33}$ | $0.02\,^{+0.00}_{-0.01}$ | - | $1.12\,^{+0.24}_{-0.43}$ |
| SDSS J105300.23+174932.9 | PG1159 | $100^d$ | 10 | 7.00 | 0.50 | 0.030 | 0.010 | 16.80 | 140 | $1.48\,^{+0.05}_{-0.05}$ | $0.02\,^{+0.02}_{-0.02}$ | $0.12\,^{+0.37}_{-0.27}$ | $0.59\,^{+0.03}_{-0.03}$ |
| SDSS J121523.08+120300.7 | PG1159 | $100^a$ | 10 | 7.53 | 0.25 | 0.030 | 0.010 | 18.17 | 367 | $1.63\,^{+0.19}_{-0.32}$ | $0.02\,^{+0.00}_{-0.01}$ | $0.59\,^{+0.52}_{-0.51}$ | $1.32\,^{+0.28}_{-0.49}$ |
| SDSS J123930.61+244321.7 | PG1159 | $100^d$ | 15 | 7.50 | 0.50 | 0.050 | 0.010 | 18.34 | 423 | $1.86\,^{+0.23}_{-0.43}$ | $0.03\,^{+0.15}_{-0.15}$ | $0.93\,^{+10.02}_{-9.87}$ | $1.81\,^{+0.47}_{-0.90}$ |
| SDSS J141556.26+061822.5 | PG1159 | $120^d$ | 10 | 7.50 | 0.30 | 0.030 | 0.010 | 17.48 | 142 | $1.86\,^{+0.15}_{-0.23}$ | $0.02\,^{+0.02}_{-0.02}$ | $0.45\,^{+0.92}_{-0.85}$ | $0.97\,^{+0.17}_{-0.25}$ |
| SDSS J191845.01+624343.7 | PG1159 | $100^d$ | 10 | 7.20 | 0.30 | 0.060 | 0.010 | 17.62 | 224 | $1.53\,^{+0.07}_{-0.08}$ | $0.02\,^{+0.02}_{-0.02}$ | $0.22\,^{+0.51}_{-0.47}$ | $0.88\,^{+0.06}_{-0.07}$ |

**Table** C.2: (continued)

| Star | Catagory | $T_{eff}$ (kK) | ± | $\log g$ (cm s$^{-2}$) | ± | $E_{(B-V)}$ | ± | G (mag) | # | Luminosity ($L_\odot$) | Radius ($R_\odot$) | Mass ($M_\odot$) | Distance (kpc) |
|---|---|---|---|---|---|---|---|---|---|---|---|---|---|
| PN K 2-16 | [WC11] | 30$^e$ | 5 | - | - | 0.330 | 0.010 | 12.09 | 400 | 4.16 $^{+0.18}_{-0.25}$ | 4.45 $^{+1.33}_{-1.60}$ | - | 7.31 $^{+1.49}_{-2.10}$ |
| PN M 4-18 | [WC11] | 31$^e$ | 6 | - | - | 0.520 | 0.012 | 13.54 | 413 | 3.93 $^{+0.16}_{-0.22}$ | 3.18 $^{+1.50}_{-1.59}$ | - | 8.30 $^{+1.50}_{-2.05}$ |
| HD 184738 | [WC9] | 47$^f$ | 10 | - | - | 0.347 | 0.003 | 10.25 | 198 | 4.08 $^{+0.09}_{-0.11}$ | 1.66 $^{+3.68}_{-3.68}$ | - | 1.76 $^{+0.18}_{-0.22}$ |
| PN M 3-15 | [WC4-6] | 55$^e$ | 7 | - | - | 1.011 | 0.038 | 16.87 | 95 | 3.65 $^{+0.27}_{-0.54}$ | 0.74 $^{+0.41}_{-0.56}$ | - | 2.19 $^{+0.67}_{-1.35}$ |
| PN M 1-32 | [WC4-5] | 66$^e$ | 8 | - | - | 0.827 | 0.043 | 15.39 | 153 | 3.53 $^{+0.16}_{-0.23}$ | 0.45 $^{+0.30}_{-0.31}$ | - | 2.75 $^{+0.48}_{-0.72}$ |
| NGC 40 | [WC8] | 71$^f$ | 10 | - | - | 0.337 | 0.003 | 11.45 | 248 | 3.94 $^{+0.05}_{-0.06}$ | 0.62 $^{+0.90}_{-0.90}$ | - | 2.00 $^{+0.11}_{-0.12}$ |
| PN Hb 4 | [WC3-4] | 86$^e$ | 9 | - | - | 1.083 | 0.027 | 17.08 | 139 | 3.96 $^{+0.30}_{-0.53}$ | 0.43 $^{+0.37}_{-0.43}$ | - | 3.13 $^{+1.06}_{-1.91}$ |
| PN A66 78 | Of-WR(C) | 113$^g$ | 8 | - | - | 0.141 | 0.001 | 13.15 | 206 | 3.12 $^{+0.09}_{-0.10}$ | 0.09 $^{+0.04}_{-0.04}$ | - | 1.63 $^{+0.16}_{-0.19}$ |
| IC 1747 | [WC4] | 126$^e$ | 11 | - | - | 1.001 | 0.028 | 15.70 | 397 | 3.80 $^{+0.13}_{-0.18}$ | 0.17 $^{+0.20}_{-0.20}$ | - | 3.38 $^{+0.49}_{-0.68}$ |
| NGC 2371 | [WC3] | 135$^g$ | 15 | - | - | 0.040 | 0.001 | 14.79 | 161 | 3.18 $^{+0.10}_{-0.13}$ | 0.07 $^{+0.28}_{-0.28}$ | - | 1.96 $^{+0.23}_{-0.29}$ |
| NGC 2452 | [WC3] | 141$^e$ | 12 | - | - | 0.924 | 0.128 | 16.91 | 298 | 3.78 $^{+0.27}_{-0.40}$ | 0.13 $^{+0.20}_{-0.21}$ | - | 2.93 $^{+0.72}_{-1.24}$ |
| Sand 3 | [WC3] | 150$^h$ | 25 | - | - | 0.020 | 0.000 | 13.91 | 245 | 3.23 $^{+0.05}_{-0.06}$ | 0.06 $^{+1.66}_{-1.66}$ | - | 1.43 $^{+0.08}_{-0.09}$ |
| NGC 6905 | [WC3] | 150$^f$ | 10 | - | - | 0.138 | 0.006 | 14.55 | 238 | 3.63 $^{+0.09}_{-0.12}$ | 0.10 $^{+0.07}_{-0.07}$ | - | 2.57 $^{+0.27}_{-0.34}$ |
| NGC 5189 | [WC2] | 165$^h$ | 18 | - | - | 0.859 | 0.042 | 14.44 | 328 | 4.21 $^{+0.07}_{-0.07}$ | 0.16 $^{+1.03}_{-1.03}$ | - | 1.70 $^{+0.09}_{-0.10}$ |
| HS 2209+8229 | O(He) | 110$^i$ | 10 | 6.00 | 0.30 | 0.23 | 0.04 | 16.28 | 226 | 3.22 $^{+0.10}_{-0.14}$ | 0.11 $^{+0.11}_{-0.11}$ | 0.46 $^{+0.99}_{-0.91}$ | 2.28 $^{+0.28}_{-0.37}$ |
| HS 1522+6615 | O(He) | 130$^i$ | 10 | 5.90 | 0.20 | 0.03 | 0.01 | 16.87 | 244 | 3.74 $^{+0.15}_{-0.29}$ | 0.15 $^{+0.12}_{-0.13}$ | 0.62 $^{+1.08}_{-1.10}$ | 5.65 $^{+1.34}_{-2.00}$ |
| PN K 1-27 | O(He) | 135$^i$ | 5 | 6.40 | 0.30 | 0.06 | 0.02 | 16.05 | 252 | 4.11 $^{+0.12}_{-0.22}$ | 0.21 $^{+0.03}_{-0.05}$ | 3.98 $^{+4.13}_{-2.84}$ | 5.40 $^{+0.99}_{-1.43}$ |
| KPD 0005+5106 | O(He) | 200$^i$ | 20 | 6.70 | 0.30 | 0.07 | 0.01 | 13.29 | 467 | 3.44 $^{+0.03}_{-0.03}$ | 0.04 $^{+0.36}_{-0.36}$ | 0.35 $^{+5.82}_{-5.81}$ | 0.39 $^{+0.01}_{-0.01}$ |

*a.* Kleinman et al. (2013), *b.* Holberg et al. (1998), *c.* Guerrero and De Marco (2013), *d.* Werner, K. et al. (2014), *e.* Peña et al. (2003), *f.* Marcolino et al. (2007),*g.* Herald and Bianchi (2004),*h.* Keller et al. (2014),*i.* Reindl et al. (2014)

**Table C.3:** Atmospheric parameters, extinction, G magnitudes and distances used in the calculation of Luminosities, Radii and Masses presented here. For stars which do not have a published error on tempertautre or gravity we have assumed the values of 501K and 0.21 dex respectively. * indicates that an AAVSO light curve is available in the date range of *Gaia* DR2 observations.

| Star | Catagory | $T_{eff}$ (K) | $\pm$ | $\log g$ (cm s$^{-2}$) | $\pm$ | $E_{(B-V)}$ | $\pm$ | G (mag) | # | Luminosity (L$_\odot$) | Radius (R$_\odot$) | Mass (M$_\odot$) | Distance (kpc) |
|---|---|---|---|---|---|---|---|---|---|---|---|---|---|
| HD 182040* | HdC | 5400$^a$ | 501 | 0.50 | 0.21 | 0.18 | 0.00 | 6.71 | 140 | 2884.60 $^{+209.94}_{-240.65}$ | 61.36 $^{+2.23}_{-2.56}$ | 0.43 $^{+0.28}_{-0.17}$ | 0.95 $^{+0.04}_{-0.04}$ |
| HD 137613* | HdC | 5400$^a$ | 501 | 0.50 | 0.21 | 0.16 | 0.01 | 7.17 | 158 | 2551.51 $^{+290.09}_{-368.25}$ | 57.71 $^{+3.28}_{-4.16}$ | 0.38 $^{+0.25}_{-0.16}$ | 1.13 $^{+0.08}_{-0.09}$ |
| HD 175893* | HdC | 5400$^a$ | 501 | 0.50 | 0.21 | 0.13 | 0.01 | 9.16 | 139 | 3156.55 $^{+642.42}_{-1046.91}$ | 64.19 $^{+6.53}_{-10.64}$ | 0.48 $^{+0.32}_{-0.24}$ | 3.27 $^{+0.44}_{-0.58}$ |
| HD 148839* | HdC | 5472$^b$ | 914 | 0.81 | 0.21 | 0.07 | 0.00 | 8.15 | 520 | 1823.13 $^{+161.93}_{-194.61}$ | 47.51 $^{+2.11}_{-2.54}$ | 0.53 $^{+0.34}_{-0.21}$ | 1.70 $^{+0.09}_{-0.10}$ |
| HD 173409* | HdC | 6100$^a$ | 501 | 0.50 | 0.21 | 0.14 | 0.01 | 9.34 | 138 | 959.17 $^{+116.16}_{-150.26}$ | 27.73 $^{+1.68}_{-2.17}$ | 0.09 $^{+0.06}_{-0.04}$ | 2.03 $^{+0.15}_{-0.18}$ |
| DY Per* | RCrB | 3500$^c$ | 501 | 0.00 | 0.21 | 0.55 | 0.01 | 9.41 | 314 | 3989.77 $^{+399.92}_{-477.33}$ | 171.79 $^{+8.61}_{-10.28}$ | 1.08 $^{+0.69}_{-0.44}$ | 1.22 $^{+0.07}_{-0.08}$ |
| SV Sge* | RCrB | 4010$^d$ | 501 | - | - | 0.42 | 0.01 | 9.47 | 276 | 4231.52 $^{+623.02}_{-853.11}$ | - | - | 2.15 $^{+0.20}_{-0.24}$ |
| S Aps* | RCrB | 4200$^e$ | 501 | - | - | 0.12 | 0.01 | 9.29 | n/a | 6606.65 $^{+981.91}_{-1367.18}$ | - | - | 4.16 $^{+0.40}_{-0.48}$ |
| LT Dra* | RCrB | 4259$^f$ | 501 | - | - | 0.04 | 0.00 | 7.09 | 258 | 322.88 $^{+7.18}_{-6.50}$ | - | - | 0.38 $^{+0.00}_{-0.00}$ |
| WX CrA* | RCrB | 4805$^d$ | 501 | - | - | 0.06 | 0.01 | 10.34 | 123 | 4501.74 $^{+1430.33}_{-2569.14}$ | - | - | 6.96 $^{+1.49}_{-2.13}$ |
| U Aqr* | RCrB | 5400$^a$ | 501 | 0.50 | 0.21 | 0.05 | 0.01 | 11.66 | 116 | 615.78 $^{+202.16}_{-399.64}$ | 28.35 $^{+4.65}_{-9.20}$ | 0.09 $^{+0.07}_{-0.07}$ | 5.11 $^{+1.15}_{-1.74}$ |
| GU Sgr* | RCrB | 6250$^g$ | 250 | 0.50 | 0.50 | 0.37 | 0.01 | 9.94 | 160 | 6252.94 $^{+1719.92}_{-3186.81}$ | 67.44 $^{+9.28}_{-17.19}$ | 0.52 $^{+1.14}_{-0.45}$ | 5.00 $^{+0.92}_{-1.34}$ |
| V482 Cyg* | RCrB | 6500$^g$ | 250 | 0.50 | 0.50 | 0.96 | 0.08 | 10.22 | 339 | 12978.83 $^{+3478.08}_{-3792.18}$ | 89.83 $^{+12.04}_{-13.12}$ | 0.93 $^{+2.03}_{-0.69}$ | 3.59 $^{+0.30}_{-0.36}$ |
| R CrB* | RCrB | 6750$^g$ | 250 | 0.50 | 0.50 | 0.03 | 0.00 | 5.69 | n/a | 8116.58 $^{+982.61}_{-1286.21}$ | 65.88 $^{+3.99}_{-5.22}$ | 0.50 $^{+1.08}_{-0.35}$ | 1.34 $^{+0.10}_{-0.12}$ |
| RS Tel* | RCrB | 6750$^g$ | 250 | 1.25 | 0.50 | 0.17 | 0.01 | 10.06 | 98 | 7424.72 $^{+2235.23}_{-3858.77}$ | 63.01 $^{+9.48}_{-16.37}$ | 2.57 $^{+5.62}_{-2.21}$ | 7.86 $^{+1.59}_{-2.21}$ |
| V2552 Oph* | RCrB | 6750$^h$ | 250 | 0.50 | 0.30 | 0.76 | 0.14 | 10.56 | 165 | 13518.96 $^{+6595.48}_{-8796.57}$ | 85.02 $^{+20.74}_{-27.66}$ | 0.83 $^{+0.92}_{-0.68}$ | 5.74 $^{+1.09}_{-1.56}$ |
| RT Nor* | RCrB | 7000$^g$ | 250 | 1.50 | 0.50 | 0.39 | 0.01 | 10.08 | 485 | 9976.39 $^{+2887.43}_{-5137.71}$ | 67.91 $^{+9.83}_{-17.49}$ | 5.32 $^{+11.60}_{-4.55}$ | 6.74 $^{+1.31}_{-1.86}$ |
| VZ Sgr* | RCrB | 7000$^g$ | 250 | 0.50 | 0.50 | 0.50 | 0.01 | 10.12 | 156 | 9014.76 $^{+2812.17}_{-5344.75}$ | 64.56 $^{+10.07}_{-19.14}$ | 0.48 $^{+1.05}_{-0.43}$ | 5.59 $^{+1.18}_{-1.75}$ |
| RY Sgr* | RCrB | 7250$^g$ | 250 | 0.75 | 0.50 | 0.13 | 0.01 | 6.27 | 132 | 13924.83 $^{+1900.15}_{-2520.54}$ | 74.79 $^{+5.10}_{-6.77}$ | 1.15 $^{+2.49}_{-0.81}$ | 2.01 $^{+0.17}_{-0.20}$ |
| XX Cam* | RCrB | 7250$^g$ | 250 | 0.75 | 0.50 | 0.27 | 0.01 | 7.06 | 523 | 6153.74 $^{+573.50}_{-670.35}$ | 49.72 $^{+2.32}_{-2.71}$ | 0.51 $^{+1.10}_{-0.35}$ | 1.57 $^{+0.08}_{-0.09}$ |
| UV Cas* | RCrB | 7250$^g$ | 250 | 0.50 | 0.50 | 1.01 | 0.01 | 9.96 | 294 | 13846.16 $^{+1730.66}_{-2215.72}$ | 74.58 $^{+4.66}_{-5.97}$ | 0.64 $^{+1.39}_{-0.45}$ | 3.11 $^{+0.24}_{-0.28}$ |
| Y Mus* | RCrB | 7250$^g$ | 250 | 0.75 | 0.50 | 0.50 | 0.01 | 9.99 | 379 | 9434.71 $^{+1804.88}_{-2751.98}$ | 61.57 $^{+5.89}_{-8.98}$ | 0.78 $^{+1.69}_{-0.58}$ | 5.39 $^{+0.66}_{-0.86}$ |
| UW Cen* | RCrB | 7500$^g$ | 250 | 1.00 | 0.50 | 0.32 | 0.01 | 10.24 | 730 | 6862.70 $^{+1862.77}_{-3259.39}$ | 49.07 $^{+6.66}_{-11.65}$ | 0.88 $^{+1.91}_{-0.73}$ | 6.66 $^{+1.21}_{-1.69}$ |
| FQ Aqr | Ex-He | 8750$^i$ | 300 | 0.30 | 0.30 | 0.10 | 0.02 | 9.46 | 467 | 4725.04 $^{+1299.19}_{-2377.99}$ | 29.91 $^{+4.11}_{-7.53}$ | 0.07 $^{+0.07}_{-0.05}$ | 4.88 $^{+0.89}_{-1.29}$ |

**Table** C.3: (continued)

| Star | Catagory | $T_{\text{eff}}$ (K) | ± | $\log g$ (cm s$^{-2}$) | ± | $E_{(B-V)}$ | ± | G (mag) | # | Luminosity ($L_\odot$) | Radius ($R_\odot$) | Mass ($M_\odot$) | Distance (kpc) |
|---|---|---|---|---|---|---|---|---|---|---|---|---|---|
| LS IV-14 109 | Ex-He | $9500^i$ | 250 | 1.00 | 0.20 | 0.45 | 0.05 | 11.00 | 152 | $1418.37\,^{+332.67}_{-459.86}$ | $13.90\,^{+1.63}_{-2.25}$ | $0.07\,^{+0.04}_{-0.03}$ | $3.02\,^{+0.37}_{-0.48}$ |
| Cod-48 10153 | Ex-He | $10400^j$ | 500 | 1.00 | 0.50 | 0.45 | 0.04 | 11.31 | 330 | $7348.88\,^{+2069.82}_{-3340.53}$ | $26.41\,^{+3.72}_{-6.00}$ | $0.25\,^{+0.55}_{-0.21}$ | $7.25\,^{+1.25}_{-1.72}$ |
| NO Ser | Ex-He | $11750^k$ | 250 | 2.30 | 0.40 | 0.77 | 0.01 | 10.12 | 115 | $11607.17\,^{+3066.53}_{-5981.99}$ | $26.00\,^{+3.43}_{-6.70}$ | $4.92\,^{+7.55}_{-3.90}$ | $3.04\,^{+0.54}_{-0.81}$ |
| V2244 Oph | Ex-He | $12750^k$ | 250 | 1.75 | 0.25 | 0.50 | 0.02 | 10.87 | 133 | $14419.01\,^{+4777.73}_{-8655.43}$ | $24.61\,^{+4.08}_{-7.39}$ | $1.24\,^{+1.05}_{-0.92}$ | $6.69\,^{+1.49}_{-2.15}$ |
| PV Tel | Ex-He | $13750^i$ | 400 | 1.60 | 0.25 | 0.13 | 0.01 | 9.23 | 259 | $28039.29\,^{+8424.03}_{-14965.53}$ | $29.51\,^{+4.43}_{-7.87}$ | $1.26\,^{+1.05}_{-0.87}$ | $7.08\,^{+1.43}_{-2.03}$ |
| LSS 99 | Ex-He | $15330^l$ | 500 | 1.90 | 0.25 | 0.88 | 0.04 | 12.06 | 165 | $19699.25\,^{+5737.32}_{-9567.16}$ | $19.90\,^{+2.90}_{-4.83}$ | $1.15\,^{+0.95}_{-0.75}$ | $6.92\,^{+1.26}_{-1.76}$ |
| MV Sgr* | RCrB | $16000^m$ | 500 | 2.48 | 0.30 | 0.33 | 0.01 | 13.27 | 108 | $1810.52\,^{+491.11}_{-839.87}$ | $5.54\,^{+0.75}_{-1.28}$ | $0.34\,^{+0.35}_{-0.23}$ | $7.72\,^{+1.40}_{-1.94}$ |
| HD 124448 | Ex-He | $16100^j$ | 300 | 2.30 | 0.25 | 0.11 | 0.01 | 9.94 | 138 | $1487.97\,^{+453.09}_{-1064.61}$ | $4.96\,^{+0.75}_{-1.77}$ | $0.18\,^{+0.15}_{-0.15}$ | $2.04\,^{+0.43}_{-0.71}$ |
| LSS 4357 | Ex-He | $16130^l$ | 500 | 2.00 | 0.25 | 0.45 | 0.04 | 12.44 | 149 | $3317.87\,^{+1053.32}_{-1864.78}$ | $7.38\,^{+1.17}_{-2.07}$ | $0.20\,^{+0.17}_{-0.14}$ | $5.93\,^{+1.19}_{-1.73}$ |
| V1920 Cyg | Ex-He | $16300^j$ | 900 | 1.70 | 0.35 | 0.31 | 0.02 | 10.26 | 272 | $17111.09\,^{+4651.72}_{-8184.02}$ | $16.40\,^{+2.23}_{-3.92}$ | $0.49\,^{+0.62}_{-0.36}$ | $5.98\,^{+1.07}_{-1.52}$ |
| BD+10 2179 | Ex-He | $17300^n$ | 300 | 2.80 | 0.10 | 0.02 | 0.00 | 9.92 | 98 | $1818.05\,^{+559.70}_{-1302.74}$ | $4.75\,^{+0.73}_{-1.70}$ | $0.52\,^{+0.21}_{-0.39}$ | $2.36\,^{+0.50}_{-0.83}$ |
| DY Cen* | Ex-He | $19500^o$ | 500 | 2.15 | 0.10 | 0.32 | 0.01 | 13.24 | 248 | $6821.20\,^{+1737.94}_{-2674.54}$ | $7.24\,^{+0.92}_{-1.42}$ | $0.27\,^{+0.10}_{-0.12}$ | $11.90\,^{+1.98}_{-2.57}$ |
| HD 144941 | Ex-He | $23200^p$ | 500 | 3.90 | 0.10 | 0.25 | 0.02 | 10.09 | 384 | $3662.36\,^{+576.30}_{-782.64}$ | $3.75\,^{+0.29}_{-0.40}$ | $4.06\,^{+1.23}_{-1.21}$ | $1.82\,^{+0.17}_{-0.21}$ |
| BX Cir | Ex-He | $23390^q$ | 90 | 3.38 | 0.02 | 0.49 | 0.02 | 12.56 | 326 | $3333.80\,^{+646.18}_{-991.48}$ | $3.52\,^{+0.34}_{-0.52}$ | $1.08\,^{+0.22}_{-0.33}$ | $3.79\,^{+0.47}_{-0.61}$ |
| V652 Her* | Ex-He | $24550^r$ | 500 | 3.68 | 0.05 | 0.05 | 0.00 | 10.52 | 400 | $668.15\,^{+96.68}_{-135.27}$ | $1.43\,^{+0.10}_{-0.14}$ | $0.36\,^{+0.07}_{-0.08}$ | $1.17\,^{+0.11}_{-0.13}$ |
| GALEX J184559.8-413827 | Ex-He | $26170^s$ | 750 | 4.22 | 0.10 | 0.08 | 0.00 | 14.59 | 133 | $199.23\,^{+55.18}_{-109.08}$ | $0.69\,^{+0.10}_{-0.19}$ | $0.29\,^{+0.11}_{-0.17}$ | $3.71\,^{+0.70}_{-1.05}$ |
| LSS 5121 | Ex-He | $29800^t$ | 1830 | 3.00 | 0.50 | 0.65 | 0.02 | 13.17 | 147 | $12283.76\,^{+2476.60}_{-3765.32}$ | $4.16\,^{+0.42}_{-0.64}$ | $0.63\,^{+1.37}_{-0.47}$ | $5.56\,^{+0.71}_{-0.92}$ |
| LS IV+6 2 | Ex-He | $31800^u$ | 800 | 4.05 | 0.10 | 0.21 | 0.02 | 12.14 | 159 | $1184.40\,^{+187.38}_{-255.17}$ | $1.13\,^{+0.09}_{-0.12}$ | $0.53\,^{+0.16}_{-0.16}$ | $1.83\,^{+0.17}_{-0.21}$ |
| BPS CS 22940-0009 | Ex-He | $33700^v$ | 500 | 4.70 | 0.10 | 0.05 | 0.00 | 13.98 | 500 | $224.68\,^{+40.85}_{-63.56}$ | $0.44\,^{+0.04}_{-0.06}$ | $0.35\,^{+0.11}_{-0.12}$ | $2.15\,^{+0.26}_{-0.33}$ |
| V2076 Oph | Ex-He | $34000^w$ | 501 | 2.80 | 0.21 | 0.45 | 0.02 | 9.78 | 107 | $35112.73\,^{+10455.10}_{-23166.09}$ | $5.40\,^{+0.80}_{-1.78}$ | $0.67\,^{+0.47}_{-0.51}$ | $2.17\,^{+0.44}_{-0.70}$ |
| BD+37 442 | Ex-He | $48000^{x,y}$ | 501 | 4.00 | 0.25 | 0.05 | 0.00 | 9.95 | 78 | $13834.83\,^{+4221.60}_{-10550.61}$ | $1.70\,^{+0.26}_{-0.65}$ | $1.05\,^{+0.88}_{-0.93}$ | $1.55\,^{+0.33}_{-0.56}$ |
| BD+37 1977 | Ex-He | $48000^{l,z}$ | 501 | 4.00 | 0.21 | 0.01 | 0.00 | 10.13 | 242 | $8124.36\,^{+1629.93}_{-2718.85}$ | $1.30\,^{+0.13}_{-0.22}$ | $0.62\,^{+0.41}_{-0.32}$ | $1.36\,^{+0.18}_{-0.24}$ |
| LSE 153 | Hot-sdO | $70000^{aa}$ | 1500 | 4.8 | 0.15 | 0.11 | 0.01 | 11.29 | 150 | $2530.78\,^{+254.71}_{-315.63}$ | $0.34\,^{+0.02}_{-0.02}$ | $0.27\,^{+0.11}_{-0.09}$ | $0.63\,^{+0.03}_{-0.04}$ |

**Table** C.3: (continued)

| Star | Catagory | $T_{eff}$ (K) | ± | $\log g$ (cm s$^{-2}$) | ± | $E_{(B-V)}$ | ± | G (mag) | # | Luminosity ($L_\odot$) | Radius ($R_\odot$) | Mass ($M_\odot$) | Distance (kpc) |
|------|----------|------|---|------|---|-------|---|---|---|------------|--------|------|----------|
| LSE 263 | Hot-sdO | 72300$^{aa}$ | 5380 | 5.49 | 0.11 | 0.06 | 0.01 | 11.67 | 268 | 2585.11 $^{+428.03}_{-639.11}$ | 0.32 $^{+0.06}_{-0.05}$ | 1.18 $^{+0.49}_{-0.49}$ | 0.76$^{+0.06}_{-0.09}$ |
| LSE 259 | Hot-sdO | 75000$^{aa}$ | 10000 | 4.4 | 0.30 | 0.20 | 0.01 | 12.52 | 218 | 13057.76 $^{+1406.73}_{-1701.91}$ | 0.68 $^{+0.94}_{-0.94}$ | 0.42 $^{+1.24}_{-1.18}$ | 1.95 $^{+0.10}_{-0.12}$ |

*a.* Hema et al. (2012), *b.* Casagrande et al. (2011), *c.* Keenan and Barnbaum (1997), *d.* Bergeat et al. (2002), *e.* Rao and Lambert (2015), *f.* McDonald et al. (2017), *g.* Asplund et al. (1997), *h.* Rao et al. (2014), *i.* Pandey et al. (2006), *j.* Pandey and Reddy (2006), *k.* Pandey et al. (2001), *l.* Jeffery (1998), *m.* Jeffery et al. (1988), *n.* Kupfer et al. (2017), *o.* Jeffery and Heber (1993), *p.* Harrison and Jeffery (1997), *q.* Woolf and Jeffery (2002), *r.* Jeffery et al. (1999), *s.* Jeffery (2017), *t.* Jeffery et al. (2001a), *u.* Jeffery et al. (1998), *v.* Naslim et al. (2010), *w.* Rauch (1996), *x.* Jeffery and Hamann (2010), *y.* La Palombara et al. (2015), *z.* Darius et al. (1979), *aa.* Husfeld et al. (1989)

# References

Adelman-McCarthy, J. K., Agüeros, M. A., Allam, S. S., Allende Prieto, C., Anderson, K. S. J., Anderson, S. F., Annis, J., Bahcall, N. A., Bailer-Jones, C. A. L., Baldry, I. K., Barentine, J. C., Bassett, B. A., Becker, A. C., Beers, T. C., Bell, E. F., Berlind, A. A., Bernardi, M., Blanton, M. R., Bochanski, J. J., Boroski, W. N., Brinchmann, J., Brinkmann, J., Brunner, R. J., Budavári, T., Carliles, S., Carr, M. A., Castander, F. J., Cinabro, D., Cool, R. J., Covey, K. R., Csabai, I., Cunha, C. E., Davenport, J. R. A., Dilday, B., Doi, M., Eisenstein, D. J., Evans, M. L., Fan, X., Finkbeiner, D. P., Friedman, S. D., Frieman, J. A., Fukugita, M., Gänsicke, B. T., Gates, E., Gillespie, B., Glazebrook, K., Gray, J., Grebel, E. K., Gunn, J. E., Gurbani, V. K., Hall, P. B., Harding, P., Harvanek, M., Hawley, S. L., Hayes, J., Heckman, T. M., Hendry, J. S., Hindsley, R. B., Hirata, C. M., Hogan, C. J., Hogg, D. W., Hyde, J. B., Ichikawa, S.-i., Ivezić, Ž., Jester, S., Johnson, J. A., Jorgensen, A. M., Jurić, M., Kent, S. M., Kessler, R., Kleinman, S. J., Knapp, G. R., Kron, R. G., Krzesinski, J., Kuropatkin, N., Lamb, D. Q., Lampeitl, H., Lebedeva, S., Lee, Y. S., Leger, R. F., Lépine, S., Lima, M., Lin, H., Long, D. C., Loomis, C. P., Loveday, J., Lupton, R. H., Malanushenko, O., Malanushenko, V., Mandelbaum, R., Margon, B., Marriner, J. P., Martínez-Delgado, D., Matsubara, T., McGehee, P. M., McKay, T. A., Meiksin, A., Morrison, H. L., Munn, J. A., Nakajima, R., Neilsen, Jr., E. H., Newberg, H. J., Nichol, R. C., Nicinski, T., Nieto-Santisteban, M., Nitta, A., Okamura, S., Owen, R., Oyaizu, H., Padmanabhan, N., Pan, K., Park, C., Peoples, Jr., J., Pier, J. R., Pope, A. C., Purger, N., Raddick, M. J., Re Fiorentin, P., Richards, G. T., Richmond, M. W., Riess, A. G., Rix, H.-W., Rockosi, C. M., Sako, M., Schlegel, D. J., Schneider, D. P., Schreiber, M. R., Schwope, A. D., Seljak, U., Sesar, B., Sheldon, E., Shimasaku, K., Sivarani, T., Smith, J. A., Snedden, S. A., Steinmetz, M., Strauss, M. A., SubbaRao, M., Suto, Y., Szalay, A. S., Szapudi, I., Szkody, P., Tegmark, M., Thakar, A. R., Tremonti, C. A., Tucker, D. L., Uomoto, A., Vanden Berk, D. E., Vandenberg, J., Vidrih, S., Vogeley, M. S., Voges, W., Vogt, N. P., Wadadekar, Y., Weinberg, D. H., West, A. A., White, S. D. M., Wilhite, B. C., Yanny, B., Yocum, D. R., York, D. G., Zehavi, I., and Zucker, D. B. (2008). VizieR Online Data Catalog: The SDSS Photometric Catalog, Release 6 (Adelman-McCarthy+, 2007). *VizieR Online Data Catalog*, 2282:0. (Cited on pages 154 and 171.)

Ahmad, A., Behara, N. T., Jeffery, C. S., Sahin, T., and Woolf, V. M. (2007). An abundance analysis of a chemically peculiar B star - JL 87 . *A&A*, 465:541–547. (Cited on pages 79, 154 and 188.)

Ahmad, A. and Jeffery, C. S. (2003). Physical parameters of helium-rich subdwarf B stars from medium resolution optical spectroscopy. *A&A*, 402:335–342. (Cited on pages 19, 77 and 188.)

Ahmad, A. and Jeffery, C. S. (2004). The evolution of helium-rich subdwarf-B stars. *Ap&SS*, 291:253–260. (Cited on page 19.)

Ahmad, A. and Jeffery, C. S. (2005). Discovery of pulsation in a helium-rich subdwarf B star. *A&A*, 437:L51–L54. (Cited on pages 19 and 42.)

Ahn, C. P., Alexandroff, R., Allende Prieto, C., Anderson, S. F., Anderton, T., Andrews, B. H., Aubourg, É., Bailey, S., Balbinot, E., Barnes, R., Bautista, J., Beers, T. C., Beifiori, A., Berlind, A. A., Bhardwaj, V., Bizyaev, D., Blake, C. H., Blanton, M. R., Blomqvist, M., Bochanski, J. J.,

# REFERENCES

Bolton, A. S., Borde, A., Bovy, J., Brandt, W. N., Brinkmann, J., Brown, P. J., Brownstein, J. R., Bundy, K., Busca, N. G., Carithers, W., Carnero, A. R., Carr, M. A., Casetti-Dinescu, D. I., Chen, Y., Chiappini, C., Comparat, J., Connolly, N., Crepp, J. R., Cristiani, S., Croft, R. A. C., Cuesta, A. J., da Costa, L. N., Davenport, J. R. A., Dawson, K. S., de Putter, R., De Lee, N., Delubac, T., Dhital, S., Ealet, A., Ebelke, G. L., Edmondson, E. M., Eisenstein, D. J., Escoffier, S., Esposito, M., Evans, M. L., Fan, X., Femenía Castellá, B., Fernández Alvar, E., Ferreira, L. D., Filiz Ak, N., Finley, H., Fleming, S. W., Font-Ribera, A., Frinchaboy, P. M., García-Hernández, D. A., García Pérez, A. E., Ge, J., Gé nova-Santos, R., Gillespie, B. A., Girardi, L., González Hernández, J. I., Grebel, E. K., Gunn, J. E., Guo, H., Haggard, D., Hamilton, J.-C., Harris, D. W., Hawley, S. L., Hearty, F. R., Ho, S., Hogg, D. W., Holtzman, J. A., Honscheid, K., Huehnerhoff, J., Ivans, I. I., Ivezić, Ž., Jacobson, H. R., Jiang, L., Johansson, J., Johnson, J. A., Kauffmann, G., Kirkby, D., Kirkpatrick, J. A., Klaene, M. A., Knapp, G. R., Kneib, J.-P., Le Goff, J.-M., Leauthaud, A., Lee, K.-G., Lee, Y. S., Long, D. C., Loomis, C. P., Lucatello, S., Lundgren, B., Lupton, R. H., Ma, B., Ma, Z., MacDonald, N., Mack, C. E., Mahadevan, S., Maia, M. A. G., Majewski, S. R., Makler, M., Malanushenko, E., Malanushenko, V., Manchado, A., Mandelbaum, R., Manera, M., Maraston, C., Margala, D., Martell, S. L., McBride, C. K., McGreer, I. D., McMahon, R. G., Ménard, B., Meszaros, S., Miralda-Escudé, J., Montero-Dorta, A. D., Montesano, F., Morrison, H. L., Muna, D., Munn, J. A., Murayama, H., Myers, A. D., Neto, A. F., Nguyen, D. C., Nichol, R. C., Nidever, D. L., Noterdaeme, P., Nuza, S. E., Ogando, R. L. C., Olmstead, M. D., Oravetz, D. J., Owen, R., Padmanabhan, N., Palanque-Delabrouille, N., Pan, K., Parejko, J. K., Parihar, P., Pâris, I., Pattarakijwanich, P., Pepper, J., Percival, W. J., Pérez- Fournon, I., Pérez-Ràfols, I., Petitjean, P., Pforr, J., Pieri, M. M., Pinsonneault, M. H., Porto de Mello, G. F., Prada, F., Price-Whelan, A. M., Raddick, M. J., Rebolo, R., Rich, J., Richards, G. T., Robin, A. C., Rocha-Pinto, H. J., Rockosi, C. M., Roe, N. A., Ross, A. J., Ross, N. P., Rossi, G., Rubiño-Martin, J. A., Samushia, L., Sanchez Almeida, J., Sánchez, A. G., Santiago, B., Sayres, C., Schlegel, D. J., Schlesinger, K. J., Schmidt, S. J., Schneider, D. P., Schultheis, M., Schwope, A. D., Scóccola, C. G., Seljak, U., Sheldon, E., Shen, Y., Shu, Y., Simmerer, J., Simmons, A. E., Skibba, R. A., Skrutskie, M. F., Slosar, A., Sobreira, F., Sobeck, J. S., Stassun, K. G., Steele, O., Steinmetz, M., Strauss, M. A., Streblyanska, A., Suzuki, N., Swanson, M. E. C., Tal, T., Thakar, A. R., Thomas, D., Thompson, B. A., Tinker, J. L., Tojeiro, R., Tremonti, C. A., Vargas Magaña, M., Verde, L., Viel, M., Vikas, S. K., Vogt, N. P., Wake, D. A., Wang, J., Weaver, B. A., Weinberg, D. H., Weiner, B. J., West, A. A., White, M., Wilson, J. C., Wisniewski, J. P., Wood-Vasey, W. M., Yanny, B., Yèche, C., York, D. G., Zamora, O., Zasowski, G., Zehavi, I., Zhao, G.-B., Zheng, Z., Zhu, G., and Zinn, J. C. (2012). The Ninth Data Release of the Sloan Digital Sky Survey: First Spectroscopic Data from the SDSS-III Baryon Oscillation Spectroscopic Survey. *The Astrophysical Journal Supplement Series*, 203:21. (Cited on page 171.)

Altmann, M., Edelmann, H., and de Boer, K. S. (2004). Studying the populations of our Galaxy using the kinematics of sdB stars. *A&A*, 414:181–201. (Cited on pages 74, 82 and 83.)

Appenzeller, I. (2013). *Introduction to Astronomical Spectroscopy.* (Cited on pages xiii and 31.)

Arenou, F., Luri, X., Babusiaux, C., Fabricius, C., Helmi, A., A., R., and et al. (2017). Gaia data release 1. catalogue data validation: procedures, statistics and conclusions. *A&A special Gaia volume.* (Cited on page 80.)

Asplund, M., Gustafsson, B., Kiselman, D., and Eriksson, K. (1997). Line-blanketed model atmospheres for R Coronae Borealis stars and hydrogen-deficient carbon stars. *A&A*, 318:521–534. (Cited on page 193.)

Astraatmadja, T. L. and Bailer-Jones, C. A. L. (2016). Estimating distances from parallaxes. III. Distances of two million stars in the Gaia DR1 catalogue. *ArXiv e-prints.* (Cited on pages 81 and 154.)

Aznar Cuadrado, R. and Jeffery, C. S. (2002). Physical parameters for subdwarf B stars with composite spectra. *A&A*, 385:131–142. (Cited on pages 128 and 154.)

Bailer-Jones, C. A. L. (2015). Estimating Distances from Parallaxes. *PASP*, 127:994. (Cited on page 98.)

Ballester, P., Modigliani, A., Boitquin, O., Cristiani, S., Hanuschik, R., Kaufer, A., and Wolf, S. (2000). The UVES Data Reduction Pipeline. *The Messenger*, 101:31–36. (Cited on pages 35 and 43.)

Banik, I. and Zhao, H. (2018). The escape velocity curve of the Milky Way in modified Newtonian dynamics. *MNRAS*, 473:419–430. (Cited on page 108.)

Barbier-Brossat, M. and Figon, P. (2000). Catalogue général de vitesses radiales moyennes pour les étoiles galactiques. Mean radial velocities catalog of galactic stars. *A&AS*, 142:217–223. (Cited on page 169.)

Barnes, S. I., Cottrell, P. L., Albrow, M. D., Frost, N., Graham, G., Kershaw, G., Ritchie, R., Jones, D., Sharples, R., Bramall, D., Schmoll, J., Luke, P., Clark, P., Tyas, L., Buckley, D. A. H., and Brink, J. (2008). The optical design of the Southern African Large Telescope high resolution spectrograph: SALT HRS. In *Society of Photo-Optical Instrumentation Engineers (SPIE) Conference Series*, volume 7014 of *Society of Photo-Optical Instrumentation Engineers (SPIE) Conference Series*. (Cited on pages xiii and 32.)

Beers, T. C., Doinidis, S. P., Griffin, K. E., Preston, G. W., and Shectman, S. A. (1992). Spectroscopy of hot stars in the Galactic halo. *AJ*, 103:267–296. (Cited on pages 154 and 155.)

Beers, T. C., Rossi, S., O'Donoghue, D., Kilkenny, D., Stobie, R. S., Koen, C., and Wilhelm, R. (2001). VizieR Online Data Catalog: A-G star metallicity (Beers+, 2001). *VizieR Online Data Catalog*, 732:451. (Cited on page 155.)

Bergeat, J., Knapik, A., and Rutily, B. (2002). VizieR Online Data Catalog: Carbon-rich giants in the HR diagram (Bergeat+, 2002). *VizieR Online Data Catalog*, pages J/A+A/390/967. (Cited on page 193.)

Bland-Hawthorn, J. and Gerhard, O. (2016). The Galaxy in Context: Structural, Kinematic, and Integrated Properties. *Annual Review of Astronomy and Astrophysics*, 54:529–596. (Cited on page 111.)

Bobylev, V. V. (2006). Kinematics of the Gould Belt based on open clusters. *Astronomy Letters*, 32:816–826. (Cited on pages 169 and 171.)

Bobylev, V. V., Goncharov, G. A., and Bajkova, A. T. (2007). VizieR Online Data Catalog: Orion Spiral Arm CAtalogue (OSACA) (Bobylev+, 2006). *VizieR Online Data Catalog*, 908:30821. (Cited on page 154.)

Bovy, J. (2011). *Dynamical Inference in the Milky Way*. PhD thesis, New York University. (Cited on page 89.)

Bovy, J. (2015). galpy: A python Library for Galactic Dynamics. *ApJ*, 216:29. (Cited on pages 7, 8, 9 and 85.)

Brown, W. R. (2015). Hypervelocity Stars. *ARA&A*, 53:15–49. (Cited on page 90.)

Brown, W. R., Beers, T. C., Wilhelm, R., Allende Prieto, C., Geller, M. J., Kenyon, S. J., and Kurtz, M. J. (2008). The Century Survey Galactic Halo Project III: A Complete 4300 DEG$^2$ Survey of Blue Horizontal Branch Stars in the Metal-Weak Thick Disk and Inner Halo. *AJ*, 135:564–574. (Cited on page 154.)

Casagrande, L., Schoenrich, R., Asplund, M., Cassisi, S., Ramirez, I., Melendez, J., Bensby, T., and Feltzing, S. (2011). VizieR Online Data Catalog: Geneva-Copenhagen survey re-analysis (Casagrande+, 2011). *VizieR Online Data Catalog*, pages J/A+A/530/A138. (Cited on page 193.)

Castellani, M. and Castellani, V. (1993). Mass loss in globular cluster red giants - an evolutionary investigation. *ApJ*, 407:649–656. (Cited on pages 13 and 122.)

Charpinet, S., Fontaine, G., Brassard, P., and Dorman, B. (1996). The Potential of Asteroseismology for Hot, Subdwarf B Stars: A New Class of Pulsating Stars? *ApJ*, 471:L103–L106. (Cited on page 17.)

## REFERENCES

Clayton, G. C. (1996). The R Coronae Borealis Stars. *PASP*, 108:225. (Cited on pages 12 and 96.)

Clayton, G. C. (2012). What Are the R Coronae Borealis Stars? *Journal of the American Association of Variable Star Observers (JAAVSO)*, 40:539. (Cited on page 96.)

Clayton, G. C., Geballe, T. R., and Zhang, W. (2013). Variable Winds and Dust Formation in R Coronae Borealis Stars. *AJ*, 146:23. (Cited on page 169.)

Colin, J., de Boer, K. S., Dauphole, B., Ducourant, C., Dulou, M. R., Geffert, M., Le Campion, J.-F., Moehler, S., Odenkirchen, M., Schmidt, J. H. K., and Theissen, A. (1994). Kinematics of hot subdwarfs. *A&A*, 287:38–42. (Cited on page 82.)

Copperwheat, C. M., Morales-Rueda, L., Marsh, T. R., Maxted, P. F. L., and Heber, U. (2011). Radial-velocity measurements of subdwarf B stars. *MNRAS*, 415:1381–1395. (Cited on pages 77 and 155.)

Crause, L. A., Sharples, R. M., Bramall, D. G., Schmoll, J., Clark, P., Younger, E. J., Tyas, L. M. G., Ryan, S. G., Brink, J. D., Strydom, O. J., Buckley, D. A. H., Wilkinson, M., Crawford, S. M., and Depagne, É. (2014). Performance of the Southern African Large Telescope (SALT) High Resolution Spectrograph (HRS). In *Society of Photo-Optical Instrumentation Engineers (SPIE) Conference Series*, volume 9147 of *Society of Photo-Optical Instrumentation Engineers (SPIE) Conference Series*, page 91476T. (Cited on pages xix and 38.)

Crawford, S. M. (2015). pyhrs: Spectroscopic data reduction package for SALT. Astrophysics Source Code Library. (Cited on page 39.)

Crawford, S. M., Crause, L., Depagne, É., Ilkiewicz, K., Schroeder, A., Kuhn, R., Hettlage, C., Romero Colmenaro, E., Kniazev, A., and Väisänen, P. (2016). Data reductions and data quality for the high resolution spectrograph on the Southern African Large Telescope. In *Ground-based and Airborne Instrumentation for Astronomy VI*, volume 9908, page 99082L. (Cited on page 60.)

Crowther, P. A. (2008a). Physical and Wind Properties of [WC] Stars. In Werner, A. and Rauch, T., editors, *Hydrogen-Deficient Stars*, volume 391, page 83. (Cited on page 11.)

Crowther, P. A. (2008b). Physical and Wind Properties of [WC] Stars. In Werner, A. and Rauch, T., editors, *Hydrogen-Deficient Stars*, volume 391 of *Astronomical Society of the Pacific Conference Series*, page 83. (Cited on page 126.)

Darius, J., Giddings, J. R., and Wilson, R. (1979). Discovery of mass loss from hot subdwarfs. In Willis, A. J., editor, *The First Year of IUE*, pages 363–370. (Cited on page 193.)

de Bruijne, J. H. J. and Eilers, A.-C. (2012). Radial velocities for the HIPPARCOS-Gaia Hundred-Thousand-Proper-Motion project. *A&A*, 546:A61. (Cited on page 169.)

Dekker, H., D'Odorico, S., Kaufer, A., Delabre, B., and Kotzlowski, H. (2000). Design, construction, and performance of UVES, the echelle spectrograph for the UT2 Kueyen Telescope at the ESO Paranal Observatory. In Iye, M. and Moorwood, A. F., editors, *Optical and IR Telescope Instrumentation and Detectors*, volume 4008 of *Society of Photo-Optical Instrumentation Engineers (SPIE) Conference Series*, pages 534–545. (Cited on pages xix and 34.)

Dorman, B., Rood, R. T., and O'Connell, R. W. (1993). Ultraviolet Radiation from Evolved Stellar Populations. I. Models. *ApJ*, 419:596. (Cited on page 133.)

Downes, R. A. (1986). The KPD survey for galactic plane ultraviolet-excess objects Space densities of white dwarfs and subdwarfs. *ApJS*, 61:569–584. (Cited on page 155.)

Drilling, J. S., Jeffery, C. S., Heber, U., Moehler, S., and Napiwotzki, R. (2013). An MK-like system of spectral classification for hot subdwarfs. *A&A*, 551:A31. (Cited on pages 77 and 79.)

Drilling, J. S., Moehler, S., Jeffery, C. S., Heber, U., and Napiwotzki, R. (2003). Spectral Classification of Hot Subdwarfs. In Gray, R. O., Corbally, C. J., and Philip, A. G. D., editors, *The Garrison Festschrift*, page 27. (Cited on page 9.)

Durand, S., Acker, A., and Zijlstra, A. (1998). The kinematics of 867 galactic planetary nebulae. *Astronomy and Astrophysics Supplement Series*, 132:13–20. (Cited on page 171.)

Edelmann, H. (2003). *Spectroscopic analyses of subluminous B stars: observational constraints for the theory of stellar evolution, pulsation, and diffusion*. PhD thesis, Friedrich-Alexander University Erlangen-Nürnberg. (Cited on pages 79, 82, 154, 155 and 188.)

ESO CPL Development Team (2015). EsoRex: ESO Recipe Execution Tool. Astrophysics Source Code Library. (Cited on page 43.)

Fontaine, G., Brassard, P., Charpinet, S., Green, E. M., Chayer, P., Billères, M., and Randall, S. K. (2003). A Driving Mechanism for the Newly Discovered Long-Period Pulsating Subdwarf B Stars. *ApJ*, 597:518–534. (Cited on page 18.)

Gaia Collaboration, Brown, A. G. A., Vallenari, A., Prusti, T., de Bruijne, J. H. J., Mignard, F., Drimmel, R., Babusiaux, C., Bailer-Jones, C. A. L., Bastian, U., and et al. (2016a). Gaia Data Release 1. Summary of the astrometric, photometric, and survey properties. *A&A*, 595:A2. (Cited on pages 80 and 97.)

Gaia Collaboration, Prusti, T., de Bruijne, J. H. J., Brown, A. G. A., Vallenari, A., Babusiaux, C., Bailer-Jones, C. A. L., Bastian, U., Biermann, M., Evans, D. W., and et al. (2016b). The Gaia mission. *A&A*, 595:A1. (Cited on pages 80 and 97.)

Geier, S., Kupfer, T., Heber, U., Schaffenroth, V., Barlow, B. N., Østensen, R. H., O'Toole, S. J., Ziegerer, E., Heuser, C., Maxted, P. F. L., Gänsicke, B. T., Marsh, T. R., Napiwotzki, R., Brünner, P., Schindewolf, M., and Niederhofer, F. (2015). The catalogue of radial velocity variable hot subluminous stars from the MUCHFUSS project. *A&A*, 577:A26. (Cited on pages 79, 82, 154 and 155.)

Geier, S., Marsh, T. R., Wang, B., Dunlap, B., Barlow, B. N., Schaffenroth, V., Chen, X., Irrgang, A., Maxted, P. F. L., Ziegerer, E., Kupfer, T., Miszalski, B., Heber, U., Han, Z., Shporer, A., Telting, J. H., Gänsicke, B. T., Østensen, R. H., O'Toole, S. J., and Napiwotzki, R. (2013). A progenitor binary and an ejected mass donor remnant of faint type Ia supernovae. *A&A*, 554:A54. (Cited on page 92.)

Geier, S., Østensen, R. H., Nemeth, P., Gentile Fusillo, N. P., Gänsicke, B. T., Telting, J. H., Green, E. M., and Schaffenroth, J. (2017). The population of hot subdwarf stars studied with Gaia. I. The catalog of known hot subdwarf stars. *A&A*, 600:A50. (Cited on pages xv, 10, 98, 99, 100, 102 and 126.)

Gontcharov, G. A. (2006). Radial velocities of 35495 Hipparcos stars in a common system. *Astronomical and Astrophysical Transactions*, 25:145–148. (Cited on pages 155 and 169.)

Goswami, A., Karinkuzhi, D., and Shantikumar, N. S. (2010). HE 1015-2050: Discovery of a Hydrogen-deficient Carbon Star at High Galactic Latitude. *ApJ*, 723:L238–L242. (Cited on page 96.)

Green, E. M., Fontaine, G., Reed, M. D., Callerame, K., Seitenzahl, I. R., White, B. A., Hyde, E. A., Østensen, R., Cordes, O., Brassard, P., Falter, S., Jeffery, E. J., Dreizler, S., Schuh, S. L., Giovanni, M., Edelmann, H., Rigby, J., and Bronowska, A. (2003). Discovery of A New Class of Pulsating Stars: Gravity-Mode Pulsators among Subdwarf B Stars. *ApJ*, 583:L31–L34. (Cited on page 18.)

Green, E. M., Guvenen, B., O'Malley, C. J., O'Connell, C. J., Baringer, B. P., Villareal, A. S., Carleton, T. M., Fontaine, G., Brassard, P., and Charpinet, S. (2011). The Unusual Variable Hot B Subdwarf LS IV$-14°116$. *ApJ*, 734:59. (Cited on pages 19, 20, 42, 57 and 139.)

## REFERENCES

Guerrero, M. A. and De Marco, O. (2013). Analysis of far-UV data of central stars of planetary nebulae: Occurrence and variability of stellar winds. *A&A*, 553:A126. (Cited on page 190.)

Han, Z., Podsiadlowski, P., Maxted, P. F. L., Marsh, T. R., and Ivanova, N. (2002). The origin of subdwarf B stars - I. The formation channels. *MNRAS*, 336:449–466. (Cited on page 91.)

Harrison, P. M. and Jeffery, C. S. (1997). A spectral analysis of the hydrogen-deficient star HD 144941. *A&A*, 323:177–182. (Cited on page 193.)

Heber, U. (1986). The atmosphere of subluminous B stars. II - Analysis of 10 helium poor subdwarfs and the birthrate of sdB stars. *A&A*, 155:33–45. (Cited on page 9.)

Heber, U. (2009). Hot Subdwarf Stars. *ARA&A*, 47:211–251. (Cited on page 9.)

Heber, U. (2016). Hot Subluminous Stars. *PASP*, 128(8):082001. (Cited on pages 10 and 15.)

Heber, U., Dreizler, S., Werner, K., Engels, D., and Hagen, H.-J. (1996). Helium-rich stars from the HS, PG and KPD surveys. In Jeffery, C. S. and Heber, U., editors, *Hydrogen Deficient Stars*, volume 96 of *Astronomical Society of the Pacific Conference Series*, page 241. (Cited on page 154.)

Heber, U., Jones, G., and Drilling, J. S. (1986). High resolution spectroscopy of six new extreme helium stars. In Hunger, K., Schoenberner, D., and Kameswara Rao, N., editors, *IAU Colloq. 87: Hydrogen Deficient Stars and Related Objects*, volume 128 of *Astrophysics and Space Science Library*, pages 67–72. (Cited on page 59.)

Heber, U. and Schoenberner, D. (1981). Colours and effective temperatures of extreme helium stars. *A&A*, 102:73–80. (Cited on page 126.)

Hema, B. P., Pandey, G., and Lambert, D. L. (2012). The Galactic R Coronae Borealis Stars: The $C_2$ Swan Bands, the Carbon Problem, and the $^{12}C/^{13}C$ Ratio. *ApJ*, 747:102. (Cited on page 193.)

Herald, J. E. and Bianchi, L. (2004). Far-Ultraviolet Spectroscopic Analyses of Four Central Stars of Planetary Nebulae. *ApJ*, 609:378–391. (Cited on page 190.)

Holberg, J. B., Barstow, M. A., and Sion, E. M. (1998). A High-Dispersion Spectroscopic Survey of the Hot White Dwarfs: The IUE NEWSIPS SWP Echelle Data Set. *The Astrophysical Journal Supplement Series*, 119:207–238. (Cited on page 190.)

Hubrig, S., Kurtz, D. W., Bagnulo, S., Szeifert, T., Schöller, M., Mathys, G., and Dziembowski, W. A. (2004). Measurements of magnetic fields over the pulsation cycle in six roAp stars with FORS 1 at the VLT. *A&A*, 415:661–669. (Cited on page 57.)

Hunger, K. and Kaufmann, J. P. (1973). Spectralphotometry and quantitative analysis of the hydrogen-deficient stars HD 144941 and CPD -69 2698. *A&A*, 25:261. (Cited on page 169.)

Husfeld, D., Butler, K., Heber, U., and Drilling, J. S. (1989). Non-LTE analysis of extremely helium-rich stars. The hot sdO stars LSE 153, 259 and 263. *A&A*, 222:150–170. (Cited on pages 129 and 193.)

Iben, I., J. (1984). On the frequency of planetary nebula nuclei powered by helium burning and on the frequency of white dwarfs with hydrogen-deficient atmospheres. *ApJ*, 277:333–354. (Cited on page 17.)

Irrgang, A., Wilcox, B., Tucker, E., and Schiefelbein, L. (2013). Milky Way mass models for orbit calculations. *A&A*, 549:A137. (Cited on page 81.)

Jeffery, C. S. (1998). Spectral analysis of the high-gravity extreme helium star LSIV+6 deg2. *MNRAS*, 294:391–398. (Cited on page 193.)

Jeffery, C. S. (2008). Hydrogen-Deficient Stars: An Introduction. In Werner, A. and Rauch, T., editors, *Hydrogen-Deficient Stars*, volume 391 of *Astronomical Society of the Pacific Conference Series*, page 3. (Cited on pages iv, 142 and 144.)

Jeffery, C. S. (2011). Photometric Variability of the Chemically Peculiar Hot Subdwarf LS IV-14 d116. *Information Bulletin on Variable Stars*, 5964. (Cited on page 19.)

Jeffery, C. S. (2017). GALEX J184559.8-413827: a new extreme helium star identified using SALT. *MNRAS*, 470:3557–3565. (Cited on pages 130 and 193.)

Jeffery, C. S., Ahmad, A., Naslim, N., and Kerzendorf, W. (2015a). Radial-velocity measurements of the pulsating zirconium star: LS IV$-14°116$. *MNRAS*, 446:1889–1894. (Cited on pages 19, 21 and 42.)

Jeffery, C. S., Baran, A. S., Behara, N. T., Kvammen, A., Martin, P., Naslim, N., Østensen, R. H., Preece, H. P., Reed, M. D., Telting, J. H., and Woolf, V. M. (2017). Discovery of a variable lead-rich hot subdwarf: UVO 0825+15. *MNRAS*, 465:3101–3124. (Cited on pages 42, 80 and 188.)

Jeffery, C. S., Drilling, J. S., and Heber, U. (1987). A radial velocity survey of extremely hydrogen-deficient stars. *MNRAS*, 226:317–339. (Cited on page 169.)

Jeffery, C. S. and Hamann, W. R. (2010). Stellar winds and mass loss from extreme helium stars. *MNRAS*, 404:1698–1710. (Cited on page 193.)

Jeffery, C. S., Hamill, P. J., Harrison, P. M., and Jeffers, S. V. (1998). Spectral analysis of the low-gravity extreme helium stars LSS 4357, LS II+33.5 deg and LSS 99. *A&A*, 340:476–482. (Cited on page 193.)

Jeffery, C. S. and Heber, U. (1993). Spectral analysis of DY Centauri, a hot R Coronae Borealis star with an unusually high hydrogen content. *A&A*, 270:167–176. (Cited on page 193.)

Jeffery, C. S., Heber, U., and Hamann, W. R. (1986). Ultraviolet spectroscopy of the hydrogen-deficient star HD 144941: The energy distribution and the stellar wind. In Rolfe, E. J., editor, *New Insights in Astrophysics. Eight Years of UV Astronomy with IUE*, volume 263 of *ESA Special Publication*, pages 369–372. (Cited on page 96.)

Jeffery, C. S., Heber, U., Hill, P. W., Dreizler, S., Drilling, J. S., Lawson, W. A., Leuenhagen, U., and Werner, K. (1996). A catalogue of hydrogen-deficient stars. In Jeffery, C. S. and Heber, U., editors, *Hydrogen Deficient Stars*, volume 96 of *Astronomical Society of the Pacific Conference Series*, page 471. (Cited on page 126.)

Jeffery, C. S., Heber, U., Hill, P. W., and Pollacco, D. (1988). High-resolution spectroscopy of the hot R CrB star MV Sgr. *MNRAS*, 231:175–189. (Cited on page 193.)

Jeffery, C. S., Hill, P. W., and Heber, U. (1999). The chemical composition of the pulsating helium star V652 Her. *A&A*, 346:491–500. (Cited on page 193.)

Jeffery, C. S., Kurtz, D., Shibahashi, H., Starling, R. L. C., Elkin, V., Montañés-Rodríguez, P., and McCormac, J. (2015b). Subaru and Swift observations of V652 Herculis: resolving the photospheric pulsation. *MNRAS*, 447:2836–2851. (Cited on pages 22, 23, 60, 66 and 169.)

Jeffery, C. S. and Ramsay, G. (2018). K2 spots rotation in the helium star HD144941. *MNRAS*, 475:L122–L124. (Cited on page 131.)

Jeffery, C. S. and Schönberner, D. (2006). Stellar archaeology: the evolving spectrum of FG Sagittae. *A&A*, 459:885–899. (Cited on page 18.)

Jeffery, C. S., Starling, R. L. C., Hill, P. W., and Pollacco, D. (2001a). Cyclic and secular variation in the temperatures and radii of extreme helium stars. *MNRAS*, 321:111–130. (Cited on page 193.)

# REFERENCES

Jeffery, C. S., Woolf, V. M., and Pollacco, D. L. (2001b). Time-resolved spectral analysis of the pulsating helium star V652 Her. *A&A*, 376:497–517. (Cited on pages 21, 43, 63 and 140.)

Justham, S., Wolf, C., Podsiadlowski, P., and Han, Z. (2009). Type Ia supernovae and the formation of single low-mass white dwarfs. *A&A*, 493:1081–1091. (Cited on page 92.)

Karl, C., Heber, U., Jeffery, S., Napiwotzki, R., and Geier, S. (2006). Spectroscopic Analysis of Sdb Binaries from the Spy Project. *Baltic Astronomy*, 15:151–158. (Cited on page 155.)

Kawka, A., Vennes, S., O'Toole, S., Németh, P., Burton, D., Kotze, E., and Buckley, D. A. H. (2015). New binaries among UV-selected, hot subdwarf stars and population properties. *MNRAS*, 450:3514–3548. (Cited on page 90.)

Keenan, P. C. and Barnbaum, C. (1997). The Spectrum Near Maximum Light of the Unusual R Coronae Borealis Variable DY Persei. *Publications of the Astronomical Society of the Pacific*, 109:969–976. (Cited on page 193.)

Keller, G. R., Bianchi, L., and Maciel, W. J. (2014). UV spectral analysis of very hot H-deficient [WCE]-type central stars of planetary nebulae: NGC 2867, NGC 5189, NGC 6905, Pb 6 and Sand 3. *MNRAS*, 442:1379–1395. (Cited on page 190.)

Kharchenko, N. V., Scholz, R.-D., Piskunov, A. E., Röser, S., and Schilbach, E. (2007a). Astrophysical supplements to the ASCC-2.5: Ia. Radial velocities of 55000 stars and mean radial velocities of 516 Galactic open clusters and associations. *Astronomische Nachrichten*, 328:889. (Cited on page 154.)

Kharchenko, N. V., Scholz, R. D., Piskunov, A. E., Röser, S., and Schilbach, E. (2007b). Astrophysical supplements to the ASCC-2.5: Ia. Radial velocities of 55000 stars and mean radial velocities of 516 Galactic open clusters and associations. *Astronomische Nachrichten*, 328:889. (Cited on page 169.)

Kilkenny, D., Crause, L. A., and van Wyk, F. (2005). Period changes in the pulsating extreme helium stars V652 Her and BX Cir. *MNRAS*, 361:559–564. (Cited on page 60.)

Kilkenny, D., Fontaine, G., Green, E. M., and Schuh, S. (2010). A Proposed Uniform Nomenclature for Pulsating Hot Subdwarf Stars. *Information Bulletin on Variable Stars*, 5927. (Cited on page 42.)

Kilkenny, D., Heber, U., and Drilling, J. S. (1988a). A catalogue of spectroscopically identified hot subdwarf stars. *South African Astronomical Observatory Circular*, 12:1–80. (Cited on page 105.)

Kilkenny, D., Heber, U., and Drilling, J. S. (1988b). A catalogue of spectroscopically identified hot subdwarf stars. *South African Astronomical Observatory Circular*, 12:1–80. (Cited on page 188.)

Kilkenny, D. and Koen, C. (1995). The detection of small-amplitude variations in the extreme helium star LSS 3184. *MNRAS*, 275:327–330. (Cited on page 59.)

Kilkenny, D., Koen, C., Stobie, R. S., O'Donoghue, D., Lynas-Gray, A. E., and Kawaler, S. D. (1997). A New Class of Pulsating Star Discovered in the EC Survey. In Philip, A. G. D., Liebert, J., Saffer, R., and Hayes, D. S., editors, *The Third Conference on Faint Blue Stars*, page 77. (Cited on pages 17 and 18.)

Kilkenny, D. and Muller, S. (1989). Radial velocities and spectral types for a sample of faint blue stars. *saaoc*, 13:69–82. (Cited on page 154.)

Kilkenny, D. and Pauls, L. (1990). Analysis of high-latitude blue stars. V - Some low-dispersion results. *MNRAS*, 244:133–137. (Cited on pages 19 and 41.)

Kilkenny, D. and Worters, H. L. (2014). The ephemeris of the pulsating Helium star BX Cir. *MNRAS*, 439:2074–2077. (Cited on pages 60 and 61.)

Kleinman, S. J., Kepler, S. O., Koester, D., Pelisoli, I., Peçanha, V., Nitta, A., Costa, J. E. S., Krzesinski, J., Dufour, P., Lachapelle, F. R., Bergeron, P., Yip, C.-W., Harris, H. C., Eisenstein, D. J., Althaus, L., and Córsico, A. (2013). SDSS DR7 White Dwarf Catalog. *The Astrophysical Journal Supplement Series*, 204:5. (Cited on page 190.)

Kordopatis, G., Hill, V., Irwin, M., Gilmore, G., Wyse, R. F. G., Tolstoy, E., de Laverny, P., Recio-Blanco, A., Battaglia, G., and Starkenburg, E. (2013). VizieR Online Data Catalog: Foreground Galactic stars properties (Kordopatis+, 2013). *VizieR Online Data Catalog*, 355:50012. (Cited on page 154.)

Kupfer, T., Geier, S., Heber, U., Østensen, R. H., Barlow, B. N., Maxted, P. F. L., Heuser, C., Schaffenroth, V., and Gänsicke, B. T. (2015). Hot subdwarf binaries from the MUCHFUSS project. Analysis of 12 new systems and a study of the short-period binary population. *A&A*, 576:A44. (Cited on page 128.)

Kupfer, T., Przybilla, N., Heber, U., Jeffery, C. S., Behara, N. T., and Butler, K. (2017). Quantitative spectroscopy of extreme helium stars Model atmospheres and a non-LTE abundance analysis of BD+10deg2179. *MNRAS*, 471:877–890. (Cited on pages 130 and 193.)

Kurtz, D. W., Elkin, V. G., and Mathys, G. (2005). Probing the magnetoacoustic boundary layer in the peculiar magnetic star 33 Lib (HD 137949)*. *MNRAS*, 358:L6–L10. (Cited on page 52.)

La Palombara, N., Esposito, P., Mereghetti, S., Novara, G., and Tiengo, A. (2015). Follow-up observations of X-ray emitting hot subdwarf stars: the He-rich sdO BD +37° 1977. *A&A*, 580:A56. (Cited on page 193.)

Landolt, A. U. (1975). On the optical variability of the helium stars HD 160641 and BD +13 3224. *ApJ*, 196:789–790. (Cited on page 20.)

Lang, K. R. (1974). *Astrophysical formulae: A compendium for the physicist and astrophysicist.* (Cited on page 124.)

Lenz, P. and Breger, M. (2005). Period04 User Guide. *Communications in Asteroseismology*, 146:53–136. (Cited on page 46.)

Lindegren, L., Lammers, U., Bastian, U., Hernández, J., Klioner, S., Hobbs, D., Bombrun, A., Michalik, D., Ramos-Lerate, M., Butkevich, A., Comoretto, G., Joliet, E., Holl, B., Hutton, A., Parsons, P., Steidelmüller, H., Abbas, U., Altmann, M., Andrei, A., Anton, S., Bach, N., Barache, C., Becciani, U., Berthier, J., Bianchi, L., Biermann, M., Bouquillon, S., Bourda, G., Brüsemeister, T., Bucciarelli, B., Busonero, D., Carlucci, T., Castañeda, J., Charlot, P., Clotet, M., Crosta, M., Davidson, M., de Felice, F., Drimmel, R., Fabricius, C., Fienga, A., Figueras, F., Fraile, E., Gai, M., Garralda, N., Geyer, R., González-Vidal, J. J., Guerra, R., Hambly, N. C., Hauser, M., Jordan, S., Lattanzi, M. G., Lenhardt, H., Liao, S., Löffler, W., McMillan, P. J., Mignard, F., Mora, A., Morbidelli, R., Portell, J., Riva, A., Sarasso, M., Serraller, I., Siddiqui, H., Smart, R., Spagna, A., Stampa, U., Steele, I., Taris, F., Torra, J., van Reeven, W., Vecchiato, A., Zschocke, S., de Bruijne, J., Gracia, G., Raison, F., Lister, T., Marchant, J., Messineo, R., Soffel, M., Osorio, J., de Torres, A., and O'Mullane, W. (2016). Gaia Data Release 1. Astrometry: one billion positions, two million proper motions and parallaxes. *A&A*, 595:A4. (Cited on page 80.)

Liu, J.-C. and Zhu, Z. (2010). Rotation curve of the Galactic outer disk derived from radial velocities and UCAC3 proper motions of carbon stars. *Research in Astronomy and Astrophysics*, 10:541–552. (Cited on page 169.)

Liu, Z.-W., Pakmor, R., Seitenzahl, I. R., Hillebrandt, W., Kromer, M., Röpke, F. K., Edelmann, P., Taubenberger, S., Maeda, K., Wang, B., and Han, Z. W. (2013). The Impact of Type Ia Supernova Explosions on Helium Companions in the Chandrasekhar-mass Explosion Scenario. *ApJ*, 774:37. (Cited on page 93.)

# REFERENCES

Luo, A.-L., Zhao, Y.-H., Zhao, G., Deng, L.-C., Liu, X.-W., Jing, Y.-P., Wang, G., Zhang, H.-T., Shi, J.-R., Cui, X.-Q., Chu, Y.-Q., Li, G.-P., Bai, Z.-R., Wu, Y., Cai, Y., Cao, S.-Y., Cao, Z.-H., Carlin, J. L., Chen, H.-Y., Chen, J.-J., Chen, K.-X., Chen, L., Chen, X.-L., Chen, X.-Y., Chen, Y., Christlieb, N., Chu, J.-R., Cui, C.-Z., Dong, Y.-Q., Du, B., Fan, D.-W., Feng, L., Fu, J.-N., Gao, P., Gong, X.-F., Gu, B.-Z., Guo, Y.-X., Han, Z.-W., He, B.-L., Hou, J.-L., Hou, Y.-H., Hou, W., Hu, H.-Z., Hu, N.-S., Hu, Z.-W., Huo, Z.-Y., Jia, L., Jiang, F.-H., Jiang, X., Jiang, Z.-B., Jin, G., Kong, X., Kong, X., Lei, Y.-J., Li, A.-H., Li, C.-H., Li, G.-W., Li, H.-N., Li, J., Li, Q., Li, S., Li, S.-S., Li, X.-N., Li, Y., Li, Y.-B., Li, Y.-P., Liang, Y., Lin, C.-C., Liu, C., Liu, G.-R., Liu, G.-Q., Liu, Z.-G., Lu, W.-Z., Luo, Y., Mao, Y.-D., Newberg, H., Ni, J.-J., Qi, Z.-X., Qi, Y.-J., Shen, S.-Y., Shi, H.-M., Song, J., Song, Y.-H., Su, D.-Q., Su, H.-J., Tang, Z.-H., Tao, Q.-S., Tian, Y., Wang, D., Wang, D.-Q., Wang, F.-F., Wang, G.-M., Wang, H., Wang, H.-C., Wang, J., Wang, J.-N., Wang, J.-L., Wang, J.-P., Wang, J.-X., Wang, L., Wang, M.-X., Wang, S.-G., Wang, S.-Q., Wang, X., Wang, Y.-N., Wang, Y., Wang, Y.-F., Wang, Y.-F., Wei, P., Wei, M.-Z., Wu, H., Wu, K.-F., Wu, X.-B., Wu, Y.-Z., Xing, X.-Z., Xu, L.-Z., Xu, X.-Q., Xu, Y., Yan, T.-S., Yang, D.-H., Yang, H.-F., Yang, H.-Q., Yang, M., Yao, Z.-Q., Yu, Y., Yuan, H., Yuan, H.-B., Yuan, H.-L., Yuan, W.-M., Zhai, C., Zhang, E.-P., Zhang, H.-W., Zhang, J.-N., Zhang, L.-P., Zhang, W., Zhang, Y., Zhang, Y.-X., Zhang, Z.-C., Zhao, M., Zhou, F., Zhou, X., Zhu, J., Zhu, Y.-T., Zou, S.-C., and Zuo, F. (2015). The first data release (DR1) of the LAMOST regular survey. *Research in Astronomy and Astrophysics*, 15:1095. (Cited on page 154.)

Luri, X., Brown, A. G. A., Sarro, L. M., Arenou, F., Bailer-Jones, C. A. L., Castro-Ginard, A., de Bruijne, J., Prusti, T., Babusiaux, C., and Delgado, H. E. (2018). Gaia Data Release 2: using Gaia parallaxes. *ArXiv e-prints*. (Cited on page 98.)

Ma, X., Hopkins, P. F., Wetzel, A. R., Kirby, E. N., Angles-Alcazar, D., Faucher-Giguere, C.-A., Keres, D., and Quataert, E. (2016). The Structure and Dynamical Evolution of the Stellar Disk of a Simulated Milky Way-Mass Galaxy. *ArXiv e-prints*. (Cited on page 88.)

Marcolino, W. L. F., Hillier, D. J., de Araujo, F. X., and Pereira, C. B. (2007). Detailed Far-Ultraviolet to Optical Analysis of Four [WR] Stars. *ApJ*, 654:1068–1086. (Cited on page 190.)

Martin, P. and Jeffery, C. S. (2017). LS IV$-14°116$ : A Time-Resolved Spectroscopic Study. *Open Astronomy*, 26:240–245. (Cited on page 41.)

Martin, P., Jeffery, C. S., Naslim, N., and Woolf, V. M. (2017). Kinematics of Subluminous O and B Stars by Surface Helium Abundance. *MNRAS*, 467:68–82. (Cited on pages 41, 73 and 169.)

Maxted, P. f. L., Heber, U., Marsh, T. R., and North, R. C. (2001). The binary fraction of extreme horizontal branch stars. *MNRAS*, 326:1391–1402. (Cited on page 77.)

McDonald, I., Zijlstra, A. A., and Watson, R. A. (2017). VizieR Online Data Catalog: Parameters and IR excesses of Gaia DR1 stars (McDonald+, 2017). *VizieR Online Data Catalog*, page J/MNRAS/471/770. (Cited on page 193.)

Miller Bertolami, M. M. and Althaus, L. G. (2006). Full evolutionary models for PG 1159 stars. Implications for the helium-rich O(He) stars. *A&A*, 454:845–854. (Cited on pages 132 and 138.)

Miller Bertolami, M. M., Althaus, L. G., Unglaub, K., and Weiss, A. (2008). Modeling He-rich subdwarfs through the hot-flasher scenario. *A&A*, 491:253–265. (Cited on pages 126, 133 and 137.)

Miller Bertolami, M. M., Córsico, A. H., and Althaus, L. G. (2011). On the Challenging Variability of LS IV-14deg116: Pulsational Instabilities Excited by the epsilon-Mechanism. *ApJ*, 741:L3+. (Cited on page 139.)

Miyamoto, M. and Nagai, R. (1975). Three-dimensional models for the distribution of mass in galaxies. *PASJ*, 27:533–543. (Cited on pages 7 and 85.)

Moehler, S., Richtler, T., de Boer, K. S., Dettmar, R. J., and Heber, U. (1990). Hot subluminous stars at high galactic latitudes. I - Spectra and Stromgren photometry. *A&A*, 86:53–74. (Cited on page 9.)

Montañés Rodríguez, P. and Jeffery, C. S. (2002). Non-linear radial pulsation models for the early-type helium stars ¡ASTROBJ¿V652 Her¡/ASTROBJ¿ and ¡ASTROBJ¿BX Cir¡/ASTROBJ¿. *A&A*, 384:433–440. (Cited on page 21.)

Napiwotzki, R., Drechsel, H., Heber, U., Karl, C., Pauli, E., Christlieb, N., Hagen, H., Reimers, D., Koester, D., Moehler, S., Homeier, D., Leibundgut, B., Renzini, A., Marsh, T. R., Nelemans, G., and Yungelson, L. (2003). Search for double degenerate progenitors of supernovae type Ia with SPY. In D. de Martino, R. Silvotti, J.-E. Solheim, & R. Kalytis, editor, *NATO ASIB Proc. 105: White Dwarfs*, pages 39–+. (Cited on page 76.)

Naslim, N., Geier, S., Jeffery, C. S., Behara, N. T., Woolf, V. M., and Classen, L. (2012). The helium-rich subdwarf CPD–20 1123: a post-common-envelope binary evolving on to the extended horizontal branch. *MNRAS*, 423:3031–3038. (Cited on pages 91, 128, 154 and 188.)

Naslim, N., Jeffery, C. S., Ahmad, A., Behara, N. T., and Şahìn, T. (2010). Abundance analyses of helium-rich subluminous B stars. *MNRAS*, 409:582–590. (Cited on pages 79, 188 and 193.)

Naslim, N., Jeffery, C. S., Behara, N. T., and Hibbert, A. (2011). An extremely peculiar hot subdwarf with a 10 000-fold excess of zirconium, yttrium and strontium. *MNRAS*, 412:363–370. (Cited on pages 10, 19, 41, 44, 73, 80, 91, 128 and 188.)

Naslim, N., Jeffery, C. S., Hibbert, A., and Behara, N. T. (2013). Discovery of extremely lead-rich subdwarfs: does heavy metal signal the formation of subdwarf B stars? *MNRAS*, 434:1920–1929. (Cited on pages 10, 19, 73, 79, 80, 91 and 188.)

Navarro, J. F., Frenk, C. S., and White, S. D. M. (1996). The Structure of Cold Dark Matter Halos. *ApJ*, 462:563. (Cited on pages 7 and 85.)

Németh, P., Kawka, A., and Vennes, S. (2012). A selection of hot subluminous stars in the GALEX survey - II. Subdwarf atmospheric parameters. *MNRAS*, 427:2180–2211. (Cited on page 188.)

O'Toole, S. J. and Heber, U. (2006). Abundance studies of sdB stars using UV echelle HST/STIS spectroscopy. *A&A*, 452:579–590. (Cited on page 9.)

Paczynski, B. (1976). Common Envelope Binaries. In Eggleton, P., Mitton, S., and Whelan, J., editors, *Structure and Evolution of Close Binary Systems*, volume 73 of *IAU Symposium*, page 75. (Cited on page 14.)

Pandey, G., Kameswara Rao, N., Lambert, D. L., Jeffery, C. S., and Asplund, M. (2001). Abundance analyses of cool extreme helium stars. *MNRAS*, 324:937–959. (Cited on page 193.)

Pandey, G., Lambert, D. L., Jeffery, C. S., and Rao, N. K. (2006). An Analysis of Ultraviolet Spectra of Extreme Helium Stars and New Clues to Their Origins. *ApJ*, 638:454–471. (Cited on page 193.)

Pandey, G. and Reddy, B. E. (2006). Abundance analysis of the cool extreme helium star LSS3378. *MNRAS*, 369:1677–1682. (Cited on page 193.)

Pauli, E.-M., Napiwotzki, R., Altmann, M., Heber, U., Odenkirchen, M., and Kerber, F. (2003). 3D kinematics of white dwarfs from the SPY project. *A&A*, 400:877–890. (Cited on pages 86, 88 and 113.)

Pauli, E.-M., Napiwotzki, R., Heber, U., Altmann, M., and Odenkirchen, M. (2006). 3D kinematics of white dwarfs from the SPY project. II. *A&A*, 447:173–184. (Cited on pages 82, 83 and 88.)

Peña, M., Medina, S., and Stasińska, G. (2003). Characteristics of Planetary Nebulae with [WC] Central Stars. In Reyes-Ruiz, M. and Vázquez-Semadeni, E., editors, *Revista Mexicana de Astronomia y Astrofisica Conference Series*, volume 18 of *Revista Mexicana de Astronomia y Astrofisica Conference Series*, pages 84–89. (Cited on page 190.)

# REFERENCES

Pigott, E. and Englefield, H. C. (1797). On the Periodical Changes of Brightness of Two Fixed Stars. By Edward Pigott, Esq. Communicated by Sir Henry C. Englefield, Bart. F. R. S. *Philosophical Transactions of the Royal Society of London Series I*, 87:133–141. (Cited on page 11.)

Ramspeck, M., Heber, U., and Edelmann, H. (2001). Early type stars at high galactic latitudes. II. Four evolved B-type stars of unusual chemical composition. *A&A*, 379:235–244. (Cited on page 188.)

Randall, S. K., Bagnulo, S., Ziegerer, E., Geier, S., and Fontaine, G. (2015). The enigmatic He-sdB pulsator LS IV$-14°116$ : new insights from the VLT. *A&A*, 576:A65. (Cited on pages 41, 74, 81, 90 and 154.)

Rao, N. K. and Lambert, D. L. (2015). Mid-infrared variations of R Coronae Borealis stars. *MNRAS*, 447:3664–3677. (Cited on page 193.)

Rao, R., Girart, J. M., Lai, S.-P., and Marrone, D. P. (2014). Detection of a Magnetized Disk around a Very Young Protostar. *ApJ*, 780:L6. (Cited on page 193.)

Rauch, T. (1996). NLTE analysis of the extreme helium star HD 160641. In Jeffery, C. S. and Heber, U., editors, *Hydrogen Deficient Stars*, volume 96, page 174. (Cited on page 193.)

Reindl, N., Rauch, T., Werner, K., Kruk, J. W., and Todt, H. (2014). On helium-dominated stellar evolution: the mysterious role of the O(He)-type stars. *A&A*, 566:A116. (Cited on pages 13 and 190.)

Roeser, S., Demleitner, M., and Schilbach, E. (2010). The PPMXL Catalog of Positions and Proper Motions on the ICRS. Combining USNO-B1.0 and the Two Micron All Sky Survey (2MASS). *AJ*, 139:2440–2447. (Cited on page 80.)

Ryabchikova, T., Sachkov, M., Weiss, W. W., Kallinger, T., Kochukhov, O., Bagnulo, S., Ilyin, I., Landstreet, J. D., Leone, F., Lo Curto, G., Lüftinger, T., Lyashko, D., and Magazzù, A. (2007). Pulsation in the atmosphere of the roAp star HD 24712. I. Spectroscopic observations and radial velocity measurements. *A&A*, 462:1103–1112. (Cited on pages 55 and 57.)

Saio, H. (1993). Excitation of the pulsation in the helium star V 652 HER. *MNRAS*, 260:465–467. (Cited on pages 21 and 59.)

Saio, H. and Jeffery, C. S. (2002). Merged binary white dwarf evolution: rapidly accreting carbon-oxygen white dwarfs and the progeny of extreme helium stars. *MNRAS*, 333:121–132. (Cited on pages 131 and 137.)

Savitzky, A. and Golay, M. J. E. (1964). *Analytical Chemistry*, 36:1627–39. (Cited on page 44.)

Schlafly, E. F. and Finkbeiner, D. P. (2011). Measuring Reddening with Sloan Digital Sky Survey Stellar Spectra and Recalibrating SFD. *ApJ*, 737:103. (Cited on pages 81 and 123.)

Schuh, S., Huber, J., Green, E. M., O'Toole, S. J., Dreizler, S., Heber, U., and Fontaine, G. (2005). Discovery of a Long-Period Photometric Variation in the V361 Hya Star HS 0702+6043. In Koester, D. and Moehler, S., editors, *14th European Workshop on White Dwarfs*, volume 334 of *Astronomical Society of the Pacific Conference Series*, page 530. (Cited on page 18.)

Smart, R. L. and Nicastro, L. (2013). VizieR Online Data Catalog: The Initial Gaia Source List (IGSL) (Smart, 2013). *VizieR Online Data Catalog*, 1324. (Cited on page 129.)

Sperauskas, J. and Bartkevicius, A. (2002). Radial velocities of population II binary stars. I. *Astronomische Nachrichten*, 323:139–148. (Cited on page 155.)

Stroeer, A., Heber, U., Lisker, T., Napiwotzki, R., Dreizler, S., Christlieb, N., and Reimers, D. (2007). Hot subdwarfs from the ESO supernova Ia progenitor survey. II. Atmospheric parameters of subdwarf O stars. *A&A*, 462:269–280. (Cited on pages 79, 154 and 188.)

Thejll, P., Bauer, F., Saffer, R., Liebert, J., Kunze, D., and Shipman, H. L. (1994). Analysis of Helium-rich Subdwarf O Stars. I. NLTE Models, Methods, and FITS for 21 Palomar Green Survey sdO's. *ApJ*, 433:819. (Cited on page 188.)

Tillich, A., Heber, U., Geier, S., Hirsch, H., Maxted, P. F. L., Gänsicke, B. T., Marsh, T. R., Napiwotzki, R., Østensen, R. H., and Scholz, R.-D. (2011). The Hyper-MUCHFUSS project: probing the Galactic halo with sdB stars. *A&A*, 527:A137. (Cited on pages 92 and 93.)

Tisserand, P. (2012). Tracking down R Coronae Borealis stars from their mid-infrared WISE colours. *A&A*, 539:A51. (Cited on page 96.)

Tisserand, P., Clayton, G. C., Bessell, M. S., Welch, D. L., Kamath, D., Wood, P. R., Wils, P., Wyrzykowski, Ł., Mróz, P., and Udalski, A. (2018). A plethora of new R Coronae Borealis stars from a dedicated spectroscopic follow-up survey. *ArXiv e-prints*. (Cited on pages 11 and 96.)

van Leeuwen, F. (2007). Validation of the new Hipparcos reduction. *A&A*, 474:653–664. (Cited on page 82.)

Viton, M., Deleuil, M., Tobin, W., Prevot, L., and Bouchet, P. (1991). The Spacelab-1 Very Wide Field Survey of UV-excess objects. II - Analysis of 7 stars of various nature. *A&A*, 242:175–187. (Cited on pages 19 and 41.)

Warner, B. (1967). The hydrogen-deficient carbon stars. *MNRAS*, 137:119. (Cited on pages 11 and 96.)

Weidemann, V. and Bues, I. (1967). On the Scale of Bolometric Corrections. *Zeitschrift für Astrophysik*, 67:415. (Cited on page 124.)

Werner, K., Rauch, T., and Kepler, S. O. (2014). New hydrogen-deficient (pre-) white dwarfs in the sloan digital sky survey data release 10. *A&A*, 564:A53. (Cited on page 190.)

Wesemael, F., Green, R. F., and Liebert, J. (1985). Spectrophotometric and model-atmosphere analyses of the hot DO and DAO white dwarfs from the Palomar-Green survey. *ApJS*, 58:379–411. (Cited on pages 12 and 97.)

Woolf, V. M. and Jeffery, C. S. (2000). Physical properties of the pulsating hydrogen-deficient star lss 3184 (BX Cir). *A&A*, 358:1001–1006. (Cited on pages 21, 22 and 140.)

Woolf, V. M. and Jeffery, C. S. (2002). Temperature and gravity of the pulsating extreme helium star LSS 3184 ( BX Cir ) through its pulsation cycle. *A&A*, 395:535–540. (Cited on pages 21, 140 and 193.)

Yu, S. and Jeffery, C. S. (2011). Star formation history, double degenerates and Type Ia supernovae in the thin disc. *MNRAS*, 417:1392–1401. (Cited on page 91.)

Yuan, H. B. and Liu, X. W. (2013). Hunting for extremely faint planetary nebulae in the SDSS spectroscopic database. *MNRAS*, 436:718–739. (Cited on page 171.)

Zacharias, N., Monet, D. G., Levine, S. E., Urban, S. E., Gaume, R., and Wycoff, G. L. (2004). The Naval Observatory Merged Astrometric Dataset (NOMAD). In *American Astronomical Society Meeting Abstracts*, volume 36 of *Bulletin of the American Astronomical Society*, page 1418. (Cited on page 80.)

Zhang, X. and Jeffery, C. S. (2012). Evolutionary models for double helium white dwarf mergers and the formation of helium-rich hot subdwarfs. *MNRAS*, 419:452–464. (Cited on pages 14, 16, 59, 91, 126, 131, 132, 133, 137 and 138.)

Zhang, X., Jeffery, C. S., Chen, X., and Han, Z. (2014). Post-merger evolution of carbon-oxygen + helium white dwarf binaries and the origin of R Coronae Borealis and extreme helium stars. *MNRAS*, 445:660–673. (Cited on pages 91 and 137.)

Ziegerer, E., Volkert, M., Heber, U., Irrgang, A., Gänsicke, B. T., and Geier, S. (2015). Candidate hypervelocity stars of spectral type G and K revisited. *A&A*, 576:L14. (Cited on page 80.)